

Laboratory and Field Performance of Buried Steel-Reinforced High Density Polyethylene (SRHDPE) Pipes in a Ditch Condition under a Shallow Cover

By
Deep Kumar Khatri
B.E., Tribhuvan University, (Institute of Engineering, Pulchowk Campus), Nepal, 2007
M.Sc., University of Kansas, Kansas, USA, 2012.

Submitted to the Department of Civil, Environmental, and Architectural Engineering and Graduate Faculty of the University of Kansas in partial fulfillment of the requirements for the degree of Doctor of Philosophy

.....

Dr. Jie Han, Chairperson

Committee members

Dr. Ron B. Gonzalez, Associate Professor

.....

Dr. Robert L. Parsons, Professor

.....

Dr. Anil Misra, Professor

.....

Date Defended: May 19, 2014

Dr. Steven D. Schrock, Associate Professor

**The Dissertation Committee for Deep Kumar Khatri certifies that
this is the approved version of the following Dissertation:**

**Laboratory and Field Performance of Buried Steel-
Reinforced High Density Polyethylene (SRHDPE) Pipes in a
Ditch Condition under a Shallow Cover**

.....

Dr. Jie Han, Chairperson

Date approved: May 19, 2014

ABSTRACT

Metal and plastic pipes have been used extensively as storm sewers and buried drainage structures in transportation projects. Metal pipes have high strength and stiffness but are susceptible to corrosion from wastewaters containing acid, and from aggressive soils. Plastic pipes are resistant to corrosion, erosion, and biological attack but have certain disadvantages including lower long-term strength and stiffness (dimensional reliability), buckling, and tearing of pipe wall. To address the disadvantages of metal and plastic pipes, a new product, steel-reinforced high-density polyethylene (SRHDPE) pipe, has been developed and introduced to the market, which has high-strength steel reinforcing ribs wound helically and covered by corrosion-resistant high density polyethylene (HDPE) resin inside and outside. The steel reinforcement adds ring stiffness to the pipe to maintain the cross-section shape during installation and to support overburden stresses and traffic loading. The HDPE resin protects the steel against corrosion and provides a smooth inner wall. The combination of steel and plastic materials results in a strong and durable material with a smooth inner wall. Different methods are available for the design of metal and plastic pipes. The American Water Works Association (AWWA) Manual M11 (2004) provided the design procedure for metal pipes and the 2007 ASHTO LRFD Bridge Design Specifications had separate design procedures for metal and plastic pipes. However, it is not clear whether any of these procedures for metal and plastic pipes can be used to design an SRHDPE pipe. Moreover, no approved installation or design specification is available **SPECIFICALLY** for the SRHDPE pipes.

Some research has been conducted on SRHDPE pipes to understand the performance of SRHDPE pipes in the laboratory including the laboratory tests conducted by Khatri (2012). To investigate the performance of the pipe with various backfills, in addition to the laboratory tests

conducted by Khatri (2012) with the sand backfill, a laboratory test with the crushed stone backfill was conducted in a ditch condition under 2 feet of shallow cover. This was performed in a large geotechnical testing box 10 feet long x 6.6 feet wide x 6.6 feet high. Based on the laboratory testing and analysis on the SRHDPE pipes, it can be concluded that (1) the pipe wall-soil interface should be designed as a fully bonded interface to be conservative, (2) the Giroud and Han (2004) method and the simplified distribution method in the 2007 AASHTO LRFD Bridge Design Specifications reasonably predicted the pressures on the top of the SRHDPE pipes induced by static and cyclic loadings, (3) the modified Iowa formula (1958) under predicted the deflections of the SRHDPE pipes during the installation and over-predicted the deflections during static and cyclic loadings, (4) the formula provided by Masada (2000) can be comfortably used to determine the ratio of the vertical to horizontal deflection of the SRHDPE pipe, (5) the pipe wall area was enough to resist the wall thrust during installation and loadings, and (6) the highest measured strains recorded in steel and plastic during the installation and loadings in all the tests were within the permissible values.

The laboratory tests however have some limitations. For example, the installation procedure of the pipe in the test box may be different from the field installation due to the limited space and construction equipment in the laboratory. The laboratory box tests may have a boundary effect. Therefore, a field test was conducted to verify the lab test results. The results obtained in the field test were found in agreement with the results obtained for the laboratory test during the installation and the traffic loading.

ACKNOWLEDGEMENTS

First of all, I would like to express my deep appreciation to my advisor, Prof. Jie Han, for teaching and encouraging me both personally and professionally to meet challenges that I had never before thought possible. Under his tutelage I am motivated to strive for and achieve useful skills for my future careers. I would also like to thank Prof. Robert L. Parsons, Prof. Anil Misra, associate Prof. Steven D. Schrock, and associate Prof. Ron B. Gonzalez for their valuable comments and suggestion in the development and completion of this dissertation and serving as members on my examining committee.

This research was financially sponsored by the Kansas Department of Transportation (KDOT) through the Kansas Transportation Research and New-Developments Program (K-TRAN) program. Mr. James J. Brennan, the Chief Geotechnical Engineer of KDOT, was the monitor for this project. I would like to express my thanks to Kansas Department of Transportation for providing financial support. I am also grateful to Contech Construction Products, Inc. for providing DuroMaxx pipes and to Midwest Concrete Materials, Lawrence, Kansas, for providing Backfill and base course materials. I would like to express my thanks to the Douglas county, Kansas- public work for installing the pipes in the field test. The former laboratory manager at the Department of Civil, Environment, and Architectural Engineering at the University of Kansas (KU), Mr. Howard J. Weaver, and the current laboratory manager, Mr. Mathew Maksimowicz, provided great assistance to the laboratory testing at KU. The graduate students, Ryan Corey, Xiaohui Sun, Jun Guo, and Zhen Zhang, and the undergraduate students, Brandon W. Basgall and Byron Whitted, helped to construct the test sections. Dr. Jingshan Jiang and Danny Smyl provided great assistance during the construction of the test sections. The authors would like to express their appreciations to the organizations and the individuals for their

help and support. Finally I would like to thank my family and friends for their endless supports and love.

**Dedicated to my parents,
Mr. Ram Khatri and Mrs. Goma Khatri**

TABLE OF CONTENTS

ABSTRACT	iii
ACKNOWLEDGEMENT	v
List of Tables	xi
List of Figures	xiii
1 INTRODUCTION	1
1.1 Background	1
1.2 Problem Statement	3
1.3 Research Objectives	7
1.4 Research Methodology	7
1.5 Organization of Report	8
2 LITERATURE REVIEW	9
2.1 Loads on Pipes	9
2.2 Bedding and Backfill Materials	11
2.3 Minimum Soil Cover Requirements	13
2.4 Deflection	14
<i>2.4.1 Estimation of the Pipe Stiffness (PS)</i>	19
<i>2.4.2 Estimation of the Modulus of Soil Reaction (E')</i>	21
2.5 Pipe Thrust and Buckling	26
2.6 Profile Wall Pipes and Local Buckling	28
2.7 Strain	30
2.8 Existing Design Methods for Flexible pipes	32
<i>2.8.1 Metal Pipes</i>	32
<i>2.8.2 Plastic Pipes</i>	33
2.9 Performance of Pipes under Traffic Loads	34
<i>2.9.1 Field Tests</i>	35
<i>2.9.2 Laboratory Tests</i>	36
2.10 Performance of Steel-Reinforced High Density Polyethylene (SRHDPE) Plastic Pipes	38
CHAPTER 3 MATERIAL PROPERTIES	41
3.1 Steel-Reinforced High Density Polyethylene (SRHDPE) Pipe	41
<i>3.1.1 Parallel Plate Tests</i>	43
<i>3.1.2 Stub Compression Tests</i>	62
<i>3.1.3 Summery</i>	63
3.2 Soil Types and Properties	64
<i>3.2.1 Clayey Soil and Its Characteristics</i>	64

3.2.2 <i>Bedding and Backfill Soils and Their Characteristics</i>	69
3.2.3 <i>Base Coarse and Its Characteristics</i>	79
CHAPTER 4 LARGE SCALE PLATE LOADING BOX TEST	83
4.1 Large Geotechnical Testing Box and Test Sections	83
4.2 MTS Loading System	86
4.3 Instrumentation	89
4.3.1 <i>Displacement Transducers and Tell-Tales</i>	89
4.3.2 <i>Strain Gages</i>	92
4.3.3 <i>Earth Pressure Cells</i>	96
4.4 Data Acquisition System	97
4.5 Construction of Test Section	97
4.5.1 <i>Construction of Test Section 1</i>	98
4.5.2 <i>Construction of Test Section 2</i>	105
4.5.3 <i>Construction of Test Section 3</i>	106
4.6 Quality Control	109
4.7 Data Collection	112
CHAPTER 5 FIELD PIPE INSTALLATION AND TRAFFICKING TESTS	113
5.1 Test Pipe	114
5.2 Test Site and Test Sections	115
5.3 Instrumentation	118
5.3.1 <i>Displacement Transducers and Tell-Tales</i>	119
5.3.2 <i>Strain Gages</i>	120
5.3.3 <i>Earth Pressure Cells</i>	122
5.4 Data Acquisition System	123
5.5 Construction of Test Section	123
5.6 Quality Control	139
5.7 Data Collection	143
6 DATA ANALYSIS AND RESULTS	144
6.1 Test Results from Pipe Installation	144
6.1.1 <i>Earth Pressure Results</i>	145
6.1.2 <i>Pipe Deflection Results</i>	164
6.1.3 <i>Strain Results</i>	180
6.2 Static Plate Loading and Field Trafficking Test Results	194
6.2.1 <i>Vertical Deformation of Loading Plate</i>	194
6.2.2 <i>Earth Pressure Results</i>	196
6.2.3 <i>Pipe Deflection Results</i>	214
6.2.4 <i>Strain Results</i>	228
6.3 Cyclic Plate Loading Test Result	259

6.3.1	<i>Vertical Deformation of the Loading Plate</i>	259
6.3.2	<i>Maximum Earth Pressure Results</i>	264
6.3.3	<i>Pipe Deflection Results</i>	270
6.3.4	<i>Strain Results</i>	275
6.3.5	<i>Comparison of Static and Cyclic Test Results</i>	283
6.4	Safety against Structural Failure	290
6.4.1	<i>Wall Area of Pipe</i>	290
6.4.2	<i>Global Buckling</i>	292
6.4.3	<i>Strain Limit</i>	292
6.5	Handling and Installation Requirement	292
CHAPTER 7	CONCLUSIONS AND RECOMMENDATIONS	294
7.1	Conclusions	294
7.1.1	<i>Compression Tests in Air</i>	294
7.1.2	<i>Laboratory and Field Installation</i>	294
7.1.3	<i>Static and Cyclic Plate Loading Tests</i>	296
7.2	Recommendations	297
REFERENCES		299

LIST OF TABLES

Table 1.1	Comparison of corrugated steel, HDPE, and SRHDPE pipe	5
Table 2.1	Variation of bedding constant (k) with bedding angle (Goddard, 1992)	12
Table 2.2	Minimum cover over the top of the pipe (KDOT, 2007)	14
Table 2.3	Parameters for the USBR equation (Howard, 1981)	17
Table 2.4	Pressure generated by compaction efforts (McGrath et al., 1999, as cited by Masada and Sargand, 2007)	19
Table 2.5	Typical values of E' (psi) (Howard, 1977)	22
Table 2.6	Typical Values E' (psi) (Hartley and Duncan, 1978)	22
Table 3.1	Specification of SRHDPE pipe	42
Table 3.2	Calculated pipe stiffness and equivalent bending stress values	53
Table 3.3	Specification of HMA material (provided by contractor)	82
Table 4.1	Loading increment and magnitude	77
Table 6.1	Comparison of the earth pressure (psi) measured around the pipe in the field test	210
Table 6.2	Comparison of the measured and calculated (Foster and Ahlvin, 1954) earth pressure (psi) measured the pipe in the field test	212
Table 6.3	Comparison of the average measured crown pressure (psi) with the 2007 AASHTO LRFD Design Specifications and Giroud and Han (2004) methods.	212
Table 6.4	Comparison of the deflections of the pipe	224
Table 6.5	Horizontal to vertical deflection ratio	227
Table 6.6	Comparison of the calculated and measured strains of the pipe in the field	242

Table 6.7	Permanent deformations	263
Table 6.8	Comparisons of the earth pressures around the pipe and the deflections of the pipe	286
Table 6.9	Maximum measured strains on the steel and the plastic during the installation and loading	289

LIST OF FIGURES

Figure 1.1	Cross section and 3D view of an SRHDPE pipe	2
Figure 2.1	Pipe deflection and radii of curvature of a deflected ellipse shape	20
Figure 2.2	Percentage deflection of the unplasticized PVC pipe in the near side lane (Trott and Gaunt, 1976)	35
Figure 2.3	Relative variations of the vertical diameter to the horizontal diameter for twin-wall pipes (Faragher, 1997)	37
Figure 3.1	SRHDPE pipes (from manufacturer: Contech Construction Products Inc.)	42
Figure 3.2	Test setup and instrumentation for the parallel plate load test (Khatri, 2012)	44
Figure 3.3	Symbols, locations, and orientations of strain gages on the pipe (Khatri, 2012)	46
Figure 3.4	Strain gages on the steel and plastic surfaces (Khatri, 2012)	47
Figure 3.5	Deformed pipe shapes from the photogrammetry	48
Figure 3.6	Comparison of the load-horizontal deflection curves obtained by the photogrammetry method and the displacement transducer	50
Figure 3.7	Comparison of the deformed pipe shapes from photogrammetry with the standard elliptical shapes	50
Figure 3.8	Load-deflection responses	52
Figure 3.9	Relation between the vertical and horizontal deflections of the pipes	53
Figure 3.10	Circumferential and radial strains against the applied loads on the steel at the springline	56
Figure 3.11	Circumferential and radial strains against the applied loads on the steel surface at the crown and invert	57
Figure 3.12	Strains against the applied loads on the plastic surface	59
Figure 3.13	Comparison of strains developed on the steel rib and plastic surfaces in the radial direction at the springline	61
Figure 3.14	Specimen crushing in the stub compression test	62
Figure 3.15	Grain size distributions of the clayey soils	65
Figure 3.16	Flow curves of the clayey soils	66
Figure 3.17	Compaction curve for clay	67
Figure 3.18	Densities, vane shear strength, and CBR curves	68
Figure 3.19	Stress-strain curves at different moisture contents	68
Figure 3.20	Grain size distribution of the sand	70
Figure 3.21	Large direct shear box tests for the KR sand	71
Figure 3.22	A small box plate loading test for the KR sand	72
Figure 3.23	Grain size distributions of crushed stone	74
Figure 3.24	Large direct shear box tests for the crushed stone (CS-I)	75
Figure 3.25	A small box plate loading test for the crushed stone (CS-I)	76
Figure 3.26	Grain size distribution curves of the AB-3-I and AB-3-II aggregates (Pokharel, 2010)	78

Figure 3.27	Standard Proctor Compaction curve of AB-3-II aggregate	79
Figure 3.28	Standard Proctor Compaction curve of AB-3-I aggregate (Pokharel, 2010)	80
Figure 3.29	CBR curve of the AB-3 aggregate (Pokharel, 2010)	80
Figure 3.30	A small box plate loading test for the AB-3-I aggregate	81
Figure 4.1	Large geotechnical testing box and loading system	84
Figure 4.2	Plate loading test sections	85
Figure 4.3	Cyclic loading details	88
Figure 4.4	Loading plate	89
Figure 4.5	Displacement transducers inside the pipe section	90
Figure 4.6	Tell-tales fixed on the pipe specimen	91
Figure 4.7	Displacement transducers for deflection measurements	91
Figure 4.8	Strain gages fixed outside of pipe specimen	93
Figure 4.9	Strain gages fixed inside of the pipe specimen	93
Figure 4.10	Symbols, locations, and orientations of strain gages on the pipe	94
Figure 4.11	Earth pressure cells around the pipe section	97
Figure 4.12	3D perspective drawing of the box with the wooden shoring to make a trench of 6.6 ft x 4 ft x 4.5 ft	99
Figure 4.13	Compaction of surrounding soil using the vibratory plate compactor.	100
Figure 4.14	Compaction of surrounding soil using the jackhammer	100
Figure 4.15	A polyethylene plastic sheet placed to cover the exposed fat clay	101
Figure 4.16	Bedding material and the earth pressure cell EI0 installed at the invert of the pipe	102
Figure 4.17	Fully instrumented pipes in the trench in Test Section 1	103
Figure 4.18	Backfill up to the springline in Test Section 1	104
Figure 4.19	Earth pressure cells at the springline in Test Section 1	104
Figure 4.20	Compaction of base course using the vibratory plate compactor in Test Section 1	105
Figure 4.21	Backfilling up to the springline in Test Section 3	107
Figure 4.22	Earth pressure cells at the springline in Test Section 3	107
Figure 4.23	Earth pressure cells at the crown in Test Section 3	108
Figure 4.24	Cross section of test section including the soil lifts and earth pressure cells.	109
Figure 4.25	Vane shear test on the fat clay	110
Figure 4.26	LWD test on the fat clay	110
Figure 4.27	CBR profiles in Test Section 1	111
Figure 4.28	Displacement transducers fixed to a reference beam	112
Figure 5.1	Test SRHDPE pipes with bell and spigot joints in the field test	114
Figure 5.2	Location Map of the field test	115
Figure 5.3	Road section in the field test	116
Figure 5.4	Field Test Sections	117

Figure 5.5	Displacement transducers inside the pipe section in the field	119
Figure 5.6	Strain gages fixed outside of the pipe in the field	121
Figure 5.7	Symbols, locations, and orientations of the strain gages on the pipe in the field	121
Figure 5.8	Earth pressure cells around the pipe section in the field tests	123
Figure 5.9	An existing corrugated metal pipe under service	124
Figure 5.10	Construction of trench	125
Figure 5.11	Marking centerline before dumping bedding materials	126
Figure 5.12	Construction of the beddings	127
Figure 5.13	Marking wheel paths	127
Figure 5.14	The earth pressure cell E_{10} installed at the invert of the pipe	128
Figure 5.15	Galvanized steel end sections	129
Figure 5.16	Placing a pipe in the trench	129
Figure 5.17	Fully instrumented pipes in the trench	130
Figure 5.18	Backfilling and compacting with vibratory plate compactors and tamping hammer	131
Figure 5.19	Backfilling up to springline	132
Figure 5.20	A bobcat used to dump and level soils	133
Figure 5.21	The compacted AB-3-II surface before placing the HMA base	133
Figure 5.22	Earth pressure cells, E_{s0} and E_{s18} at the springline and E_{C0} and E_{C12} at the crown	134
Figure 5.23	Test truck used in loading the culvert	135
Figure 5.24	Axle load configuration of the test truck	136
Figure 5.25	The test truck applying static loads	136
Figure 5.26	A truck dumping HMA for the HMA surface	137
Figure 5.27	HMA dumped and leveled using the bobcat	138
Figure 5.28	Vibratory roller compacting the HMA base	138
Figure 5.29	Schedule details of construction of test sections in the field including the soil lifts and earth pressure cells	139
Figure 5.30	LWD test on the compacted AB-3-II	140
Figure 5.31	CBR profiles on the western test section	141
Figure 5.32	A small box used for density determination	143
Figure 6.1	Measured earth pressures around the pipe during installation in Test Section 1	146
Figure 6.2	Comparison of measured and calculated pressures at the crown during installation in Test Section 1	147
Figure 6.3	Calculated lateral earth pressure coefficients (K) at the springline	148
Figure 6.4	Calculated lateral earth pressure coefficients (K) at the springline and shoulder in Test Section 1	149

Figure 6.5	Measured pressures around the pipe during the installation in Test Section 3	150
Figure 6.6	Comparison of measured and calculated pressures at the crown during the installation and vertical arching factor (VAF) in Test Section 3	151
Figure 6.7	The measured lateral pressures at the shoulder, springline, and haunch with the measured and calculated vertical pressures at the springline in Test Section 3	152
Figure 6.8	Calculated lateral earth pressure coefficients (K) at the shoulder, haunch, and springline in Test Section 3	153
Figure 6.9	Measured earth pressures around the pipe during installation in Test Section A	154
Figure 6.10	Comparison of measured and calculated pressures at the crown during installation in Test Section A	155
Figure 6.11	Measured and calculated lateral earth pressures at the springline in Test Section A	156
Figure 6.12	Lateral earth pressure coefficients (K) at the springline in Test Section A	157
Figure 6.13	Measured earth pressures around the pipe during installation in Test Section B	158
Figure 6.14	Comparison of measured and calculated pressures at the crown during installation in Test Section B	160
Figure 6.15	Measured lateral and overburden pressures at the springline in Test Section B	161
Figure 6.16	Lateral earth pressure coefficients (K) at the springline in Test Section B	161
Figure 6.17	Measured deflections of the pipe during the installation in Test Section 1	165
Figure 6.18	Relations between the measured vertical and horizontal deflections during the installation in Test Section 1	166
Figure 6.19	Comparison of the measured and calculated horizontal deflections by the Iowa formula in Test Section 1	166
Figure 6.20	Measured deflections of the pipe during the installation in Test Section 3	168
Figure 6.21	Relations between the measured vertical and horizontal deflections during the installation in Test Section 3	168
Figure 6.22	Comparison of the measured and calculated horizontal deflections by the Iowa formula in Test Section 3	169
Figure 6.23	Measured deflections of the pipe during the installation in Test Section A	170
Figure 6.24	Relations between the measured vertical and horizontal deflections during the installation in Test Section A	171
Figure 6.25	Comparison of the measured and calculated horizontal deflections by the Iowa formula in Test Section A	172
		173
Figure 6.26	Deflection produced by the tamping hammer during the compaction at the pipe shoulder in Test Section A	173

Figure 6.27	Deflection produced by the smooth wheel vibratory roller during the compaction before placing the HMA base in Test Section A	173
Figure 6.28	Measured deflections of the pipe during the installation in Test Section B	174
Figure 6.29	Relations between the measured vertical and horizontal deflections during the installation in Test Section B	175
Figure 6.30	Comparison of the measured and calculated horizontal deflections by the Iowa formula in Test Section B	175
Figure 6.31	Deflection produced by the vibratory plate compactor during the compaction at the pipe shoulder in Test Section B	176
Figure 6.32	Deflection produced by the smooth wheel vibratory roller during the compaction before placing the HMA base in Test Section B	177
Figure 6.33	Comparison of the measured deflections of the SRHDPE pipes during the installation	179
Figure 6.34	Comparison of calculated and measured horizontal deflections of the SRHDPE pipes during the installation	180
Figure 6.35	Measured strains on the steel surface during the installation in Test Section 1	181
Figure 6.36	Measured strains on the plastic ribs during the installation in Test Section 1	182
Figure 6.37	Measured strains on the plastic at inside and outside pipe wall during the installation in Test Section 1	182
Figure 6.38	Measured strains on the steel during the installation in Test Section 3	184
Figure 6.39	Measured strains on the plastic ribs during the installation in Test Section 3	184
Figure 6.40	Measured strains on the plastic at inside and outside pipe wall during the installation in Test Section 3	185
Figure 6.41	Measured strains on the steel surface during the installation in Test Section A	187
Figure 6.42	Measured strains on the plastic ribs during the installation in Test Section A	187
Figure 6.43	Measured strains on the plastic at inside and outside pipe wall during the installation in Test Section A	188
Figure 6.44	Measured strains on the steel during the installation in Test Section B	190
Figure 6.45	Measured strains on the plastic ribs during the installation in Test Section B	191
Figure 6.46	Measured strains on the plastic at inside and outside pipe wall during the installation in Test Section B	191
Figure 6.47	Settlement of the loading plate versus applied pressure under static loads	195
Figure 6.48	Measured earth pressures around the pipe in Test 1	197
Figure 6.49	Measured earth pressures around the pipe in Test 2	198
Figure 6.50	Measured and calculated earth pressure (E_{IF}) at the backfill-base course interface in Test 3	199
Figure 6.51	Measured earth pressures around the pipe in Test 3	200
Figure 6.52	Axle loads on the pipe in Test Section A	202

Figure 6.53	Measured earth pressures around the pipe under truck loading on Test Section A	202
Figure 6.54	Axle loads on the pipe in Test Section B	204
Figure 6.55	Measured earth pressures around the pipe under truck loading on Test Section B	204
Figure 6.56	Measured earth pressures around the pipe in Test 1 and Test 2	205
Figure 6.57	Measured earth pressures around the pipe in Test 1 and Test 3	206
Figure 6.58	Comparison of the measured crown pressures with the 2007 AASHTO LRFD Bridge Design Specifications and Giroud and Han (2004) methods	207
Figure 6.59	Calculated lateral earth pressure coefficients (K) at the springline from the measured pressures in Test 3	208
Figure 6.60	Comparison of the lateral earth pressure coefficients (K) at the shoulder, springline, and haunch in Test 3	209
Figure 6.61	Deflections of the pipe under the static load in Test 1	214
Figure 6.62	Deflections of the pipe under the static load in Test 2	215
Figure 6.63	Deflections of the pipe under the static load in Test 3	216
Figure 6.64	Deflections of the pipe under the truck loading in Test Section A	218
Figure 6.65	Deflections of the pipe under the truck loading in Test Section B	219
Figure 6.66	Comparison of the deflections of the pipe in Tests 1 and 2	220
Figure 6.67	Comparison of the deflection of the pipe in Tests 1 and 3	221
Figure 6.68	Relation between the horizontal and vertical deflections at the center of the pipe	222
Figure 6.69	Comparison of the measured and calculated vertical deflections by the Iowa formula	223.
Figure 6.70	Measured strains on the steel ribs in Test 1	229
Figure 6.71	Measured and calculated strains on the steel ribs at the springline in the circumferential direction	229
Figure 6.72	Measured strains on the plastic at ribs in Test 1	230
Figure 6.73	Simplified load transfer mechanism	231
Figure 6.74	Measured and calculated strains on the plastic cover at the rib at the pipe crown in the radial direction in Test 1	231
Figure 6.75	Measured strains on the inside and outside plastic wall of the pipe in Test 1	232
Figure 6.76	Measured strains on the steel ribs in Test 2	
Figure 6.77	Measured and calculated strains on the steel at the springline in the circumferential direction in Test 2	234
Figure 6.78	Measured strains on the plastic cover at the ribs in Test 2	235
Figure 6.79	Measured and calculated strains on the plastic cover at the rib at the pipe crown in the radial direction in Test 2	235
Figure 6.80	Measured strains on the inside and outside plastic walls of the pipe in Test 2	236
Figure 6.81	Measured strains on the steel ribs in Test 3	237
Figure 6.82	Measured and calculated strains on the steel rib at the springline in the	238

	circumferential direction in Test 3	
Figure 6.83	Measured strains on the plastic cover at the ribs in Test 3	239
Figure 6.84	Measured and calculated strains on the plastic cover at the ribs at the pipe crown in the radial direction in Test 3	239
Figure 6.85	Measured strains on the inside and outside plastic wall of the pipe in Test 3	240
Figure 6.86	Measured strains on the steel ribs in Test Section A	242
Figure 6.87	Measured strains on the plastic at ribs in Test Section A	243
Figure 6.88	Measured strains on the inside and outside plastic wall of the pipe in Test Section A	245
Figure 6.89	Measured strains on the inside and outside plastic wall of the pipe in Test Section A	247
Figure 6.90	Measured strains on the steel ribs in Test Section B	248
Figure 6.91	Measured strains on the plastic at ribs in Test Section B	249
Figure 6.92	Measured strains on the inside and outside plastic wall of the pipe in Test Section B	251
Figure 6.93	Measured strains on the inside and outside plastic wall of the pipe in Test Section B	253
Figure 6.94	Comparison of the strains measured on steel in the laboratory tests	254
Figure 6.95	Comparison of the measured strains on the plastic cover at the ribs in the laboratory tests.	255
Figure 6.96	Comparison of the strains measured on the outside and inside the pipe at the valley in between ribs	256
Figure 6.97	Comparison of the strains measured on the steel and plastic in the laboratory tests	257
Figure 6.98	Comparison of the strains measured on the steel and plastic in the laboratory tests	258
Figure 6.99	Vertical deformation of the loading plate under cyclic loading in Test 1	260
Figure 6.100	Vertical deformation of the loading plate under cyclic loading in Test 1	261
Figure 6.100	Vertical deformation of the loading plate under cyclic loading in Test 3	262
Figure 6.102	Vertical deformation of the loading plate under static and cyclic loadings	263
Figure 6.103	Measured maximum earth pressures around the pipe under cyclic loading in Test 1	265
Figure 6.104	Measured maximum earth pressures around the pipe under cyclic loading in Test 2	266
Figure 6.105	Measured maximum earth pressure at the backfill-base course interface in Test 3	267
Figure 6.106	Measured maximum earth pressures around the pipe under cyclic loading in Test 3	267
Figure 6.107	Comparison of the maximum earth pressures around the pipe under cyclic loading in Tests 1 and 2	269
Figure 6.108	Comparison of the maximum earth pressures around the pipe under cyclic loading in Tests 1 and Test 3	269
Figure 6.109	Maximum deflections of the pipe under cyclic loading in Test 1	270

Figure 6.110	Maximum deflections of the pipe under cyclic loading in Test 2	271
Figure 6.111	Maximum deflections of the pipe under cyclic loading in Test 3	272
Figure 6.112	Comparison of the maximum deflections of the pipe under cyclic loading in Tests 1 and 2	273
Figure 6.113	Comparison of the maximum deflections of the pipe under cyclic loading in Tests 1 and 3	274
Figure 6.114	Relationship between the maximum horizontal and vertical deflections at the center of the pipe under cyclic loading	275
Figure 6.115	Measured maximum strains on steel under cyclic loading in Test 1	277
Figure 6.116	Measured maximum strains on the plastic cover at ribs under cyclic loading in Test 1	277
Figure 6.117	Measured maximum strains on the inside and outside walls of the pipe during cyclic loading in Test 1	278
Figure 6.118	Measured maximum strains on the steel under cyclic loading in Test 2	279
Figure 6.119	Measured maximum strains on the plastic cover at the ribs under cyclic loading in Test 2	280
Figure 6.120	Measured maximum strains on the inside and outside plastic walls of the pipe during cyclic loading in Test 2	280
Figure 6.121	Measured maximum strains on the steel under cyclic loading in Test 3	282
Figure 6.122	Measured maximum strains on the plastic cover at the ribs under cyclic loading in Test 3	282
Figure 6.123	Measured maximum strains on the inside and outside pipe walls of the pipe under cyclic loading in Test 3	283
Figure 6.124	Comparison of the measured earth pressures around the pipe under static and cyclic loads in Test 1	284
Figure 6.125	Comparison of the earth pressures around the pipe under static and cyclic loads in Test 2	285
Figure 6.126	Comparison of the earth pressures around the pipe under static and cyclic loads in Test 3	285
Figure 6.127	Comparison of the deflections of the pipe under static and cyclic loads in Test 1	287
Figure 6.128	Comparison of the deflections of the pipe under static and cyclic loads in Test 2	287
Figure 6.129	Comparison of the deflections of the pipe under static and cyclic loads in Test 3	288.

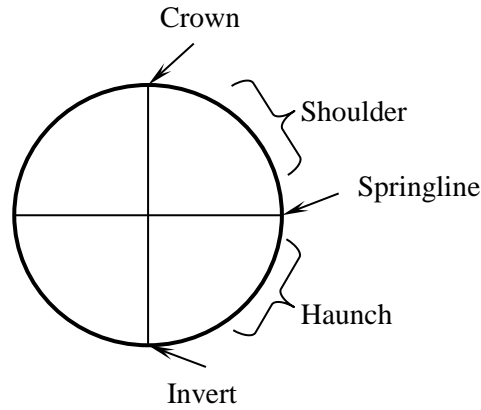
CHAPTER 1 INTRODUCTION

1.1 Background

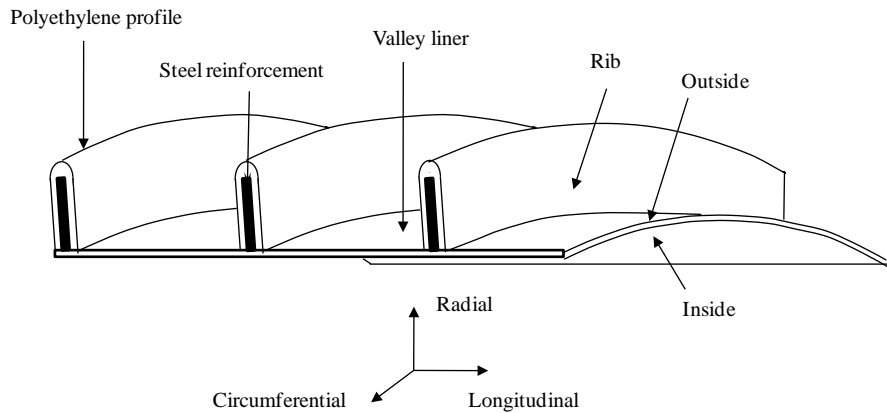
In 1824, iron pipes were developed in England and steel pipes came in existence in 1855. From 1860 to 1900, more than 2 million feet of steel pipe was installed in the United States (Watkins, 2006 as cited by Whidden, 2009). Subsequently, pipe systems of different materials, ranging from rigid concrete to flexible thermal plastics, came into use as buried or underground drainage structures in civil engineering. In more recent times, metal and plastic pipes with various profile walls have been manufactured to provide higher pipe stiffness. The inherent strength, stiffness, corrosion resistance, lightness, flexibility, and ease of joining are the characteristics that are often given as reasons for using a particular material.

Metal pipes have high strength and stiffness but are susceptible to corrosion from wastewater containing acid, and from aggressive soils. Plastic pipes are resistant to corrosion, erosion, and biological attack but have certain disadvantages including lower long-term strength and stiffness (dimensional reliability), buckling, and tearing of the pipe wall. For the fiscal years 2013 to 2016, the state of Kansas has an estimated obligation of 9.8 million dollars for culvert replacement and repair (KDOT 2012). Steel-Reinforced High Density Polyethylene (SRHDPE) pipe, while not applicable to all conditions, is a new product recently used for buried pipes with the potential for expanded use. The cross section and 3D view of an SRHDPE pipe section are shown in **FIGURE 1.1**. This type of pipe has high-strength steel reinforcing ribs wound helically and covered with corrosion-resistant High Density Polyethylene (HDPE) resin inside and outside. The steel reinforcement adds ring stiffness to the pipe to maintain the cross-section

shape during the installation and to support the soil overburden and traffic loading. The HDPE resin protects the steel against corrosion and provides the smooth inner wall.



a) Cross section of a pipe.



b) 3D view of an SRHDPE pipe section

FIGURE 1.1 Cross section and 3D view of an SRHDPE pipe, Khatri (2012)

In pipe design, pipes are generally divided into two categories, rigid and flexible. Concrete, clay, and cast iron pipes are examples of rigid pipes while steel, aluminum, and plastic

pipes are usually considered flexible. Rigid pipes are designed to be stiffer than the surrounding soil and to resist the applied loads by their inherent strength. Flexible pipes are defined as those that will deflect at least 2% without structural distress (Goddard, 1994) and rely on the capacity of the surrounding soil to carry a major portion of the applied load through ring deformation to activate the lateral passive resistance of the soil. As a result, backfill quality and compaction are the most important factors in ensuring satisfactory performance of flexible pipes. A rigid pipe requires good embedment for load distribution while a flexible pipe requires the utmost effort in backfilling and compaction, and is more prone to distresses and failures during and after installation. For all buried pipes, rigid or flexible, the structural performance is dependent on the soil-structure interaction. The type and anticipated behavior of the material around pipes must be considered for the proper design of the pipes (1990 AASHTO Standard Specification for Highway Bridges, as cited by Goddard 1994). Each type of pipe may have one or more performance limits based on type, material, and wall design.

1.2 Problem statement

There are various methods for the design of metal and plastic pipes. The 2007 AASHTO Bridge Design Specifications has separate design procedures for metal and plastic pipes. The American Water Works Association (AWWA) M11 (2004) also has a design procedure for metal pipes while Gumbel and Wilson (1981), Chambers et al. (1980), and Moser (2008) provided design procedures for plastic pipes. However, it is not clear whether any of these procedures for metal and plastic pipes can be used to design an SRHDPE pipe. Moreover, there is no approved installation or design specification for this type of pipe so far. **TABLE 1.1** shows the comparison of corrugated steel, HDPE, and SRHDPE pipes based on the installation and design requirements.

Some research has been conducted on SRHDPE pipes to understand the performance of SRHDPE pipes in the laboratory including the laboratory tests conducted by Khatri (2012). Khatri (2012) provided extensive instrumentation to evaluate the performance of the buried SRHDPE pipes in a large-geotechnical box with Kansas River sand as backfill. Since pipes are installed in various backfills, a performance of SRHDPE pipes have to be investigated with different other common backfills. The laboratory tests however have some limitations. For example, the installation procedure of the pipe in the test box may be different from the field installation due to the limited space and construction equipment in the laboratory. The laboratory box tests may have a boundary effect. Therefore, a field test has to be conducted to verify the lab test results.

TABLE 1.1 Comparisons of corrugated steel, HDPE, and SRHDPE pipe

Material	Corrugated steel pipe	HDPE pipe	SRHDPE pipe
Applicable material specification	ASTM A885, AASHTO-M36	ASTM F 2306, AASHTO M 294	ASTM F 2562
Significant material requirement	Dimensions and properties of pipe cross-sections (mechanical and chemical requirements and minimum seam strength) should be as per specifications.	Virgin resins must be used. Cell class 434400C Material must have ability to withstand stress cracking	Vertically placed thin metals (helically) encapsulated by HDPE plastic
Installation specification	ASTM A 798, AASHTO LRFD Bridge Construction Specifications (Section 26) (1998)	ASTM D 2321, AASHTO LRFD Bridge Construction Specifications (Section 30) (2010)	Do not exist
Design Specification	ASTM A796, AASHTO LRFD Bridge Design Specification (Section 12.7) (2007)	ASTM A796, AASHTO LRFD Bridge Design Specification (Section 12.12) (2007)	Do not exist
Trench width	The ASTM C 789 standard and the 1998 AASHTO LRFD Bridge Construction Specifications (Section 26) state minimum trench width = outer diameter, plus sufficient room for compaction equipment.	The 2010 AASHTO LRFD Bridge Construction Specifications (Section 30) states minimum trench width = 1.5 times outer diameter +12 in.	No nationally approved installation or design specification. Research indicates that deflection limits will be significantly lower than conventional HDPE pipes.

Source: <http://www.concrete-pipe.org/pdf/InstallationComparisonInspectorsContractors.pdf>

TABLE 1.1 Comparisons of corrugated steel, HDPE, and SRHDPE pipe (continued)

Material	Corrugated steel pipe	HDPE pipe	SRHDPE pipe
Foundation and trench wall support	<p>Foundation: Moderately firm to hard in-situ soil or stabilized soil or compacted material.</p> <p>In-situ soil at foundation and trench walls should be strong enough to support pipe and compaction of embedment materials.</p>	<p>Moderately firm to hard in-situ soil or stabilized soil or compacted material.</p> <p>In-situ foundation and trench wall soil should be strong enough to support pipe and compaction of embedment materials.</p> <p>Confirmation of strength of foundation at 90-95% standard Proctor compaction</p>	
Bedding materials	<p>Uniform support and grade.</p> <p>No compaction directly under pipe</p>	<p>Uniform support and grade.</p> <p>Coarse-grained soils</p> <p>Thickness of normal earth foundation: minimum 4 in.</p> <p>In rock, thickness: minimum 6 in.</p> <p>No compaction directly under pipe</p>	
Haunch materials	<p>Haunch materials provide structural strength of flexible pipe/soil system.</p> <p>Materials same as used in bedding zone.</p> <p>Place materials in by hand. 90% minimum compaction</p>	<p>Haunch materials provide majority of structural strength of flexible pipe/soil system.</p> <p>Materials same as used in bedding zone.</p> <p>Place materials in by hand Place in 6 in. lifts. 90% minimum compaction (per section 30)</p>	

Source: <http://www.concrete-pipe.org/pdf/InstallationComparisonInspectorsContractors.pdf>

TABLE 1.1 Comparisons of corrugated steel, HDPE, and SRHDPE pipe (continued)

Material	Corrugated steel pipe	HDPE pipe	SRHDPE pipe
Embedment Materials	<p>Compact to required density in 6 to 12 in. lifts up to a diameter of a pipe/8, or 12 in. above top of a pipe according to installation types.</p> <p>Usually requires imported/selected material.</p>	<p>Compaction to required density in 6in. lifts to 12 in. above top of a pipe.</p> <p>Removal of trench box must not allow movement of compacted material.</p> <p>Usually requires imported select material.</p>	
Inspection techniques	<p>The 1998 AASHTO LRFD Bridge Construction Specifications (Section 26) limits the deflection of pipe: Deflection $\leq 5\%$ (acceptable)</p>	<p>The 2010 AASHTO LRFD Bridge Construction Specifications (Section 30.5.6) limits the deflection of pipe: Deflection $\leq 5\%$ (acceptable)</p>	

Source: <http://www.concrete-pipe.org/pdf/InstallationComparisonInspectorsContractors.pdf>

1.3 Research Objective

The objective of this research was to evaluate properties of the SRHDPE pipe. The effects of the SRHDPE properties on the load transfer mechanism were investigated during the installation and service under simulated static and cyclic traffic loading by large-scale plate loading laboratory tests. The laboratory test results were verified by conducting a field test.

1.4 Research Methodology

The research methodology adopted for this research includes: (1) a literature review on different theories and design methods from early age to current practice for predicting structural performance of both rigid and flexible buried pipes, (2) tests conducted to evaluate the properties of the SRHDPE pipe in air, (3) large-scale box tests on the SRHDPE pipe to evaluate the

performance during installation and service under static and cyclic loading, (4) A field study on the SRHDPE pipe to verify the lab test results, and (4) establishment of a design procedure for SRHDPE pipes during the installation and service. The pipe property tests and large-scale box tests were conducted at the Department of Civil, Environmental, and Architectural Engineering in the University of Kansas (KU). A field test was carried out on E 1000 Road in Lawrence, Kansas.

1.5 Organization of Dissertation

This dissertation is organized in seven chapters. Chapter One presents an introduction including the background, problem statement, research objective, and research methodology. Chapter Two is a detailed literature review on backfill materials, laboratory and field works, theories, and design methods from early age to current practice for predicting structural performance of buried pipes both rigid and flexible. Chapter Three describes the properties of all materials used in large-scale box tests. Chapter Four provides detailed construction procedures of the laboratory test sections and instrumentations. Chapter Five give detailed construction procedures of the field test sections and instrumentations. The data analysis and the test results are presented in Chapter Six. Chapter Seven provides the summary of test results and conclusions obtained from this research and recommendations for future study.

CHAPTER 2 LITERATURE REVIEW

This section presents a review of past studies on the structural performance of both rigid and flexible buried pipes as applicable to the research objective. It reviews important and pertinent theories and design methods, from inception to current practice, for predicting structural performance of buried pipes. A summary of both laboratory and field tests pertinent to those design theories is included. The literature review also discusses the studies that have been conducted to examine the performance of the Steel-Reinforced High Density Polyethylene (SRHDPE) pipes.

2.1 Loads on Pipes

Marston (1913) and Marston (1930) proposed the theory to calculate the loads on the top of rigid and flexible pipes. The Marston theory is applied to rigid pipes for both trench and embankment conditions whereas the Marston theory is applied to flexible pipes only for embankment conditions. The theoretical basis for the Marston trench load is the soil friction at the trench walls that is indifferent to the type of pipe. Therefore, there are some arguments for the use of the Marston trench load on a flexible pipe design in the United States (Schrock, 1993).

For a metal pipe, the 2007 AASHTO LRFD Bridge Design Specifications considers the load on the pipe due to the weight of a soil column above the pipe. For concrete and thermoplastic pipes, the 2007 AASHTO LRFD Bridge Design Specifications expresses the load (W) on the pipes under typical embankment conditions as the product of the soil column load ($W_{sp} = \gamma_s H$) and the vertical arching factor (VAF) as follows:

$$W = \text{VAF} \times W_{sp} \quad 2.1$$

The vertical arching factor (VAF) depends on the ratio of the stiffness of soil at the sides of a pipe to the pipe stiffness. If the soil stiffness is higher than the pipe stiffness, the VAF is less than 1.0 (i.e., the load on the pipe is decreased). If the soil stiffness is less than the pipe stiffness, the VAF is greater than 1.0 (i.e., the load on the pipe is increased). The VAF for a concrete pipe is presented in the 2007 AASHTO LRFD Bridge Design Specifications. The vertical arching factors (VAFs) for flexible pipes can be calculated using the simplified **EQUATIONS 2.2 to 2.4** proposed by McGrath (1998) based on Burns and Richard (1964):

For a fully-bonded interface between pipe and soil,

$$VAF = 1.06 - 0.96 \left(\frac{S_H - 0.7}{S_H + 1.75} \right) \quad 2.2$$

For a free-slip interface,

$$VAF = 0.76 - 0.71 \left(\frac{S_H - 0.7}{S_H + 1.75} \right) \quad 2.3$$

$$S_H = \frac{M_s}{EA/R} \quad 2.4$$

where S_H = the hoop stiffness parameter, M_s = the constrained modulus of elasticity of soil (to be discussed in **SECTION 2.4.2**), E = Young's modulus of elasticity of the pipe material, A = the wall cross-sectional area of the pipe, and R = the radius of the pipe.

The method proposed by McGrath (1998) has been incorporated into the 2000 AASHTO LRFD Bridge Design Specifications for the design of a thermoplastic pipe.

The load (W) on a pipe due to a truck wheel can be estimated using a stress distribution method. The 1992 AASHTO LRFD Bridge Design Specifications considers the wheel load as a point load on the surface and distributes it on a square area of a width of 1.5 times the fill depth. More recently, the 2007 AASHTO LRFD Bridge Design Specifications considers the wheel load to be uniformly distributed over a tire contact area, which is projected by increasing the area by either 1.15 times the fill depth in select granular backfill or the fill depth in all other cases. Giroud and Han (2004) suggested an approximate solution for the vertical stress distribution angle from a base course to a subgrade based on Burmister's theoretical solution (Burmister, 1958) as follows:

$$\tan \alpha_1 = \tan \alpha_o \left[1 + 0.204 \left(\frac{E_1}{E_2} - 1 \right) \right] \quad 2.5$$

where α_1 = the stress distribution angle in the base coarse, α_o = the reference stress distribution angle for a uniform medium defined by $E_1=E_2$, E_1 = the modulus of elasticity of base coarse, and E_2 = the modulus of elasticity of subgrade. The reference distribution angle for a uniform medium was taken as 27° (i.e., 2:1 distribution).

2.2 Bedding and Backfill Materials

Bedding and backfilling are critical procedures for pipe installation for the satisfactory performance of pipes. Proper bedding and backfilling lead to the transfer of loads on a pipe to the bedding and surrounding soil. Based on a bedding type, bedding constant (k) was introduced in flexible pipe design (Goddard, 1992). The bedding constant (k) versus the bedding angle is shown in **TABLE 2.1**.

TABLE 2.1 Variation of bedding constant (k) with bedding angle (Goddard, 1992)

Bedding Angle (degrees)	Bedding Constant (K)
0	0.11
30	0.108
45	0.105
60	0.102
90	0.096
120	0.09
180	0.083

The 2007 KDOT Pipe and Culvert Specifications considers the bedding thickness, quality of material, and compaction of bedding materials in buried pipe design. Backfill quality and compaction are the two most important factors in ensuring satisfactory performance of flexible pipes. For flexible pipes, a wide range of non-cohesive backfill materials are strongly preferred over other soils for ease of compaction, high earth pressure response from the side (i.e., springline), and stability of the pipes when backfill materials are saturated and confined. However, other backfill materials, such as silty sand (SM) and clayed sand (SC), are acceptable for economic purposes under conditions where there are low to moderate loads (Molin, 1981) and where high levels of compaction effort at the moisture content close to the optimum level to get the required percent compaction are obtainable (ASTM A798, and ASTM D2321).

The low stiffness of flexible pipe can limit compaction effort of the backfill because of possible distortion and uplift of the pipe. The 2007 AASHTO LRFD Bridge Design Specifications requires a minimum pipe stiffness to reduce the distortion, and specifically for plastic pipe, also to reduce the strain in the pipe wall which is dependent on the pipe stiffness and the compaction effort. Over-compacted soil can limit lateral deformation of the pipe during loading so that the potential for pipe buckling in the vicinity of the crown is greatly increased (Cameron, 2006). Initial deformation in flexible pipes is favorable if not excessive (Webb et al,

1996). Roger, et al. (1996), as cited by Cameron (2006), addressed the non-symmetric distortion of the pipe created by filling sand to one side of the pipe first before filling the other side rather than bringing up both levels simultaneously. The ratio of the profile/rib clear spacing of corrugated profile pipes or rib wall plastic pipes to the maximum size of the backfill material should be less than 0.6 or larger than 2.6 to prevent the development of loose void spaces around the pipes (Sargand et al., 1996). According to the 2007 AASHTO LRFD Bridge Design Specifications, the maximum particle size of a bedding material should be 1.25 in.

Small trench width for pipe embedment is adequate if the in-situ soil is stiffer than the backfill material (Howard, 1997), but the compaction effort is restricted by the geometry of the trench and the sensitivity of the installed flexible pipe to compaction of the backfill. According to the 2007 Kansas Department of Transportation (KDOT) specification for pipes and culverts, a trench should have a minimum width equal to 12 in. plus 1.5 times the diameter of the pipe.

2.3 Minimum Soil Cover Requirements

With a thin soil cover, the pipe will experience high stress concentrations at the crown, which may cause collapse of the pipe. Therefore, precautions should be taken when designing shallow installations under roadways. **TABLE 2.2** shows the 2007 KDOT Pipe and Culvert specifications requirement for the minimum cover over the top of a pipe. Katona (1988) proposed an empirical relationship for the determination of the minimum soil cover thickness by ignoring the contribution of the pavement thickness under various standard AASHTO truck loadings.

TABLE 2.2 Minimum cover over the top of the pipe (KDOT, 2007)

PE and PVC size (inches)	Axle Load (kips)			
	18 to 50	50 to 75	75-110	110 to 150
	Soil Cover (feet)			
12 to 36	2.0	2.5	3.0	3.0
42 to 48	3.0	3.0	3.5	4.0
54 to 60	3.0	3.0	3.5	4.0

2.4 Deflection

Flexible pipes are designed to transmit the load on the pipe to the soil at the sides of the pipe. As the load on the pipe increases, the vertical diameter decreases and the horizontal diameter increases. The increase in the horizontal diameter is resisted by the soil at the sides of the pipe. The cross-sectional ring and soil section deflect according to the ratio of the load on the ring to the modulus of elasticity of the pipe-soil system. The overall material modulus is complicated by the pipe, soil, and soil-structure interaction in buried systems. The material modulus becomes a combination of the structural modulus (stiffness) of the pipe and the modulus (stiffness) of the soil (Spangler, 1941). Therefore,

$$deflection = \frac{soil\ load}{pipe\ stiffness + soil\ stiffness} \quad 2.6$$

Spangler (1941) incorporated the effects of the surrounding soil on the pipe deflection and derived the Iowa formula (**EQUATION 2.7**) to determine the deflection of a flexible pipe:

$$\Delta X = \frac{D_L k W R^3}{E I + 0.061 e R^4} \quad 2.7$$

where D_L = the deflection lag factor, k = the bedding constant (presented in **TABLE 2.1**), W = Marston's load per unit length of the pipe, R = the mean radius of the pipe, e = the modulus of

passive resistance of side fill, and ΔX = the horizontal deflection or change in diameter. Spangler (1941) developed the Iowa formula for predicting the deflection of a flexible pipe (i.e., corrugated steel pipe or CSP). The 5% vertical deflection of the pipe diameter was an early-developed limit state for a CSP.

Watkins and Spangler (1958) determined that “e” could not possibly be a true modulus of passive resistance. A new soil parameter, the modulus of soil reaction $E' = e \times R$, was defined, and the Iowa formula was modified for the prediction of the horizontal deflection (ΔX) as follows:

$$\Delta X = \frac{D_L k W}{0.149 PS + 0.061 E'} \quad 2.8$$

$$E' = \frac{\frac{P_h}{\Delta X}}{D} \quad 2.9$$

where PS = the pipe stiffness (to be discussed in **SECTION 2.4.1**), P_h = the pressure at the side of a pipe caused by forcing the side of the pipe into the backfill, and D = the diameter of the pipe.

The modified Iowa formula **EQUATION 2.8** was derived assuming that the vertical and horizontal deflections would be approximately equal in magnitude. However, the literature (Masada, 1996) indicates that vertical deflection would be higher than horizontal deflection in most installation conditions. To predict the vertical deflection of pipes, Masada (2000) derived the relation using the same approach suggested by Spangler (1941) and making no new assumptions beyond those made by Spangler as follows:

$$\frac{\Delta D_V}{\Delta D_H} = 1 + \frac{0.0094 E'}{PS} \quad 2.10$$

where E' = the modulus of the subgrade reaction and PS = the pipe stiffness. **EQUATION 2.10** is used to predict the vertical deflection of pipe if the horizontal deflection is known. More research has been carried out to predict the vertical deflection of the pipe. Howard (1981) proposed an empirical USBR (United States Department of the Interior: Bureau of Reclamation) equation as follows to predict the vertical deflection (ΔY) of a buried flexible pipe based on back-calculated parameters from the field installations:

$$\Delta Y(\%) = T_f \left[\frac{0.07 \gamma H}{E I / R^3 + S_f D_f} + C_f \right] + I_f \quad 2.11$$

where T_f = the time-lag factor (dimensionless, 0.07 was suggested), γ = the backfill unit weight, $E I / R^3$ = the pipe stiffness, S_f = the soil stiffness factor, C_f = the construction factor, percent vertical deflection, I_f = the inspection factor, percent vertical deflection, and D_f = the design factor (dimensionless) and values were given for three cases A, B, and C. Case A was used for comparing actual deflections against calculated theoretical deflections. Case B was used when desired deflections were equal to or less than the theoretical deflection plus 0.5% deflection. Case C was used when the deflection is a critical for a pipe design.

EQUATION 2.11 has several features that are improved from the Iowa formula such as the prediction of the deflection immediately after backfilling, the prediction of the long-term deflection based on the initial deflection and the design factors depending on the needs of the user and the soil stiffness factor (S_f) rather than the modulus of soil reaction. The parameters used in the USBR equation are listed in **TABLE 2.3**. This method should only be used when the

depth of cover is less than 50 ft and the trench wall support is as good as or better than the pipe bedding.

TABLE 2.3 Parameters for the USBR equation (Howard, 1981)

Bedding Soil Classification (USCS)	Degree of Compaction**			
	Dumped	Slight < 85% P <40% RD	Moderate 80- 95% P 40-70% RD	High >95% P >70% RD
<u>Highly compressible fine-grained soils</u> CH, MH, OH, OL	Soils with medium to high plasticity or with significant organic content. No data available.			
<u>Fine-grained soils</u> Soils with medium to no plasticity with less than 25% coarse-grained particles CL, ML, CL-ML	S _f = 3 T _f = 1.5* C _f = 2.0 D _f for A=1.0 B=0.5 C=0.3	S _f = 12 T _f = 2* C _f = 2.0 D _f for A=1.0 B=0.5 C=0.3	S _f = 24 T _f = 2.5* C _f = 1.5 D _f for A=1.0 B=0.67 C=0.5	S _f = 100 T _f = 2.5* C _f = 1.5 D _f for A=1.0 B=0.75 C=0.67
<u>Sandy or gravelly fine grained soils</u> soils with medium to no plasticity with more than 25% coarse-grained particles CL, ML, CL-ML <u>Coarse -grained soils with fines</u> Sands, gravels with more than 12% fines GM, GC,SM, SC	S _f = 10 T _f = 1.5* C _f = 2.0 D _f for A=1.0 B=0.5 C=0.3	S _f = 24 T _f = 2.0* C _f = 2.0 D _f for A=1.0 B=0.5 C=0.3	S _f = 60 T _f = 2.5* C _f = 1.5 D _f for A=1.0 B=0.67 C=0.5	S _f = 150 T _f = 2.5* C _f = 1.0 D _f for A=1.0 B=0.75 C=0.67
<u>Clean Coarse grained soils</u> Sands, gravels with less than 12% fines GW, GP, SW, SP or any soil beginning with one of these symbols (i.e. GP-GM)	S _f = 12 T _f = 1.5 C _f = 2.0 D _f for A=1.0 B=0.67 C=0.5	S _f = 40 T _f = 2.0 C _f = 2.0 D _f for A=1.0 B=0.67 C=0.5	S _f = 120 T _f = 2.5 C _f = 1.0 D _f for A=1.0 B=0.75 C=0.67	S _f = 200 T _f = 2.5 C _f = 0.5 D _f for A=1.0 B=1.0 C=0.75
<u>Crushed rock</u>	S _f = 60 T _f = 2.0 C _f = 1.0 D _f for A = 1.0 B = 0.67 C = 0.5		S _f = 200 T _f = 3.0 C _f = 0.5 D _f for A=1.0 B=1.0 C=0.75	

*Double T_f value if bedding will become saturated.

** %P = % of standard Proctor maximum dry density and %RD = % relative density.

McGrath (1998) proposed the expression for the prediction of vertical deflection of pipe taking the contributions of both bending stiffness factor ($S_B = M_s R^3/EI$) and the hoop stiffness factor ($S_H = M_s R^3/EI$) as follows:

$$\frac{\Delta y}{D} = \left(\frac{q_v}{\frac{EA}{R} + 0.57M_s} \right) + \left(\frac{D_L K q_v}{\frac{EI}{R^3} + 0.061M_s} \right) \quad 12$$

where M_s = the constrained modulus, R = the radius of the pipe, E = Young's modulus of elasticity of pipe material, I = the moment of inertia of the pipe wall, q_v = the overburden pressure on the top of the pipe, A = the pipe wall cross-sectional area, D_L = the deflection lag factor, and k = the bedding constant.

During the initial backfilling, the flexible pipe deforms into a shape similar to a vertical ellipse (McGrath et al. 1998). This so called "peaking behavior" due to lateral force generated by the compactor and the mass of the backfill placed on both sides of the pipe can be predicted by **EQUATION 2.13** developed by Masada and Sargand (2007). The peaking behavior continues until the backfill reaches the crown of the pipe.

$$\frac{\Delta y}{D} = \frac{4.7P_c + K_o \gamma_s R}{3.874PS} \quad 2.13$$

where P_c = the pressure generated by the compaction efforts (shown in TABLE 2.4), $K_o = 1 - \sin \phi_s$, ϕ_s = the internal friction angle of granular backfill soil, γ_s = the unit weight of the backfill soil, R = the radius of the pipe, D = the diameter of the pipe, and PS = the pipe stiffness.

TABLE 2.4 Pressure generated by compaction efforts (McGrath et al., 1999 as cited by Masada and Sargand, 2007).

Backfill Soil Type	Pressure P_c (psi/in.) generated by	
	Vibratory plate	Rammer
Sand	0.03	0.39
Crushed stone	0.06	0.80

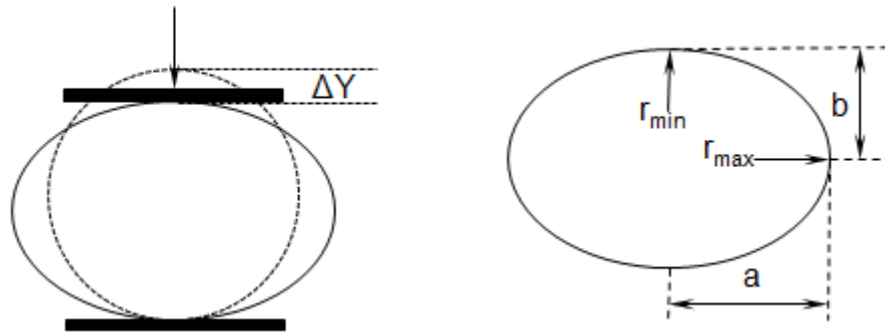
2.4.1 Estimation of the Pipe Stiffness (PS)

The parallel plate test (ASTM D2412-02) is a standardized test to ensure that the bending stiffness and strength of the thermoplastic pipe meet specified levels of performance. For the SRHDPE pipe, the ASTM Standard F2562/F2562M applies specifically. The parallel plate load test does not guarantee successful field performance; however, the AASHTO M294-07 specification and KDOT use this test to verify that corrugated HDPE pipes have minimum pipe stiffness at 5% deflection to pipe diameter, and no buckling or loss of load before 20% deflection. The stiffness criterion at 5% deflection to pipe diameter is important for handling and installation of pipes, while the 20% deflection criterion provides necessary ultimate load capacity. The parallel plate load test also ensures that the pipe generally maintains its elliptical shape and that the basic design assumptions as asserted by the Iowa formula and other design methods are appropriate. The pipe stiffness can be obtained by dividing the force (F) per unit length of a pipe specimen by the resulted deflection (ΔY) at the prescribed percentage deflection (**FIGURE 2.1a**):

$$\text{Pipe stiffness (PS)} = \frac{F}{\Delta Y}$$

2.14

The stiffness factor (EI) is the product of pipe stiffness (PS) and the quantity $0.149R^3$ (Timoshenko and Gere, 1961).



(a) Pipe deflection

(b) Minimum and maximum radii

FIGURE 2.1 Pipe deflection and radii of curvature of a deflected ellipse shape

EQUATION 2.15 can be used to calculate the moment at any point along the cross-section in a deformed pipe based on its elastic behavior:

$$M = EI \dots \left(\frac{1}{R_i} - \frac{1}{R_0} \right) \tag{2.15}$$

where R_0 = the original radius of the pipe section before loading and R_i = the radius of the pipe cross-section at the point where the moment is to be determined after deformation under a load.

The moments at the crown and the springline of the pipe are calculated using the maximum and minimum radii of the pipe cross-section, $R_{\max} = a^2/b$ and $R_{\min} = b^2/a$, respectively in which 'a' is

the major semi diameter and ‘b’ is the minor semi diameter of the elliptical section (**FIGURE 2.1b**). The bending stress (σ_b) is calculated using the bending equation, $\sigma_b = M/S$, where S= is the section modulus at the location where the moment (M) is applied.

2.4.2 Estimation of the Modulus of Soil Reaction (E’)

Since the pipe stiffness (PS) for flexible pipes is 0.8 to 4.25 percent of the soil modulus (E’) in most cases, the ring stiffness factor has little influence on the deflection of pipes in comparison with the soil stiffness factor (Watkins et al., 1973). E’ is a pipe-soil interaction modulus, which is a semi-empirical constant, rather than a soil modulus alone. A table of E’ values as shown in **TABLE 2.5** was developed by Howard (1977) to predict initial deflections of buried flexible pipes at a depth of up to 50 ft. Hartley and Duncan (1987) calculated E’ based on empirical deflection equations using the field data, the elastic solution based on the constrained soil modulus (M_s), and a finite element computer program. Based on these three approaches, Hartley and Duncan (1987) found that E’ was also a function of depth and recommended sets of E’ values in **TABLE 2.6** for use in the Iowa Formula. Selig (1990) further presented E’ values using a hyperbolic finite element technique. Moore (2001) reported on the research in the USA, which leads to a revised outlook on E’ and its replacement with Young’s modulus E_s (recognized to vary with the level of vertical stress).

TABLE 2.5 Typical values of E' (psi) (Howard, 1977)

Unified Soil Classification System (USCS)	Degree of Compaction	Dumped	Slight	Moderate	High
	Level of Standard Compaction		¹ R _D <85 %	R _D = 85-95%	R _D > 95%
	Density Index		² I _D < 40%	I _D = 40 - 70%	I _D > 70%
	Coarse\Fines				
CH, MH or CH-MH (Liquid limit> 50%)	< 25% coarse	43.5	203.0	406.0	1000.5
CL, ML or CL-ML (Liquid limit< 50%)	>25% coarse	101.5	406.0	1000.5	2001.0
GM, GC, SM, SC	>12% fines	101.5	406.0	1000.5	2001.0
GW, GP,SW,SP	<12% fines	203.0	1000.5	2001.0	3001.5
Crushed Stone		1000.5	3001.5	3001.5	3000.5
Accuracy in terms of percent deflection ³		±2%	±2%	±1%	±0.5%

¹R_D = dry density ratio (i.e., the ratio of target dry density to maximum dry density for the compactive effort)

²I_D = density index (%) for a clean granular (coarse) material

³ for ±1% accuracy and predicted deflection of 3%, actual deflection would be between 2 and 4%.

TABLE 2.6 Typical Values E' (psi) (Hartley and Duncan, 1978)

Type of soil	Depth of Cover (ft)	Standard ASSHTO Relative Compaction			
		85%	90%	95%	100%
Fine-grained soils with less than 25% sand content (CL, ML, CL-ML)	0-5	500	700	1000	1500
	5-10	600	1000	1400	2000
	10-15	700	1200	1600	2300
	15-20	800	1300	1800	2600
Coarse-grained soils with fines (SM, SC)	0-5	600	1000	1200	1900
	5-10	900	1400	1800	2700
	10-15	1000	1500	2100	3200
	15-20	1100	1600	2400	3700
Coarse-grained soils with little or no fines (SP, SW, GP, GW)	0-5	700	1000	1600	2500
	5-10	1000	1500	2200	3300
	10-15	1050	1600	2400	3600
	15-20	1100	1700	2500	3800

The above E' values were obtained by back calculations. Krizek (1971) suggested replacing E' in the Iowa formula with the constrained modulus (M_s), which is a more basic soil property and define soil-structure response. Neilson (1967) simplified the Burns and Richard (1964) elastic solutions with the following approximation:

$$E' = 1.5 M_s \quad 2.16$$

$$M_s = \frac{E_s (1 - \nu_s)}{(1 + \nu_s) (1 - 2\nu_s)} \quad 2.17$$

where M_s = the constrained modulus of elasticity, E_s = the soil modulus of elasticity, and ν_s = the Poisson's ratio of soil.

For trench conditions, the backfill takes the applied load at the springline and transfers the load to the natural soil through the trench walls. The performance of the backfill material is also influenced by the resistance from the natural soil. The influence of the natural soil forming the trench walls on the lateral soil support has been addressed by Leonhardt, as cited by Cameron et al. (2006), who introduced the Leonhardt correction factor, Ω (**EQUATION 2.18**) based on the modulus of soil reaction, E' as defined in the Iowa formula (**EQUATION 2.8**). The effective side-fill stiffness is given by the product of the modulus of soil reaction E' and the correction factor Ω .

$$\Omega = \frac{1.662 + 0.639 (B/D - 1)}{(B/D - 1) + [1.662 - 0.361 (B/D - 1)] E' / E_N} \quad 2.18$$

where E_N = the Young's modulus of the natural soil forming the trench wall, B = the width of the trench, and D = the pipe diameter.

When E' is much less than E_N , the trench walls are considered rigid. If the ratio of the trench width to the pipe diameter is 2, the effective modulus for the pipe support is 2.3 times E' . As E' approaches the value of E_N , Ω is reduced. Less influence is apparent for a wider trench and the correlation factor may be ignored for a trench width to pipe diameter ratio of 5 or greater (Cameron et al., 2006).

The moduli presented above vary with stress or strain levels. Kondner (1963) proposed the use of the hyperbola for the soil stress strain relationships as shown in **EQUATION 2.19**.

$$\sigma_1 - \sigma_3 = \frac{\varepsilon}{\frac{1}{E_i} + \frac{\varepsilon}{(\sigma_1 - \sigma_3)_u}} \quad 2.19$$

where σ_1 and σ_3 are the major and minor principal stress, respectively, $(\sigma_1 - \sigma_3)_u$ is the ultimate deviator stress, ε is the axial strain, and E_i is the initial tangential modulus. The hyperbola is considered valid up to the actual soil failure point. The failure ratio, R_f , is introduced as the ratio of the actual failure deviator stress and the ultimate deviator stress and is shown in **EQUATION 2.20**.

$$R_f = \frac{(\sigma_1 - \sigma_3)_f}{(\sigma_1 - \sigma_3)_u} \quad 2.20$$

The parameters, E_i and $(\sigma_1 - \sigma_3)_u$, can be determined using the triaxial test data in a linearised hyperbolic form. Janbu (1963) presented the expression for the initial tangential modulus, E_i , with the confining stress as shown in **EQUATION 2.21**.

$$E_i = K Pa \left(\frac{\sigma_3}{Pa} \right)^n \quad 2.21$$

where σ_3 = the confining pressure and Pa = the atmospheric pressure (Pa = 14.69 Psi) which is used to non-dimensionalise the parameters K and n.

To better represent the actual behavior of soils mathematically, Duncan and Chang (1970) combined Kondner (1963) and Janbu (1963) soil models and presented the expression for the tangent modulus as shown in **EQUATION 2.22**.

$$E_t = \left[1 - \frac{R_f (1 - \sin \phi) (\sigma_1 - \sigma_3)}{2 C \cos \phi + 2 \sigma_3 \sin \phi} \right] 2 K Pa \left(\frac{\sigma_3}{Pa} \right)^n \quad 2.22$$

where C is the cohesion of soil and ϕ is the angle of internal friction which can be expressed as shown in **EQUATION 2.23** to include non-linear part of the Mohr Coulomb failure envelope.

$$\phi = \phi_o - \Delta\phi \log_{10} \left(\frac{\sigma_3}{Pa} \right) \quad 2.23$$

Duncan et al. (1980) proposed a formulation of the bulk modulus, B, of soil in term of the confining stress, σ_3 , based on data from triaxial tests as shown in **EQUATION 2.24**.

$$B_i = K_b Pa \left(\frac{\sigma_3}{Pa} \right)^m \quad 2.24$$

An alternative method for obtaining the bulk modulus is from a hydrostatic (isotropic) compression test. The best fitting curve proposed by (Selig, 1988) relating the mean applied stress, σ_m , and the volumetric strain, ϵ_{vol} , from the isotropic compression tests was hyperbola as shown in **EQUATION 2.25**. Using the hyperbola, Selig (1988) expressed the tangential bulk modulus as in **EQUATION 2.26**.

$$\sigma_m = \frac{B_i \varepsilon_{vol}}{1 - \frac{\varepsilon_{vol}}{\varepsilon_u}} \quad 2.25$$

$$B_t = B_i \left[1 + \frac{\sigma_m}{B_i \varepsilon_u} \right]^2 \quad 2.26$$

2.5 Pipe Thrust and Buckling

White and Layer (1960) proposed the compression ring theory, in which corrugated steel pipes could be designed by checking the wall strength for the possible yielding of the wall material against the weight of the soil prism above the pipe, given that standard pipe wall profiles and a uniform compacted backfill were used in the design of the pipe-soil system. Arching action was not considered by this design method. In addition, the deflection of the pipe was to be well within the standard limit of 5%.

Watkins (1960) indicated that during experiments and under some soil and pipe conditions, the pipes did buckle before a 5% vertical deflection was reached. Watkins (1960) investigated the buckling condition for the flexible pipes by running a series of tests and modifying the backfill density and stiffness, and the pipe flexibility. From his investigation, he determined that the tendency of a pipe to buckle or yield due to thrust was a function of the pipe flexibility and the soil stiffness. Meyerhof and Baikie (1963) conducted tests on curved plates in contact with sand backfill. They found similarly that buckling was a function of the pipe flexibility and the soil stiffness, which was quantified by the parameter k_b , the coefficient of soil reaction. Based on the pipe flexibility and the soil stiffness, Watkins (1966) and (1971) showed that the pipe had a wall yielding zone and a buckling zone, with a “difficult to define” transition

zone between these two zones. This result confirmed White and Layer (1960)'s compression ring theory for conditions with adequate pipe and soil stiffness. The transition zone between the buckling and yielding zones is complex because of the variations in the pipe sections, the pipe materials, and the soil backfill.

The ASTM A796 standard and the 2007 AASHTO LRFD Bridge Design Specifications (Section 12.7) suggest the critical buckling stress (f_{cr}) for corrugated steel pipes as follows:

$$\text{If } D < \frac{r}{k} \sqrt{\frac{24E}{f_u}}, f_{cr} = f_u - \frac{f_u^2}{48E} \left(\frac{\psi_s D}{r} \right)^2 \quad 2.27$$

$$\text{If } D > \frac{r}{k} \sqrt{\frac{24E}{f_u}}, f_{cr} = \frac{12E}{\left(\frac{\psi_s D}{r} \right)^2} \quad 2.28$$

where D = the pipe diameter, r = the radius of gyration of corrugation, E = the modulus of elasticity of the pipe material, ψ_s = the soil stiffness factor, and f_u = the specified minimum tensile strength

Moser (2008) recommended either of two **EQUATIONS 2.29** and **2.30** for the critical buckling stresses of circular pipes. These two equations work well for metal pipes but they are conservative for plastic pipes. The 2007 AASHTO LRFD Bridge Design Specifications also specifies the critical buckling stress (f_{cr}) for an HDPE pipe, which is determined by **EQUATION 2.31**:

$$f_{cr} = 2 \times \sqrt{\frac{E'}{1-\nu^2} \times \frac{EI}{R^3}} \quad 2.29$$

$$f_{cr} = 1.15 \times \sqrt{\frac{2EE'}{1-\nu^2} \times \left(\frac{t}{D}\right)^3} \quad 2.30$$

$$f_{cr} = 9.24 \frac{R}{A_{eff}} \sqrt{B' R_w \psi_s M_s \frac{EI}{0.149R^3}} \quad 2.31$$

where R = the radius to centroid of a pipe wall, A_{eff} = the effective wall area, ψ_s = the factor for soil stiffness (0.9), and E = the modulus of elasticity.

2.6 ProfileWall Pipes and Local Buckling

The corrugated or profile walls are formed by decentralizing the material from the pipe wall to provide higher pipe stiffness. The structural efficiency of the profile wall pipe is obtained by making wall sections deep enough with as little area as possible (i.e. the pipe wall elements are thinned as much as possible). Since a properly installed flexible pipe carries stresses largely in compression, the thin pipe wall elements are susceptible to instability in compression, or local buckling. High compressive strains developing across pipe sections may cause local buckling on various components of the profile at a stress lower than the full yield strength of the pipe wall material. Local buckling can compromise the integrity of a pipe. Bryan (1891) introduced the critical buckling stress equation of plates:

$$\sigma_{cr} = \frac{k_b \pi^2 E}{12(1-\nu^2) \left(\frac{w}{t}\right)^2} \quad 2.32$$

where k_b = buckling coefficient, E = modulus of elasticity, w = plate width, t = plate thickness, and ν = Poisson's ratio.

The strength of a plate or a plate element in a built-up section can be limited by its critical buckling stress like the Euler column buckling, which is not a function of the material strength but the plate's dimensions and boundary conditions. The buckling coefficient k_b is a function of the boundary conditions of the plate, the width to thickness ratio of the plate, and the length of the plate. For most applications, the length of element is assumed relatively long, and the coefficient k_b becomes a function of the boundary conditions only. The coefficient k_b is then presented as a numeric value for the boundary conditions. If the critical buckling stress is reached before the yield strength, the plate will buckle.

It is recognized that although an individual element of a section may buckle, the structural section does not fail, but continues performing with a post-buckled strength. Von Karman (1932) and Winter (1947) investigated the post-buckling strength of steel elements and introduced the concept of effective area. The effective area A_{eff} of a section can be determined by subtracting the ineffective area of each element from the gross section area using **EQUATION 2.33**. The effective width, b_e , of an element is obtained using an effective width factor ρ for **EQUATIONS 2.34, 2.35, and 2.36**. The effective area A_{eff} of the structural section is used to determine the limit states of the structural member, such as yielding due to thrust and or bending, or column buckling.

$$A_{eff} = A_g - \frac{\sum (w - b_e)t}{w} \quad 2.33$$

$$b_e = \rho w \quad 2.34$$

$$\rho = \frac{1 - \frac{0.22}{\lambda}}{\lambda} \quad 2.35$$

$$\lambda = \left(\frac{w}{t} \right) \sqrt{\frac{\epsilon_{yc}}{k_b}} \geq 0.673 \quad 2.36$$

where ρ = effective width factor, λ = slenderness factor, w = plate width, t = thickness, and ϵ_{yc} = compressive strain limit

The potential for local buckling of the profile elements in the lined corrugated pipe has received attention since 1990s. Hashash and Selig (1990) and DiFrancesco (1993) observed ripples in the liner when they conducted field and laboratory tests on thin-wall HDPE pipes. Moore and Hu (1995) observed the three-dimensional response of a lined corrugated HDPE pipe in the hoop compression test. Moser (1998) concluded that local buckling was a critical performance limit in the tests conducted on profile-wall pipes. McGrath and Sagan (2001) proposed the stub compression test to assess local buckling capacity of profiled wall plastic pipes by modifying the American Iron and Steel Institute method used in cold-form steel design. The localized deformations were investigated for four commonly used pipe profiles (lined, corrugated, boxed, and tubular profiles) using the three-dimensional finite-element analysis (Dhar and Moore, 2006). Among these profile pipes, local bending had the greatest effect on the stresses developed in the lined, corrugated profile.

2.7 Strain

Plastic materials offer a corrosive resistant, light weight, and moldable pipe material for pipe fabrication. The plastic material can also be easily molded into a variety of shapes improving strength with respect to area of the pipe wall. With the visco-elastic properties of the plastic, new limit states were incorporated into the pipe design. Because the modulus of the plastic material changes with time, design methods may limit the allowable strain based on the

short term and long term modulus of elasticity of the plastic, depending on load duration applied to the pipe. Strain developed in the pipe is calculated as the summation of the bending strains, ring compression strains, and strains due to the Poisson's effect. Carlstrom and Molin (1966) introduced a method to determine the bending strain in the extreme fiber of a pipe based on an elastic solution of strain as a function of pipe deflection and modified by the empirical placing factor D_f . The placing factor D_f was improved by Leonhardt (1978), Bishop and Lang (1984), and Turkopp et al. (1985) which accounts for variations in strain due to pipe/soil stiffness ratio, compaction effort, and non-uniform soil stiffness.

$$\varepsilon_b = D_f \left(\frac{t}{D}\right) \left(\frac{\Delta Y}{D}\right) \quad 2.37$$

The strain due to thrust can be calculated based on the weight of the soil prism or the internal pressure on the pipe.

$$\varepsilon_r = \frac{P D}{2 A E} \quad 2.38$$

where D_f = the shape factor, t = the minimum wall thickness, ΔY = the vertical decrease in diameter, D = the mean diameter, D_o = the outside diameter, P = the pressure on pipe, A = the area of the pipe wall, and E = the modulus of elasticity of the pipe material.

Moser (2008) presented a total combined circumferential strain of the non-pressure pipe as the sum of bending strain (ε_b), ring compression strain (ε_r), and Poisson's effect strain (ε_p).

The strain induced by the Poisson's effect is determined by:

$$\varepsilon_p = -\nu \times (\text{longitudinal strain}) \quad 2.39$$

The 2007 AASHTO LRFD Bridge Design Specifications suggested the total factored combined compressive strain due to thrust (T_L) and bending in the pipe wall, ε_c , as follows:

$$\varepsilon_c = \varepsilon_b + \frac{T_L}{A_{eff} E_{50}} \times \frac{\gamma_B}{\gamma_p} \leq \frac{1.5F_u}{E_{50}} \quad 2.40$$

This combined compressive strain should be less than the limiting combined compressive strain, which is given as follows:

$$\varepsilon_{b(max)} = \frac{1.5F_u}{E_{50}} - \frac{T_L}{A_{eff} E_{50}} \times \frac{\gamma_B}{\gamma_p} \quad 2.41$$

where γ_B = the modified factor applied to the combined factor (1.5), F_u = the long-term tensile strength of the pipe wall material, A_{eff} = the effective wall area, E_{50} = the long-term modulus of the pipe wall material, and γ_p = the maximum load factor. The total factored combined tensile strain in the pipe wall should also be less than the limiting combined tensile strain.

2.8 Existing Design Methods for Flexible Pipes

2.8.1 Metal Pipe

AASHTO Method

In the 2007 AASHTO LRFD Bridge Design Specifications, metal pipes are evaluated for thrust and buckling in pipe wall. The thrust per unit length of wall of the pipe, T_L , is specified in **EQUATION 2.42**. **EQUATION 2.27** and **2.28** are used to calculate the critical buckling stress

(f_{cr}) for metal pipes. The seam resistance of the longitudinal seams should resist the thrust in corrugated steel pipes.

$$T_L = p_f \frac{D_o}{2} \quad 2.42$$

where D_o = the outside diameter and P_f = the factored vertical crown pressure.

2.8.2 Plastic Pipes

The design of plastic pipes includes:

- i. Pipe deflection
- ii. Local buckling
- iii. Pipe wall strain

AASHTO Method

In the 2007 AASHTO LRFD Bridge Design Specifications, plastic pipes are evaluated for deflection, local buckling, and strain in the pipe wall. The deflection is evaluated using the modified Iowa formula (**EQUATION 2.8**). The thrust per unit length of wall of the pipe, T_L , is specified in **EQUATION 2.42**. The area of a profile wall is reduced to an effective area A_{eff} (see **EQUATION 2.33**) for buckling effects to evaluate the resistance to axial thrust. The result of the stub compression test, AASHTO T 341, is also used to evaluate the effective area. The critical buckling stress (f_{cr}) for a plastic pipe is calculated using **EQUATION 2.31**. The strains developed on plastic pipes are evaluated using **EQUATION 2.40**.

Chambers et al. (1980)

Chambers et al. (1980) investigated buried plastic pipes and proposed a design procedure based on pipe deflection, critical strain level, and critical buckling pressure. A modified Iowa formula (**EQUATION 2.8**) is used to determine the deflection due to the soil load, traffic load, and installation. The critical wall buckling is obtained using the following equation:

$$f_{cr} = C_B C_D \sqrt{E'(PS_v)} \quad 2.33$$

where C_B = the coefficient of buckling (0.5 for earth load and 0.07 for wheel load), C_D = the correction factor to account for deflection 1.5, and $PS_v = PS_o$ (short-term pipe stiffness for a wheel load) or $PS_v = PS_{10}$ (10-year pipe stiffness for earth load).

2.9 Performance of Pipes under Traffic Loads

The existing design methods for flexible pipes described in **SECTION 2.8**, no matter whether they were developed from empirical or theoretical bases, deal with the loads on buried flexible pipes as a result of static loading. This condition often exists for pipes buried in field (or under embankments), where the applied load is the dead weight of the trench fill (or embankment) above the pipe. However, these methods are not valid for flexible pipes installed at shallower depths under temporary or permanent pavement structures used by heavy vehicles. To date there has been very little investigation of the performance of buried flexible pipes under repeated loading.

2.9.1 Field Tests

A field study was undertaken in the United Kingdom (Trott and Gaunt, 1976) to monitor the deformations of flexible pipes laid in a trench beneath a highway. Performance of the pipes was monitored during installation and highway construction under pre-service load testing and followed with the opening of the highway. This research team confirmed that the greater part of the pipe deflections occurred within the first few heavy axle loads during the construction period, after which (when the road was opened to traffic) deflections rapidly stabilized as shown in **FIGURE 2.2**. In other words, the pipes approached a state of ring compression as opposed to the earlier “ring bending” during backfilling and passage of the scrapers. This finding was further supported by other field tests, for example, Faragher et al. (2000) and McGrath et al. (2002), and by laboratory tests, for example, Rogers et al. (1995), Faragher (1997), and Moghaddas Tafreshi and Khalaj (2008).

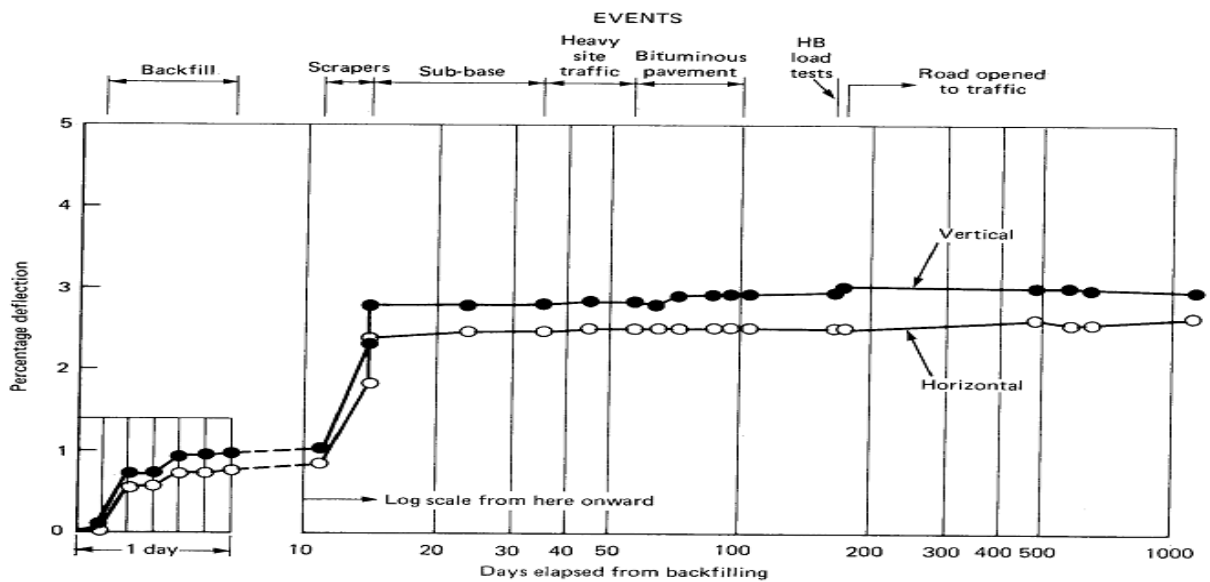


FIGURE 2.2 Percentage deflection of the unplasticized PVC pipe in the near side lane (Trott and Gaunt, 1976)

Faragher et al. (2000) carried out full-scale tests under real installation conditions to investigate the behavior of five flexible pipes of 24 in. in diameter and one flexible pipe of 42 in. in diameter buried in trenches under repeated loading. To predict the long-term pipe deformation (vertical deflection) from the initial loading cycles, power law curves were developed from the vertical deflection field data.

Arockiasamy et al. (2006) carried out totally thirty-six (36) field tests on large polyethylene, metal, and PVC pipes of 36 in. and 48 in. in diameters subjected to highway truck loading. Numerical simulations using a finite element method were also performed to determine pipe-soil interaction under live load applications. The field test results showed that the buried flexible pipes, embedded with highly compacted sand with silt, demonstrated good performance without exhibiting any visible joint opening or structural distress. A vertical deflection limit of 2% was suggested for HDPE pipes during the construction phase for highway applications.

2.9.2 Laboratory Tests

Rogers et al.(1995) investigated twin-wall annular corrugated HDPE pipes with inside diameters, ranging from 4 to 14 in., subjected to three different loads: (1) a uniform static vertical stress of 10 psi, to simulate a stationary heavy vehicle or a burial depth of approximately 13ft, (2) 1,000 cycles of 10 psi stress with 0.01 Hz frequency in a sinusoidal waveform, to simulate the heavy vehicle over a shallow buried pipe, and (3) a static stress of 20 psi, to simulate a burial depth of approximately 26ft. The applied pressure taken to simulate the heavy truck was the calculated pressure on the top of the pipe due to the stationary heavy vehicle on a pavement surface. The results showed that good performance could be achieved with plastic pipes when buried with care in a wide variety of pipe surrounding materials. In addition, the strain profiles indicated that the maximum tensile strains occurred at the pipe crown, whereas

the distribution of strains around the circumference depended on the type of surrounding material and loadings.

Faragher (1997) conducted laboratory tests on 24 in. diameter plastic pipes. The pipes were buried to a cover depth of 3 ft 3 in. in lightly compacted sand, heavily compacted sand, and gravel backfills. The pipe was first subjected to 10 psi surcharge (static) stress and then to the repeated application of a surface stress of 10 psi, with a frequency of 0.01 Hz in a truncated sinusoidal waveform and plateaus at the maximum and minimum points. As a result, more rapid loading was achieved than that of a pure sine wave. This loading procedure was relatively severe due to the large impact. In addition, the pipe was subjected to 20 psi surcharge (static) stress. The effect of surrounding conditions on the pipe deformation is demonstrated in **FIGURE 2.3** for complete loading. The pipe surrounded with the gravel and heavily compacted sand deformed much less throughout the loading than the pipe with lightly compacted sand.

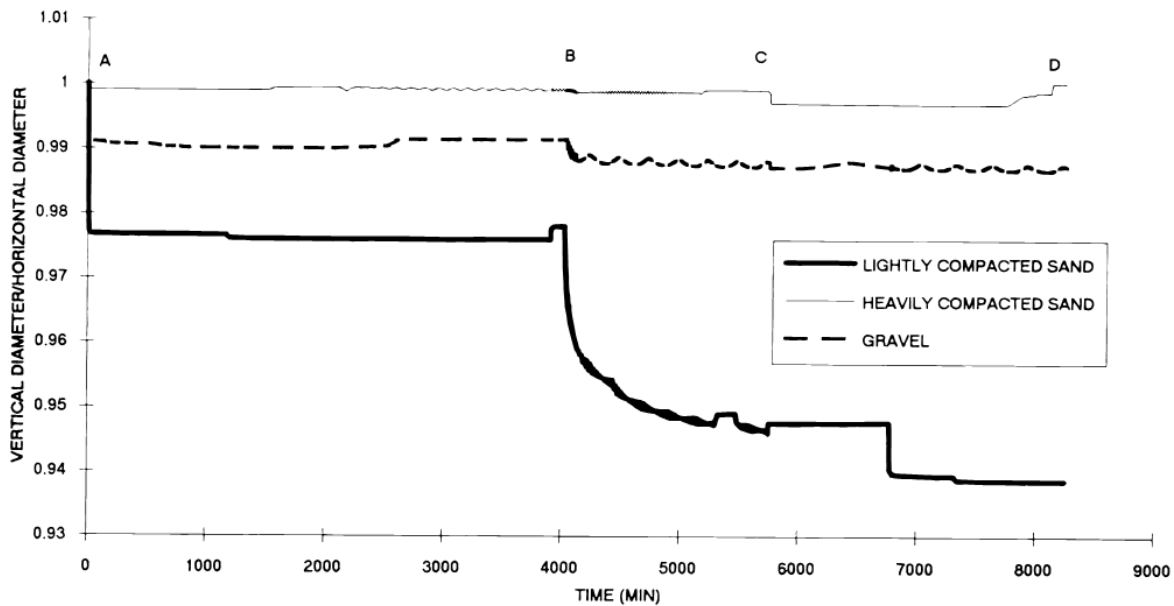


FIGURE 2.3 Relative variations of the vertical diameter to the horizontal diameter for twin-wall pipes (Faragher, 1997)

Mir Mohammad Hosseini and Moghaddas Tafreshi (2002) conducted tests on 4 in. diameter thin steel pipes buried in a test tank with a dimension of 32in. x 32 in. x 32in. to evaluate the behavior of the pipes under different loading conditions. Both cyclic and monotonic loads were applied using a loading plate. Soil density and pipe burial depth were varied. It was found that the soil density and the pipe burial depth are the two most important factors affecting the soil–pipe interaction. The pipe under the cyclic load with low amplitude might have the same deformation under a cyclic load with high amplitude, provided the cycles of the load continued for a long period. Moghaddas Tafreshi and Khalaj (2008) conducted similar tests with various repeated loads at the magnitudes of 36, 60, and 80psi under plate loading and their results supported Mir Mohammad Hosseini and Moghaddas Tafreshi (2002)’s findings.

2.10 Performance of Steel-Reinforced High Density Polyethylene (SRHDPE) plastic pipes

Steel-Reinforced or Steel-Ribbed High Density Polyethylene (SRHDPE) plastic pipes are a new product recently used for buried systems. Moser (2008) performed research on SRHDPE pipes with different pipe diameters embedded into the soil compacted at 87% of standard Proctor density. The test results showed that the SRHDPE pipe behaved the same as a low stiffness corrugated metal flexible pipe. Moore (2009) conducted a comprehensive study on SRHDPE pipes of 24 and 60 inches in diameter. Stub compression tests and hoop compression tests carried out on various diameter pipes demonstrated that the helically-wound steel ribs maintained wall stability (local buckling) at the required burial depth to a sufficient factor of safety. To evaluate the performance of a deeply buried pipe system, large-scale buried pipe tests were conducted on 24 and 60 in. diameter pipes. The tests showed that the pipe deflections were under the permissible limit (5%) and the pipe deformed like a conventional flexible metal culvert. Moore (2009) concluded that the conventional AASHTO design method for the

deflection of a flexible steel pipe can be used to design the SRHDPE pipe with respect to pipe deformation.

Steel-reinforced and conventional HDPE pipes were installed with crushed stone backfill on the Manhead road, north of Randolph Utah, by the Utah Department of Transportation (UDOT) (Folkman, 2011). They were monitored to evaluate the relative performance of these two pipes. The method of the installation for both pipes was identical. The pipes were 24 in. in diameter. Two pipes of each type were installed in parallel at a distance of 5 in. spacing. The soil cover over the pipes was approximately 3 feet. The deflections of the pipes were measured immediately after the installation and during the service life to determine the changes in horizontal and vertical diameters. Both the steel-reinforced and conventional HDPE pipes have performed adequately to date. The conventional HDPE pipe had larger deflections than the steel reinforced HDPE pipe, which was less sensitive to the installation. The maximum vertical and horizontal deflections were -2.86 % and 3.01 %, respectively for the steel reinforced HDPE pipe, while the conventional HDPE pipe had -6.77 % vertical deflection and 6.90 % horizontal deflection right after the construction of the test sections. In addition, the maximum vertical and horizontal deflections were -2.35 % and 2.50 %, respectively for the steel-reinforced HDPE pipe, while the HDPE pipe had -6.53 % vertical deflections and 6.40 % horizontal deflections after one year of installation. The reason for the reduction of the deflections of the pipes after one year was not determined at that time (Folkman, 2011).

Three steel-reinforced HDPE pipes, which had a diameter of 48 in. and a length of 100 ft, were tested by installing them beneath the Sunshine Road in Fort Benning, Georgia (Hardert, 2011). A 28 ft thick fill was placed over the pipes with a two-lane road across the fill. The deflected cross-sections of the pipes were determined using a laser device measuring the distance

to the wall of the pipe from a center point every 20° around the pipe. The deflections of the pipes measured in September, 2010 and 2011 were reported. Based on the deflected shape measurements, the pipes underwent some minor movements but maintained relatively uniform round and symmetrical shapes. In one year, the greatest increases in the vertical and horizontal diameters were 0.13 and 0.10 ft, and the greatest decrease in the vertical and horizontal diameters were 0.12 and 0.09 ft.

Masajedian (2011) conducted the experimental study on the steel-reinforced high density polyethylene (SRHDPE) pipes subjected to the simulated soil load to investigate the behavior and failure modes of the pipes and compared the results obtained from the tests conducted on corrugated metal pipes under the identical test conditions. The pipes of diameter 24 in., 36 in., and 48 in. were tested with ASTM C-33 sand and ¾ in. gravel backfills by applying the load using the concrete slab at the interval of 2 kips until failure. From the comparative study, Masajedian (2011) concluded that (a) the higher compaction of backfills increases the performance of the SRHDPE pipe better than that of the corrugated pipe, (b) the plastic cover at the ribs buckles earlier than the steel ribs at the failure. (c) Corrugated metal pipe and steel reinforced high density polyethylene pipes exhibited different failure modes. The failure mode of SRHDPE pipes were governed by the out of place buckling whereas CMP failed by the continuous hoop type buckling. From all these failure modes Masajedian (2011) recommended that the same specification cannot be implemented for both SRHDPE and CMP pipes.

CHAPTER 3 MATERIAL PROPERTIES

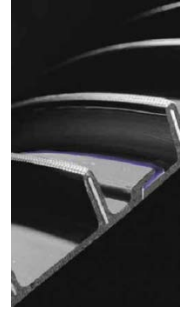
This chapter reports the types of materials and test methods used and the properties of the materials obtained in this study. Various test methods were conducted to evaluate the stiffness and buckling resistance of the SRHDPE pipe sections under vertical compression in air. To evaluate the installation damage of the SRHDPE pipes used in the laboratory tests, the stiffness of virgin and exhumed pipes were determined and compared. In addition, tests were performed to obtain the physical and mechanical properties of soils, which were used in both laboratory and field tests.

3.1 Steel-Reinforced High Density Polyethylene (SRHDPE) Pipe

SRHDPE pipes of 24 and 36 in. in diameters, manufactured and provided by Contech Construction Products Inc., were used in this research. The pipes of 24 in. in diameter were used for the laboratory tests and the pipes of 36 in. in diameter were used for the field test. This type of pipe has high-strength steel reinforcing ribs wound helically and covered by corrosion-resistant High Density Polyethylene (HDPE) resin inside and outside. **FIGURE 3.1** shows pictures of SRHDPE pipes. The pipe profile is manufactured using a high-quality stress-rated thermoplastic that meets the requirement of ASTM F2562/F2562M. The specifications of the SRHDPE pipes are provided in **TABLE 3.1** based on the manufacturer's data:



a) SRHDPE pipes



b) Section of the rib wall

FIGURE 3.1 SRHDPE pipes (from manufacturer: Contech Construction Products Inc.)

TABLE 3.1 Specification of the SRHDPE pipe (Source: Contech Construction Products Inc.)

Pipes	24 in. dia. pipe	36 in. dia. pipe
Plastic Resins Cell classification	345464C (as per ASTM D3350)	345464C (as per ASTM D3350)
Materials	Steel and HDPE	Steel and HDPE
Structure type	Helical pipe	Helical pipe
Nominal pipe diameter (in.)	24	36
Pipe outside diameter (in.)	24.9	37.1
Pipe inside diameter (in.)	23.6	35.4
Steel rib height (in.)	0.51	0.66
Steel rib thickness (in.)	0.058	0.065
Rib spacing (in.)	1	1.25
Pipe wall area (A) (in. ² /ft) (neglecting plastic)	0.35496	0.3575
Min. Waterway wall thickness (in.)	0.082	0.082
Moment of inertia (I) (in. ⁴ /in.) of pipe wall (neglecting plastic)	0.000641	0.001557
Modulus of elasticity of Steel (E) (ksi)	29,000	29,000
Yield strength of steel (F_y) (ksi)	80	80
Tensile strength of steel (F_u) (ksi)	85	85
Radius of gyration (r) (in.) (neglecting plastic)	0.147	0.228

The tests used to evaluate the properties of the SRHDPE pipe sections are discussed in **SECTIONS 3.1.1 to 3.1.4.**

3.1.1 Parallel Plate Tests

The parallel plate tests were carried out (a) to obtain the load and deformation characteristics of the SRHDPE pipe, (b) to determine the maximum load capacity of the pipe, (c) to observe the failure modes of the pipe per ASTM F2562/F2562M, and (d) to check the specification compliance of pipe stiffness. The parallel plate tests were only conducted on 24 in. diameter pipes. Three tests were conducted on the virgin pipe (i.e., not used in the test) while one more test was conducted on the exhumed pipe (i.e., exhumed from the laboratory test section after the test was completed). The test on the exhumed pipe was conducted to investigate the damage on the pipe during the installation of the pipe and loading on test sections (the installation and the loading procedures were discussed in **SECTIONS 4.2 and 4.5.** Three test specimens of each 14 in. long were cut from a single virgin pipe whereas only one test specimen of 14 in. long was obtained from the central section of the exhumed pipe. A universal testing machine was used to apply the compression load. The pipe was compressed at the rate of 0.5 ± 0.01 in. /min. up to a vertical deflection equal to 5 % pipe diameter. The rate was then increased to 3 in. /min. up to a vertical deflection equal to 20 % pipe diameter for flattening. This test procedure followed ASTM F2562/F2562M. The parallel plate test results for the virgin pipe were discussed by Khatri (2012) in his Master's study. The results are also presented in this study to compare those of the parallel plate test on the exhumed pipe and to determine the possible damage caused by the installation and simulation of static and dynamic traffic loading.

Instrumentation

The test specimen of the exhumed pipe was instrumented in the same way as in the test specimens of the virgin pipe by Khatri (2012). Extensive instrumentations with displacement transducers and photogrammetry were used to monitor the changes in shape of both virgin and exhumed pipes during loading as shown in **FIGURE 3.2**. The LiDAR Scanner, used for the tests on the virgin pipe to obtain the deflected shapes of pipe, was not set up for the exhumed pipe. It is because deflected shapes change rapidly and Khatri (2012) found that the LiDAR is applicable only if the point of interest is not rapidly changing.

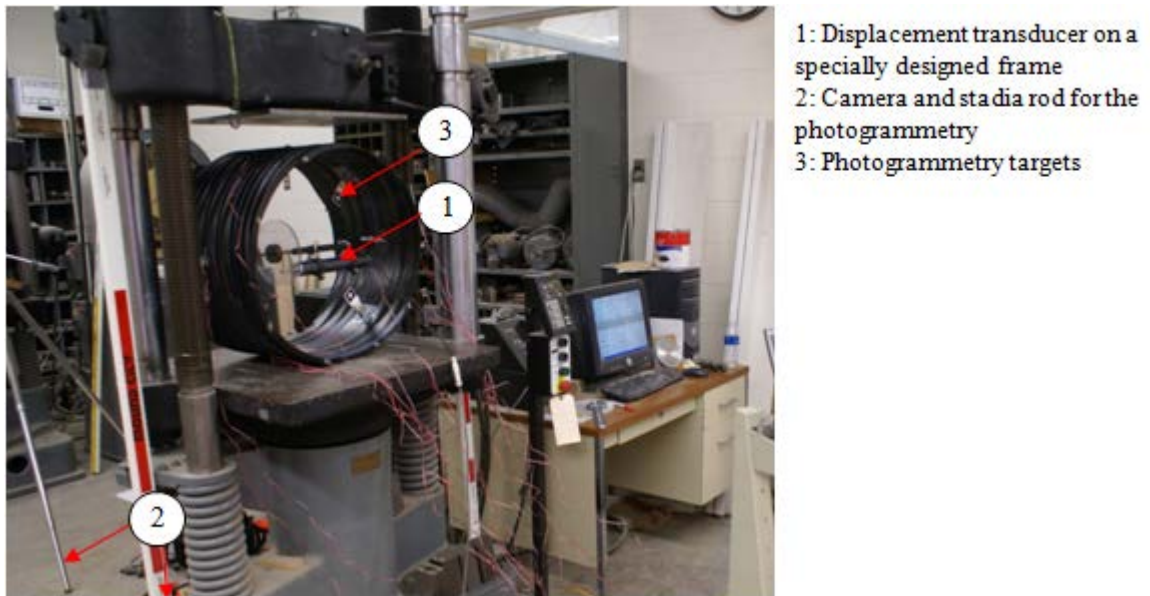
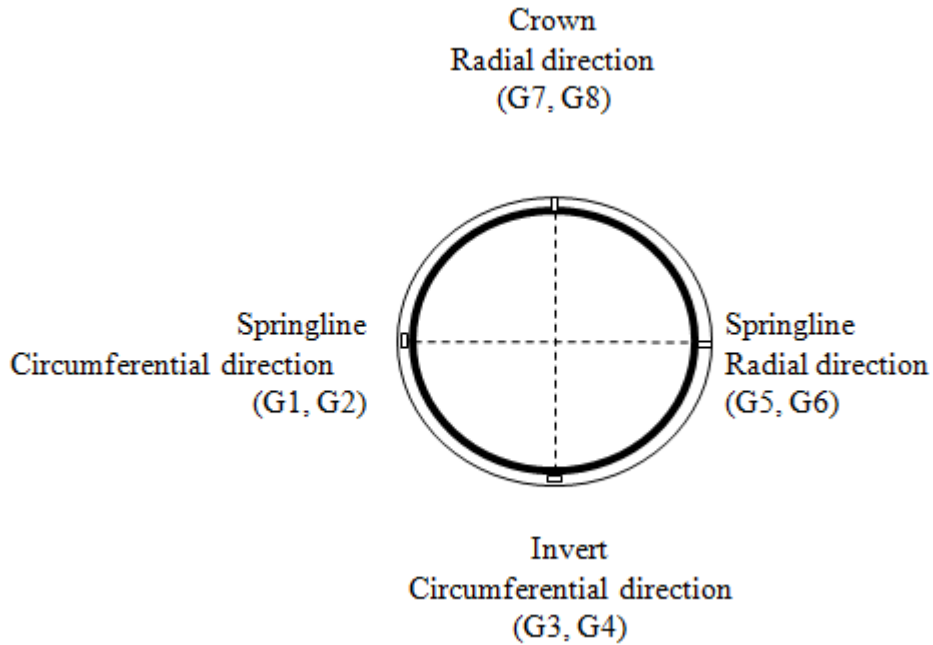


FIGURE 3.2 Test setup and instrumentation for the parallel plate load test (Khatri, 2012)

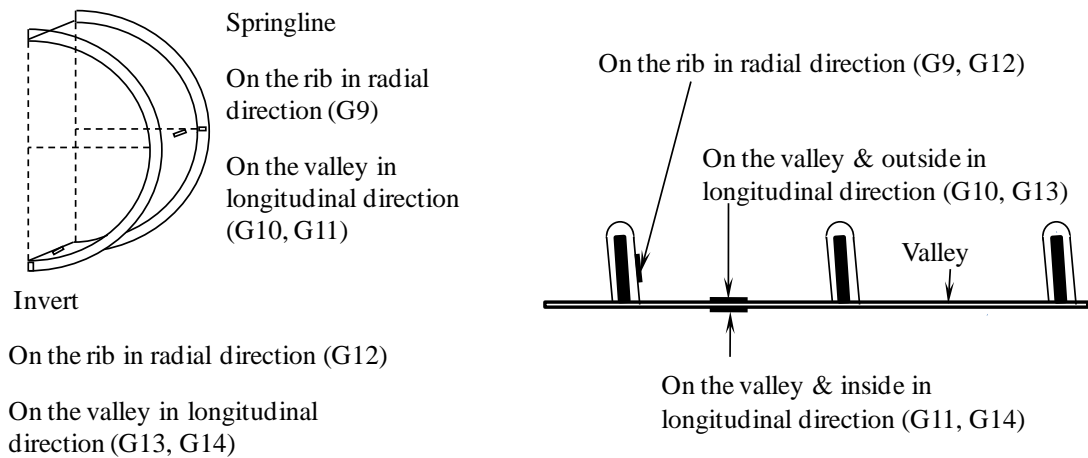
The displacement transducer in the compression machine measured the vertical deflection of the pipe during loading. The horizontal displacement of the pipe was measured by another

displacement transducer installed horizontally on a specially designed frame in the center of the pipe. For the photogrammetry method, targets were fixed on the inside wall of the pipe at 90° intervals. Photos of the deformed pipe during the test were taken at a time interval of 10 seconds.

Fourteen uniaxial, foil-type electrical resistance strain gages (labeled as G1 to G14) were used to measure the circumferential, radial, and longitudinal strains of the pipe at various locations (**FIGURE 3.3**). Eight strain gages were affixed at the center of the specimens on the steel surface at the crown, invert, and springline to determine both radial and circumferential strains. The plastic cover was removed at the desired locations to place the strain gages on the steel surface. Since the steel rib height was too small to attach the strain gages on the top of the rib, they were fixed at the neutral axis of the steel rib. In addition, six strain gages were placed on the plastic surfaces at ribs, inside and outside between the ribs (i.e., valley) to measure the strains in the plastic. For example, G10 and G13 were outside while G11 and G14 were inside. These four strain gages were used to measure the strains in the plastic in the longitudinal direction. **FIGURE 3.4** shows the strain gages fixed on both steel and plastic.

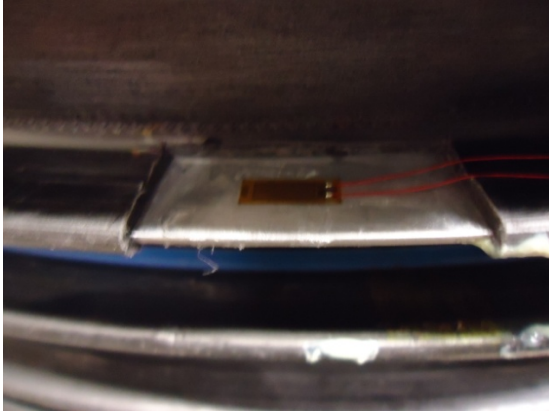


a) On the steel

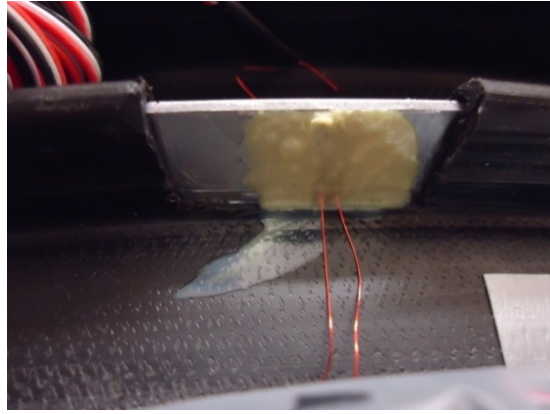


b) On the plastic surfaces

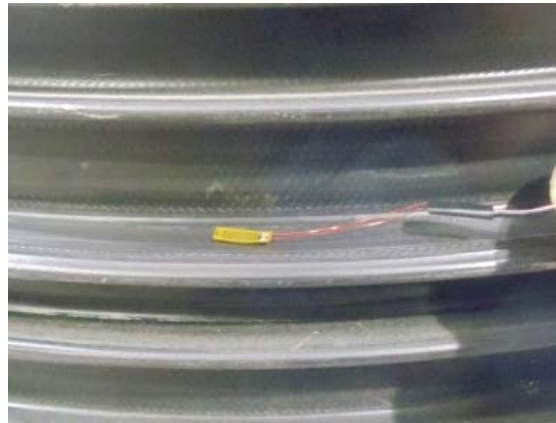
FIGURE 3.3 Symbols, locations, and orientations of strain gages on the pipe (Khatri, 2012)



a) On steel (circumferential direction)



b) On the steel (radial direction)
with coating material



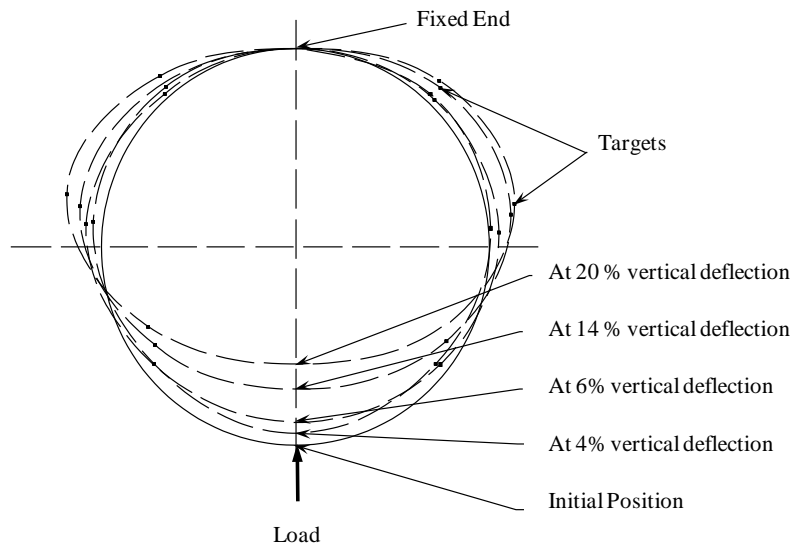
(c) On plastic (circumferential direction)

FIGURE 3.4 Strain gages on the steel and plastic surfaces (Khatri, 2012)

Test Results and Discussions

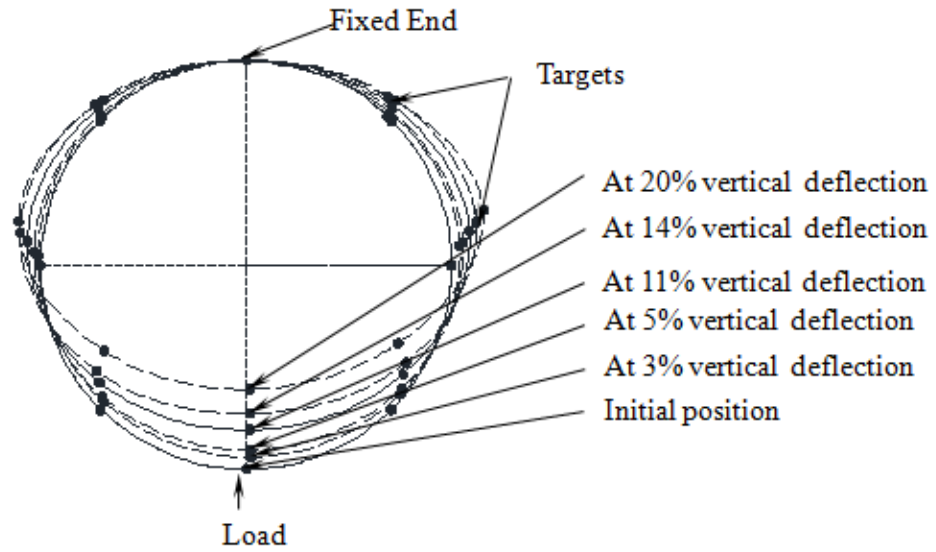
Deformed Pipe Shape. The displacement transducers could only measure the deflections of the pipes in the vertical and horizontal directions. Photogrammetry was used to generate the deformed shapes (**FIGURE 3.5**) of the test specimens. The deformed shapes (**FIGURE 3.5c**) of the exhumed pipe had the similar shapes as compared to the shapes obtained on the virgin pipe

(FIGURES 3.5a and b). The load-horizontal deflection curves of the test specimens from the photogrammetry method are compared well with those from the displacement transducer measurement for both virgin and exhumed pipes as shown in FIGURE 3.6. Therefore, the photogrammetry was able to capture the deformation of the pipe during the loading. From FIGURE 3.6, it is clear that for the particular horizontal deflection of the pipe, the load carried by the test specimens for both virgin and exhumed pipe were approximately same (for example, at 4% horizontal deflection, all pipe specimens carried approximately 681 lbf). This proves that the exhumed pipe was not damaged during the installation and the simulated traffic loadings. In addition, the deformed shapes of the pipe in Test 2 at 6 % and 14 % vertical deflections to the pipe diameter under the load in air were compared with the standard elliptical shapes (FIGURE 3.7) and it was confirmed that the deformed shapes of the pipes resembled closely with the elliptical shapes.

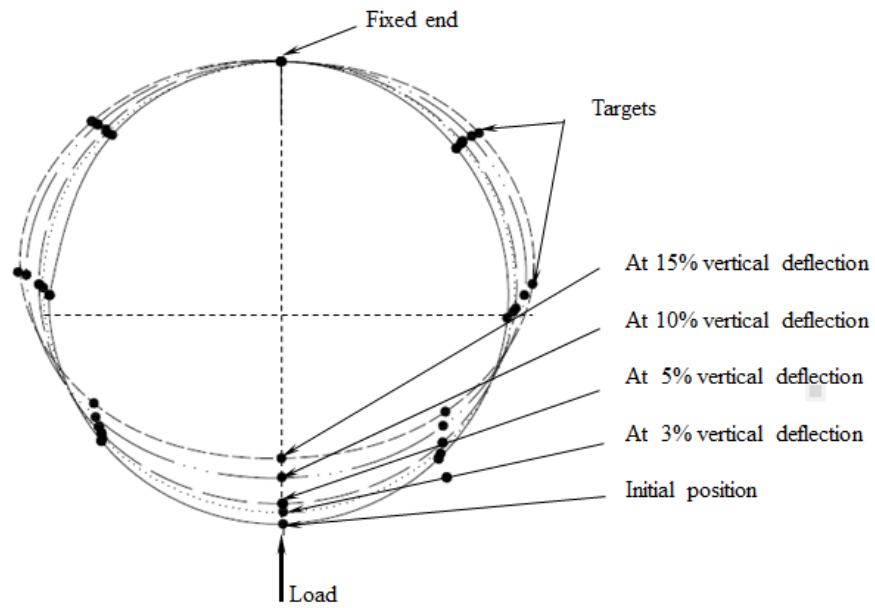


a) Test 2_virgin pipe

FIGURE 3.5 Deformed pipe shapes from the photogrammetry



(b) Test 3_virgin pipe



(c) Exhumed pipe

FIGURE 3.5 Deformed pipe shapes from the photogrammetry (continued)

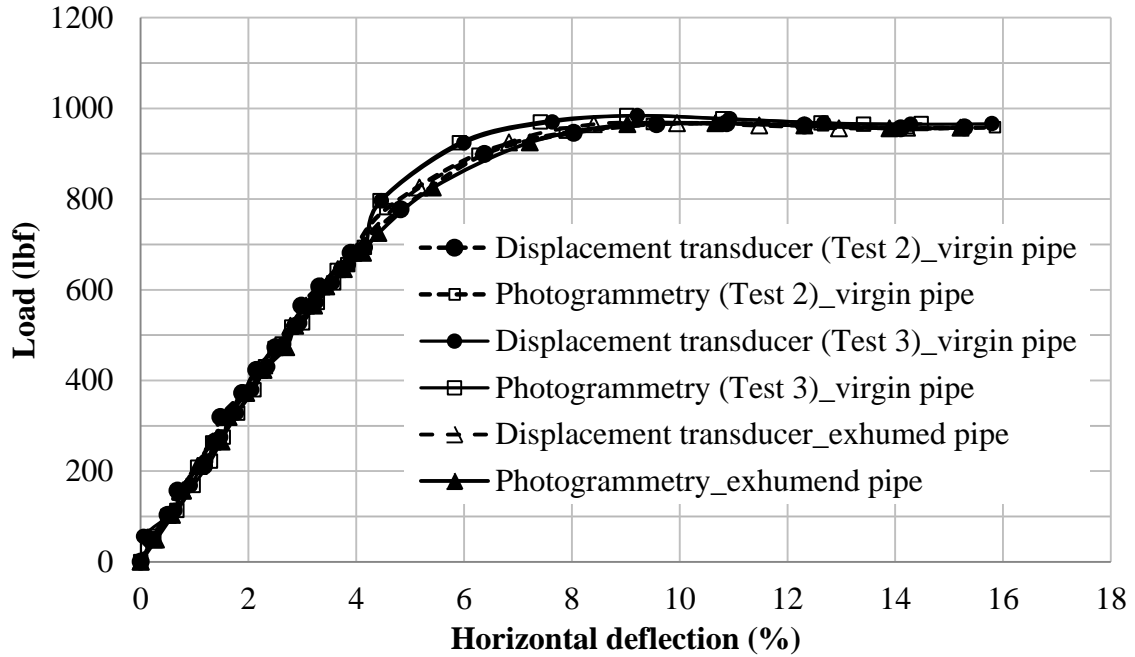


FIGURE 3.6 Comparison of the load-horizontal deflection curves obtained by the photogrammetry method and the displacement transducer

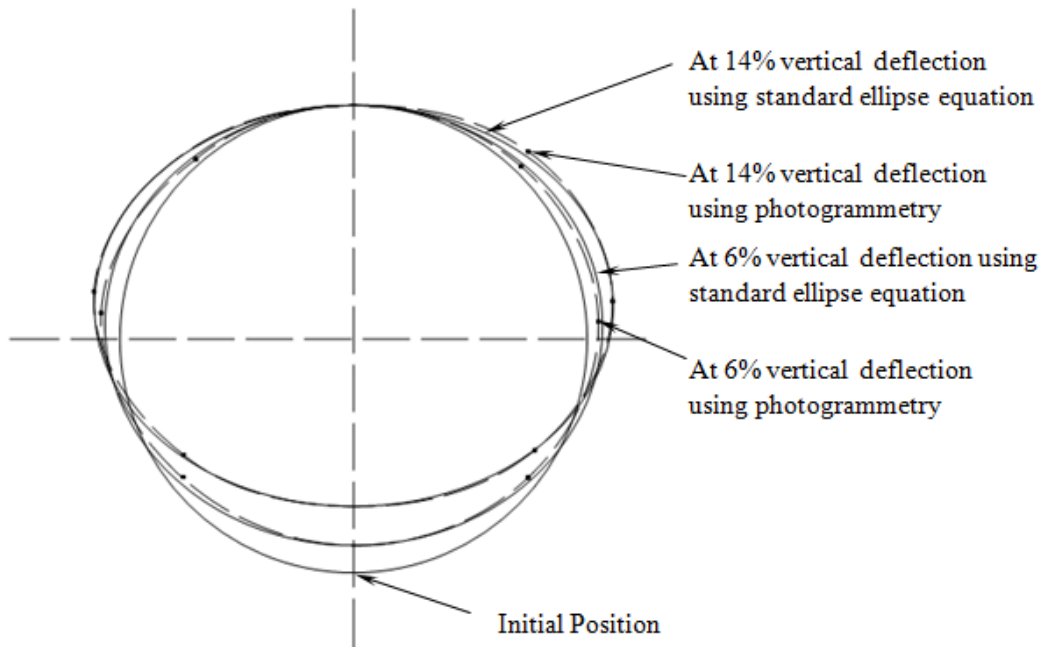


FIGURE 3.7 Comparison of the deformed pipe shapes from photogrammetry with the standard elliptical shapes

Load-deflection Responses. **FIGURE 3.8** shows the load-deflection responses, the horizontal and vertical deflections measured from the displacement transducer measurements, of the test specimens. The load-deflection response of the exhumed pipe specimen showed the similar behavior of the virgin pipe specimens. It is shown that both test specimens from the virgin and exhumed pipes started yielding at approximately 6% vertical deflection to pipe diameter. The average ultimate load capacity of 960 lbf was reached at approximately 10 % vertical deflection due to the out of plane buckling (will be discussed in the strain measurement section later) occurring on the ribs at the springline of the pipes. Neither valley liner nor wall crack was observed on the plastic. Based on visual observation, no reverse curve developed at the crown of the pipe during the test until 20% vertical deflection to pipe diameter was reached. **FIGURE 3.9** shows the vertical deflection was approximately 1.25 times the horizontal deflection for both virgin and exhumed pipes. From the above discussion, it is clear that the exhumed pipe retained its properties even after the installation of the pipe and the simulated traffic loading. Therefore, it is concluded that there was no damage on the exhumed pipe during the installation and the loading.

The pipe stiffness was calculated using **EQUATION 2.12** at 5% vertical deflection to pipe diameter. The bending stresses (σ_b) on the steel ribs were calculated using the bending equation ($\sigma_b=M/S$, where M = the bending moment at the section where stress is to be determined and S = the section modulus of the pipe wall) in which the moments calculated by **EQUATION 2.13**. The bending stresses (σ_b) were calculated at the springline and crown and corresponded to the yield load at approximately 6% vertical deflection to pipe diameter, assuming an axisymmetric (2D) geometry and isotropic material for simplicity. The calculated pipe stiffness and bending stresses in the extreme fiber of the steel reinforcement at 6%

deflection for both virgin and exhumed pipes' specimen are shown in **TABLE 3.2**. The extreme fiber bending stresses obtained are close to the steel yield values provided by the manufacturer. In addition, the calculated stiffness is more than the specified value (34 psi) per ASTM F2562/F2562M for Class 1 pipe of 24 in. in diameter at 5% vertical deflection to pipe diameter. Furthermore, the load at 20 % deflection is higher than 75 % of the peak load, although the peak load was reached before 20 % deflection. This result satisfies the buckling limit criterion per ASTM F2562/F2562M.

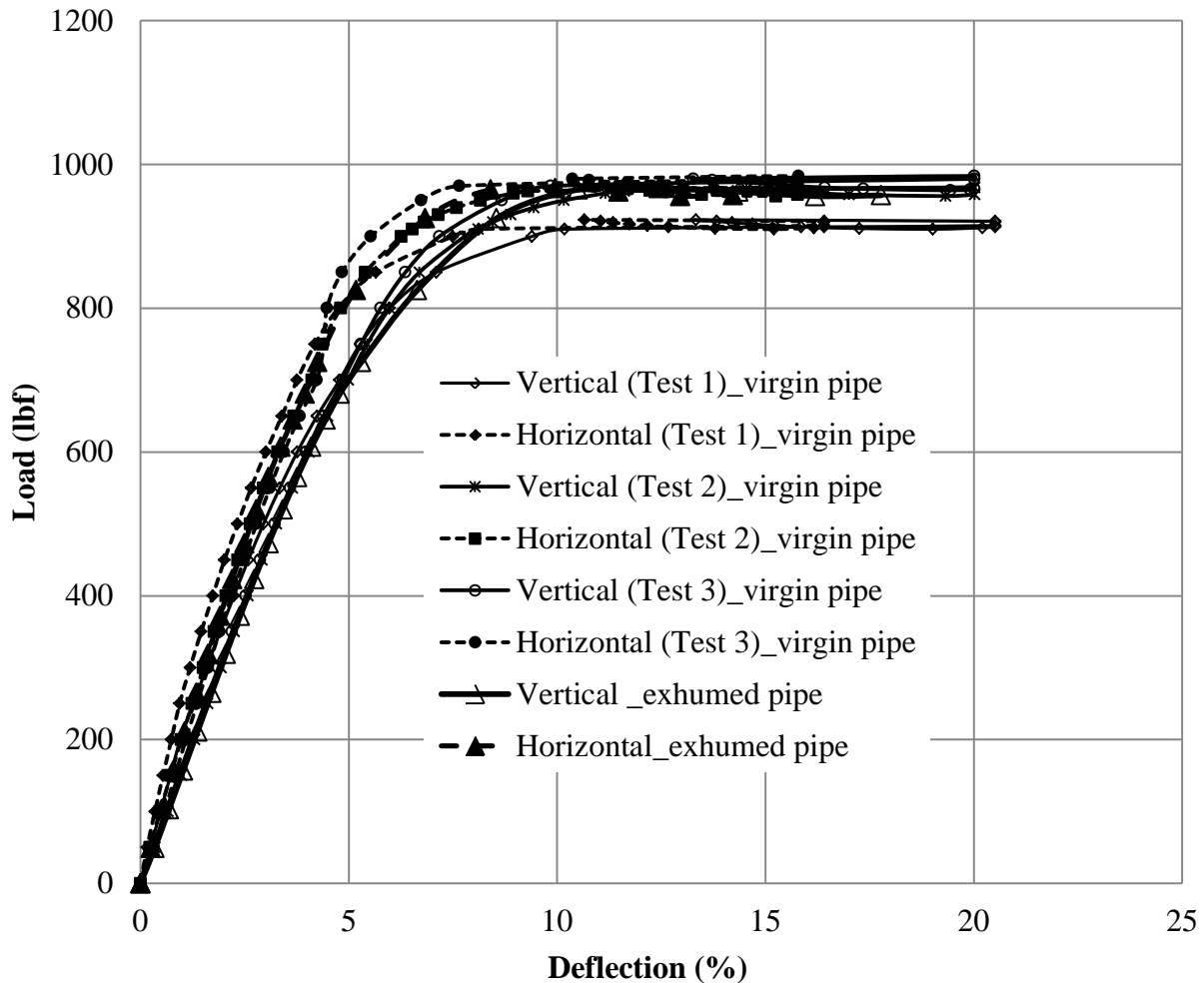


FIGURE 3.8 Load-deflection responses

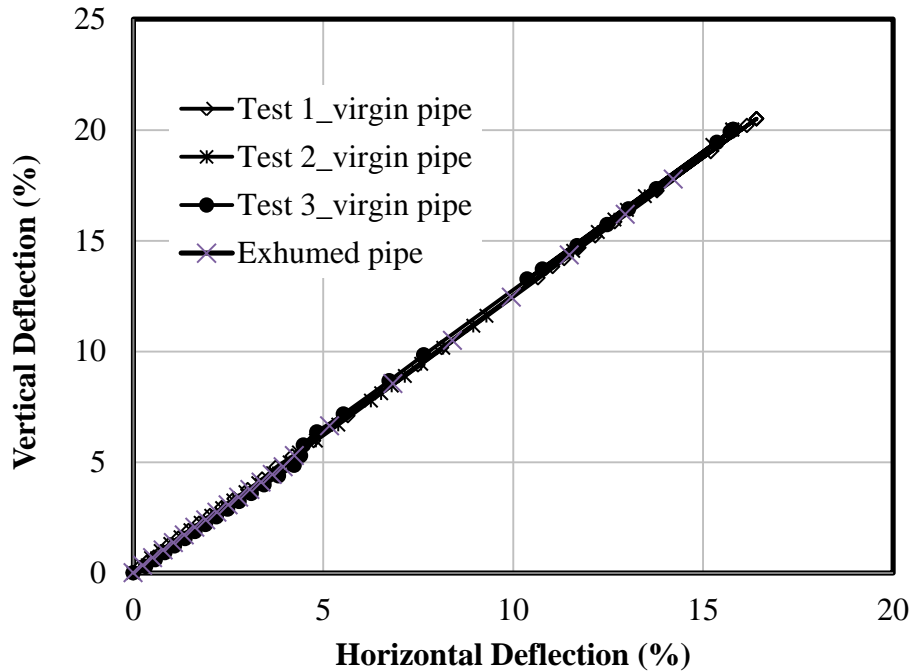


FIGURE 3.9 Relation between the vertical and horizontal deflections of the pipes

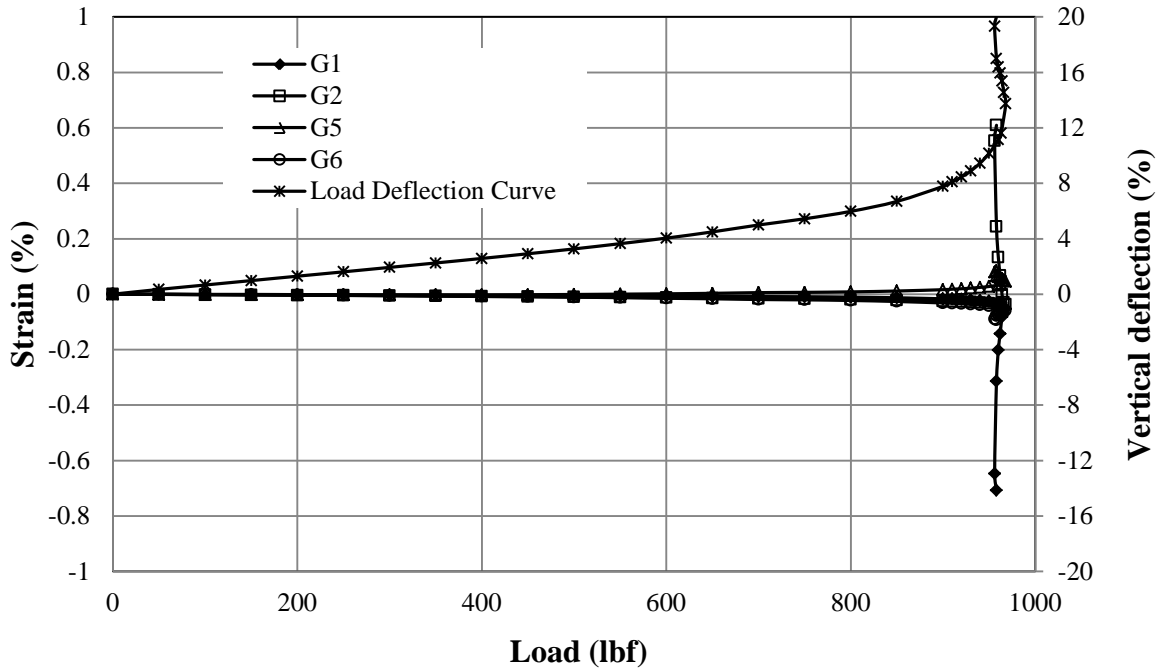
TABLE 3.2 Calculated pipe stiffness and equivalent bending stress values

Pipe	Test No.	Load(at 5% vertical deflection) (lbf)	Pipe stiffness (at 5% vertical deflection) (psi)	Initial pipe stiffness (based on the initial slope of the curve) (psi)	Equivalent Bending stress, σ_b	
					At springline (ksi)	At crown (ksi)
Virgin	1	727	43	56	78	71
	2	701	42	51	85	78
	3	715	43	48	81	68
	Avg.	714	43	52	81	72
Exhumed		701	42	51	114	88

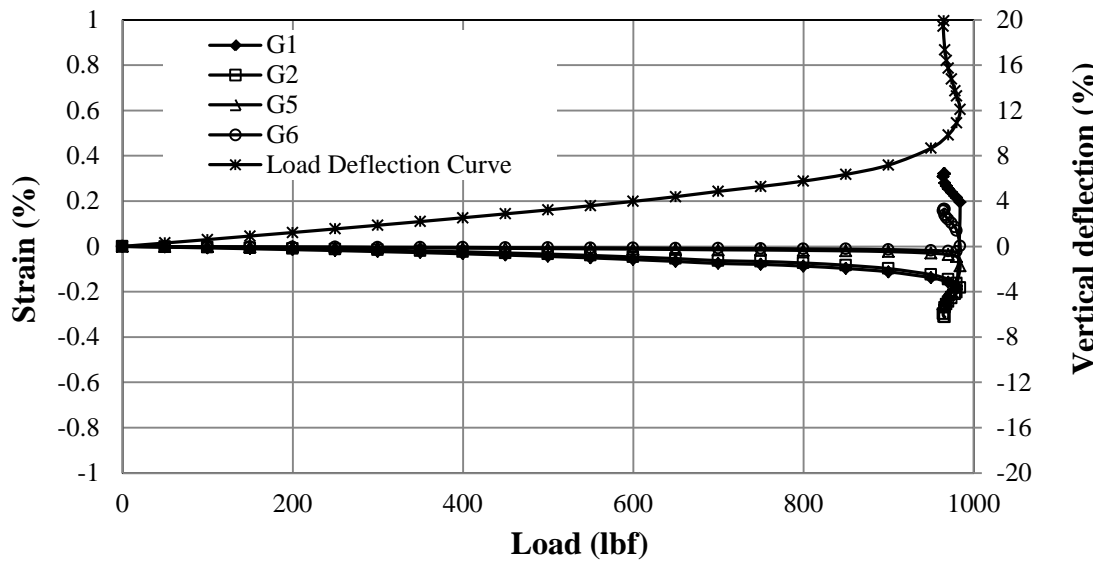
Strain. The above test results reflected the overall behavior of the SRHDPE pipes; however, local behavior of the pipes is important for the failure mechanisms of the pipes. Strain gages were attached on both steel and plastic surfaces of the test specimens to measure the strain developments in the pipes and to facilitate understanding of the possible failure mechanisms of the pipes. The strain gages were not attached in the first specimen (Test 1) of the virgin pipe. The symbols, locations, and orientations of the fourteen strain gages are presented in **FIGURE 3.3**. The strains measured on the HDPE surfaces were adjusted by multiplying a factor of 1.29 to account for the stiffness difference between strain gage and glue as suggested by Brachman et al. (2008). All the strain data are plotted against applied compressive loads in **FIGURE 3.10** to **3.12**. Positive values imply tensile strains while negative values are compressive strains.

FIGURE 3.10 shows the circumferential and radial strains developed on the steel surface of both virgin and exhumed pipes' specimens at the springline. For the virgin pipe, the maximum circumferential strain of 0.7% (G1, compressive strain) developed in Test 2 while the maximum radial strain of 0.28% (G5, tensile strain) developed in Test 3 (**FIGURES 3.10a and b**). **FIGURE 3.10c** shows that the maximum circumferential strain of 0.51% (G1, compressive strain) and the maximum radial strain of 0.029% (G5, tensile strain) were developed for the exhumed pipe. **FIGURE 3.10** shows that the circumferential and radial strains were small (less than 0.1%) before the yielding of the pipes. The strains suddenly increased when the loads were close to the ultimate load capacity of the pipes. Both strain gages (G1 and G2 in all test specimens) in the circumferential direction at the springline had compressive strains before the failure of the pipes. At the failure of the pipes, the two strain gages (one on each side of the steel rib) in the circumferential or radial direction showed one positive and one negative strain, which indicate the out of plane buckling of the steel ribs.

FIGURE 3.11 shows the circumferential and radial strains versus the applied loads on the steel surface at the crown and invert. The strains at the crown and invert showed the same trends for both virgin and exhumed pipe specimens. At the crown, both strain gages (G7 and G8) in the radial directions showed small tensile strains while at the invert, both strain gages (G3 and G4) in the circumferential direction had small compressive strains. **FIGURE 3.12** shows that the strain developments on the plastic were similar for both virgin and exhumed pipe specimens. The magnitudes of the strains in Test 3 were larger than those in Test 2. Most of the strain gages on the plastic of the exhumed pipe specimen were even lower than the strain gages on the plastic for the virgin pipe specimen. This suggests that the HDPE plastic was not damaged during the installation and the simulated traffic loading. The maximum strains (G10 and G11) developed on the plastic were approximately 2.5% in the valley inside and outside of the pipes in the longitudinal direction at the springline in Test 3, but they had opposite signs (i.e., tensile vs. compressive strain). From **FIGURE 3.13**, it is also clear that at the ribs, the plastic had much larger strains than the steel. In other words, the strains at the steel and plastic at the ribs are not compatible.

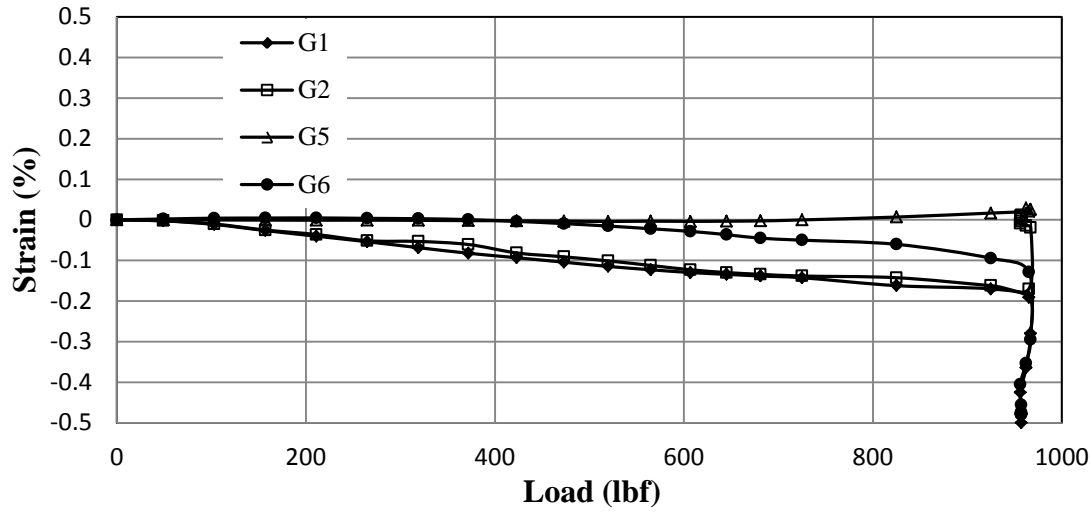


(a) Test 2



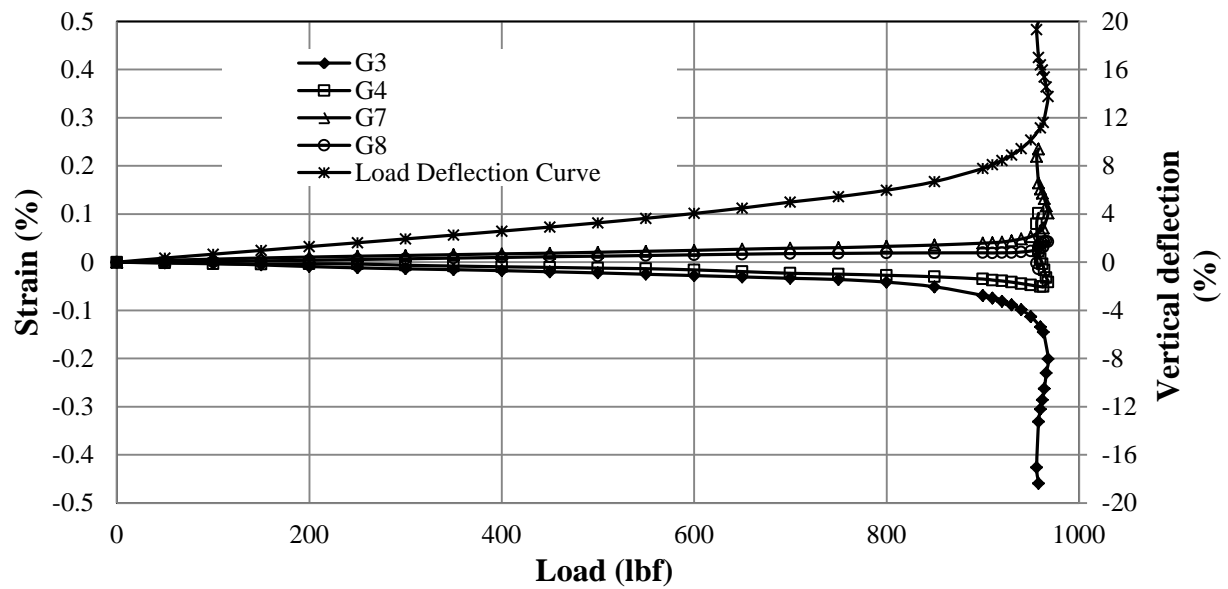
(b) Test 3

FIGURE 3.10 Circumferential and radial strains against the applied loads on the steel at the springline



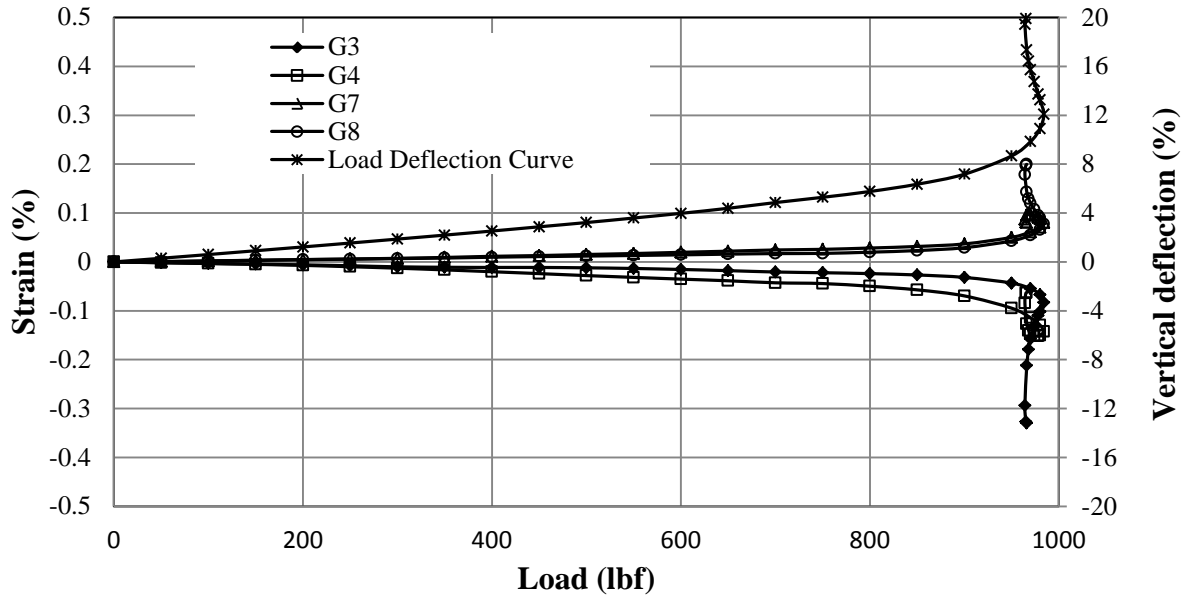
(c) Exhumed pipe

FIGURE 3.10 Circumferential and radial strains against the applied loads on the steel at the springline (continued)

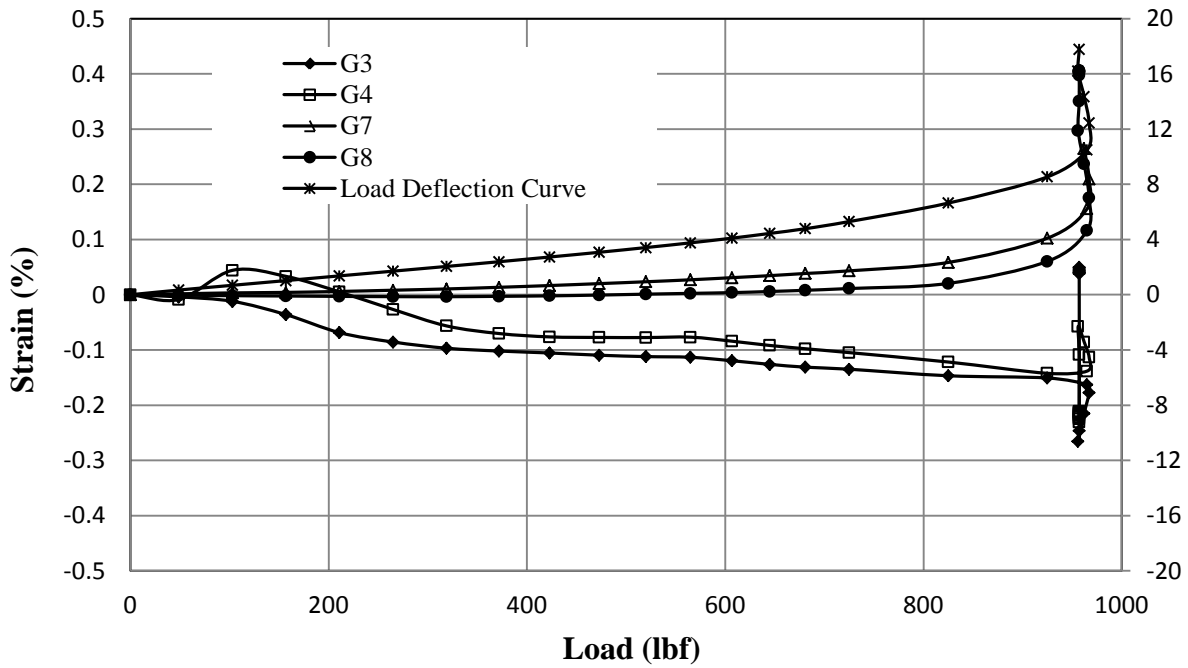


(a) Test 2

FIGURE 3.11 Circumferential and radial strains against the applied loads on the steel surface at the crown and invert

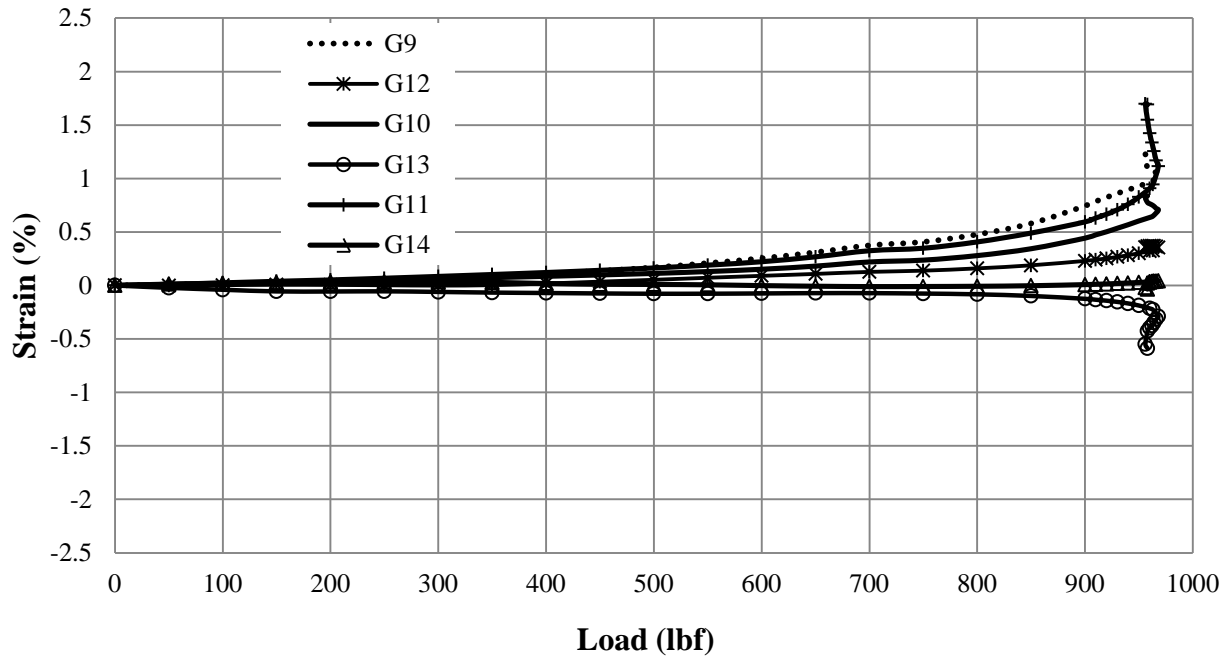


(b) Test 3

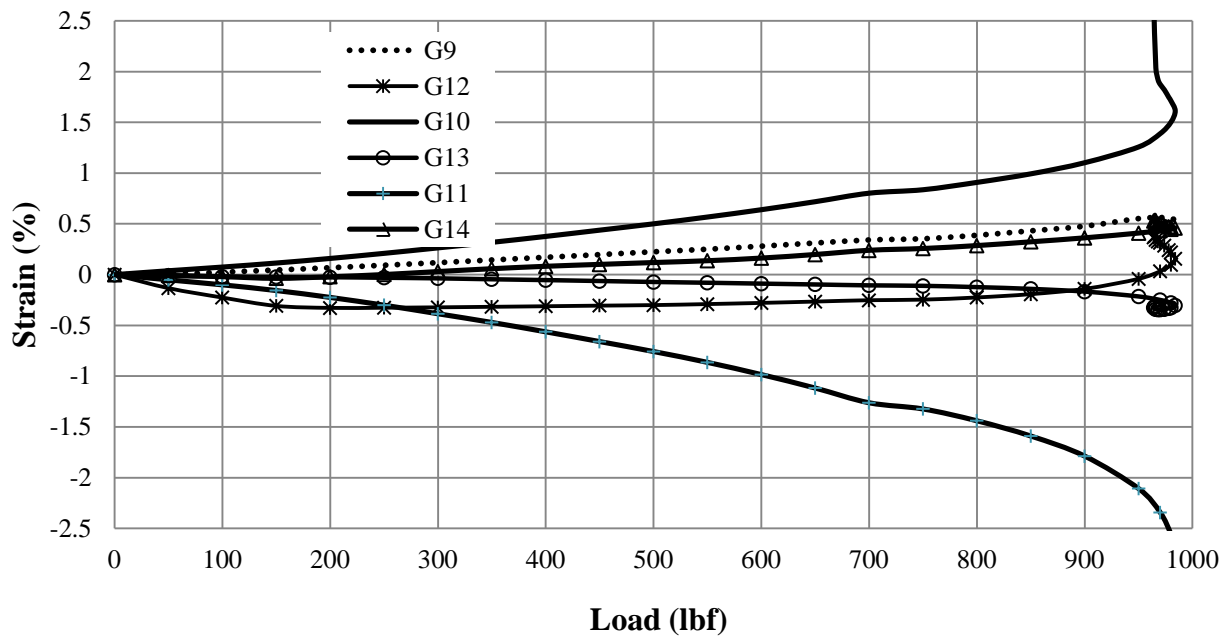


(c) Exhumed pipe

FIGURE 3.11 Circumferential and radial strains against the applied loads on the steel surface at the crown and invert (continued)

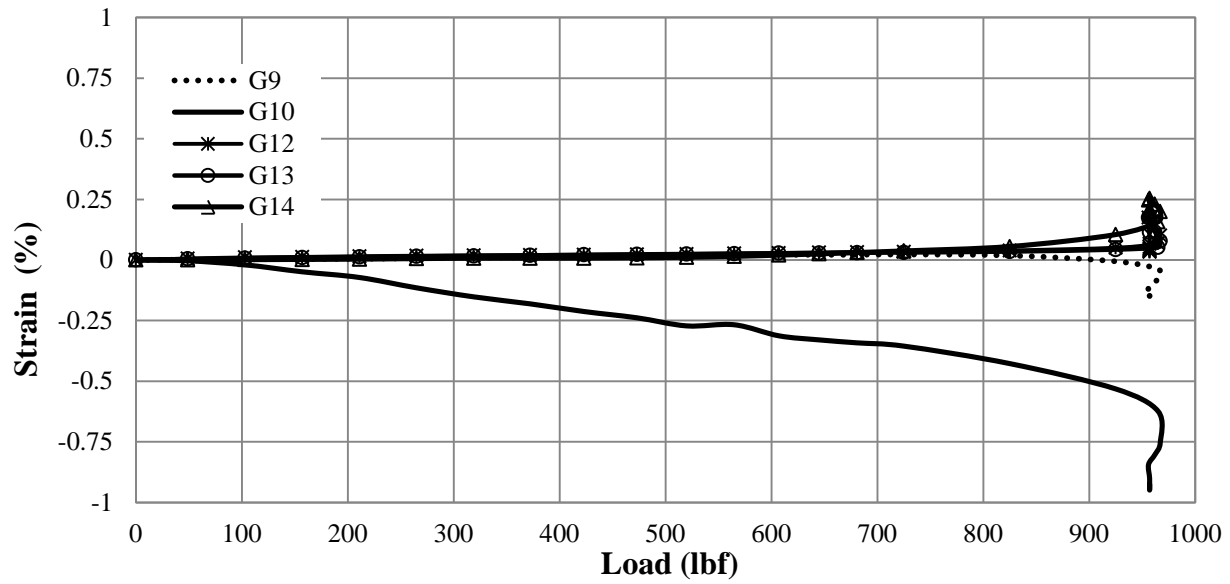


(a) Test 2



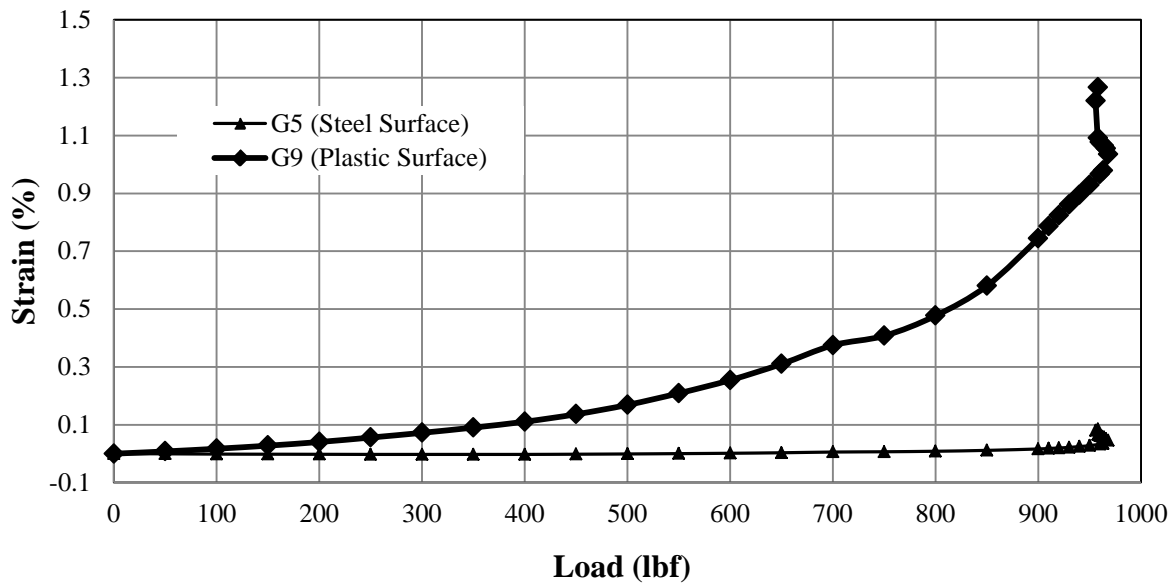
(b) Test 3

FIGURE 3.12 Strains against the applied loads on the plastic surface



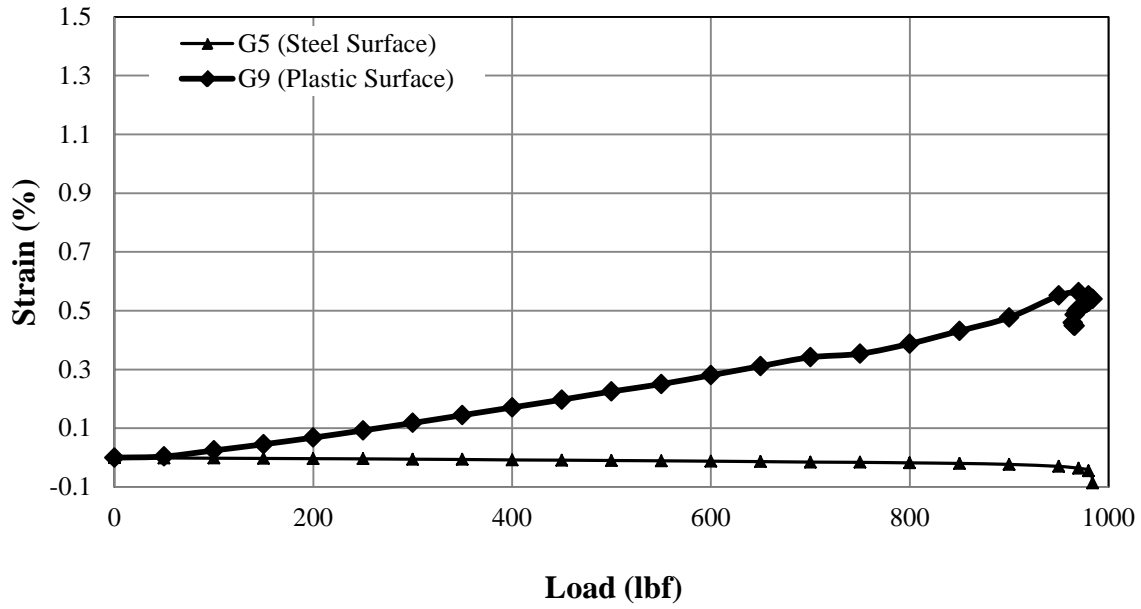
(c) Exhumed pipe

FIGURE 3.12 Strains against the applied loads on the plastic surface (continued)

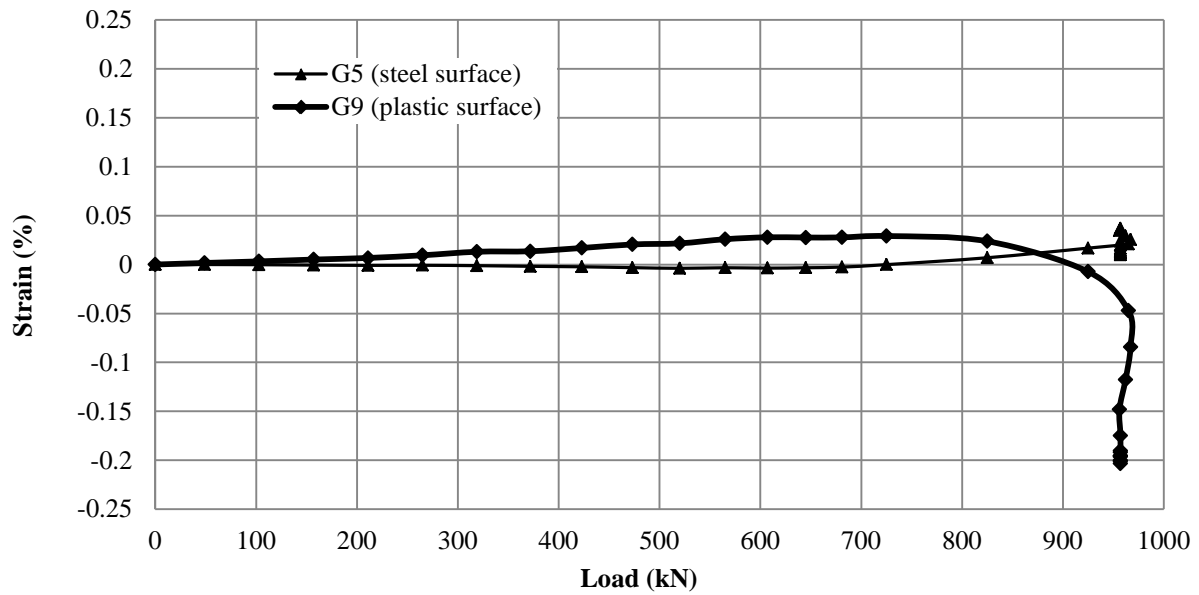


(a) Test 2

FIGURE 3.13 Comparison of strains developed on the steel rib and plastic surfaces in the radial direction at the springline



(b) Test 3



(c) Exhumed pipe

FIGURE 3.13 Comparison of strains developed on the steel rib and plastic surfaces in the radial direction at the springline (continued)

3.1.2 Stub Compression Tests

Stub compression tests were carried out on four specimens, as per NCHRP report 631 (McGrath et al., 2009), to evaluate the resistance to local buckling due to the compressive circumferential strain in the pipe. Each specimen was compressed in a universal test machine between two rigid plates at the rate of 0.05 ± 0.01 in. /min until the failure of the specimen. The specimens were carefully cut from a 24 in. diameter pipe to make the ends parallel to each other and to the radial line through the center of the specimen. The test specimens had a longitudinal length of 3 in. (i.e., three periods) and circumferential length of 2 in. **FIGURE 3.14** shows a picture of the specimen taken during the test.



FIGURE 3.14 Specimen crushing in the stub compression test

From the test results, the ultimate axial forces ranged from 2,904 to 3,758 lbf with an average value of 3,231 lbf with a total variation among the samples of 29.4 %. The test details were described by Khatri (2012). Moore (2009) found an ultimate axial load of 4,200 lbf with a variation of 68%. These high variations were due to lack of precision to cut the specimen ends so that each rib was loaded uniformly. Moore (2009) later prepared the specimens with a

machine shop mill to provide the precise specimen ends. The similar technique was used by the independent testing laboratory, TRI on the SRHDPE pipe of 24 in. in diameter and an ultimate axial load of 5,986 lbf was found with a variation of 3.8%.

In addition, the longitudinal properties and the creep behavior of the 24 in. diameter pipe were discussed in details by Khatri (2012).

3.1.3 Summery

The data from the parallel plate tests conducted in air on the 24 in. virgin SRHDPE pipes by Khatri (2012) in his Master's study were presented above. The parallel plate test on the 24 in. pipe exhumed from the test section was also conducted in this study to investigate the possible damage occurring on the pipe during the installation and the simulated traffic loading. The following conclusions can be drawn from this study:

The virgin pipe met both minimum pipe stiffness and buckling limit criteria according to ASTM F2562/F2562M (Khatri, 2012). Parallel plate test result on the exhumed pipe also shows that the exhumed pipe satisfied the minimum pipe stiffness and buckling limit criteria. The ultimate load carried by the exhumed pipe specimen was nearly equal to the ultimate loads carried by the virgin pipe specimens. The virgin and exhumed pipes both started yielding at approximately 6% vertical deflection to pipe diameter and reached the ultimate load capacity at approximately 10% vertical deflection. The vertical deflection of the virgin and exhumed SRHDPE pipe tested in the parallel plate load tests was approximately 1.25 times the horizontal deflection. The above comparison on global behavior of the pipe specimens suggested that the installation and the simulated traffic loadings did not damage the structural integrity of the

SRHDPE pipe. In addition, the strains measured for local behavior on the steel and plastic showed that the strains on the exhumed pipe specimen were not much different than the strains measured on the steel and strains on the virgin pipe specimen. This result further suggests that the SRHDPE pipe was not damaged. The out of plane buckling on the ribs of the pipe wall at high level of load occurred on both virgin and exhumed pipe specimen. The measured strains on plastic ribs were higher than strains of the steel during loading, indicating the strain incompatibility of steel ribs and plastic during the loading. The photogrammetry method became effective to obtain the deflected shapes of the pipe under loading. The deflected shape of the SRHDPE pipe was found to be elliptical.

3.2 Soil Types and Properties

In this section, the properties of soils used in both laboratory and field tests were studied by conducting various laboratory tests.

3.2.1 Clayey Soil and Its Characteristics

In the laboratory, a clayey soil (hereinafter referred as Clay-I) was used as the surrounding soil. An in-situ soil recovered from the field test was also found to be a clay soil (hereinafter referred as Clay-II). The properties of these two surrounding soils were evaluated through various laboratory tests conducted at KU, including hydrometer, Atterberg limits, and specific gravity.

The grain-size distributions of the soils were determined using the hydrometer tests performed in accordance with ASTM D422-63 and are shown in **FIGURE 3.15**. For the clayey soil (Clay-I), the liquid limit of 54 % (**FIGURE 3.16a**) and the plastic limit of 26% were obtained from the Atterberg limits tests following ASTM D4318-05. The liquid limit of 54.5 %

(FIGURE 3.16b) and the plastic limit of 30% were obtained for the clay soil (Clay-II). Based on the Atterberg limits and the grain size distributions, both clayey soils were classified as fat clay (CH) soils according to the Unified Soil Classification System (USCS). The soil specific gravity (ASTM D854-10) of 2.71 was obtained for both of them. Since the grain size distributions, liquid and plastic limits, and specific gravity are similar for both clayey soils, the laboratory tests such as compaction tests, unconfined compression tests etc. were only conducted on the clayey soil (Clay-I). The properties obtained for the Clay-I soil were used even for the clayey soil (Clay-II) in the analysis in this study.

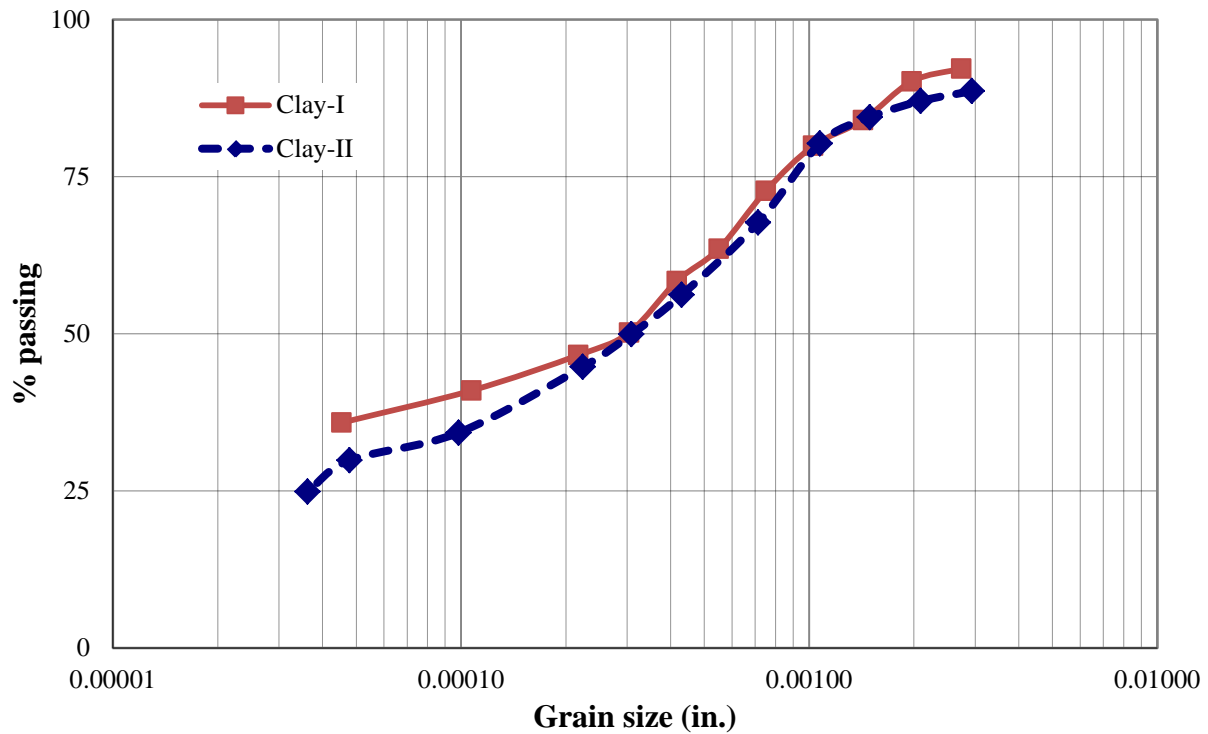
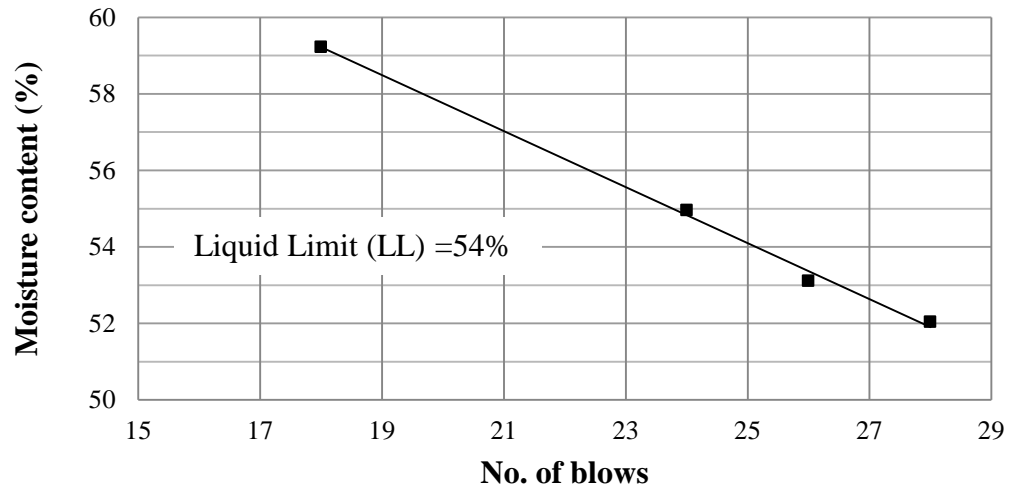
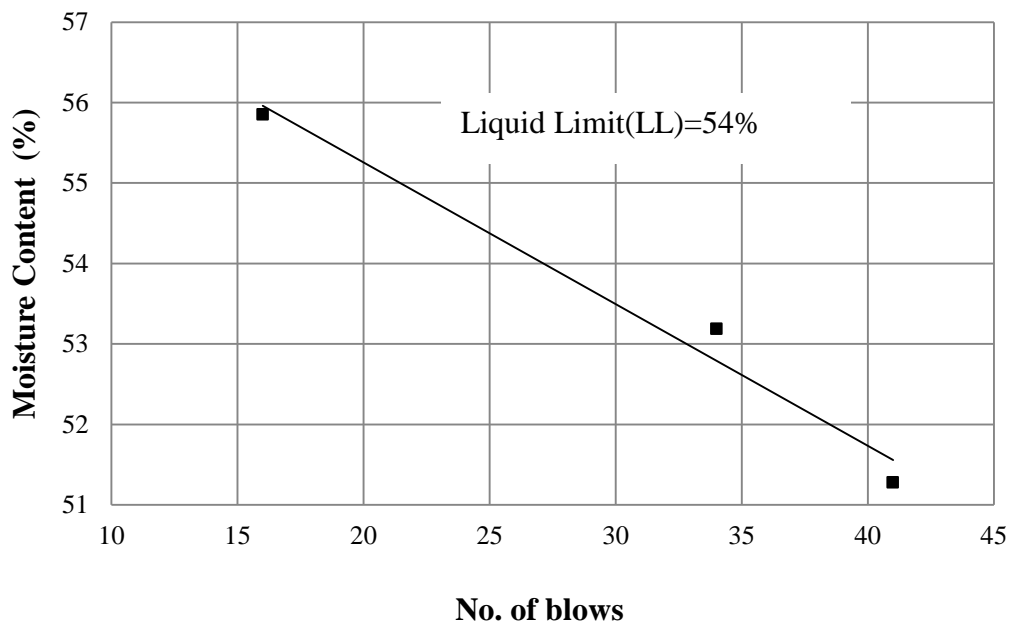


FIGURE 3.15 Grain size distributions of the clayey soils



(a) Clayey soil (Clay-I)



(b) Clayey soil (Clay-II)

FIGURE 3.16 Flow curves of the clayey soils

The standard Proctor test was conducted on the clayey soil (Clay-I) in accordance with ASTM D698-07. The maximum dry density was determined to be 97.8 pcf, and its corresponding optimum moisture content (OMC) was 24%. The compaction curve is shown in **FIGURE 3.17**.

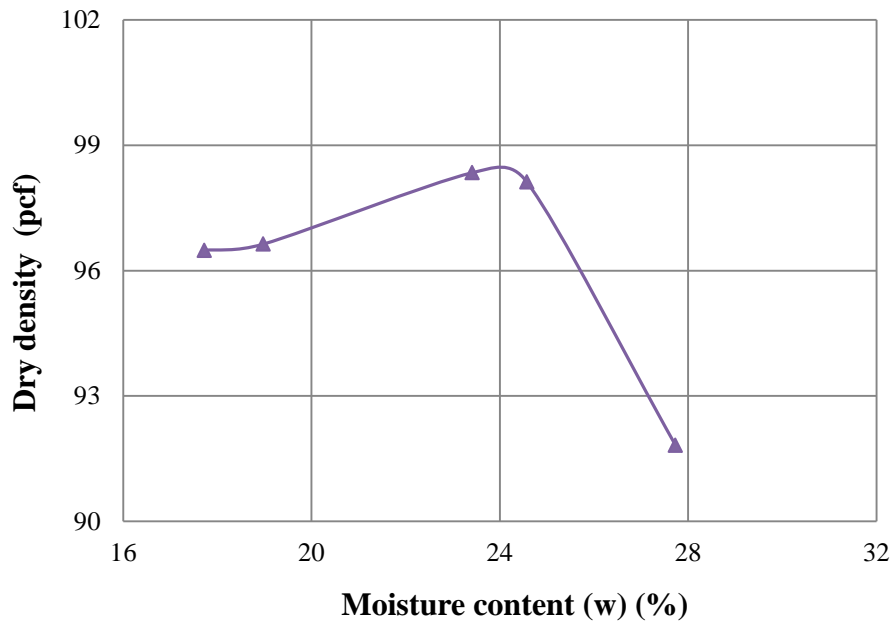


FIGURE 3.17 Compaction curve for Clay-I

For the clayey soil (Clay-I), modified compaction, vane shear, and CBR tests were also conducted. The maximum dry density was determined to be 104 pcf and the optimum moisture content was 21%. A correlation between the CBR value and the vane shear strength (c_u) was established ($c_u=298$ CBR, where c_u is in psf and CBR in percentage). The compaction curves, vane shear strengths, and CBR values are shown in **FIGURE 3.18**. Unconfined compression tests (ASTM D 2166) were also carried out at different moisture contents with the soil specimens of 2.8 in. diameter and 5.6 in. height. The stress-strain curves obtained from the unconfined compression tests are shown in **FIGURE 3.19**.

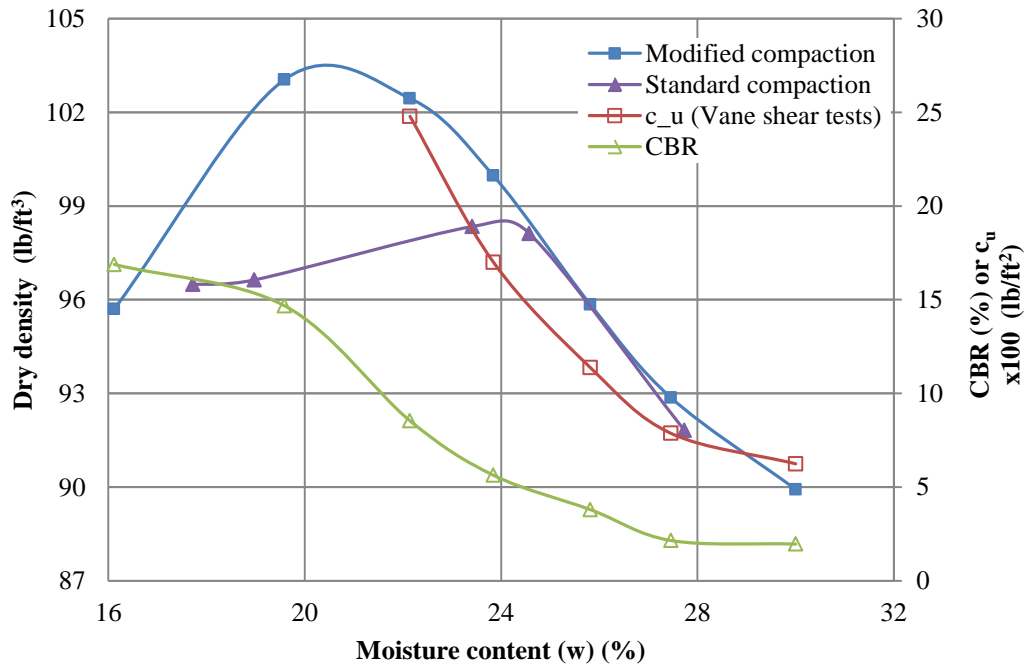


FIGURE 3.18 Densities, vane shear strength, and CBR curves

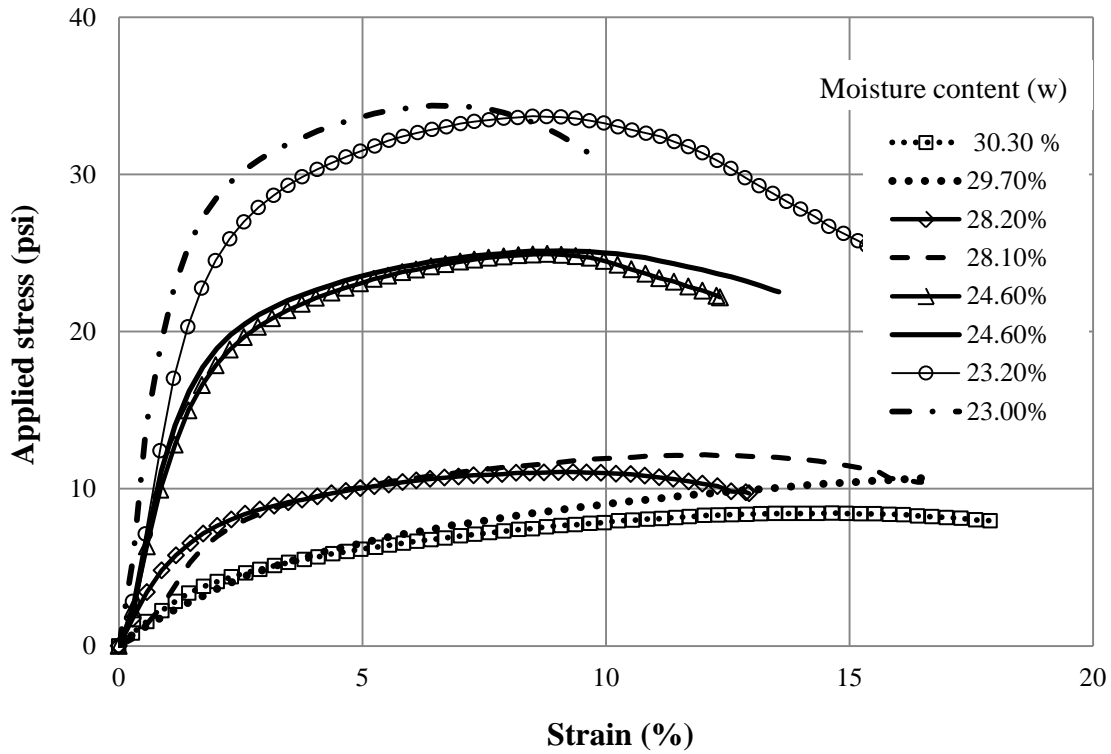


FIGURE 3.19 Stress-strain curves at different moisture contents

3.2.2 Bedding and Backfill Soils and Their Characteristics

Three different materials, Kansas River sand also known as pea gravel (hereinafter referred as KR sand), crushed stone also known as clean aggregate (hereinafter referred as CS), and AB-3 aggregate materials (hereinafter referred as AB-3-II) were used as bedding materials. For all test sections both in the laboratory and field, the soil used as the bedding material was also used as the backfill material. Two types of crushed stones, one in the laboratory tests (hereinafter referred as CS-I) and other in the field test (hereinafter referred as CS-II), were used.

KR Sand

Kansas River sand is a poorly-graded sand based on the USCS, which was used as the backfill and bedding materials in two box tests in laboratory. **FIGURE 3.20** shows the grain size distribution of this sand, which had a mean size of 0.022 in., a uniformity coefficient C_u of 3.18, and a curvature coefficient C_c of 0.93. The minimum and maximum unit weights were 102 and 120 pcf based on the minimum and maximum density tests conducted in accordance with ASTM D4254-00 and ASTM D4253-00, respectively. The minimum and maximum density values were used to evaluate the relative density of the sand. The relative compaction of the sand was correlated to the relative density using the relation, $R = 80 + 0.2D_r$, suggested by Lee and Singh (1971). The peak frictional angle of 37° was obtained by the large direct shear tests on the sand compacted at 70% relative density according to ASTM D3080 (**FIGURE 3.21**).

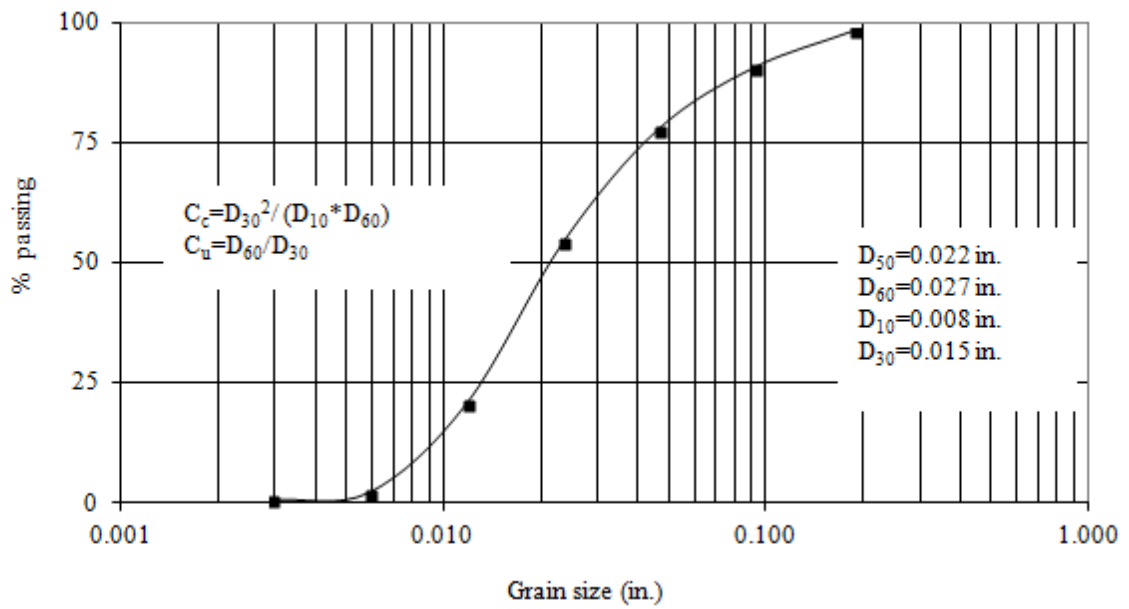
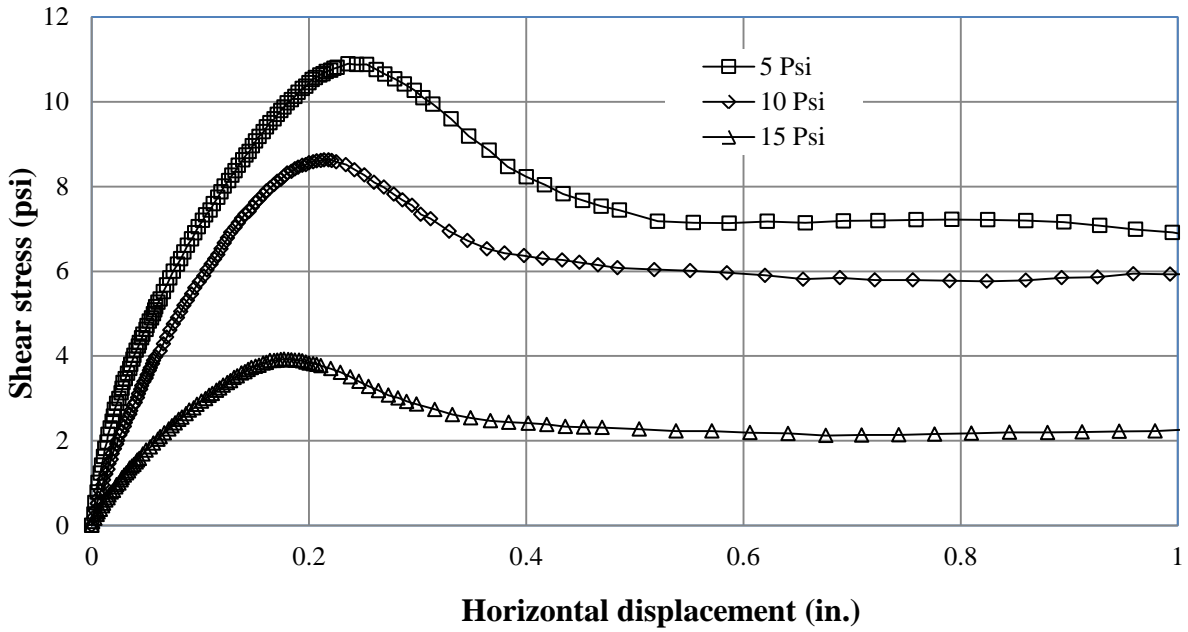


FIGURE 3.20 Grain size distribution of the sand

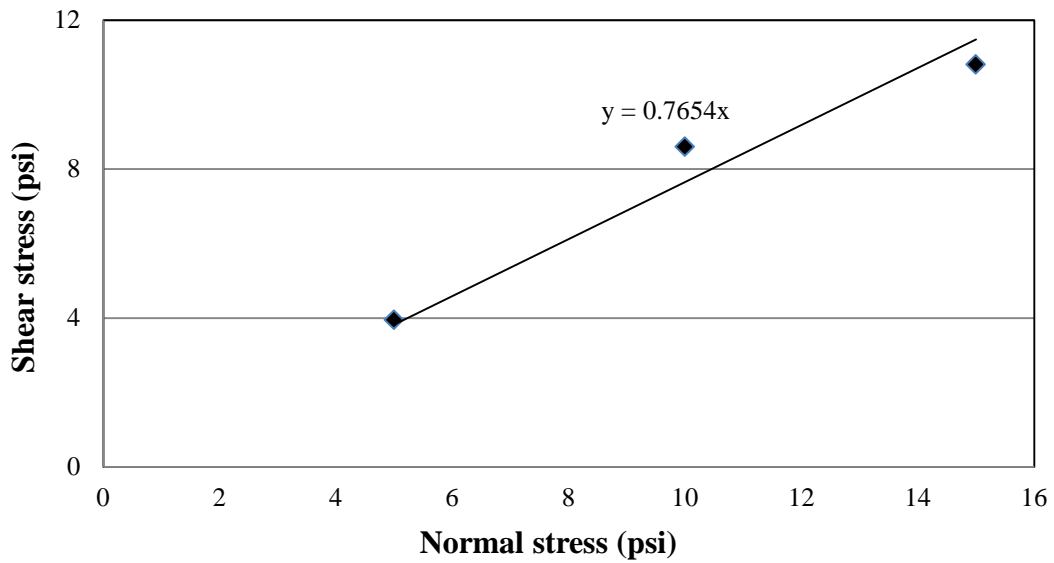


(a) Large direct shear test set up



(b) Shear stress vs. displacement curves

FIGURE 3.21 Large direct shear box tests for the KR sand



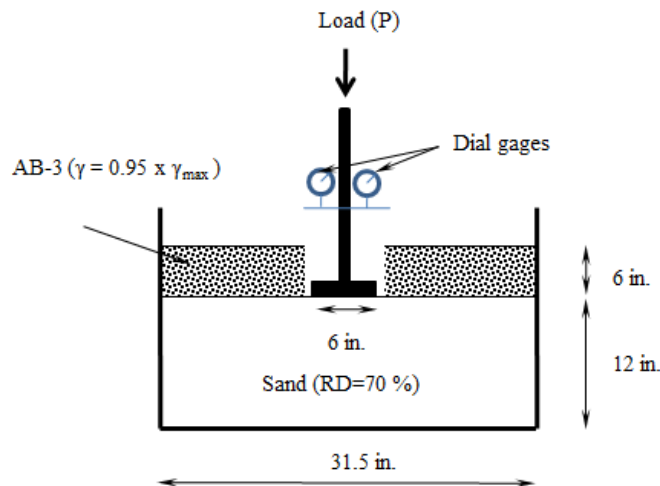
(c) Shear vs. normal stress

FIGURE 3.21 Large direct shear box tests for the KR sand (continued)

A small box plate-loading test was carried out to estimate the modulus of the KR sand as shown in **FIGURE 3.22a**. A 12 in. thick sand layer was compacted at 70 % relative density. To provide the confinement on the surface of the sand, a six in. thick AB-3-I material (used as base course material in the laboratory test discussed in chapter 4 was compacted on the top of the sand at 95% maximum dry density with 9% moisture content. A loading plate of 6 in. diameter was used to apply vertical loads and three dial gages were used to measure settlements of the loading plate. From the load deflection curve (**FIGURE 3.22b**), the elastic modulus, E, of the KR sand was found to be 2,027 psi using the elastic formula (**EQUATION 3.1**). The poison's ratio (ν) of 0.33 was taken for the modulus calculation of the sand.

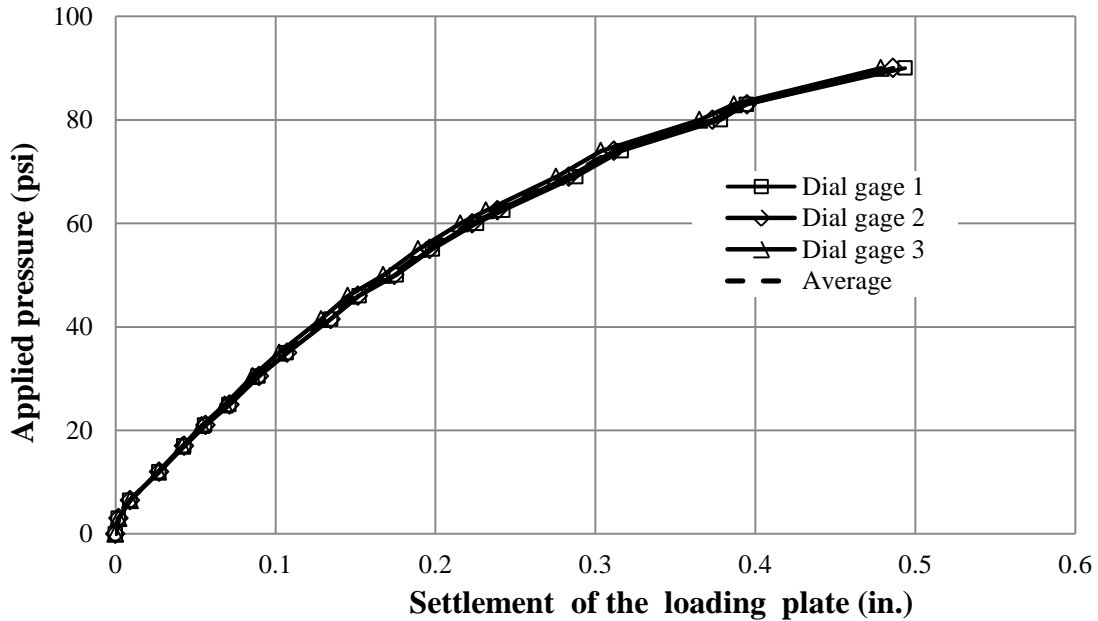
$$E = 0.79(1 - \nu^2) D \frac{P}{\delta} \quad 3.1$$

where ν is the poison's ratio (0.33) , D is the diameter of the loading plate, and p is the applied pressure corresponding to the settlement of the plate, δ , in the linear elastic region of the curve (**FIGURE 3.21b**).



(a) Schematic diagram of test set up

FIGURE 3.22 A small box plate loading test for the KR sand



(b) Pressure-settlement curves

FIGURE 3.22 A small box plate loading test for the KR sand (continued)

Crushed Stone

CS-I. Crushed stone (CS-I), used as bedding and backfill materials in one laboratory box test, was poorly graded based on the USCS. **FIGURE 3.23** shows the grain size distribution of the crushed stone (CS-I). It had a mean size of 0.44 in., a uniformity coefficient C_u of 2.3, and a curvature coefficient C_c of 1.01. The minimum and maximum unit weights of the crushed stone (CS-I) were 86 and 103 pcf determined by conducting the minimum and maximum density tests (ASTM D4254-00 and ASTM D4253-00). The peak frictional angle of the crushed stone (CS-I) was 53° , obtained by direct shear tests (ASTM D3080), in which the crushed stone (CS-I) was placed by raining particles into the box from a height of approximately 2 ft. (**FIGURE 3.24**). A

small box plate loading test as described above for the KR sand, was carried out to estimate the modulus of the crushed stone (CS-I), which was determined to be 1,125 psi (the crushed stone was rained into the box from the height of approximately 2 ft. and leveled) (FIGURE 3.25). The raining of the crushed stone into the box from a two foot height resulted in the relative density of 50 %.

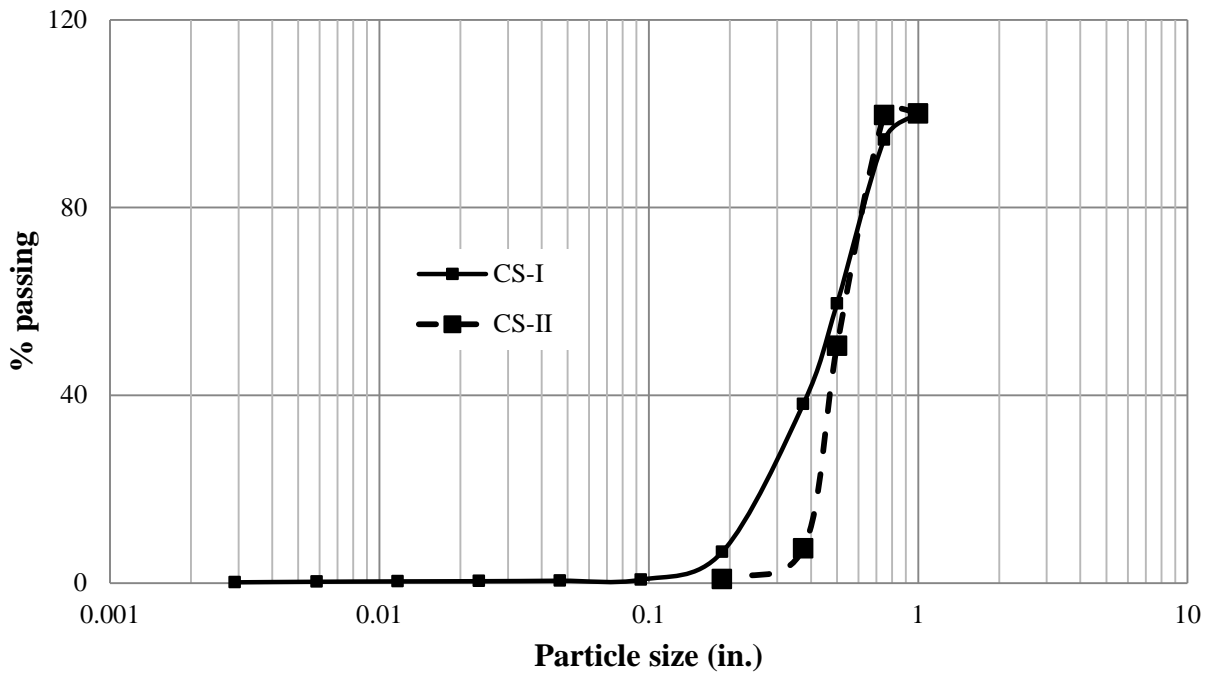
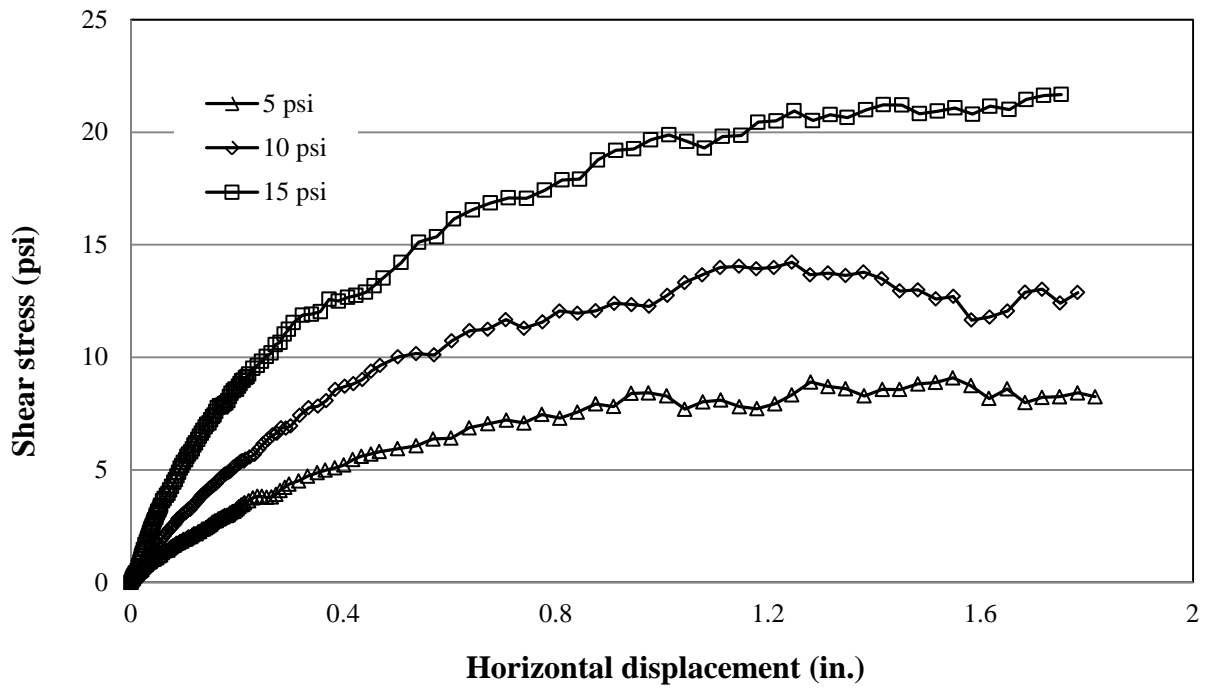
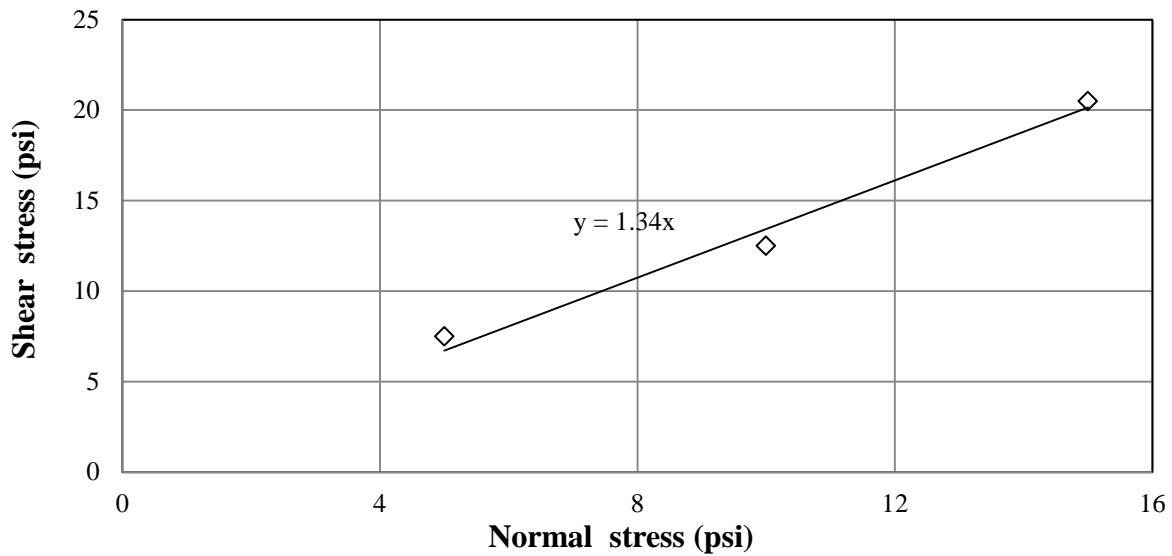


FIGURE 3.23 Grain size distributions of the crushed stone

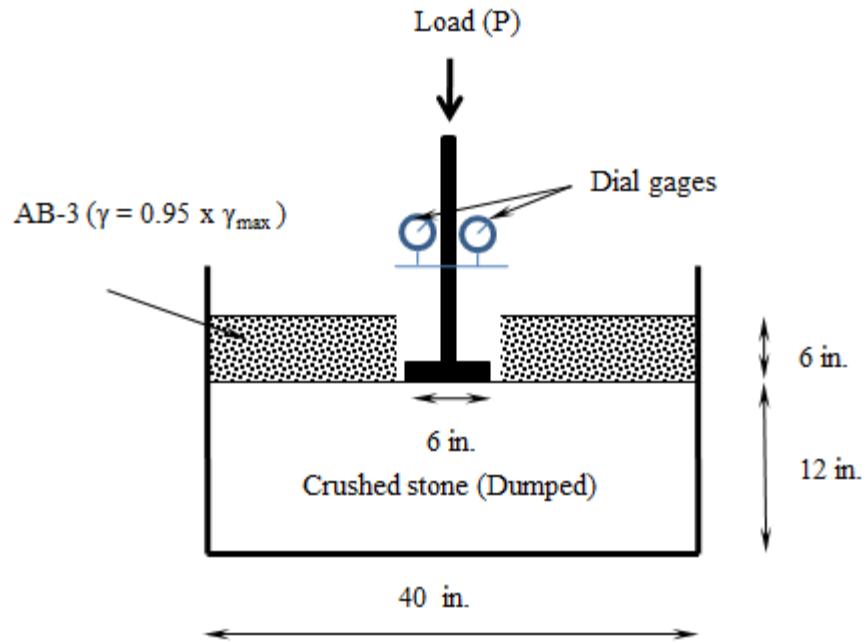


(a) Shear stress vs. displacement curves

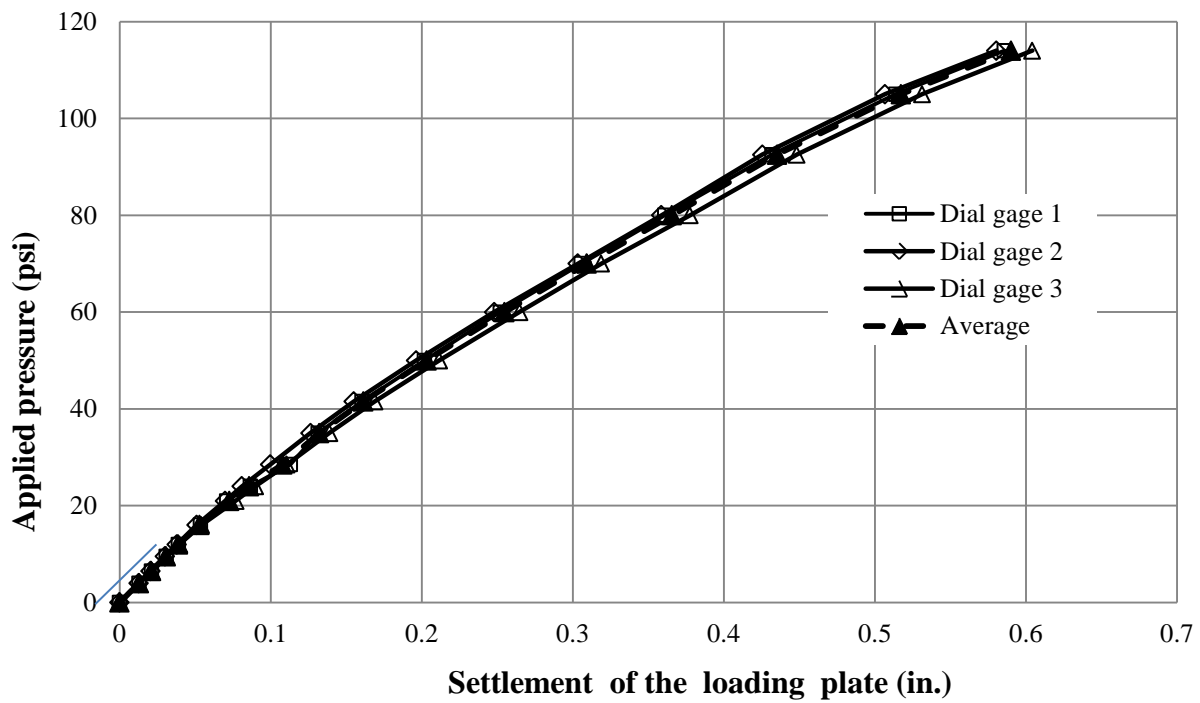


(b) Shear vs. normal stress

FIGURE 3.24 Large direct shear box tests for the crushed stone (CS-I)



(a) Schematic diagram of test set up



(b) Pressure-settlement curves

FIGURE 3.25 A small box plate loading test for the crushed stone (CS-I)

CS-II. Crushed stone (CS-II), used as bedding and backfill materials in one of the sections in the field, was poorly graded based on the USCS. **FIGURE 3.23** shows the grain size distribution of the crushed stone (CS-II). It had a mean size of 0.50 in., a uniformity coefficient C_u of 1.28, and a curvature coefficient C_c of 0.95. The minimum and maximum unit weights of the crushed stone (CS-II) were 87 and 100 pcf determined by conducting the minimum and maximum density tests (ASTM D4254-00 and ASTM D4253-00). A small box plate loading test as described above for the KR sand, was carried out to estimate the modulus of the crushed stone (CS-II), which was determined to be 1,145 psi (the crushed stone was rained into the box from the height of approximately 5 ft. and leveled). The raining of the crushed stone into the box from a five foot height resulted in the relative density of 58 %. Since the grain size distributions, minimum and maximum densities, and elastic modulus determined for the crushed stone (CS-II) are nearly similar to the corresponding values calculated for the crushed stone (CS-I), the frictional angle calculated for the calculated for the crushed stone (CS-I) was also used as in the frictional angle for the crushed stone (CS-II) in the analysis in this study. The modulus of the crushed stone (CS-II) compacted at the relative density of 79% was determined to be 1,700 psi from the plate loading test conducted as described above for the KR sand.

AB-3-II aggregate. AB-3-II aggregate were used as bedding and backfill materials in one of the sections in the field. The grain size distribution of the AB-3-II aggregate is shown in **FIGURE 3.26**. The AB-3-II aggregate was well-graded with a mean size of 0.1 in., a uniformity coefficient C_u of 55, and a curvature coefficient C_c of 1.043. The fine particles of the AB-3-II aggregate had a liquid limit of 18. **FIGURE 3.27** shows the compaction curve of the AB-3 aggregate by the standard Proctor compaction tests, which resulted in a maximum dry density of 141 pcf at the optimum moisture content of approximately 8%. A small box plate loading test as

described above for the KR sand, was carried out to estimate the modulus of the lightly compacted and compacted AB-3-II aggregate, which was determined to be 1,336 and 2,675 psi, respectively. The lightly compacted and compacted AB-3-II aggregate were prepared at the maximum density of and 95% of the maximum dry density at the moisture content of 4.5 % and 7.5%, respectively.

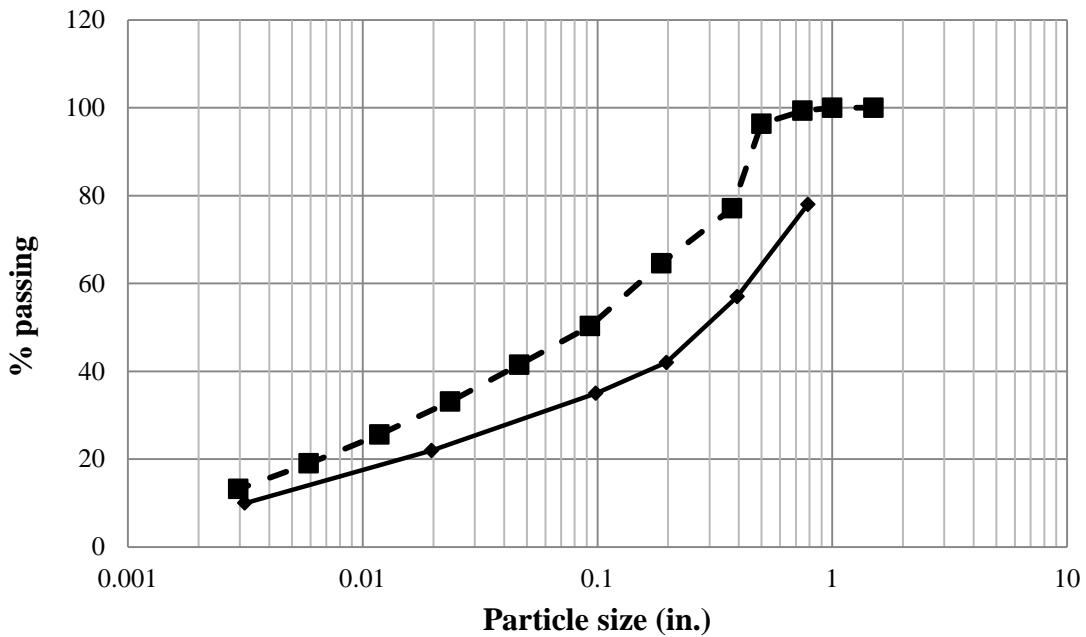


FIGURE 3.26 Grain size distribution curves of the AB-3-I and AB-3-II aggregates

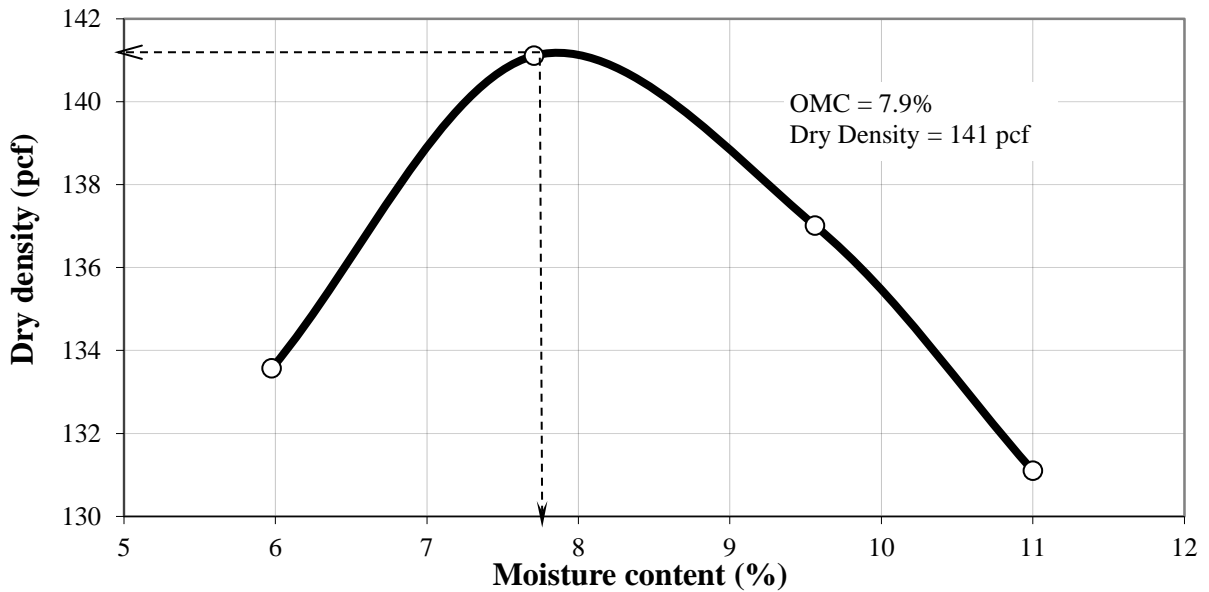


FIGURE 3.27 Standard Proctor Compaction curve of the AB-3-II aggregate

3.2.3 Base Course and Its Characteristics

KR sand and AB-3-I

KR sand and AB-3-I aggregate were used as base courses in the laboratory box tests. The KR sand used as the backfill material was also used as the base course for two laboratory box tests. The grain size distribution of the AB-3-I aggregate is shown in **FIGURE 3.26**. The AB-3-I aggregate was well-graded with a specific gravity of 2.69, a mean size of 0.27 in., a uniformity coefficient C_u of 130, and a curvature coefficient C_c of 2.25. The fine particles of the AB-3-I aggregate had a liquid limit of 20 and a plastic limit of 13. **FIGURE 3.28** shows the compaction curve of the AB-3 aggregate by the standard Proctor compaction tests, which resulted in a maximum dry density of 130 pcf at the optimum moisture content of 10%. **FIGURE 3.29** shows the CBR results of the AB-3 aggregate. A small box plate loading test as explained above for the KR sand was carried out to estimate the modulus of the AB-3 aggregate

compacted at the 95 % maximum unit weight as 5,279 psi (**FIGURE 3.30**). A 12 in. thick AB-3 layer was compacted in the box.

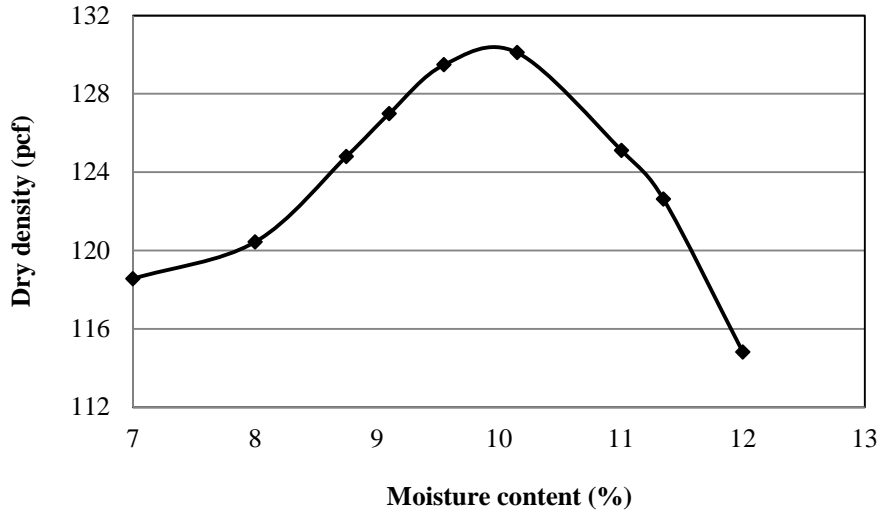


FIGURE 3.28 Standard Proctor Compaction curve of the AB-3-I aggregate (Pokharel, 2010)

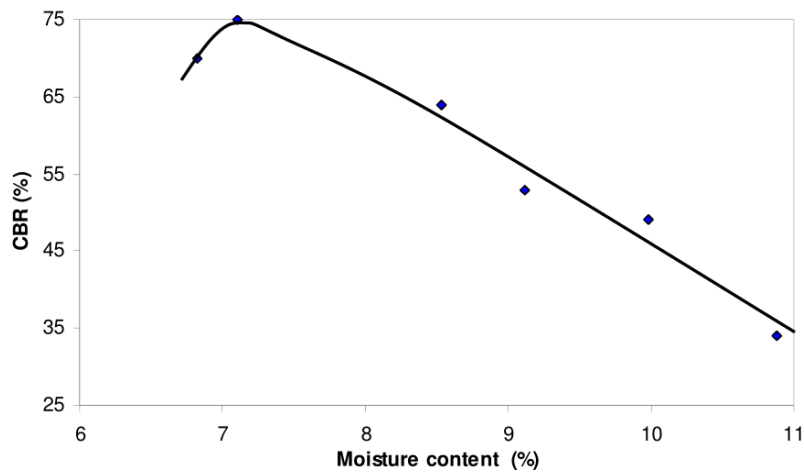
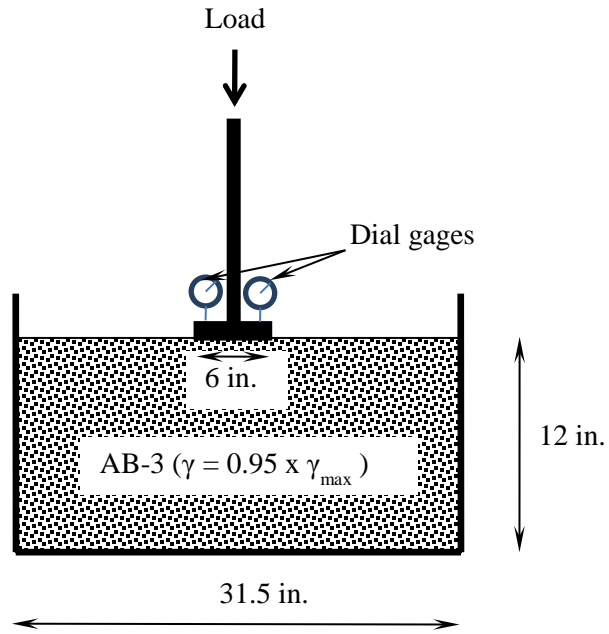
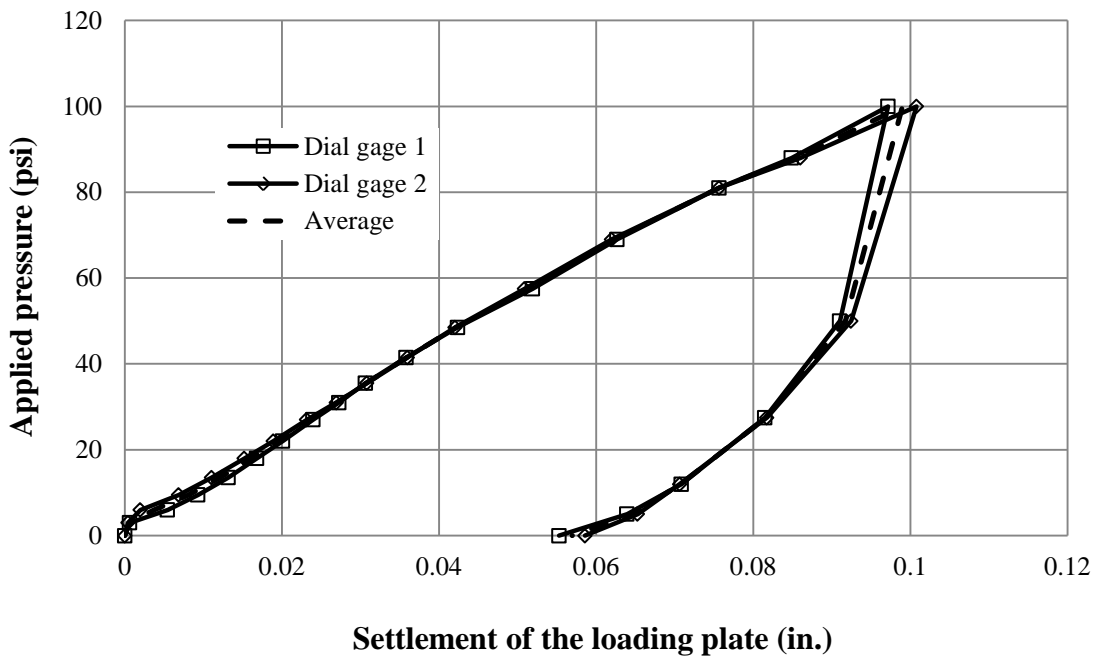


FIGURE 3.29 CBR curve of the AB-3-I aggregate (Pokharel, 2010)



(a) Schematic diagram of test set up

FIGURE 3.30 A small box plate loading test for the AB-3-I aggregate



(b) Pressure-settlement curves

FIGURE 3.30 A small box plate loading test for the AB-3-I aggregate (continued)

HMA

Hot mix asphalt (HMA) material, designated as SR-12.5A, was used as a base course material in the field. The HMA material was plant produced and contained 25% RAP and used PG 58-28 as the asphalt binder. The HMA mix had 4 % air voids. The specifications of the HMA, provided by the contractor, are given in **TABLE 3.1**.

TABLE 3.3 Specification of HMA material (provided by contractor)

Specifications Information				
Mix Designation:	SR-12.5A	Mix Spec. Provision		
Project #:	61 C0060-01	07-06013-R03		
		Specs		Special Provision
		Min.	Max.	
% Air Voids @ Design		2.0	6.0	07-06013-R03
% V.F.A. @ Design		65	78	07-06013-R03
% V.M.A. @ Design (Min.)		13.5		07-06013-R03
Dust/Binder Ratio (D/B)		NA	NA	07-06013-R03
% Gmm @ Nini (Max.)			90.5	07-06013-R03
% Gmm @ Nmax (Max.)			98.0	07-06013-R03
Tensile Strength Ratio (Min.)		80		07-06013-R03
Sand Equivalent (Min.)		40		07-06013-R03
Uncompacted Voids (Min.)		42		07-06013-R03
Coarse Aggr. Angularity (Min.)		1 Face	2 Faces	07-06013-R03
		75	NA	
% Flat & Elongated pieces (Max.)			NA	07-06013-R03

CHAPTER 4 LARGE-SCALE PLATE LOADING BOX TEST

Large-scale plate loading box tests were conducted in a large geotechnical testing box to evaluate the performance of the SRHDPE pipes under a shallow cover during the installation and loading (static and cyclic) conditions. To acquire the data from the experiment, extensive instrumentation including strain gages, displacement transducers, pressure cells, and tell-tales was installed. The preparation of the trench, bedding, backfilling, and soil cover followed the 2007 Kansas Department of Transportation Culvert and Pipe Specifications and the 1998 AASHTO LRFD Bridge Construction Specifications. Several tests, such as moisture content measurements, vane shear tests, light weight deflectometer (LWD) tests, and dynamic cone penetrometer (DCP) tests were conducted to ensure the consistency of the test sections. Three box tests were conducted, including the first test (Test 1) with sand as the backfill and the AB-3 as the base course, the second test (Test 2) with the sand as both the backfill and the base course, and third test (Test 3) with the crushed stone as the backfill and the AB-3 as the base course. The construction of the test sections for Tests 1 and 2 were discussed in details by Khatri (2012). However, the construction of test sections for Tests 1 and 2 were also summarized in this study in addition to the construction of the section for Test 3 to illustrate the construction procedures clearly.

4.1. Large Geotechnical Testing Box and Test Sections

FIGURE 4.1 shows the large geotechnical steel box used in this research, which was extended in length to 10 ft. from the existing steel box (7ft long, 6.6 ft. wide, and 6.6 ft. high) to minimize the boundary effect on test results. Three side walls and the base of the box were

fixed. The front wall was detachable with several 6 in. high steel channel sections fixed by nuts and bolts. The height of the front wall was increased with each fill lift during the preparation of the test section by adding the detachable channel sections. **FIGURE 4.2** shows the cross-section and longitudinal test sections of the box with extensive instrumentation. The test sections had a trench of 6.3 ft. long, 4 ft. wide, and 4.5 ft. deep in the Clay-I. The trench consisted of 6 in. thick bedding material, 2 ft. backfill, and 2 ft. soil cover including a 9 in. thick base course. Sections of twenty-four inch diameter SRHDPE pipes were inspected and selected based on their glossy appearance, no chalking, no sticky or tacky materials, and no blisters, voids, or other defects. The pipes were then cut into a length of 6 ft. 4 in. by a hand-held reciprocating saw.

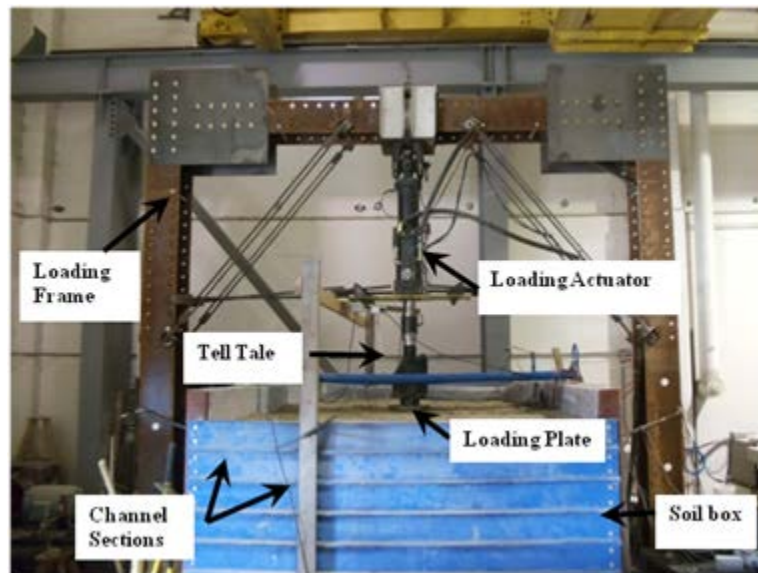
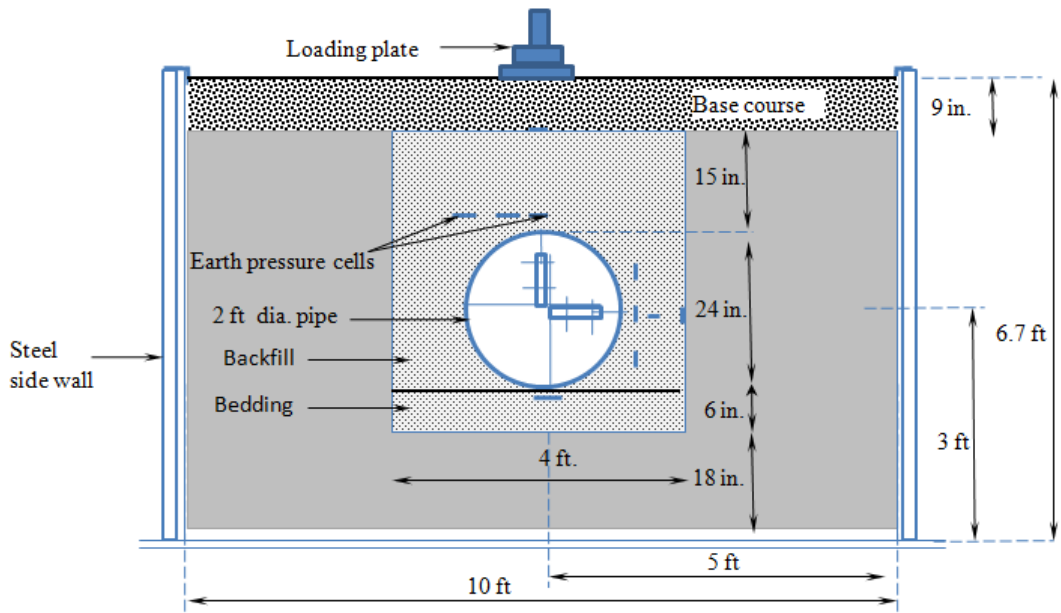
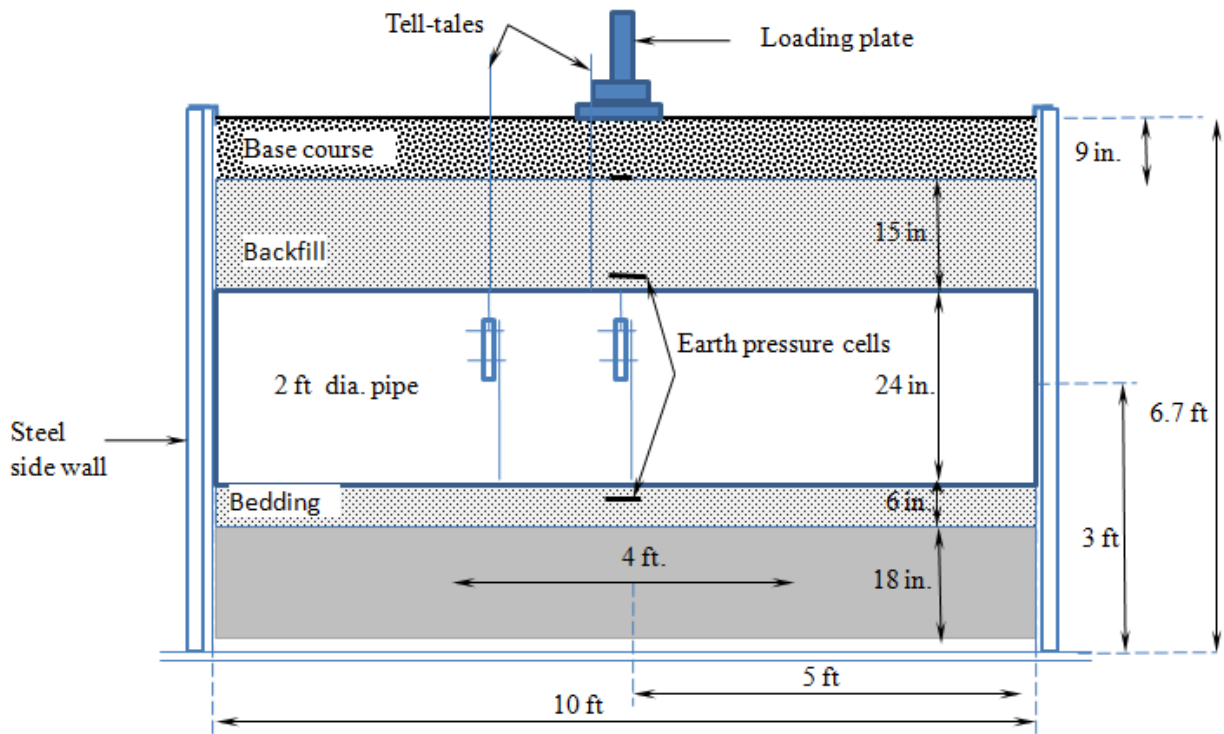


FIGURE 4.1 Large geotechnical testing box and loading system



a) Cross-section



b) Longitudinal section

FIGURE 4.2 Plate loading test sections

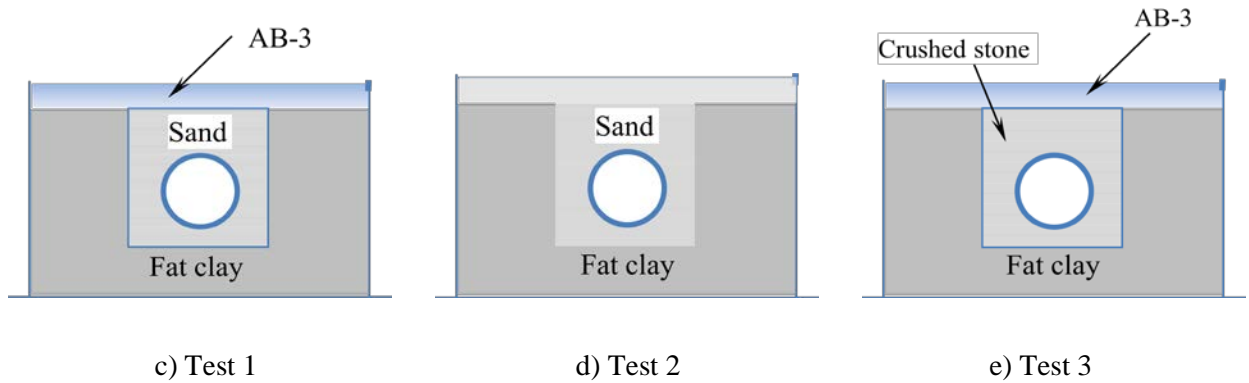


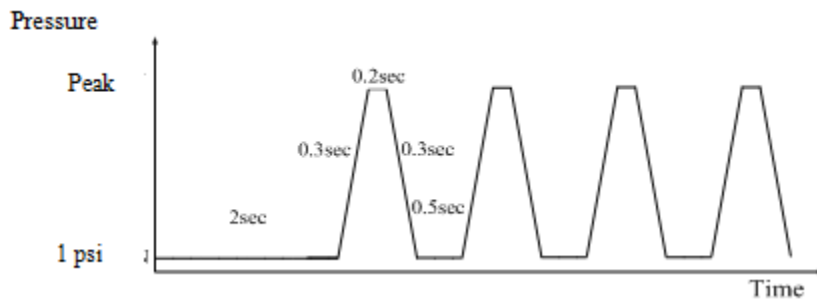
FIGURE 4.2 Plate loading test sections (continued)

4.2 MTS Loading System

A servo hydraulic MTS loading system consisting of a steel loading frame, a hydraulic actuator, and a servo-control unit connected to a data acquisition system and a hydraulic control valve, was used to apply static and cycle loads on test sections prepared in the large geotechnical testing box. The load actuator has a 55 kip capacity. The static and cyclic loads were applied as shown in **TABLE 4.1**. **FIGURES 4.3** shows the details of the cyclic loading applied to simulate the traffic loading with increasing intensities. Each cyclic load had a trough value of 1 psi, which was applied to keep the plate in contact with the surface and to prevent impact loading on the surface. The loading wave frequency was 0.77 Hz. A 1 ft. diameter loading plate was connected to the actuator to apply the load. The loading plate had a 1.18 in. thick steel plate with a 0.4 in. thick rubber base attached at the bottom to simulate a rubber tire contact. **FIGURE 4.4** shows the loading plate used in this research.

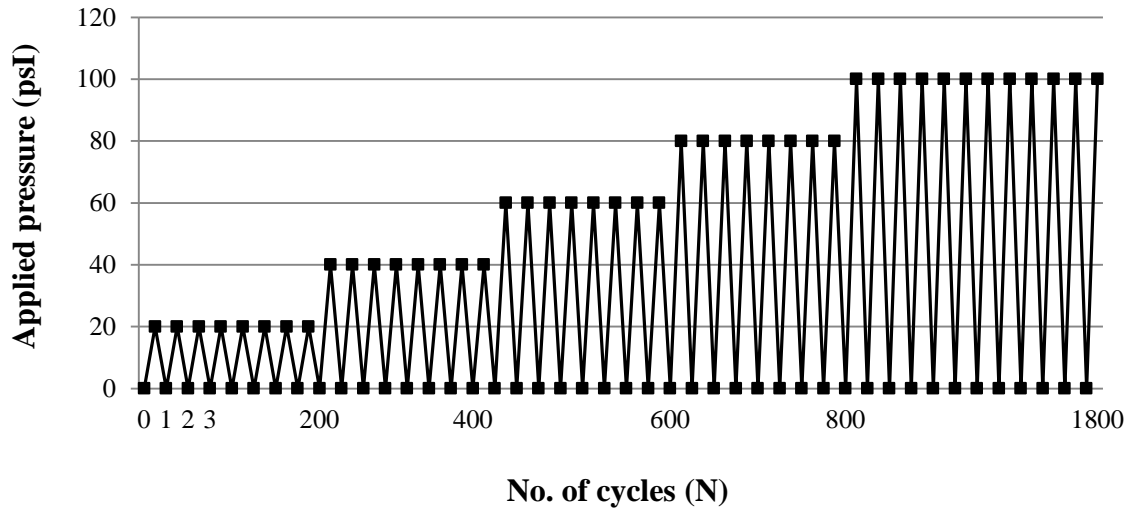
TABLE 4.1 Loading increment and magnitude

Test no	Description	Static loading (psi)		Cyclic loading (psi)	
		Increment	Max.	Increment peak (each 200 cycles)	Max. Peak (cycles)
Test 1	Sand as bedding, backfill, and AB-3 as a base coarse	10	80	20	100 (1000 cycles)
Test 2	Sand as bedding and backfill, and base course	5	50	10	50 (260 cycles)
Test 3	Crushed stone as bedding and backfill and AB-3 as a base course	10	100	20	100 (1000 cycles)

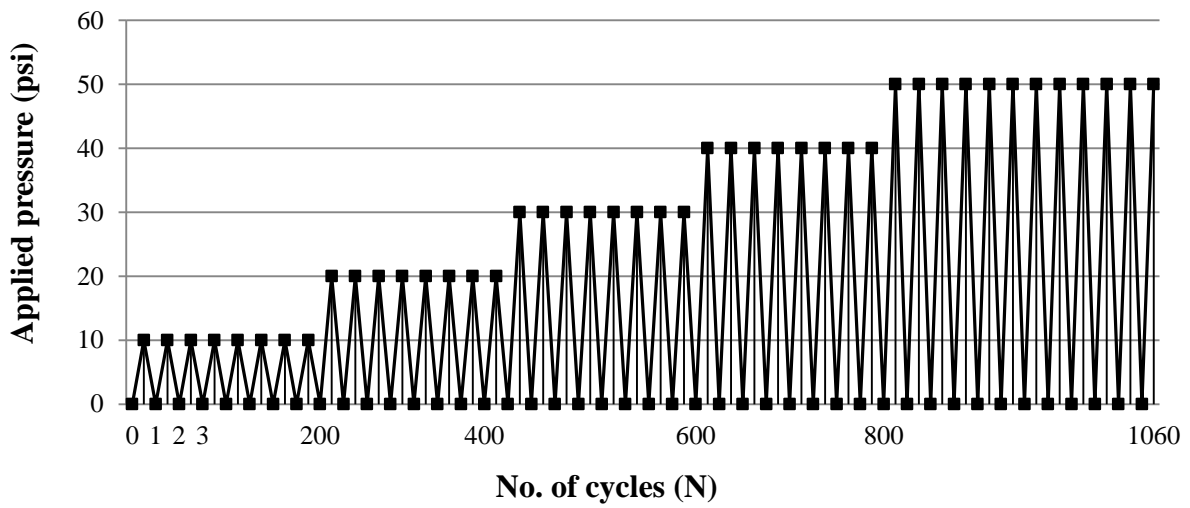


(a) Cyclic loading wave form

FIGURE 4.3 Cyclic loading details



(b) Cycle loading for Test 1 and 3



(c) Cycle loading for Test 2

FIGURE 4.3 Cyclic loading details (continued)



FIGURE 4.4 Loading plate

4.3 Instrumentation

The instrumentation used in the box tests included displacement transducers, strain gages, earth pressure cells, and tell-tales to capture the response of the pipes during the installation and loading as described in **SECTIONS 4.3.1** through **4.3.3**.

4.3.1 Displacement Transducers and Tell-Tales

Five displacement transducers, manufactured by Tokyo Sokki Kenkyujo, Co., Ltd, Japan, were used to measure the changes in vertical and horizontal diameters during the installation and loading. The transducers were fixed at a center of the pipe section and 1 ft. away from the center as shown in **FIGURE 4.5**. The transducers were fixed to the pipe wall by replacing original caps of the transducers with M2.5 flat head machine screws which had a diameter of 0.1 in., a

length of 0.47 in., and a thread size of 0.018 in. Small holes of approximately 0.079 in. were drilled to fasten the displacement transducers to the pipe wall.



FIGURE 4.5 Displacement transducers inside the pipe section

Two string pots were used to measure the vertical displacements of the crown of the pipe, at the center and 1 ft. away from the center, through the two tell-tales as shown in **FIGURE 4.6**. Each tell-tale had a hollow metal tube of 0.25 in. in diameter with 0.016 in. wall thickness. A steel rod of 0.12 in. in diameter was inside the tube. The bottom of the steel rod was fixed to the pipe crown through the nut-bolt arrangement by drilling a small hole of approximately 0.16 in. in diameter on the pipe wall. The top of the rod was then tied to the string of a string pot, fixed on a rigid support. **FIGURE 4.7** shows a schematic diagram of the displacement transducers and tell-tales. One displacement transducer was used to measure the settlement of the loading plate during the loading. In addition, one more displacement transducer was added for Test 3 to measure the settlement of the base course 1 ft. away from the center in the direction of the pipe run.



FIGURE 4.6 Tell-tales fixed on the pipe specimen

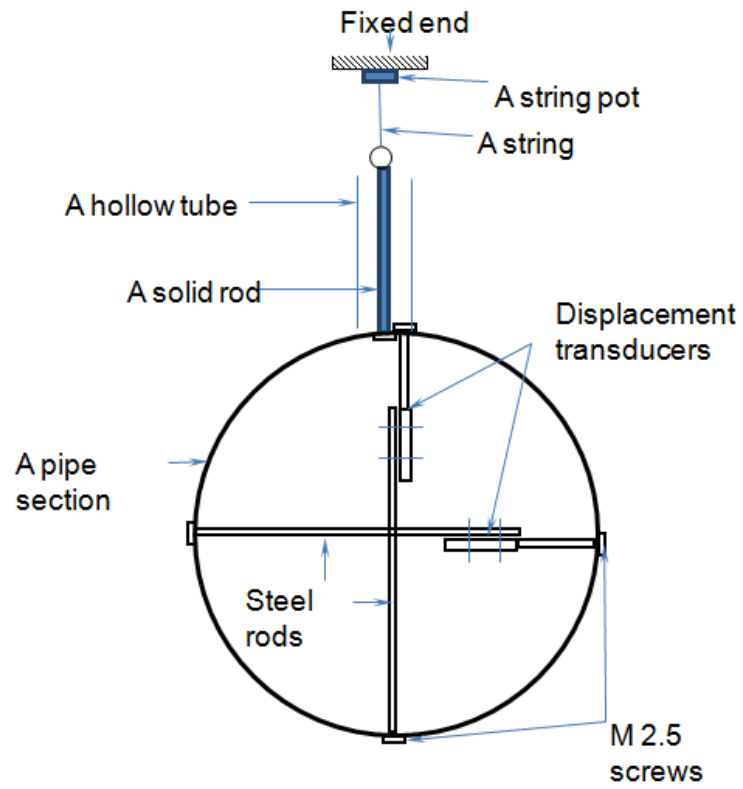


FIGURE 4.7 Displacement transducers for deflection measurements

4.3.2 Strain Gages

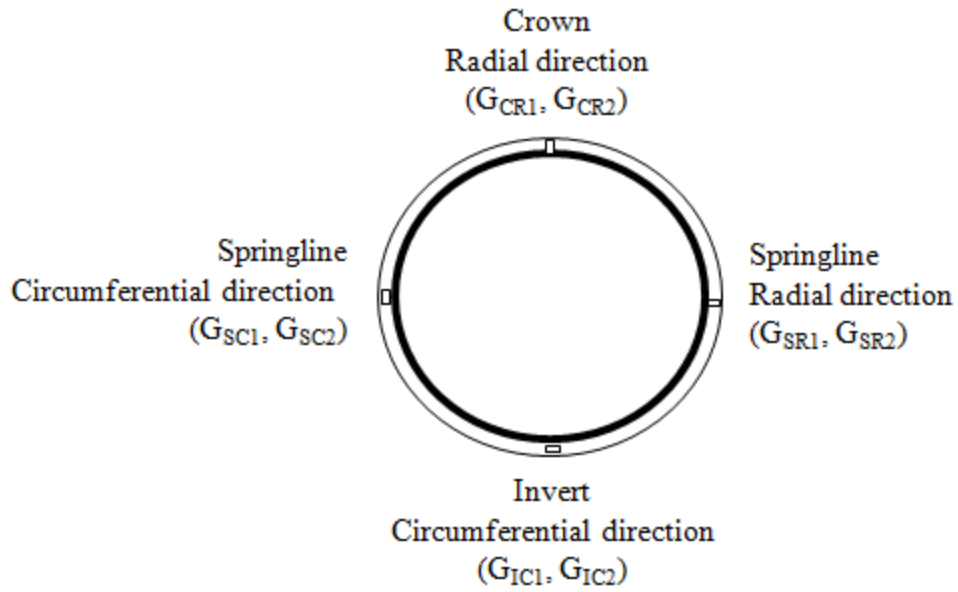
Uniaxial foil-type electrical resistance (C2A-13-250 LW -120) strain gages, manufactured by Vishay Precision Group, were used to measure the circumferential, radial, and longitudinal strains of the pipe at various locations. **FIGURES 4.8** and **4.9** show strain gages installed outside and inside of the pipe section, respectively. The symbols, locations, and orientations of the strain gages fixed on the pipe are shown in **FIGURE 4.10**. Eight strain gages labeled without a prime (') sign were affixed on the steel at the center of the specimens at the crown, invert, and springline to determine both radial and circumferential strains. The plastic cover was removed at the desired locations to place the strain gages on the steel. Since the steel rib height was too small to attach the strain gages on the top of the rib, they were fixed at the neutral axis of the steel rib. Another set of eight strain gages labeled with single prime (') symbol were placed on the plastic at ribs. In addition, eight more strain gages labeled with a double prime (") symbol were placed on the plastic, inside and outside of the pipe, between the ribs (i.e., valley) to measure the strains in the plastic. For example, the strain gage notations (G_{SC1} and G_{SC2}) without a prime symbol represent the strains on the steel. The first subscript letter of the notation represents the location of the strain gage (for example, "S" stands for springline, "I" for Invert, and "C" for crown). The second subscript letter represents the direction of strain measurement (for example, "C" and "R" stand for the circumferential and radial direction, respectively). Moreover, the third subscript letters, "1" and "2", represent the strain gages on the left and right sides of the rib or outside and inside of the valley, respectively. For example, G'_{SC2} represents the strain gage fixed on the plastic, at the left side of the rib, at the springline to measure the strain in the circumferential direction.



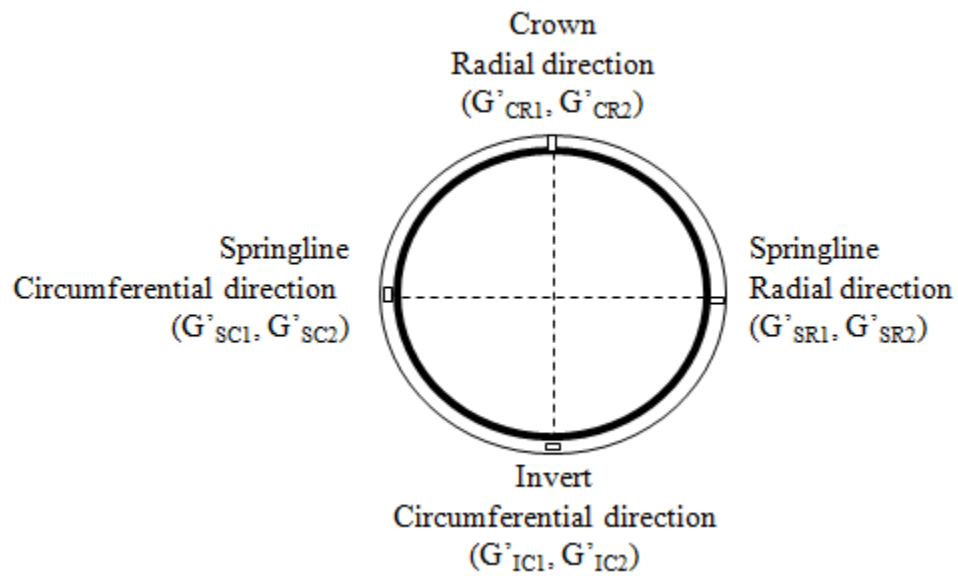
FIGURE 4.8 Strain gages fixed outside of pipe specimen



FIGURE 4.9 Strain gages fixed inside of the pipe specimen

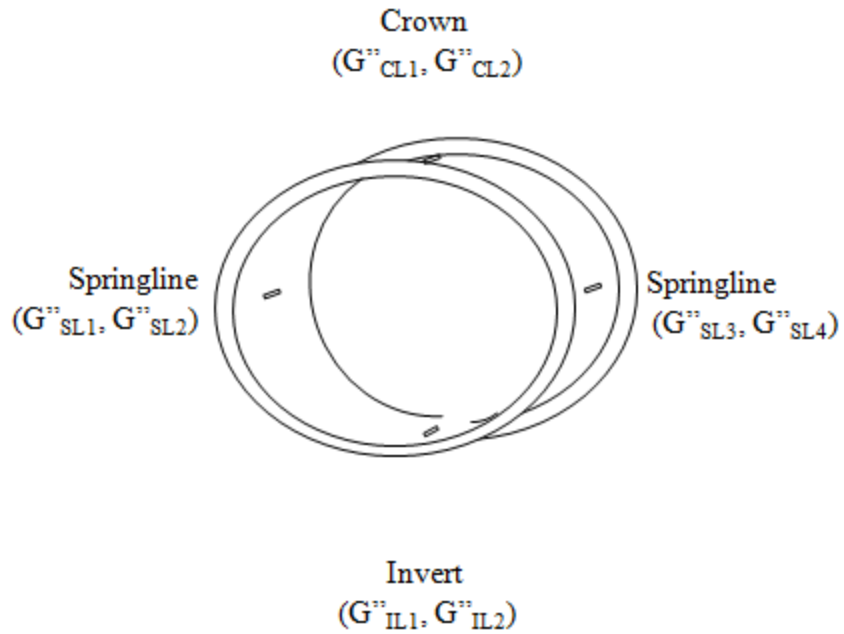


a) On the steel at ribs

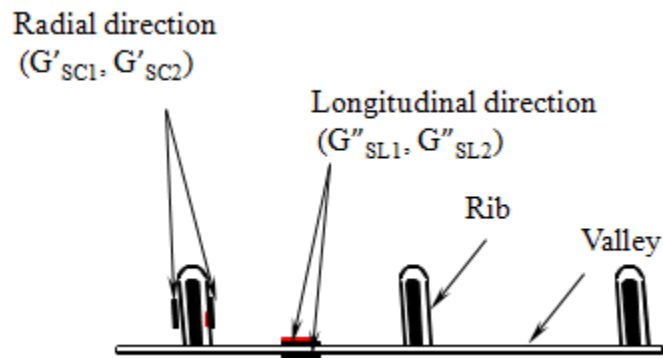


b) On the plastic at ribs

FIGURE 4.10 Symbols, locations, and orientations of strain gages on the pipe



c) In the longitudinal direction on the plastic at valley



d) Strain gages on the plastic surface

FIGURE 4.10 Symbols, locations, and orientations of strain gages on the pipe (continued)

4.3.3 Earth Pressure Cells

Ten earth pressure cells with two capacities of 29 psi and 72 psi were installed at a central vertical plane around the pipe beneath the loading plate to measure pressures developing during the installation and loading. The notations, locations, and orientations of the earth pressure cells are shown in **FIGURE 4.11**. The subscripts of the notations represent the positions at which the earth pressure cells were placed. The subscript letters I, H, S, SH, and C stand for invert, haunch, springline, shoulder, and crown of the pipe, respectively whereas the numerical value gives the horizontal distance from the position defined by the subscript letter. For example, the notations, E_{C0} and E_{C6} , represent earth pressure cells placed at the crown along the central plane and along the plane at 6 in. horizontal distance from the crown, respectively. Four pressure cells (E'_{H0} , E'_{S0} , E'_{SH0} , and E'_{S10}) labeled with the prime (') symbol were installed for the horizontal earth pressure measurement whereas the remaining pressure cells without the prime (') symbol were installed for the vertical earth pressure measurement. Five pressure cells (E'_{I0} , E'_{S0} , E'_{SH0} , E_{C0} , and E_{C6}) shown in rectangular shapes with solid fill were used for Tests 1 and 2. After analyzing Test 1 and 2 data, the decision was made to add more pressure cells, which were shown in rectangular shapes without solid fill, to capture additional information of the pressure distribution around the pipe.

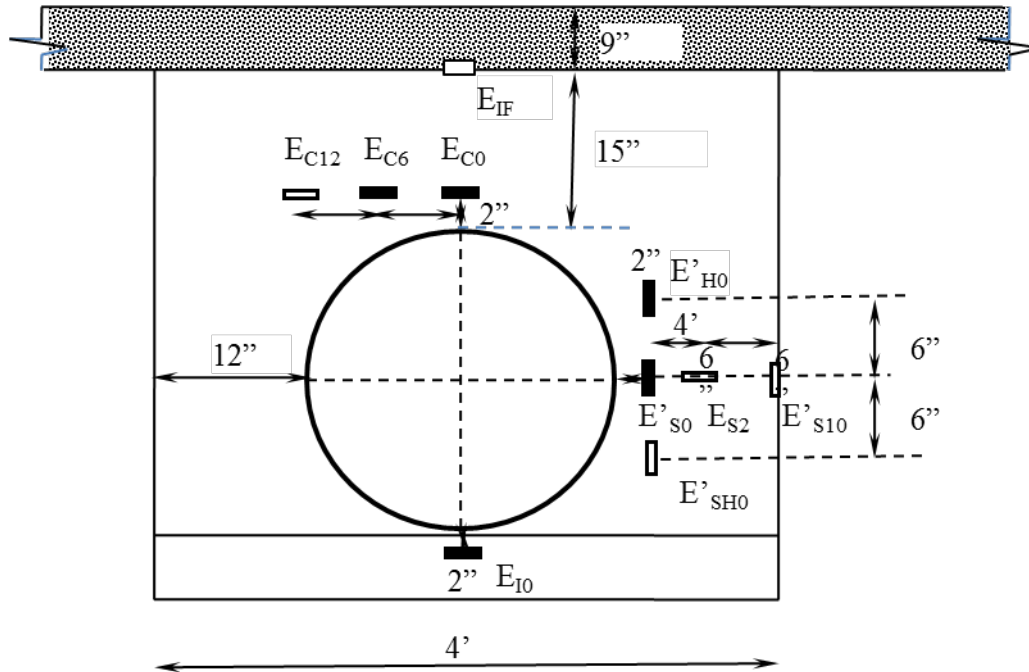


FIGURE 4.11 Earth pressure cells around the pipe section

4.4 Data Acquisition System

Four smart dynamic DC-204R data recorders with a manual channel selector were used to record the earth pressures around the pipe, strains at various locations on the steel and plastic, and deflections of the pipe.

4.5 Construction of Test Section

The test sections were constructed in the large geotechnical testing box following the test conditions proposed by Brachman et al. (2008). The detail construction procedure was described in **SECTIONS 4.5.1 to 4.5.3**.

4.5.1 Construction of Test Section 1

Surrounding Soil

Prior to the placement of the Clay-I in the box, the walls of the box were covered with a polyethylene plastic sheet to reduce the possible friction at the soil-steel interface. The reduction of the friction at the soil-steel interface may reduce the boundary effects on the test results. Moreover, the plastic-covered walls also helped to keep the moisture content of the soil constant during the construction and testing of the test sections. The walls of the box were then marked to assist the compaction of the soil in every 6 in. lift. The detachable channel sections from the front side of the box were removed for the access to the box. Then, wooden shoring as shown in **FIGURE 4.12** was constructed to form the trench because excavation of the trench was not possible by a backhoe in the laboratory. Manual excavation of the stiff in-situ soil using only shovels would be very difficult and take a prohibitively long time. Loss of moisture from the wall of the trench during the trench construction would make the trench wall stiffer. The clear width of the wooded shoring was maintained in such a way that the trench was 4 ft. wide. The trench width was selected according to the 2007 KDOT Pipe and Culvert Specifications.

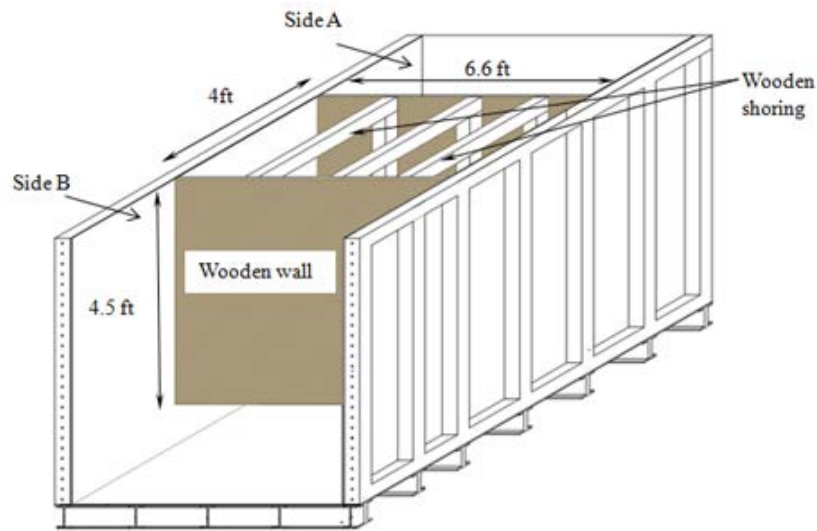


FIGURE 4.12 3D perspectives drawing of the box with the wooden shoring to make a trench of 6.6 ft. x 4 ft x 4.5 ft.

The Clay-I was kept at the moisture content of approximately 26% and was placed in compacted lifts of 6 in. and compacted by the vibratory plate compactor TPE 1830 to achieve the desired CBR value between 2 and 3%. A Bosch electric jackhammer was also used to compact the soil near the sides and corners of the box because the vibratory compactor did not work around these areas. **FIGURES 4.13** and **4.14** show the VIBCO vibratory plate compactor and the Bosch jackhammer, respectively. The Clay-I was placed and compacted until the compacted fat clay reached the height of 5 ft. 3 in. on both sides of the shored area and the height of 1.5 ft. inside the shored area. The shoring was then removed, leaving a completed 6 ft. long, 4 ft. wide, and 3 ft. 9 in. deep trench. The compacted soil was covered carefully during the construction to keep the moisture content at 26% using the plastic sheet as shown in **FIGURE 4.15**.



FIGURE 4.13 Compaction of surrounding soil using the vibratory plate compactor



FIGURE 4.14 Compaction of surrounding soil using the jackhammer



FIGURE 4.15 A polyethylene plastic sheet placed to cover the exposed fat clay

Bedding

Kansas River sand was compacted to achieve a relative density of approximately 70% using the vibratory plate compactor and controlled by the volume weight approach. The soils required for the compacted 6 in. bedding layer were weighed by using the crane and weighing scale of 2,000 lbs capacity. In each test the middle 33% of the bedding material in the direction of the pipe run was not compacted following the 2007 KDOT Pipe and Culvert Specifications. The bedding material was leveled and the earth pressure cell E_{10} was installed in the bedding material below the loading plate before the placement of the pipe in the trench as shown in **FIGURE 4.16**.

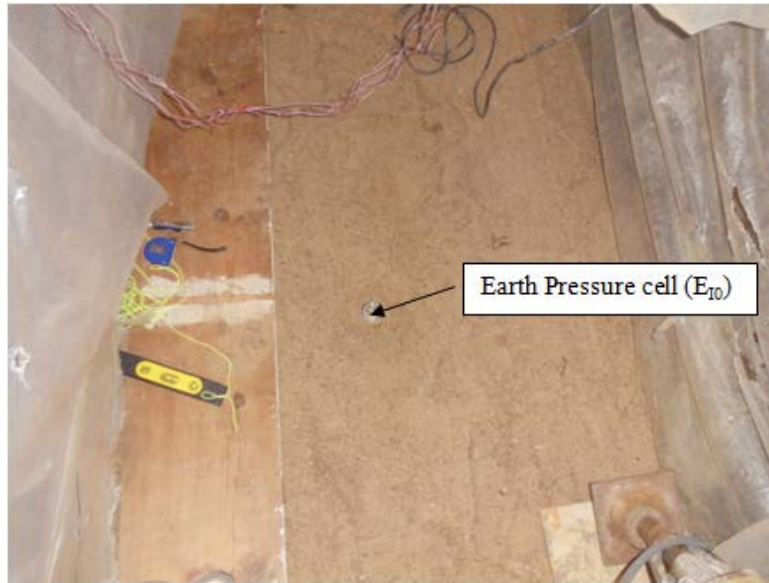


FIGURE 4.16. Bedding material and the earth pressure cell E_{10} installed at the invert of the pipe

Placement of Pipe

After the bedding was prepared, a pipe section instrumented with displacement transducers and strain gages was carefully installed, leveled, and aligned in the trench shown in **FIGURE 4.17**. The ends of the pipes were plugged by thin foam sheets to prevent the flow of the backfill into the pipe during the installation and loading as shown in **FIGURE 4.17**. All of the sensors were connected to the four separate DC-204R data recorders. The recorders were then adjusted and balanced to set all the initial values to zero. The measurements of the tell-tales were taken manually using the reference fixed point during the backfilling because the string pots described under the instrumentation section could not be placed during the construction of the test section.



FIGURE 4.17 Fully instrumented pipes in the trench in Test Section 1

Backfilling

Kansas River sand was used as a backfill material and the backfilling was performed in 6 in. compacted lifts to get a relative density of approximately 70 %. The vibratory plate compactor and the jackhammer were used for the compaction of the sand up to a height of 15 in. above the crown of the pipe. The compaction directly above the pipe surface was avoided to prevent possible damage of the pipe due to the compaction equipment. For each test, the haunch area was monitored to avoid a void in the haunch area. The backfilling was done in equal lifts on both sides of the pipe so as not to disturb the pipe alignment. **FIGURE 4.17** shows the backfill placed up to the springline. During the backfilling, the earth pressure cells were installed around the pipe for each test as described in **SECTION 4.3.3**. **FIGURE 4.19** shows the installation of the earth pressure cells at the springline during the backfilling. At the springline and shoulder, the earth pressure cells were placed vertically with a piece of plywood (2.5 in. x 3.5 in.) on the back of each earth pressure cell. The piece of plywood was attached to keep the earth pressure cell vertical during the construction of the test section. The readings of the strain gages,

displacement transducers, and earth pressure cells were taken using the DC-204R recorders after completion of each lift during the backfilling. Tell-tale readings were taken manually.



FIGURE 4.18 Backfill up to the springline in Test Section 1

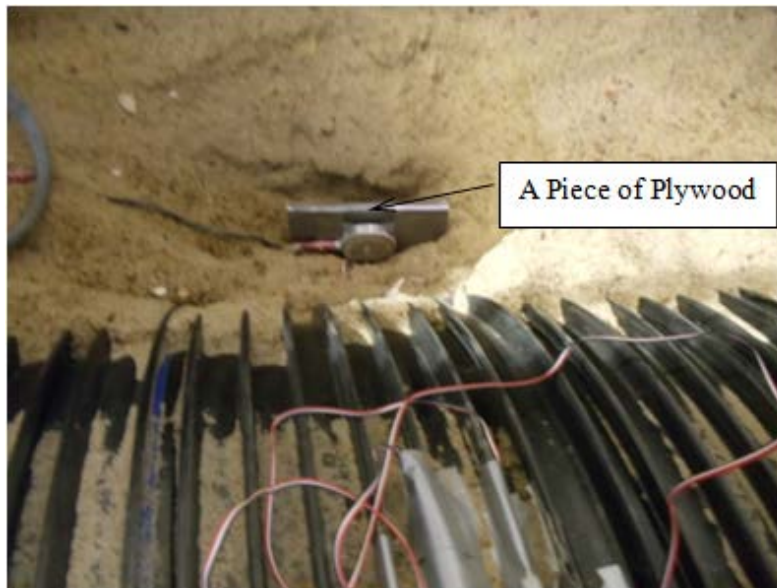


FIGURE 4.19 Earth pressure cells at the springline in Test Section 1

Base Course Preparation

After the compaction of the backfill to the same height of the Clay-I, A 9 in. thick base course (described in **SECTION 3.2.3**) was prepared. AB-3-I aggregate was used as the base course in this test and was placed and compacted uniformly in two layers by the vibratory plate compactor and the jackhammer for several passes until desired densities were achieved. The AB-3-I base course was compacted at 95 % of the maximum dry density at a moisture content of around 9% using the weight-volume approach. The quantity of soil required for each compacted lift was controlled by the volume-weight approach and weighed by the crane and weighing scale of 2,000 lb capacity. **FIGURE 4.20** shows the compaction of the base course.



FIGURE 4.20 Compaction of base course using the vibratory plate compactor in Test Section 1

4.5.2 Construction of Test Section 2

The surrounding soil, bedding, and backfill material were placed and compacted following the same procedures adopted in Test Section 1. Instead of the AB-3 base course, the

Kansas River sand was used as the base course in this test. A 9 in. thick base course was compacted uniformly in two layers by the vibratory plate compactor and the jackhammer for several passes until the desired relative density of 70 % was achieved. The quantity of soil required for the each compacted lift was controlled by the volume-weight approach and weighed by the crane and weighing scale of 2,000 lbs capacity.

4.5.3 Construction of Test Section 3

The surrounding soil and bedding were placed and compacted following the same procedures adopted in Test Section 1. However, instead of AB-3 aggregate, crushed stone was used for the bedding and backfill material. Backfilling was performed by dumping the crushed stone CS-I (no compaction) in 6 in. lift. **FIGURE 4.21** shows the backfill material placed up to the springline. The instrumentation was done as described in **SECTION 4.3** with the additional earth pressure cells. **FIGURE 4.22** and **4.23** show the earth pressure cells installed at the springline and at the crown with the piece of plywood and sand bag during the placement of the backfill. Each earth pressure cell placed vertically was attached with a piece of plywood (2.5 in. x 3.5 in.) on the back. The piece of plywood was attached to keep the earth pressure cell vertical during the construction of the test section. In addition, each earth pressure cell was covered with a sand bag. The sand bag was placed to avoid the uneven distribution of the aggregate contact on the sensor surface because the sensor area of the earth pressure cell with a 1.8 in. diameter would have few contact points for crushed stone with a $\frac{3}{4}$ in. maximum particle size.



FIGURE 4.21 Backfilling up to the springline in Test Section 3



FIGURE 4.22 Earth pressure cells at the springline in Test Section 3



FIGURE 4.23 Earth pressure cells at the crown in Test Section 3

AB-3-I aggregate was used as a base course for this test section. A 9 in. thick base course was compacted in two layers with the vibratory plate compactor and the jackhammer for several passes until the desired densities were achieved. The AB-3 base course was compacted at 95 % of the maximum dry density at a moisture content of around 9% using the weight-volume approach.

A sketch of the cross section of the test sections is shown in **FIGURE 4.24**, which presents the compaction schedule of the backfill and the base course, and also includes the locations of the earth pressure cells.

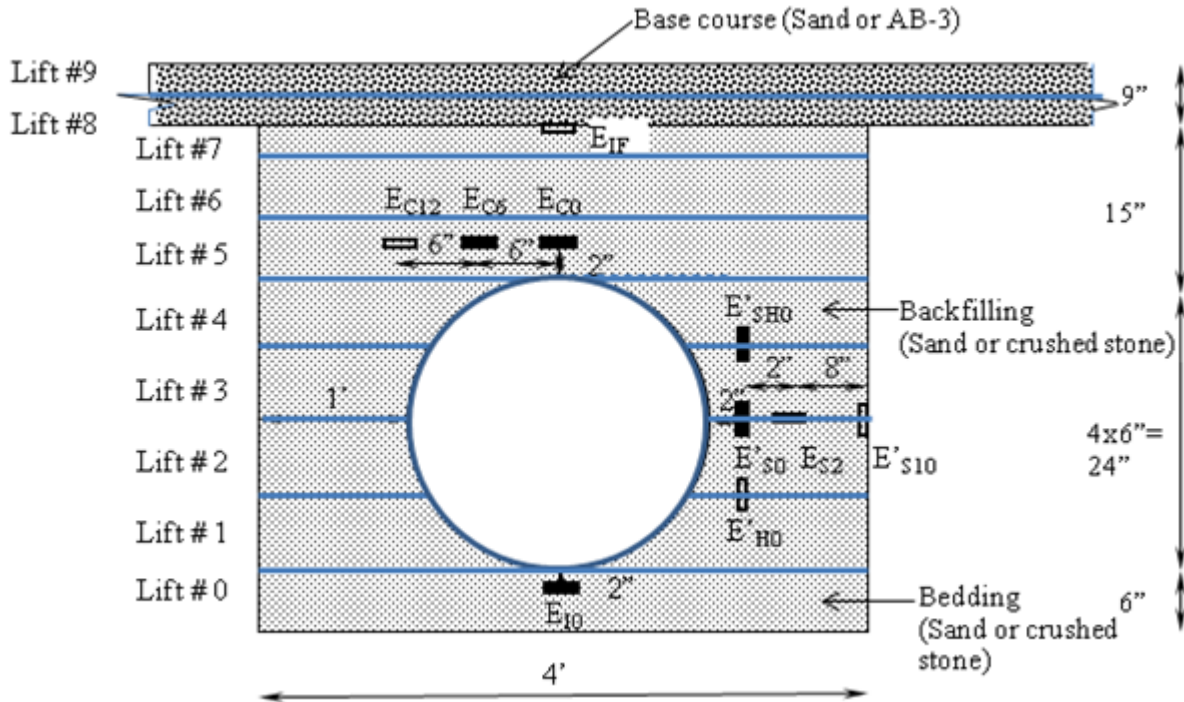


FIGURE 4.24 Cross section of test section including the soil lifts and earth pressure cells

4.6 Quality Control

The vane shear tests (ASTM D2573-08) were carried out on each compacted lift of the Clay-I to keep the CBR value between 2 and 3 %. The relation, $c_u = 298 \text{ CBR}$, established in **SECTION 3.2.1**, was used to determine the CBR values from the undrained shear strength values measured from the vane shear tests. **FIGURE 4.25** shows a picture taken during the vane shear test.

Non-destructive Light Weight deflectometer (LWD) tests were conducted over the compacted Clay-I, the Kansas River sand, and the AB-3-I aggregate at various locations during the preparation of the test sections as shown in **FIGURE 4.26**. The dynamic deformation moduli (E_{vd}) obtained from LWD tests (using a 1 ft. diameter plate) were in a range of 1,200 to

1,550 psi for the Clay-I, 2,200 to 3,050 psi for the sand, and 4,700 to 7,050 psi for the AB-3-I aggregate.



FIGURE 4.25 Vane shear test on the fat clay



FIGURE 4.26 LWD test on the fat clay

After the preparation of the test sections, Dynamic Cone Penetration (DCP) tests were carried out from the top of the base courses to the depth at four different locations following ASTM D6591-03. The relationship between the CBR value at the depth of penetration and the penetration index in inches per blow of DCP is given in **EQUATION 4.1** (Webster et al., 1992).

The CBR profiles of the test sections obtained from the DCP tests are shown in **FIGURE 4.27**. The average CBR value of the Clay-I and the AB-3-I aggregate, resulting from the DCP tests, were approximately 2.5 % and 20%, respectively.

$$CBR (\%) = \frac{292}{(PI \times 25.4)^{1.12}} \quad 4.1$$

where PI= the penetration index.

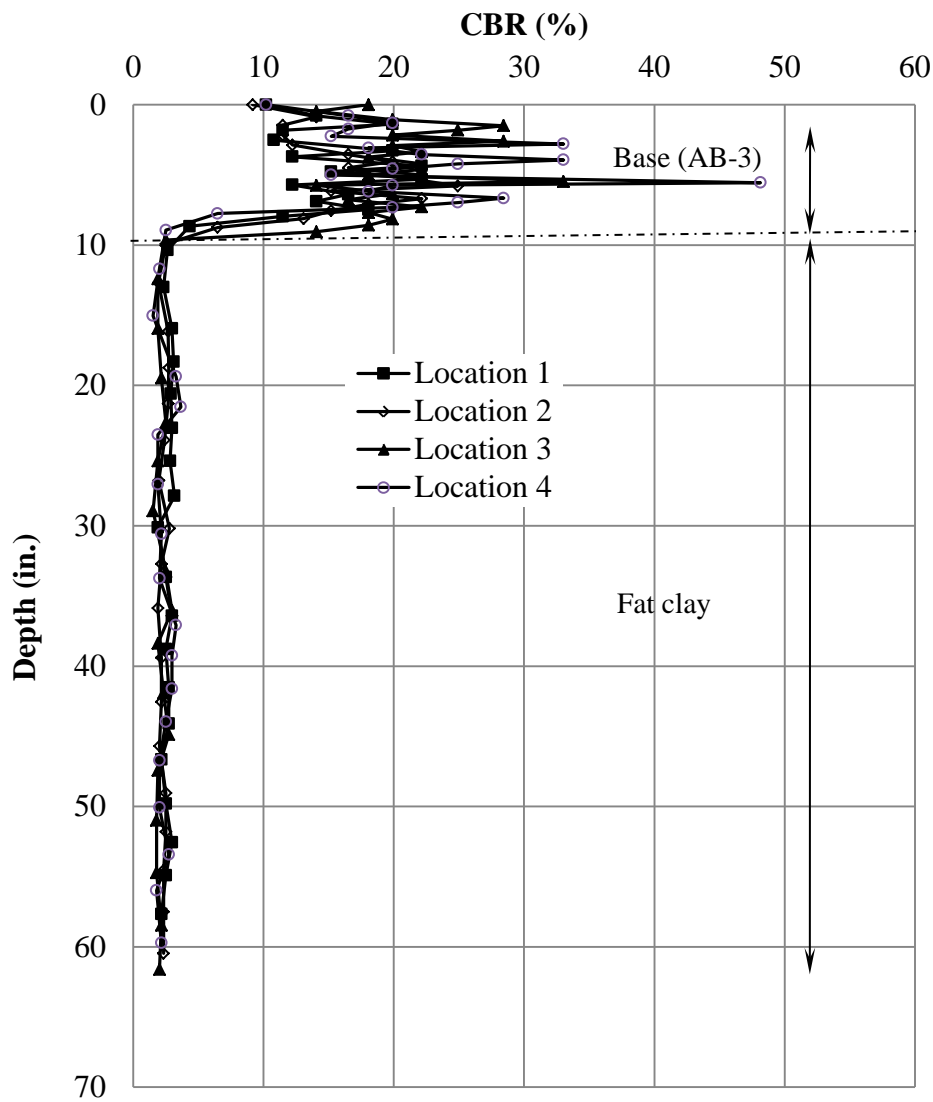


FIGURE 4.27 CBR profiles in Test Section 1

4.7 Data Collection

FIGURE 4.28 shows a test section ready for a plate loading test. All sensors were connected to the data acquisition system. The Multi-Purpose Test (MPT) software was used to apply both static and cyclic loads as mentioned in **SECTION 4.2**. For each test of the pipe, the following data were collected:

- a) The applied load and displacement of the actuator
- b) The settlement of the loading plate from the displacement transducer
- c) The displacement of the pipe crown from the tell-tale
- d) The deflection (or change of diameter) at the center and 12 in. from the center of the testing pipe from the displacement transducers
- e) The pressure distribution around the pipe using the earth pressure cells
- f) The circumferential and longitudinal strains developed on the steel and plastic at the center of the pipe under the loading plate from the strain gages



FIGURE 4.28 Displacement transducers fixed to a reference beam

CHAPTER 5 FIELD PIPE INSTALLATION AND TRAFFICKING TESTS

The laboratory tests conducted and presented in Chapter 4 have some limitations. For example, the installation procedure of the pipe in the test box was different from the field installation due to the limited space and construction equipment in the laboratory. The moisture content of the soil in the test box was kept relatively constant during installation and simulated traffic loading. The effect of the moisture content or degree of saturation of the soil on the earth pressures and deformation of the pipe was not investigated in the laboratory study, but is likely important for the performance of SRHDPE pipes in the field. The laboratory tests were completed in weeks and cannot simulate the long-term behavior of the SRHDPE pipe in the field. As usual, box tests may have a boundary effect. Therefore, a field test was conducted to verify the lab test results and to provide information that can improve the understanding of the long-term response of the SRHDPE pipes. A field study was conducted in this research to investigate the behavior of the pipes installed in a trench with a shallow cover of 3 ft. under construction and service vehicles. The SRHDPE pipes were installed on October 1 and 2, 2013 and the performance of the pipes was monitored during installation, evaluated right after the installation, and will continue being monitored for at least two years.

To acquire the data from the field test, extensive instrumentation largely the same as used in the laboratory tests (described in details by Khatri (2012) and in Chapter 4) including strain gages, displacement transducers, and pressure cells were installed. The preparation of the trench, bedding, backfilling, and soil cover followed the 2007 Kansas Department of Transportation Culvert and Pipe Specifications and the 1998 AASHTO LRFD Bridge Construction Specifications. Two test sections, the first test section (hereinafter referred as Test Section A) with the AB-3-II aggregate as both bedding and backfill materials and the second test section

(hereinafter referred as Test Section B) with the crushed stone (CS-II) as both bedding and backfill materials, were constructed. Several tests such as light weight deflectometer (LWD) and dynamic cone penetrometer (DCP) tests were conducted to determine the properties of the soils as compacted. More detailed information on the test site, the instrumentation, and the construction of the test sections is provided in the following sections.

5.1. Test Pipe

SRHDPE pipes of 36 in. in diameter, described in **SECTION 3.1**, were tested in this field study. Three SRHDPE pipes of each 24 ft. long with bell and spigot (with gasket) ends were provided by Contech Construction Products Inc. Both the bell and spigot are reinforced with steel that is fully encased in stress-rated high density polyethylene as shown in **FIGURE 5.1**. Sections of 36 inch diameter SRHDPE pipes were inspected and found that the pipes had glossy appearance, no chalking, no sticky or tacky materials, and no blisters, voids, or other defects.



FIGURE 5.1 Test SRHDPE pipes with bell and spigot joints in the field test

5.2. Test Site and Test Sections

The test site is located at 1178 north on E 1000 Road in Lawrence, Kansas (**FIGURE 5.2**). The E 1000 Road is a two-way single-lane and high-volume road. The pipe run was approximately 72 ft. long, from inlet to outlet. Galvanized steel end sections (meeting the material requirements of AAS HTO M218 and ASTM A929) were used on the inlet and outlet of the pipe. The pipe was graded at 1% slope to allow gravity flow through the pipe from the western end (upstream) to the eastern end (downstream). The road section consists of a roadway of 24 ft. long with 2% grade on each side of the roadway, a shoulder of 6 ft. wide with 4% grade on each side (the shoulder was provided for future widening of the E1000 Road), and the embankment beyond the shoulder with 6:1 grade on each side (**FIGURE 5.3**).

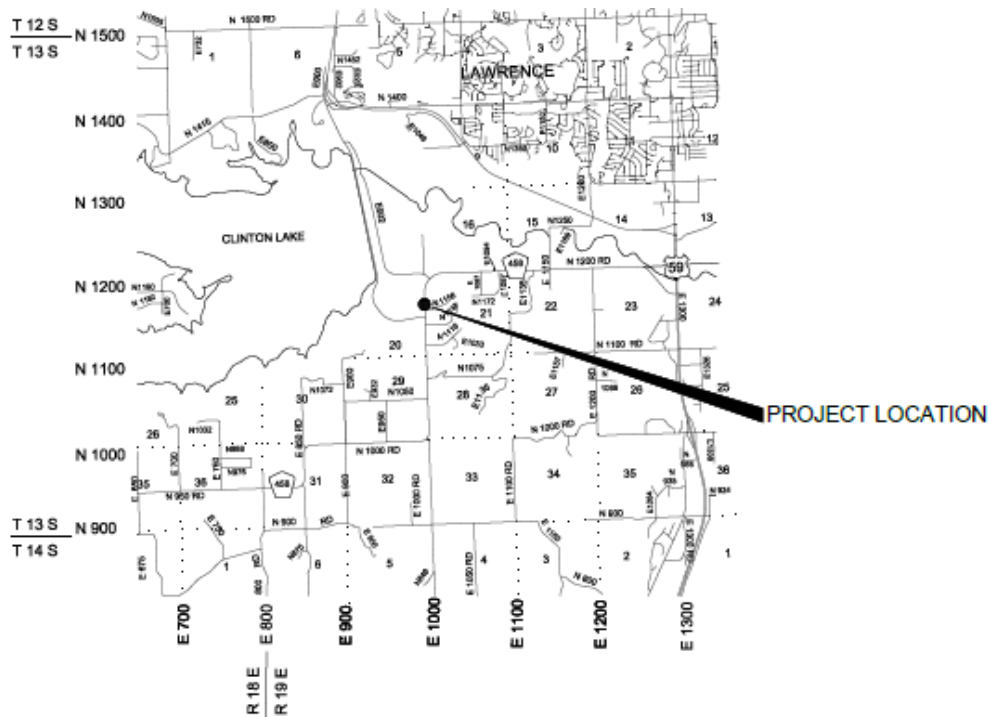


FIGURE 5.2 Location Map of the field test

In the field test, the total run of the pipe was divided into two sections from the center of the roadway. Section A with AB-3-II as both bedding and backfill materials on the western end and Section B with crushed stone (CS-II) as both bedding and backfill materials on the eastern end, were constructed. **FIGURE 5.4** shows the longitudinal and cross test sections with extensive instrumentation. The test sections had a rectangular trench of 6 ft. wide and 5 ft. 8 in. deep in in-situ soil. The trench consisted of 6 in. thick bedding material, 3 ft. backfill, and 3 ft. soil cover including a 9 in. thick HMA base and a 2 in. thick HMA surface. Section A had the AB-3-II material up to the HMA base (**FIGURE 5.4b**); however, Section B had a 6 in. thick AB-3-II material on the top of the CS-II material and then an HMA base was placed (**FIGURE 5.4c**).

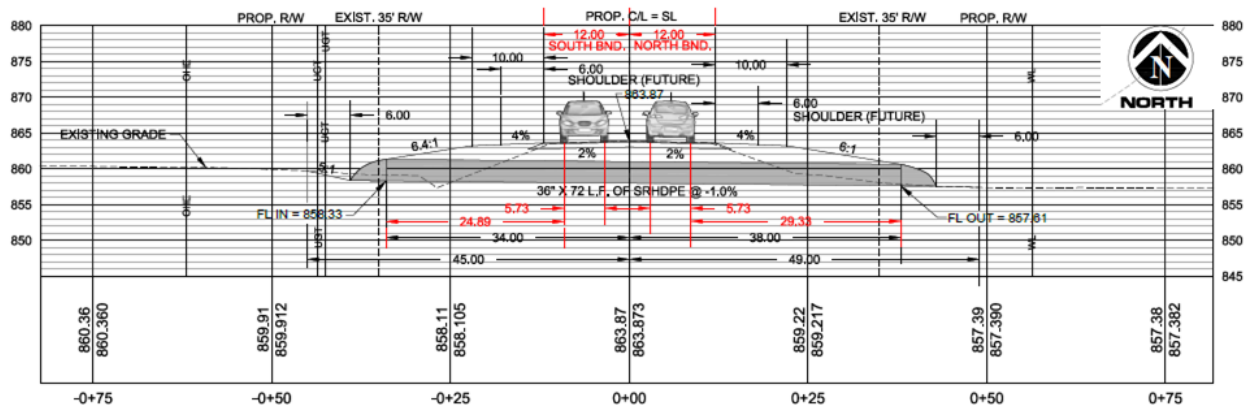
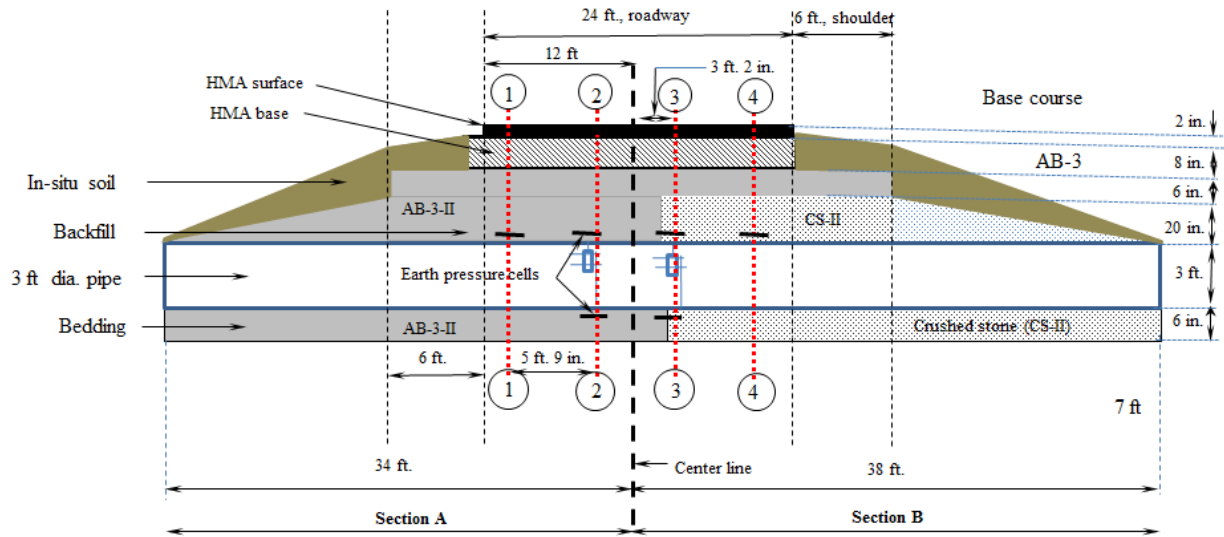
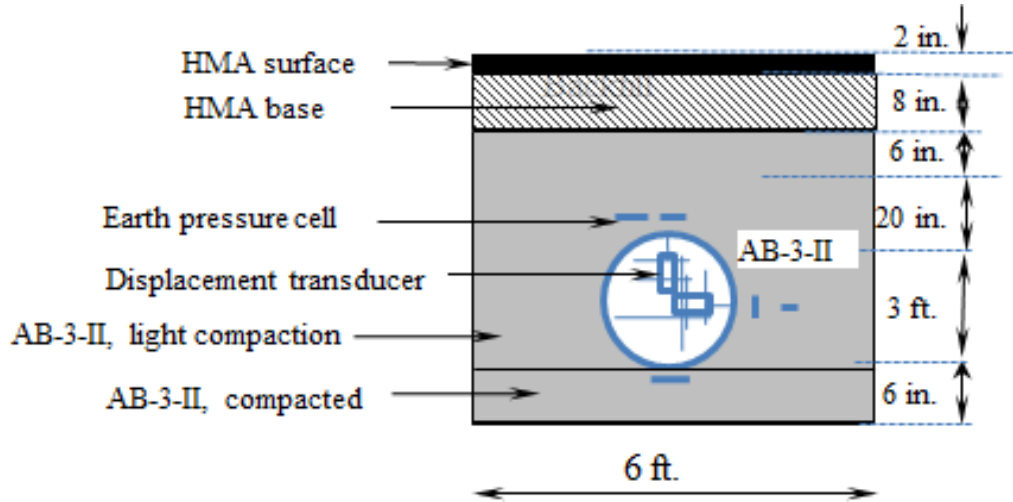


FIGURE 5.3 Road section in the field test

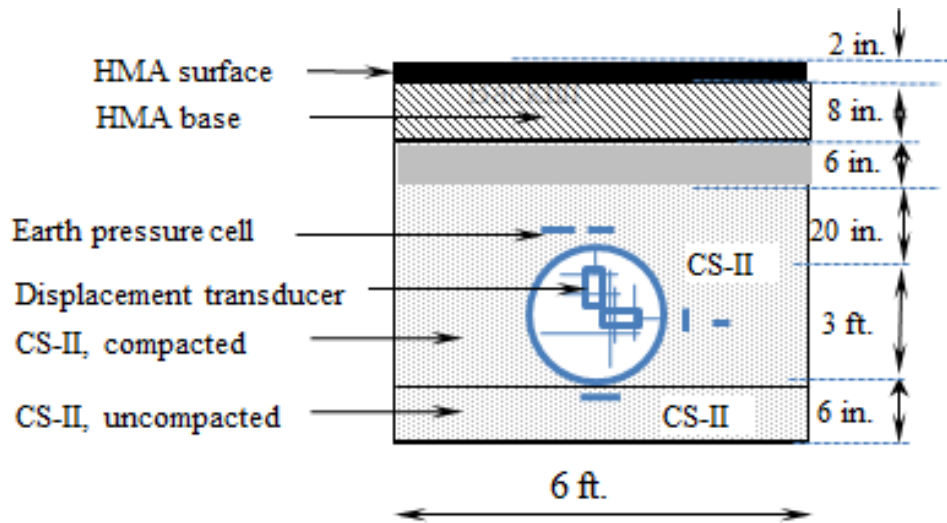


(a) Longitudinal section of the test section



(b) Section 2-2 (Section 2)

FIGURE 5.4 Test Sections B



(c) Section 3-3 (Section 3)

FIGURE 5.4 Field Test Sections (continued)

5.3 Instrumentation

The instrumentation plan was developed to collect the minimum data required to accurately characterize the structural performance of the pipe. The results from the laboratory tests (discussed in Chapter 6) indicated that the most significant pipe response would be near the crown and springline, thus the instrumentation was focused on these regions. **FIGURE 5.4a** shows four different instrumented sections. For the western test section (Section A), the pipe was instrumented at Sections 1 and 2 whereas for the eastern test section (Section B), the pipe was instrumented at Sections 3 and 4. Section 2 in the western test section (Section A) and Section 3 in the eastern test section (Section B) were instrumented under the traffic wheel paths close to the centerline of the roadway (on vertical planes). Sections 2 and 3 were instrumented extensively to capture deflections using displacement transducers, strains on pipes using strain

gages, and soil pressures around the pipe using vibrating wire pressure cells as described in **SECTIONS 5.3.1** through **5.3.3**. In addition, Sections 1 and 4 which were close to the shoulder had only one vibrating wire pressure cell installed at the crown of the pipe under each path. Three SRHDPE pipes, each of 24 ft. long, were used for the 72 ft. pipe run. The middle pipe was laid under the roadway (discussed later)

5.3.1 Displacement Transducers and Tell-Tales

Four displacement transducers, two on each test section (Sections 2 and 3), were used to measure the changes in vertical and horizontal diameters during installation and service vehicles as shown in **FIGURE 5.4**. The displacement transducers were manufactured by Tokyo Sokki Kenkyujo, Co., Ltd, Japan. In the laboratory tests, the holes were drilled thorough the pipe walls to fix the transducers on the pipes as described above in **SECTION 4.3.1** whereas in the field test, holes through the pipe walls were not made, instead epoxy glue was used with PVC pipes as shown in **FIGURE 5.5**.



FIGURE 5.5 Displacement transducers inside the pipe section in the field

5.3.2 Strain Gages

Uniaxial foil-type electrical resistance (C2A-13-250 LW -120) strain gages, manufactured by Vishay Precision Group, were used to measure the circumferential, radial, and longitudinal strains of the pipe at various locations as shown in **FIGURE 5.6**. For both pipe sections (Sections 2 and 3), the strain gages were installed outside and inside of the pipe on steel and plastic surfaces following the same procedures adopted in the laboratory tests as described in **SECTION 4.3.2**. The symbols, locations, and orientations of the strain gages fixed on the pipe in the field test were same as for the strain gages fixed in the laboratory tests (**FIGURE 4.10**). In addition, six more strain gages on each section (Sections A and B) labeled with a double prime (") symbol were placed on the plastic, inside and outside of the pipe, between the ribs (i.e., valley) to measure the strains in the plastic at the pipe crown as shown in **FIGURE 5.7**. These six strain gages were placed along the pipe run to the centerline of the roadway. For example, the strain gages notations (G''_{CL3} and G''_{CL4}) with a double prime symbol represent the strains at the pipe crown in plastic in the longitudinal direction at a distance of 4 in. from the instrumented section to the roadway centerline.



FIGURE 5.6 Strain gages fixed outside of the pipe in the field

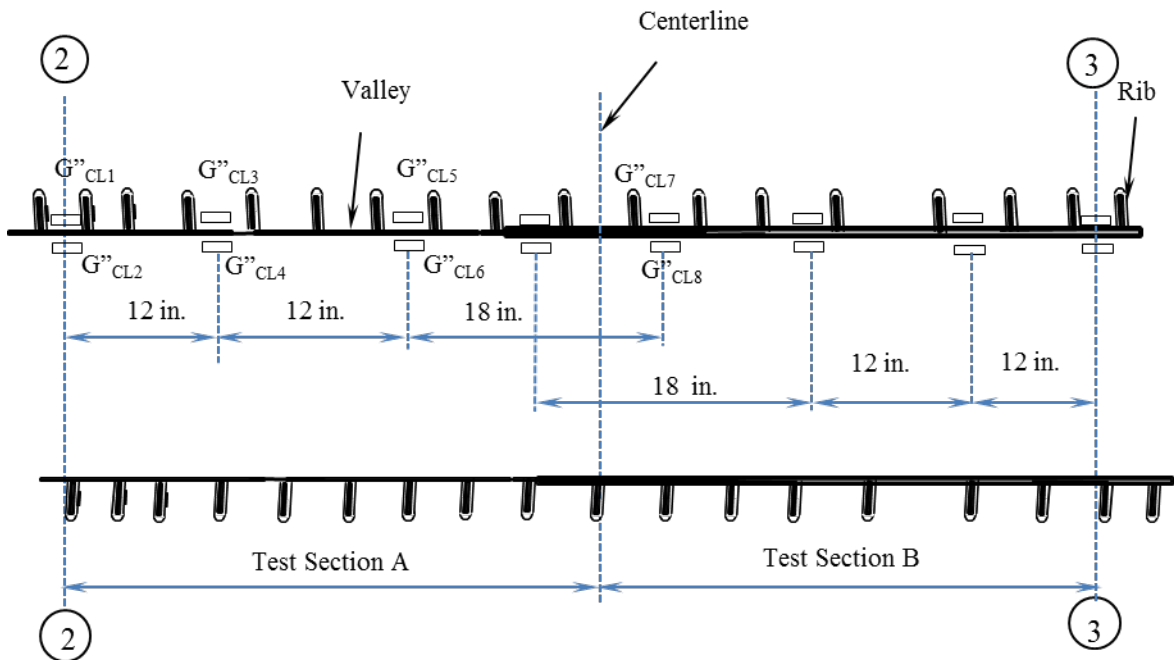


FIGURE 5.7 Symbols, locations, and orientations of the strain gages on the pipe in the field

5.3.3 Earth Pressure Cells

Twelve vibrating wire pressure cells (model 4810), manufactured by Geokon with capacity of 51 psi, were installed around the pipe under the wheel paths of the vehicles. Sections 2 and 3 had five pressure cells each whereas Section 1 and 4 had one pressure cell each at the crown of the pipe (**FIGURE 5.4**). The notations, locations, and orientations of the pressure cells are presented as in the laboratory tests (**FIGURE 5.8**). The subscripts of the notations represent the positions at which the earth pressure cells were placed. The subscript letters I, S, W, and C stand for invert, springline, wall, and crown of the pipe, respectively whereas the numerical value gives the horizontal distance from the position defined by the subscript letter. For example, the notations, E_{C0} and E_{C12} , represent earth pressure cells placed at the crown and at 12 in. horizontal distance from the crown towards the trench wall, respectively. Pressure cells, (E'_{S0} , and E'_{S18}) labeled with the prime (') symbol were installed for the horizontal earth pressure measurements whereas the remaining pressure cells without the prime (') symbol were installed for the vertical earth pressure measurements.

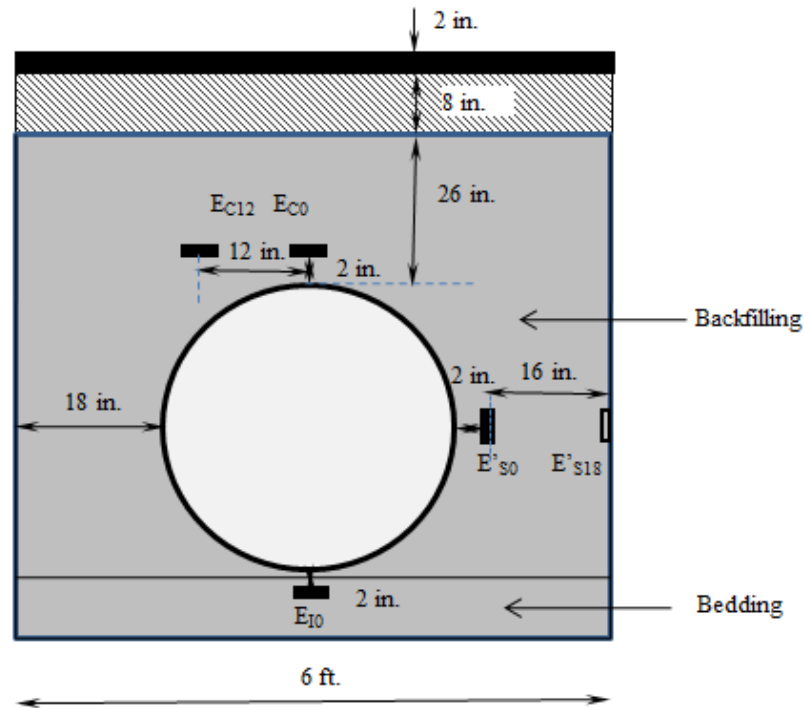


FIGURE 5.8 Earth pressure cells around the pipe section

5.4 Data Acquisition System

Two smart dynamic DC-204R data recorders were used to record data from four displacement transducers and four strain gages. A slope Indicator data logger was used to measure earth pressures around the pipe from the vibrating wire pressure cells and strains at various locations on the steel and plastic. The power to the data recorders and computers were supplied using batteries and a generator.

5.5 Construction of Test Section

An existing corrugated metal pipe of 24 in. diameter on the E 100 road at Lawrence, Kansas because of the excessive corrosion was to be replaced with SRHDPE pipes of 36 in. in

diameter. **FIGURE 5.9** shows the existing metal pipe in service. The existing metal pipe was found having lost most of its invert portions due to the corrosion. The test sections were constructed by the Douglas country Public Work and the construction procedures for both backfill test sections (Sections A and B) were discussed in **SECTIONS 5.5.1** to **5.5.3**.



FIGURE 5.9 An existing corrugated metal pipe under service

A 2000 model Case 9030B excavator was used to dig out the existing HMA base and surface, and to make the rectangular trench of 6 ft. wide as shown in **FIGURE 5.10**. The width of the trench was chosen according to the 2007 KDOT Pipe and Culvert Specifications so as to

provide working space for compaction equipment in order to properly and safely place and compact bedding, hunching, and backfill materials. A minimum trench width was maintained so as not to be less that greater of either 1.5 times the pipe outside diameter plus 12 in or the pipe outside diameter plus 12 in. on each side. The existing corrugated metal pipe was exhumed and in-situ soil was found to be clayey soil at 24% moisture content (classified later according to the USCS by conducting laboratory tests as discussed in **SECTION 3.2**). After constructing the trench, the centerline of the roadway was marked (**FIGURE 5.11**) and the construction of beddings of both western and eastern sections (Sections A and B) was started.



FIGURE 5.10 Construction of trench



FIGURE 5.11 Marking centerline before dumping bedding materials.

Bedding

AB-3-II aggregate and crushed stone (CS-II) were dumped from the height of approximately 5 to 6 ft. in the trench using the excavator on the western and eastern test sections, respectively and were leveled as shown in **FIGURE 5.12**. The beddings were not compacted on both test sections. The wheel paths on both sections were marked in order to locate the sections to be instrumented as shown in **FIGURE 5.13**. All earth pressure cells were connected to the data acquisition systems. The earth pressure cells E_{10} were installed in the bedding materials on both test sections (Sections 2 and 3) under the wheel paths close to the centerline of the road at the invert of the pipe before the placement of the pipe in the trench as shown in **FIGURE 5.14**. Before each earth pressure installation, the surface was leveled using sand, the pressure cell was placed and checked level with a spirit level, and then covered by the sand. The pressure cells

were covered by sand to minimize the effect of non-uniform contacts of the backfill materials on sensor surfaces of the pressure cells.



FIGURE 5.12 Construction of the beddings



FIGURE 5.13 Marking wheel paths



FIGURE 5.14 The earth pressure cell E_{10} installed at the invert of the pipe

Placement of Pipe

After bedding, galvanized steel end sections were connected to the ends of the pipes as shown in **FIGURE 5.15**. Each pipe was placed in the trench using the excavator (**FIGURE 5.16**). The pipes were connected to each other with the help of attached bell and spigot (with gasket) ends. The instrumented (middle) pipe was connected carefully so that the displacement transducers fixed on the pipe inside to measure vertical deflections of the pipe oriented vertically. **FIGURE 5.17** shows the pipes in the trench before backfilling. All the sensors, strain gages and displacement transducers, were connected to two separate DC-204R and the slope indicator data recorders. The recorders were then adjusted and balanced to set all the initial values to zero.



FIGURE 5.15 Galvanized steel end sections



FIGURE 5.16 Placing a pipe in the trench



FIGURE 5.17 Fully instrumented pipes in the trench

Backfilling and Soil Cover

AB-3-II aggregate and crushed stone (CS-II) were used as backfill materials. The backfilling was performed in layers approximately 6 to 9 in. lift thick after compaction. A vibratory plate compactor, Wacker WP1550AW, was used for compaction of the crushed stone (CS-II) whereas a tamping hammer, Multiequip MT65H, was used for the AB-3-II aggregate. The vibratory plate compactor, Wacker WP1550AW, consisted of a base plate of 23 in x 19.5 in. size with the operating weight of 194 lbs, vibrated at a frequency of 100 Hz. The tamping hammer, Multiequip MT65H, consisted of a shoe size of 11 in x 13 in. with the impact force of 2450 to 2900 lbs/blow, can apply 590 to 695 blows in a minute. The vibratory plate compactor and the tamping hammer were used for the compaction of the backfills and soil covers (up to a height of 26 in. above the crown of the pipe) as shown in **FIGURE 5.18**. For the AB-3-II aggregate backfill on the western test section (Section A), a light compaction was used up to the springline to avoid the excessive uplifting of the pipe. The compaction directly above the pipe surface was avoided to prevent possible damage of the pipe due to the compaction equipment.

The backfilling was done in equal lifts on both sides of the pipe so as not to disturb the pipe alignment. **FIGURE 5.19** shows the backfills placed up to the springline. To dump AB-3-II aggregate and crushed stone (CS-II) up to a height of 6 in. above the crown, the excavator was used. After that, a bobcat, 2006 model S300, was used to dump and level the soils as shown in **FIGURE 5.20**. The top 6 in. AB-3-II aggregate was placed and compacted throughout the test section using the tamping hammer and a smooth wheel vibratory roller, 2005 model Hamm HD13. The vibratory roller, which has the operating weight of 8,741 lbs, compacts soils with the centrifugal force of 14 kips for a high amplitude and 9 kips for a low amplitude vibrating at a frequency of 60 to 51 Hz. **FIGURE 5.21** shows the compacted AB-3-II aggregate surface before placing the HMA base. During the backfilling, the earth pressure cells were installed around the pipe for each test section as described in **SECTION 4.3.3** and are shown in **FIGURE 5.22**. The readings of the strain gages, displacement transducers, and earth pressure cells were taken using the data recorders after completion of each lift during backfilling.



(a) Eastern test section (Section B)

FIGURE 5.18 Backfilling and compacting with vibratory plate compactors and tamping hammer



(b) Western test section (Section A)

FIGURE 5.18 Backfilling and compacting with vibratory plate compactors and tamping hammer

(continued)



FIGURE 5.19 Backfilling up to springline



FIGURE 5.20 A bobcat used to dump and level soils



FIGURE 5.21 The compacted AB-3-II surface before placing the HMA base



(a) At pipe springline



(b) At pipe crown

FIGURE 5.22 Earth pressure cells, E_{s0} and E_{s18} at the springline and E_{C0} and E_{C12} at the crown

(continued)

Loading

After the compaction of the top 6 in. thick AB-3-II aggregate, the wheel paths of vehicles were marked on the surface for each test section to apply a truck load on the pipe as shown in **FIGURE 5.23**. A dump truck, 2004 International 7400 6x4, of 13.72 tons (empty) loaded with the HMA base course material of 15.2 tons was used as the test truck (**FIGURE 5.23**) to apply the load on the pipe to monitor the effects of the construction vehicles on the pipe. The test truck consisted of two physical axles: a front steering axle and tandem axles at the end. Seventy two percentage of total gross weight of 29 tons (sum of the weights of the empty truck and the loaded material) was carried by the rear axle and the remaining 28% was shared by the front axle. The axle configuration and the load on each axle are shown on **FIGURE 5.24**. Based on the empty weight of 13.72 tons of the truck and the ground vehicle weight rating (GVWR) of around 28 tons, the maximum axle load capacities were 10 and 23 tons for front and rear axles, respectively.



FIGURE 5.23 Test truck used in loading the culvert

The static truck load was applied on both western and eastern test sections (Sections A and B) with the rear axle: a back tire at the center between the trench wall and the pipe crown, a back tire above the pipe crown, and a middle tire above the pipe crown as shown in **FIGURE 5.25**. The contact area calculated for each rear wheel load of 5.25 tons for the tire pressure of 120 psi was found to be 87.5 in.². For each loading step, the truck was kept for a while till all readings from the displacement transducers were stable and recorded. After the truck static load, the truck was run over the pipe at a slow speed in order to capture the effect of the moving construction vehicle on the pipe.

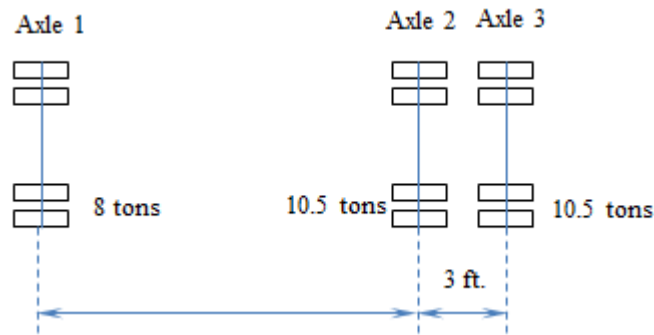


FIGURE 5.24 Axle load configuration of the test truck



(a) Back tire at the center between the trench wall and the crown (b) Back tire above the crown (c) Middle tire above the crown

FIGURE 5.25 The test truck applying static loads

HMA Base and HMA Surface Preparation

After applying the truck load, an 8 in. thick HMA base (described in **SECTION 3.2.2**) was prepared. The HMA material was placed using the dump truck (**FIGURE 5.26**), leveled using the bobcat (**FIGURE 5.27**), and compacted uniformly in a single layer by the vibratory roller (**FIGURE 5.28**) for several passes. After the HMA base, the HMA material was placed, leveled, and dumped to produce the 2 in. thick surface course.



FIGURE 5.26 A truck dumping HMA for the HMA surface



FIGURE 5.27 HMA dumped and leveled using the bobcat



FIGURE 5.28 Vibratory roller compacting the HMA base

A sketch of the cross section of the test sections is shown in **FIGURE 5.29**, which presents the compaction schedule of the backfill and the base course, and also includes the locations of the earth pressure cells.

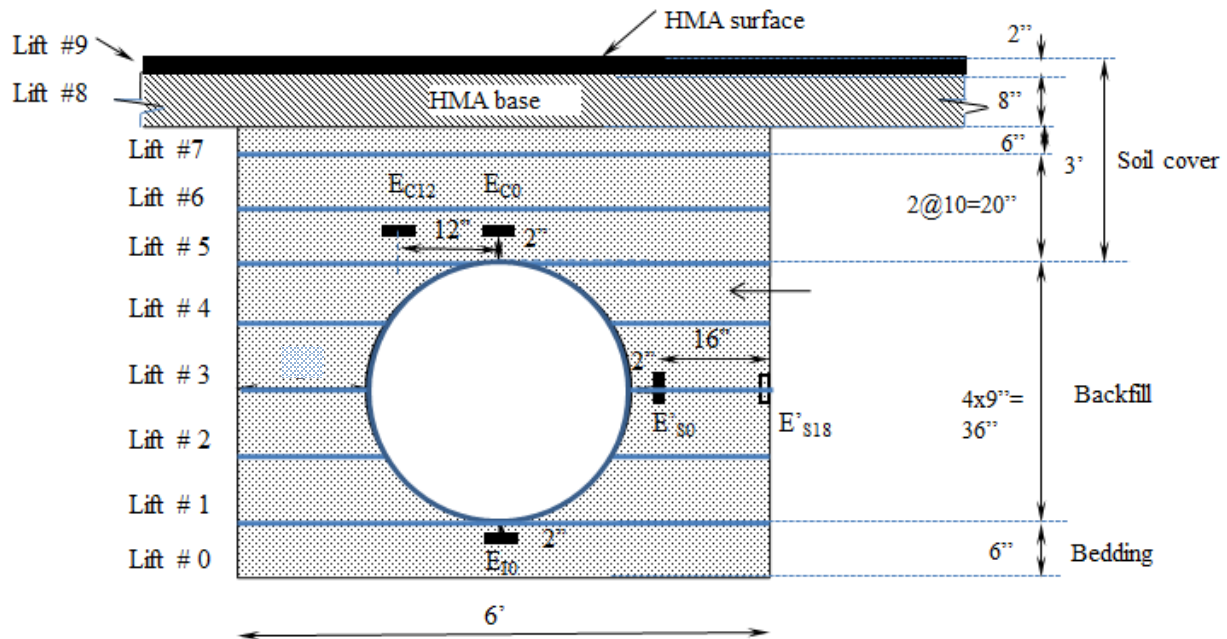


FIGURE 5.29 Schedule details of construction of test sections in the field including the soil lifts and earth pressure cells

5.6 Quality Control

The installation of the pipe on this E1000 road was planned to finish in two days. It was scheduled to open the road for the traffic in the afternoon on the second day. This resulted in a very busy schedule for the installation of the pipe. As explained earlier, the construction was performed by the Douglas County Public works; however, the installation of all the sensors, strain gages and displacement transducers at a warehouse and pressure cells at the site, were performed by the University of Kansas. The maximum efforts were used to minimize the

delayed in the construction. To control the quality of the construction, instead of slow and tedious field tests, non-destructive Light Weight deflectometer (LWD) tests were conducted over the compacted crushed stone CS-II and the AB-3 aggregate at various locations during the preparation of the test sections as shown in **FIGURE 5.30**. The dynamic deformation moduli (E_{vd}) obtained from LWD tests (using a 1 ft. diameter plate) were in a range of 2,700 and 3,700 psi with an average value of 3300 psi for the AB-3-II and 2,460 and 3,480 psi with an average value 2900 psi for the crushed stone CS-II.



FIGURE 5.30 LWD test on the compacted AB-3-II

In addition, Dynamic Cone Penetration (DCP) tests were carried out following ASTM D6591-03 on both sides of the pipe on the western test section (Section A) after the compaction of the backfill up to the pipe haunch. The DCP tests were also conducted before placing the HMA base at two different locations on the western test section (Section A) and at two locations

on the eastern section (Section B). On the eastern test section (Section B), the DCP rod was penetrated to a depth of 6 in. to the crushed stone. The relationship between the CBR value at the depth of penetration and the penetration index in inches per blow of DCP is given in **EQUATION 4.1** (Webster et al., 1992). The CBR profiles of the test section (Section A) obtained from the DCP tests are shown in **FIGURE 5.31**. The average CBR values of the compacted and light compacted AB-3 aggregate, resulting from the DCP tests, were approximately 25 % and 12%, respectively.

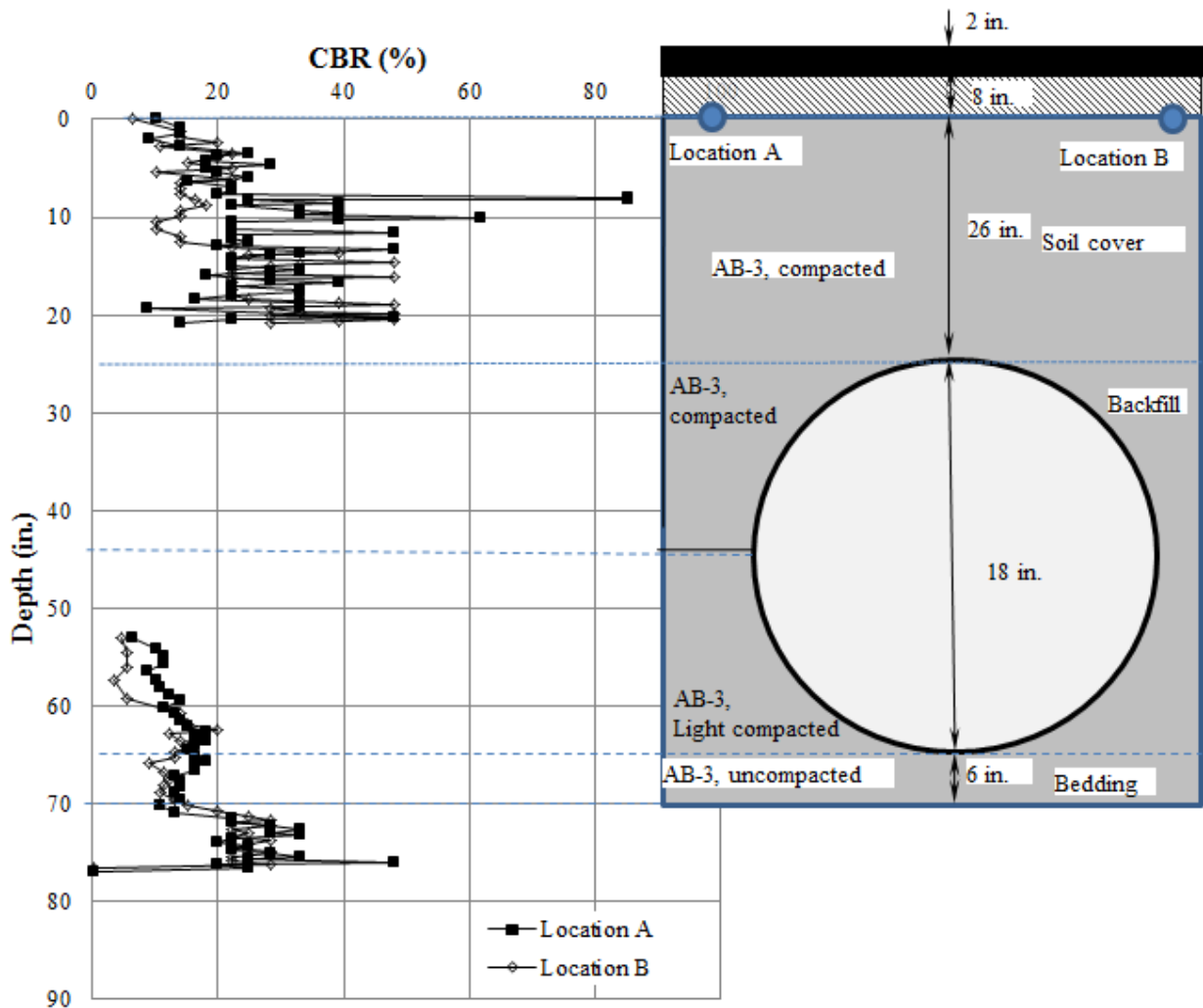


FIGURE 5.31 CBR profiles on the western test section

The densities of the AB-3-II compacted in the field were determined later by constructing test sections at the Big Spring Quarry at Lawrence. A test section of compacted AB-3-II material was constructed by compacting the material using the vibratory plate compactor till the desired CBR values of 25 % from the DCP tests and the dynamic deformation moduli (E_{vd}) values (3200 psi for the compacted AB-3-II section) from LWD tests were obtained. The densities of the compacted AB-3-II sections determined by the sand cone method following ASTM D1556-07 were found to be 127 pcf at approximately 7% moisture content.

The densities of crushed stone (CS-II) compacted in the field were determined later in the laboratory at KU. A small box of 2 ft. 7.5 in. long, 2 ft. 7.5 in. wide, and 3 ft. high was used as shown in **FIGURE 5.32**. A 2 ft. thick compacted crushed stone (CS-II) material was constructed by compacting using the vibratory plate compactor till the desired dynamic deformation moduli (E_{vd}) value of 2900 psi from LWD tests were obtained. To determine the densities of uncompact AB-3-II and crushed stone (CS-II) beddings, each material was dumped from the height of around 5 ft. and leveled in the box. The densities of the uncompact AB-3-II aggregate, uncompact crushed stone (CS-II), and compacted crushed stone (CS-II) materials determined by the weight-volume method were found to be 110, 94, and 97 pcf, respectively.



FIGURE 5.32 A small box used for density determination

5.7 Data Collection

To check the performance of the SRHDPE pipes during the installation and under the both construction and service vehicles from the extensive instrumentation described above, the data were collected using the data recorder. During the installation, data were collected when the tamping hammer and vibratory plate compactors were used for each step shown in **FIGURE 5.29**, the construction vehicles such as the excavator, the bobcat, and the vibratory roller were run over the top of the pipe, and the static truck loadings were applied over the pipe. The following data were collected:

- i) The deflection (or change of diameter) of the pipe
- ii) The pressure distribution around the pipe using the pressure cells
- iii) The circumferential and longitudinal strains developed on the steel and plastic from the strain gages

CHAPTER 6 DATA ANALYSIS AND RESULTS

This chapter contains a summary and analyses of the test results obtained from the laboratory and field tests. Three large-scale laboratory box tests and one field test were conducted and are discussed in this chapter. The test results include those obtained from the laboratory tests during the installation, static plate loading tests, and cyclic plate loading tests. The results, obtained from the field test during the installation, the construction vehicle loading, and the pipe under service vehicles, are presented. The performance of the pipe under service vehicles will be monitored for two years. In this study, the data obtained for the first six months are discussed. The data obtained from two first laboratory tests (Tests 1 and 2) were summarized by Khatri (2012). In this study, the test results obtained from Tests 1 and 2 in the laboratory are compared with the results obtained from the third test (Test 3) conducted in the laboratory and from the field test. The test results obtained during the installation and the loading are also compared with available theories and results presented by others.

6.1 Test Results from Pipe Installation

This section discusses the experimental data collected through the instrumentation and monitoring of earth pressure cells, displacement transducers, and strain gages during the installation of the pipes. In the laboratory test, since Test 2 used the same trench and the same backfill material as Test 1 and was prepared after removing the base course, the backfill material, and the pipe used in Test 1, no monitoring of sensors was taken during the re-construction of the section for Test 2. Therefore, only the installation results from two laboratory tests (Tests 1 and 3) and from the field test are presented herein. In the laboratory tests, the Kansas River (KR) sand in Test 1 and the crushed stone (CS-I) in Test 2 were used as the backfill materials whereas the crushed stone (CS-II) and the AB-3-II aggregate were used in the field test. The crushed

stone (CS-I) backfill in Test 1 conducted in the laboratory was dumped and whereas in the field, the crushed stone (CS-II) backfill was compacted. In the laboratory tests, the 9 inch thick AB-3 aggregate was used as the base course whereas in the field test, the 8 inch thick HMA base and the 2 inch thick HMA surface were used. The details of the construction steps and schedule were presented in **FIGURES 4.24** and **5.29** for the laboratory tests and the field test, respectively.

6.1.1 Earth Pressure Results

Laboratory Tests

Test 1. **FIGURE 6.1** shows the pressures developed around the pipes against the levels of construction (labeled as 1 to 9 as shown in **FIGURE 4.24**). The earth pressure cells, E_{C0} and E_{C6} , fixed at the crown and 6 in. away from the crown measured similar earth pressures during the installation. The vertical pressure recorded by the pressure cell fixed at the invert (E_{I0}) was negative. The negative pressure measured by E_{I0} continued decreasing slightly until the fill height reached 6 in. over the pipe crown (i.e., Level 5 of the construction) and then increased as the construction proceeded. This result is because all of the sensors were set to zero for initial readings after the placement of the pipe inside the trench. Therefore, the initial reading recorded by the earth pressure cell (E_{I0}) due to the weight of the pipe was not considered. As the level of construction increased, the invert of the pipe moved upward and released the vertical pressure on the pressure cell (E_{I0}).

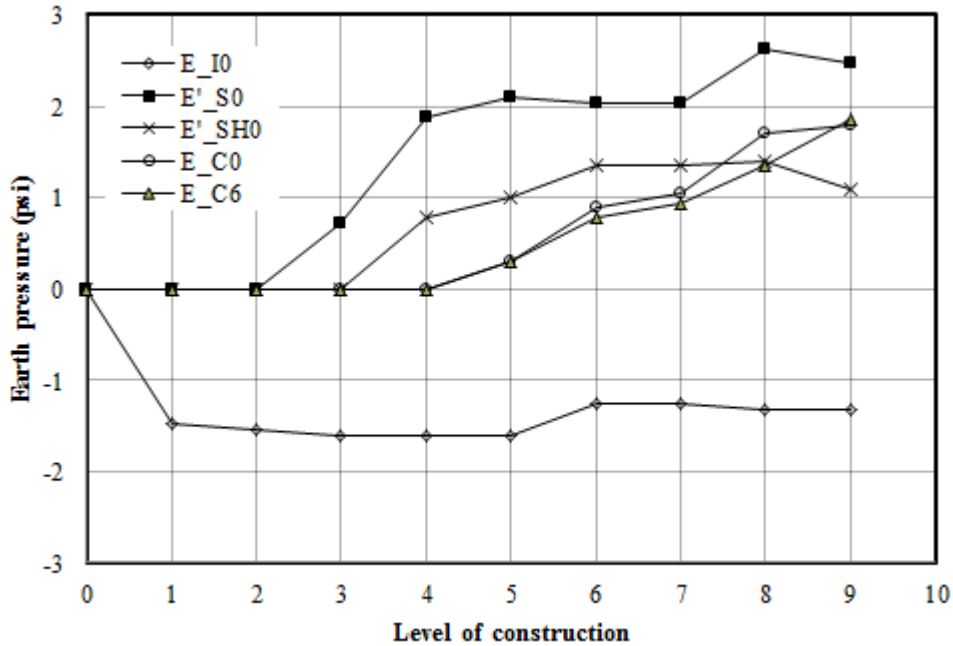


FIGURE 6.1 Measured earth pressures around the pipe during installation in Test Section 1

The overburden pressure $E_{C0, cal}$ (i.e., the unit weight of the soil (γ_s) x the thickness of the soil from the crown (H)) was calculated at the crown of the pipe. The pressure measured at the crown by the earth pressure cell (E_{C0}) was then compared with the calculated overburden vertical pressure and they are shown in **FIGURE 6.2**. The vertical arching factors (VAFs), calculated as the ratio of the measured pressure to the calculated overburden pressure at the crown, are shown in **FIGURE 6.2**. The VAFs varied from 1.15 to 1.41 with an average value of 1.26. As described by McGrath (1998), the SRHDPE pipe behaved similarly to a corrugated steel pipe based on the vertical arching factor and the hoop stiffness. In addition, the vertical arching factors calculated using Burns and Richard's no-slip and full-slip solutions (**EQUATIONS 2.2** and **2.3**) resulted in VAFs of 1.40 and 1.01, respectively. In this calculation, the hoop stiffness needed for the Burns and Richard solutions was estimated using **EQUATION 2.4** based on the

constrained modulus ($M_s = 3,000$ psi), of the backfill (i.e., the Kansas River sand), the radius of the pipe (24 in.), the area of the steel reinforcement (0.3549 in²/ft.), and the modulus of elasticity of the steel reinforcement (29,000 ksi). The constrained modulus, M_s , of the sand was back-calculated from the modulus of elasticity of the KR sand determined from the small plate loading test as described in **SECTION 3.2.2**. The vertical arching factors (VAF) from the measurement of the earth pressures on the crown were close to the vertical arching factor obtained from the Burns and Richard solutions for the no-slip case as shown in **FIGURE 6.2**. Therefore, the SRHDPE pipe should be designed based on a no-slip condition to be conservative for the VAF value.

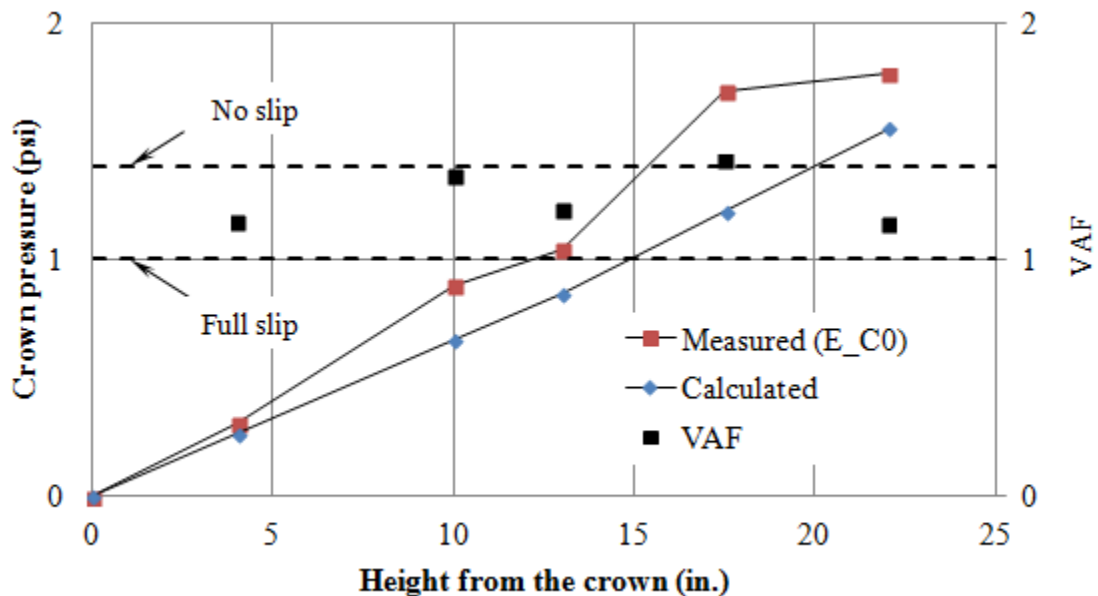


FIGURE 6.2 Comparison of measured and calculated pressures at the crown during installation in Test Section 1

FIGURE 6.3 shows the measured lateral pressures (E'_{S0} and E'_{SH0}) and the calculated overburden pressures at the springline and the shoulder. **FIGURE 6.4** shows the coefficients of lateral earth pressure (K) at the springline and the shoulder calculated as the ratio of the measured lateral pressures to the overburden pressures. **FIGURE 6.4** compares the measured coefficients at the springline and the shoulder with the lateral earth pressure coefficients, K_a , K_o , and K_p , calculated using the friction angle of the sand of 37° . The measured coefficients (K) were found to be between K_o and K_p . The coefficient (K) was the highest at Level 4 (i.e., when the fill height reached the crown of the pipe) and then decreased to a value close to the coefficient K_o . The higher values of the coefficients (K), when the construction levels were close to the pipe, may be due to the higher effect of the compaction on the pipe. It can be concluded from **FIGURE 6.4** that the lateral pressure generated by the backfill soil should be represented by a combination of the lateral earth force due to the backfill and a force generated by the compaction effort during the backfilling.

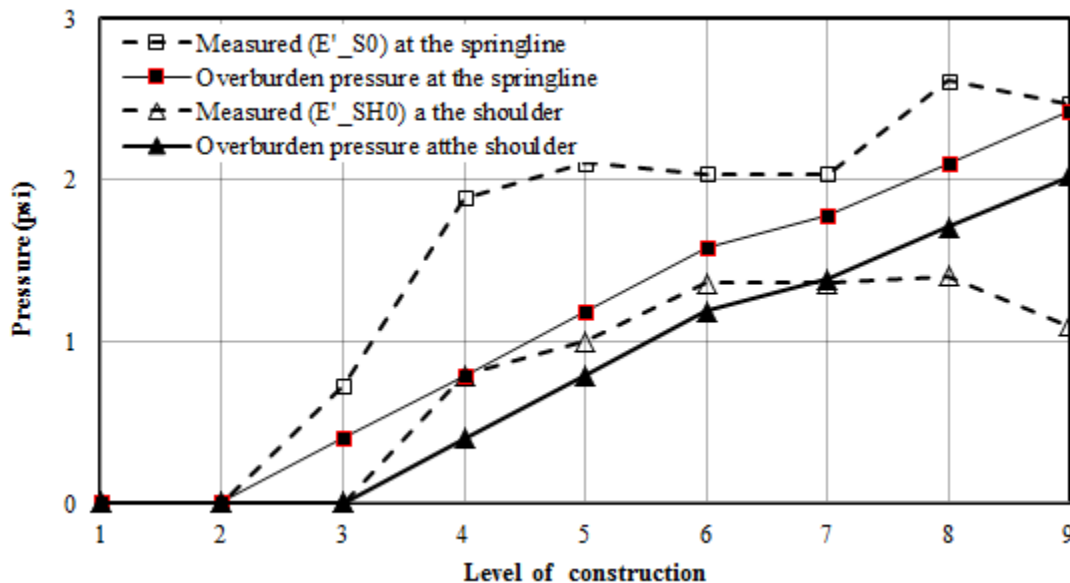


FIGURE 6.3 Calculated lateral earth pressure coefficients (K) at the springline in Test Section 1

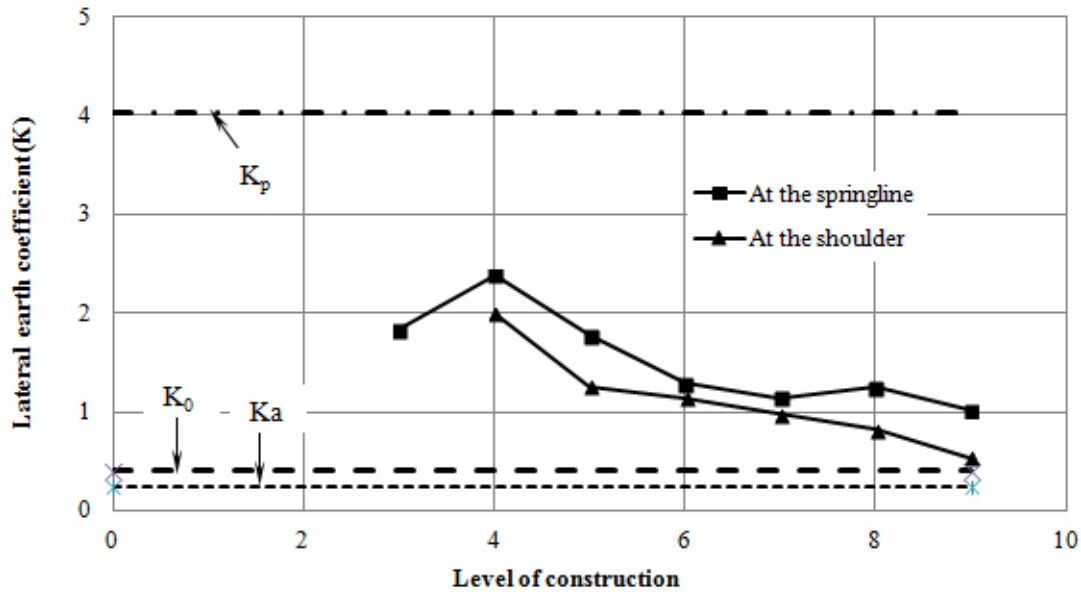


FIGURE 6.4 Calculated lateral earth pressure coefficients (K) at the springline and shoulder in Test Section 1

Test 3. **FIGURE 6.5** shows the pressures developed around the pipes against the levels of construction (labeled as 1 to 9 as shown in **FIGURE 4.24**). The earth pressure cell E_{10} fixed at the invert showed the highest pressures during the entire installation process. The earth pressure E_{10} at the invert in Test Section 1 was very different from that pressure in Test Section 3. This is because the invert of the pipe moved upward in Test Section 1 due to the compaction of the sand at the sides of the pipe and reduced the vertical pressure on the pressure cell (E_{10}) as the level of construction increased. However, the invert of the pipe did not move up in Test Section 3 since the crushed stone (i.e., the backfill material) was placed by dumping without compaction during the backfilling. The earth pressure cells, E_{C0} , E_{C6} , and E_{C12} , fixed at the crown, 6 in. and 12 in. away from the crown had the similar pressures during the installation. The pressures measured at the crown by the earth pressure cell E_{C0} were higher than the pressures at the springline

measured by the earth pressure cell E'_{s0} as the elevation of backfill was increased. The earth pressure cell E'_{sw} placed at the trench wall at the springline level showed only small changes in the pressure values during the pipe installation.

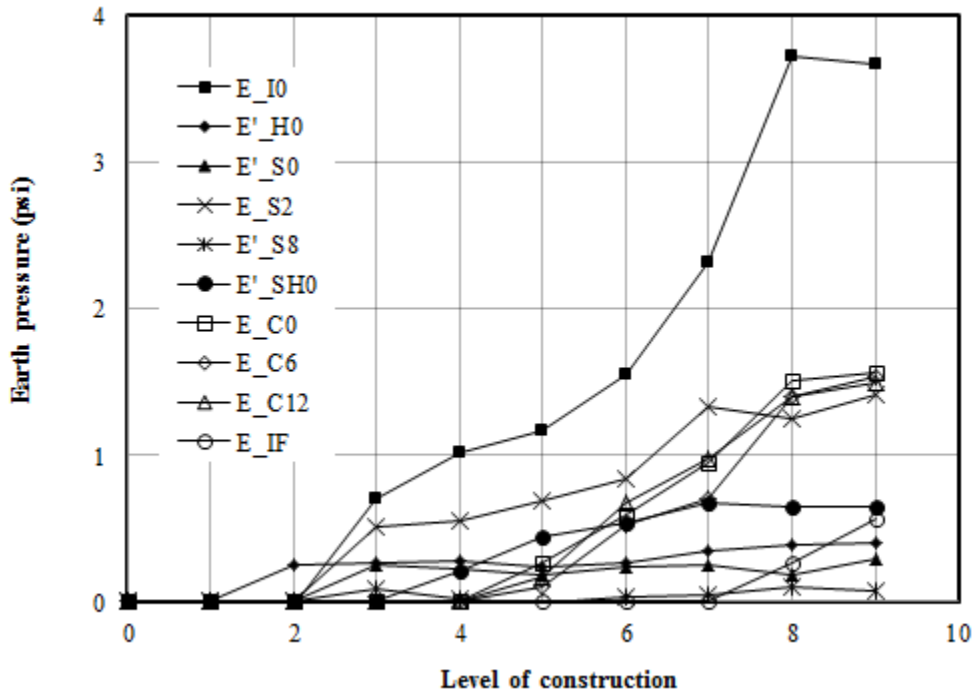


FIGURE 6.5 Measured pressures around the pipe during the installation in Test Section 3

The vertical earth pressure measured at the crown by the earth pressure cell (E_{C0}) was compared with the calculated overburden vertical pressure in **FIGURE 6.6**. **FIGURE 6.6** also shows the calculated vertical arching factors (VAFs) at the crown, ranging from 1.10 to 1.44 with an average value of 1.26. The VAFs calculated using the Burns and Richard solutions for the no-slip and full-slip conditions (**EQUATIONS 2.2** and **2.3**) were 1.42 and 1.03, respectively. The hoop stiffness needed for the Burns and Richard solutions was calculated using **EQUATION 2.4** based on the constrained modulus ($M_s = 1700$ psi) of the backfill (i.e., the

crushed stone), the radius of the pipe (24 in.), and the area (0.3549 in²/ft.) of the steel reinforcement and the modulus of elasticity of the steel reinforcement (29,000 ksi). The constrained modulus M_s was back-calculated from the modulus of elasticity of the crushed stone determined from the small plate loading test as described in **SECTION 3.2.2**. The calculated VAFs from the measurement of earth pressures are close to those obtained from the Burns and Richard solutions for the no-slip case as shown in **FIGURE 6.6**. The SRHDPE pipe should be designed based on the no-slip condition to be conservative for the VAF value.

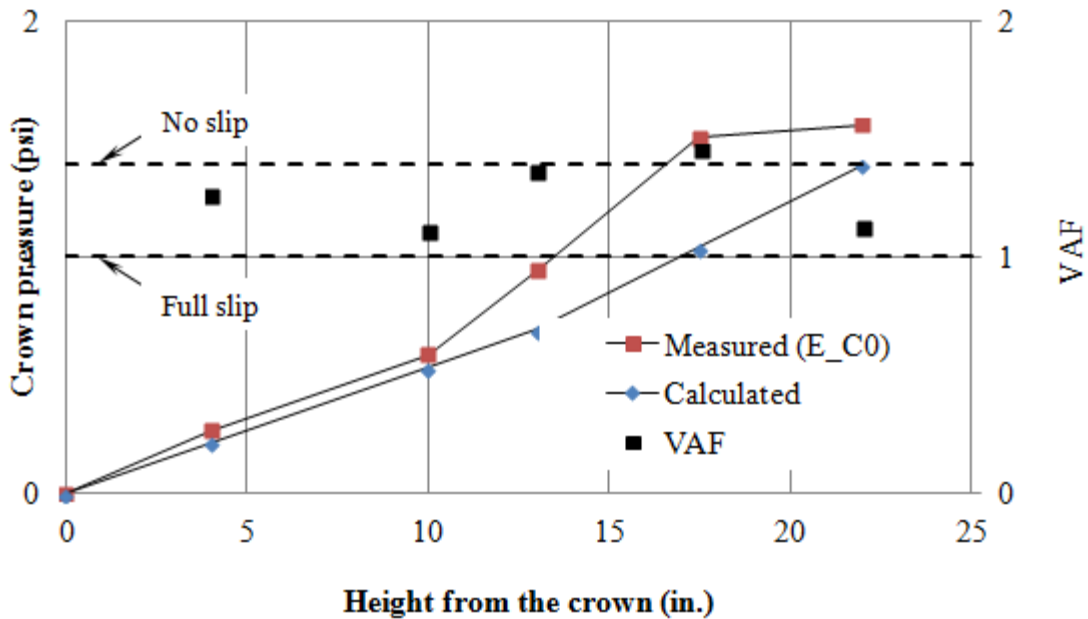


FIGURE 6.6 Comparison of measured and calculated pressures at the crown during the installation and vertical arching factor (VAF) in Test Section 3

FIGURE 6.7 shows the calculated overburden pressures at the springline were close to the vertical pressures measured by the earth pressure cell E_{S2} . Therefore, the calculated overburden pressure was used to calculate the lateral earth coefficient (K). For example, the coefficients of lateral earth pressure at the springline were calculated by dividing the lateral

pressures (E'_{s0}) measured at the springline by the overburden pressures calculated at the springline. The calculated coefficients of lateral earth pressure at the springline are shown in **FIGURE 6.8**. The average lateral earth pressure (K) was found to be 0.21, which was close to the lateral earth pressure coefficient at rest (K_0). The lateral earth pressure coefficient at rest (K_0) calculated as 0.19 using the friction angle of the crushed stone of 54° . Similarly, the lateral earth pressure coefficients (K) were calculated at the shoulder and the haunch using the pressures recorded by E'_{SH0} and E'_{H0} , respectively and are shown in **FIGURE 6.8**. **FIGURE 6.8** clearly shows that the coefficient of the lateral earth pressure (K) was close to the lateral earth pressure coefficient at rest (K_0) during the installation of the SRHDPE pipe.

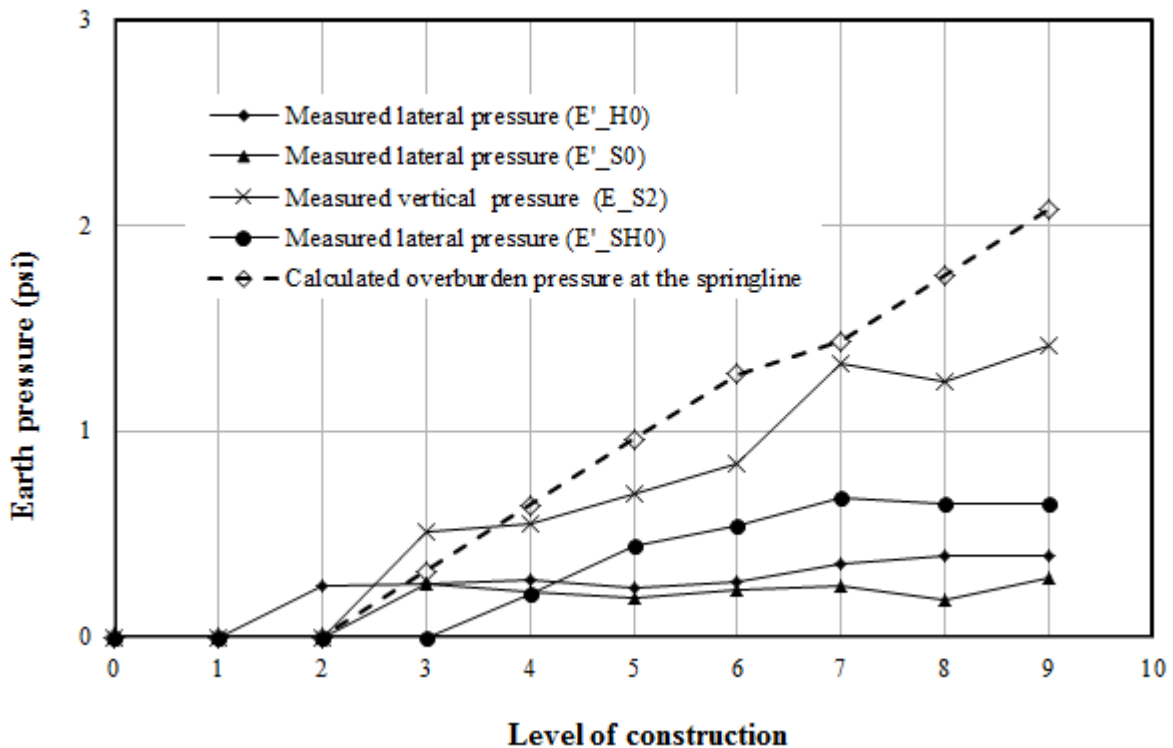


FIGURE 6.7 The measured lateral pressures at the shoulder, springline, and haunch with the measured and calculated vertical pressures at the springline in Test Section 3

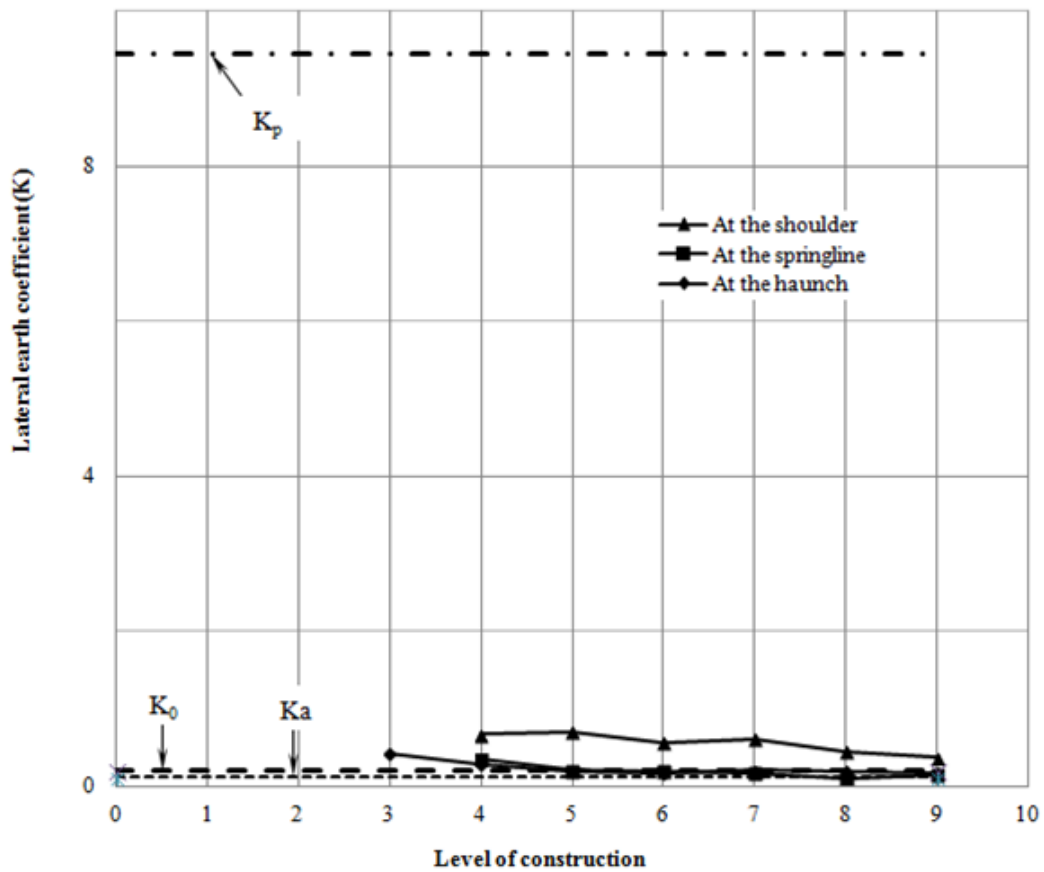


FIGURE 6.8 Calculated lateral earth pressure coefficients (K) at the shoulder, haunch, and springline in Test Section 3

Field Installation Test

Section A. **FIGURE 6.9** shows the measured earth pressures developing around the pipes against the levels of construction (labeled as 1 to 9 as shown in **FIGURE 5.29**). The pressures measured around the pipe in the field had similar trends to the pressures measured around the pipe in the laboratory tests. The earth pressure cells, 1E_{C0}, 2E_{C0}, and 2E_{C12}, fixed at the crown in Section 1, at the crown in Section 2, and at 12 in. away from the crown to the trench wall measured similar vertical earth pressures during the installation. The vertical earth pressures recorded by the pressure cell fixed at the invert (E_{I0}) were higher than the crown pressures.

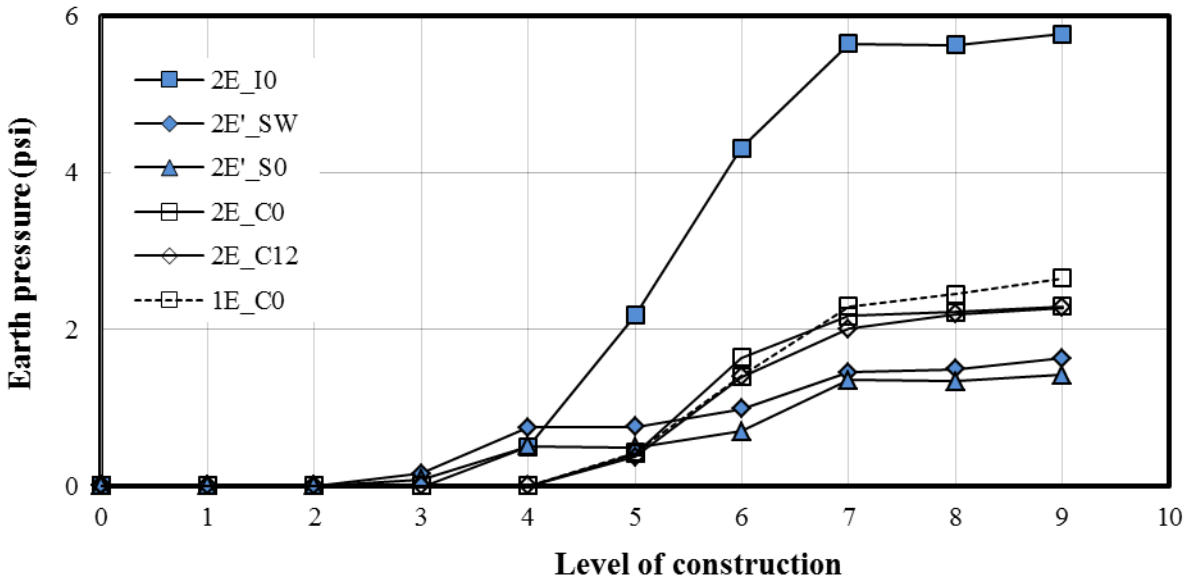


FIGURE 6.9 Measured earth pressures around the pipe during installation in Test Section A

The overburden pressure $E_{C0, cal}$ (i.e., the unit weight of the soil (γ_s) x the thickness of the soil from the crown (H)) was calculated at the crown of the pipe. The vertical earth pressures measured at the crown by the earth pressure cells ($1E_{C0}$ and $2E_{C0}$) were then compared with the calculated overburden vertical pressure and are shown in **FIGURE 6.10**. The vertical arching factors (VAFs), calculated as the ratio of the measured pressure to the calculated pressure at the crown, are shown in **FIGURE 6.10**. The VAFs varied from 1.0 to 1.41 with an average value of 1.20. As described by McGrath (1998), the SRHDPE pipe behaved similarly to a corrugated steel pipe based on the vertical arching factor and the hoop stiffness. In addition, the vertical arching factors calculated using the Burns and Richard no-slip and full-slip solutions (**EQUATIONS 2.2** and **2.3**) resulted in VAFs of 1.39 and 1.01, respectively. In this calculation, the hoop stiffness needed for the Burns and Richard solutions was estimated using **EQUATION 2.4** based on the constrained modulus ($M_s = 3,900$ psi), of the backfill (i.e., the AB-3-II

aggregate), the radius of the pipe (36 in.), the area of the steel reinforcement (0.056 in.²/ft.), and the modulus of elasticity of the steel reinforcement (29,000 ksi). The constrained modulus, M_s , of the AB-3-II aggregate was back-calculated from the modulus of elasticity of the AB-3-II aggregate determined from the small plate loading test as described in **SECTION 3.2.2**. The vertical arching factors (VAF) from the measurement of the earth pressures on the crown were in between the vertical arching factors obtained from the Burns and Richard solutions for the no-slip and full-slip cases as shown in **FIGURE 6.10**. Therefore, the SRHDPE pipe should be designed based on a no-slip condition to be conservative for the VAF value.

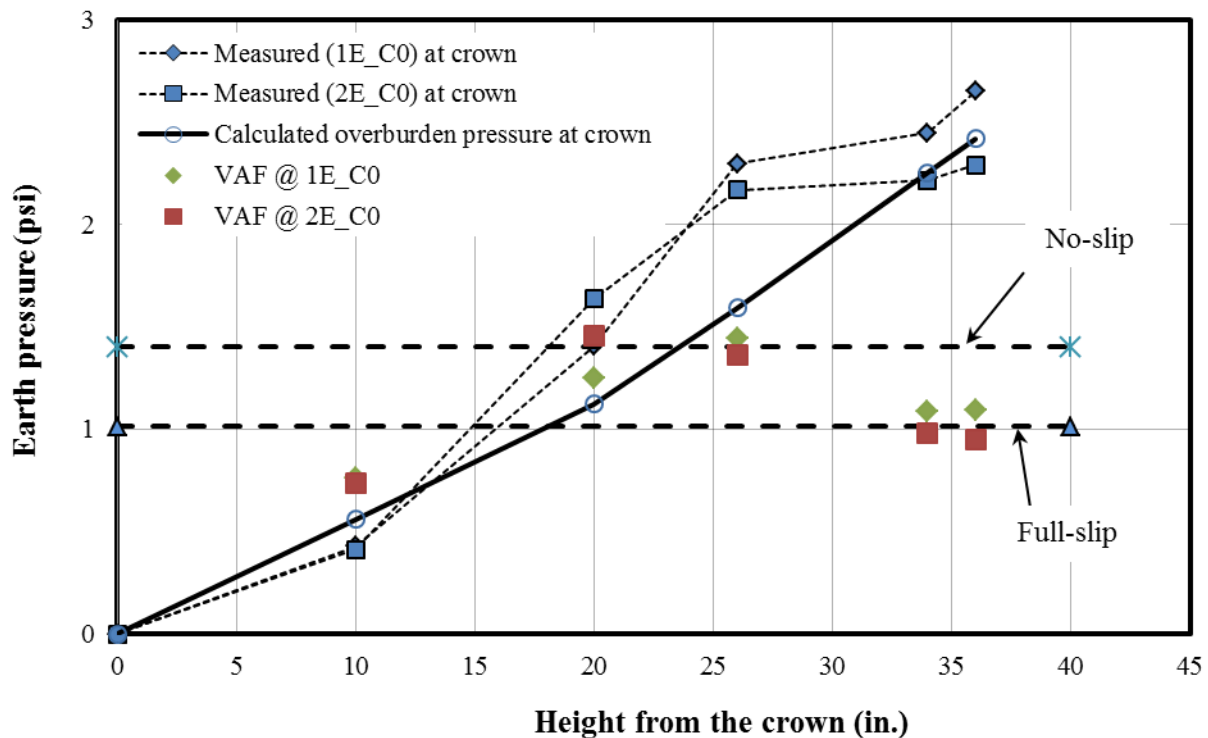


FIGURE 6.10 Comparison of measured and calculated pressures at the crown during installation in Test Section A

FIGURE 6.11 shows the measured lateral pressures, E'_{s0} and E'_{sw} , at the springline near the pipe surface and at the trench wall and the calculated overburden pressures at the springline.

FIGURE 6.12a shows the coefficients of lateral earth pressure (K) at the springline calculated as the ratio of the measured lateral pressures to the calculated overburden pressures. The lateral earth pressure coefficients were higher at the level of construction 4 (i.e., at the pipe crown) and decreased with the increased fill height. After the level of construction 6, the lateral pressures coefficients leveled. This type of behavior was also observed in the laboratory test results as discussed in **SECTION 6.1.1.1**. **FIGURE 6.12b** compares the measured coefficients at the springline with the lateral earth pressure coefficient (K_p) calculated using the friction angle and the cohesion of the AB-3-II aggregate. The friction angle of 52.4° and cohesion of 1.4 psi of the AB-3 aggregate reported by Yang (2010) was used for the calculation of the passive earth pressure coefficient using the Rankine pressure coefficient with cohesion. The measured coefficients (K) were found to be much lower than the Rankine passive pressure coefficient (K_p).

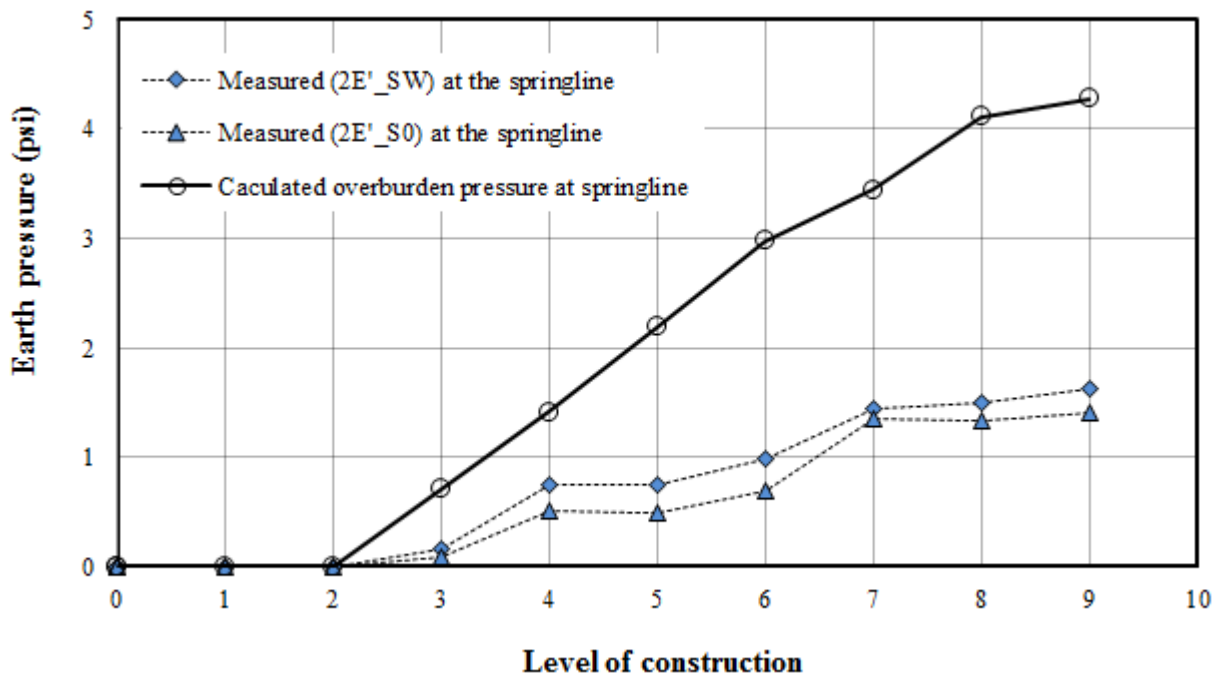
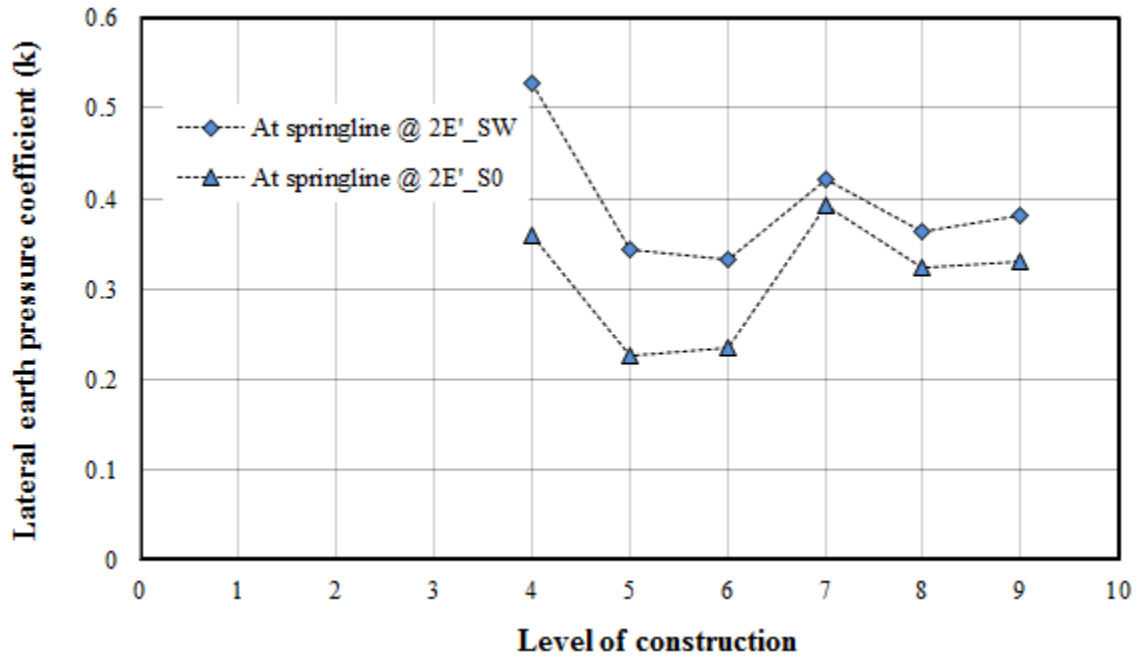
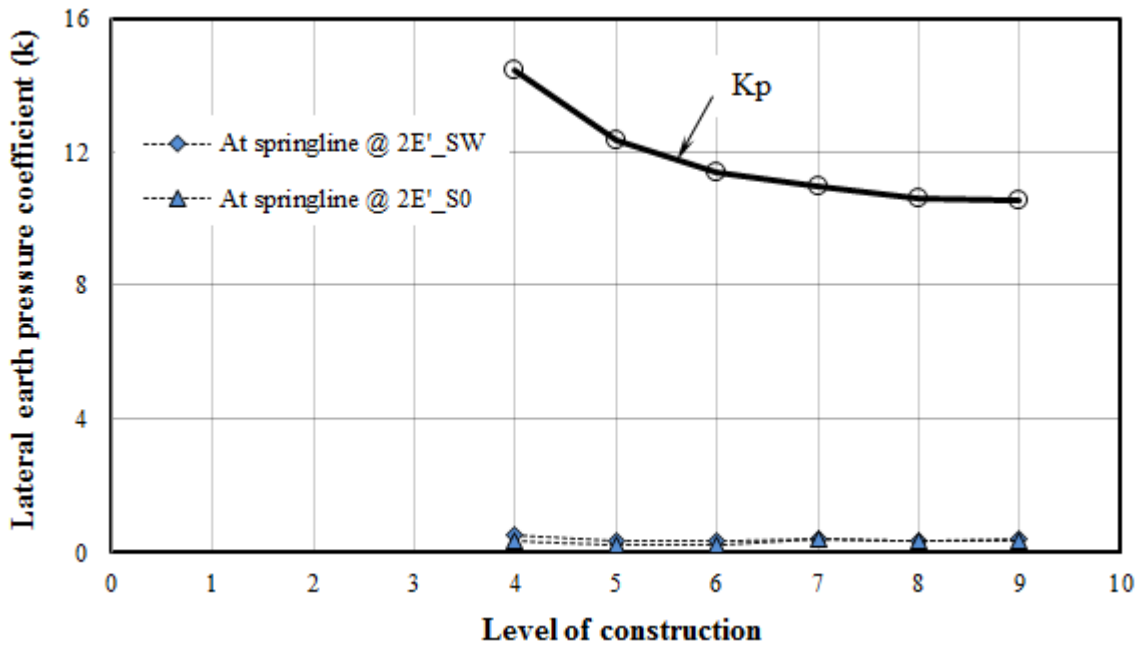


FIGURE 6.11 Measured and calculated lateral earth pressures at the springline in Test Section A



(a) Lateral earth pressure coefficients at the springline



(b) Comparison to the passive lateral earth pressure coefficients (K_p)

FIGURE 6.12 Lateral earth pressure coefficients (K) at the springline in Test Section A

Section B. **FIGURE 6.13** shows the earth pressures developing around the pipes against the levels of construction (labeled as 1 to 9 as shown in **FIGURE 5.29**). The earth pressure cells, E_{C0} and E_{C12} , fixed at the crown and 12 in. away from the crown measured similar earth pressures during the installation. The vertical pressure recorded by the pressure cell fixed at the invert (E_{I0}) was lower than the pressures measured at the pipe crown.

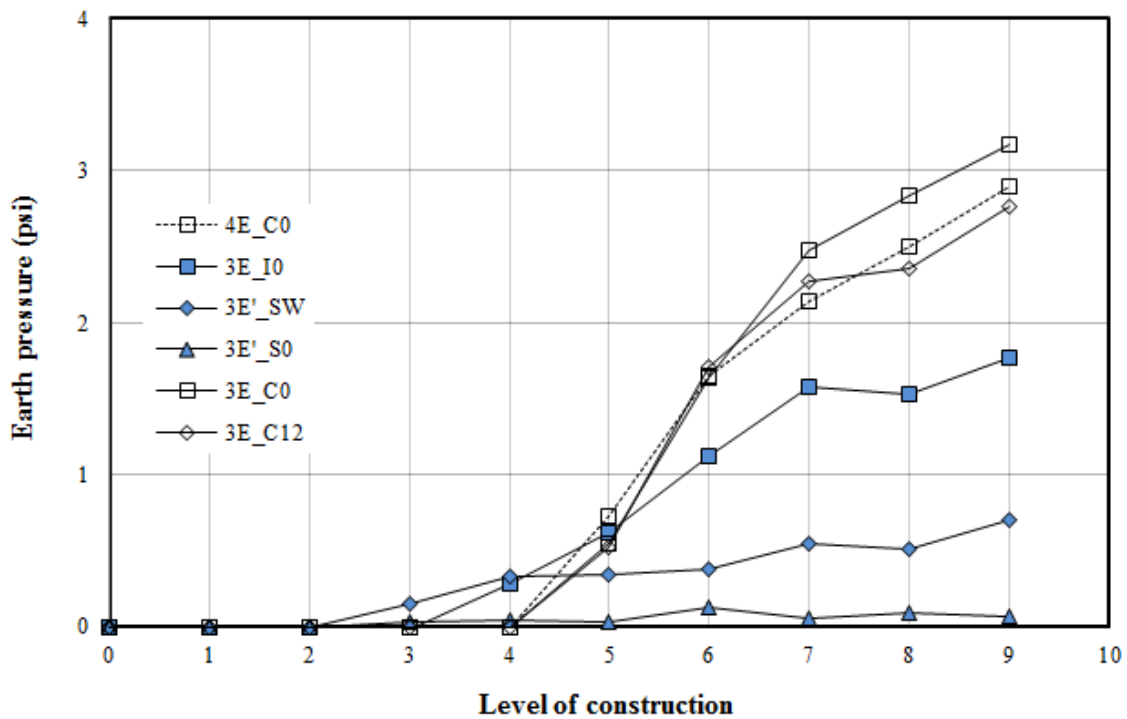


FIGURE 6.13 Measured earth pressures around the pipe during installation in Test Section B

The overburden pressure $E_{C0, cal}$ (i.e., the unit weight of the soil (γ_s) x the thickness of the soil from the crown (H)) was calculated at the crown of the pipe. The vertical earth pressures measured at the crown by the earth pressure cells ($1E_{C0}$ and $2E_{C0}$) were then compared with the

calculated overburden vertical pressure and are shown in **FIGURE 6.14**. The vertical arching factors (VAFs), calculated as the ratio of the measured pressure to the calculated pressure at the crown, are shown in **FIGURE 6.14**. The VAFs varied from 0.97 to 1.21 with average value of 1.1. As described by McGrath (1998), the SRHDPE pipe behaved similarly to a corrugated steel pipe based on the vertical arching factor and the hoop stiffness. In addition, the vertical arching factors calculated using the Burns and Richard no-slip and full-slip solutions (**EQUATIONS 2.2** and **2.3**) resulted in VAFs of 1.41 and 1.02, respectively. In this calculation, the hoop stiffness needed for the Burns and Richard solutions was estimated using **EQUATION 2.4** based on the constrained modulus ($M_s = 2,520$ psi) of the backfill (i.e., the crushed stone, CS-II), the radius of the pipe (36 in.), the area of the steel reinforcement (0.3575 in²/ft.), and the modulus of elasticity of the steel reinforcement (29,000 ksi). The constrained modulus, M_s , of the crushed stone (CS-II) was back-calculated from the modulus of elasticity determined from the small plate loading test as described in **SECTION 3.2.2**. The vertical arching factors (VAFs) from the measurement of the earth pressures on the crown were in between the vertical arching factors obtained from the Burns and Richard solutions for the no-slip and full slip cases as shown in **FIGURE 6.14**. Therefore, the SRHDPE pipe should be designed based on a no-slip condition to be conservative for the VAF value.

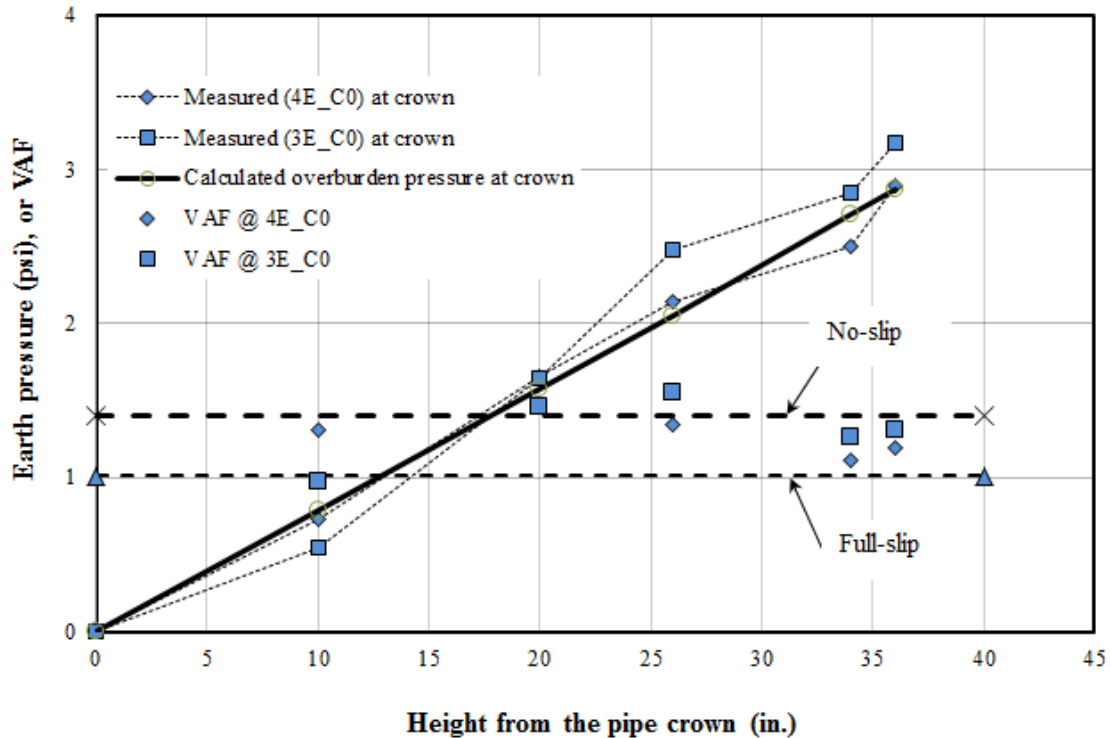


FIGURE 6.14 Comparison of measured and calculated pressures at the crown during installation in Test Section B

FIGURE 6.15 shows the measured lateral pressures, E'_{s0} and E'_{sw} , near the pipe surface and at the trench wall and the calculated overburden pressures at the springline. **FIGURE 6.16a** shows the coefficients of lateral earth pressure (K) at the springline calculated as the ratio of the measured lateral pressures to the overburden pressures. **FIGURE 6.16b** compares the measured coefficients at the springline with the lateral earth pressure coefficients, K_a , K_o , and K_p , calculated using the friction angle of the crushed stone (CS-II) of 60° . The friction angle (ϕ) of the crushed stone (CS-II) at 89% relative density (RD) (i.e., field density) was calculated using **EQUATION 6.1** developed by Theyse (2002) for his particular crushed stone.

$$\phi = 9.39 + 55.98 \times RD - 7.93S \quad 6.1$$

where S is the degree of saturation.

The measured coefficients (K) were found to be close to K_0 . The coefficient (K) was the highest at level 4 (i.e., when the fill height reached the crown of the pipe) and then decreased to a value close to the coefficient K_0 . The higher values of the coefficients (K), when the construction levels were close to the pipe, may be due to the higher effect of the compaction on the pipe.

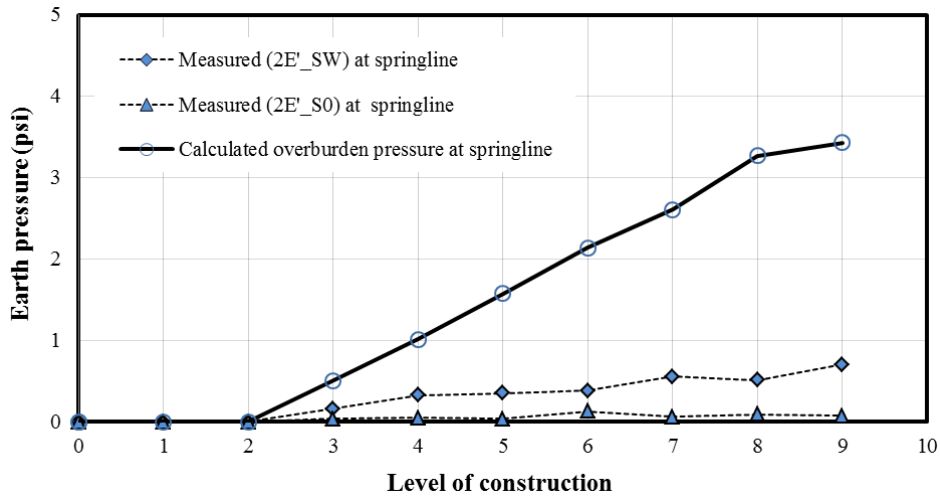
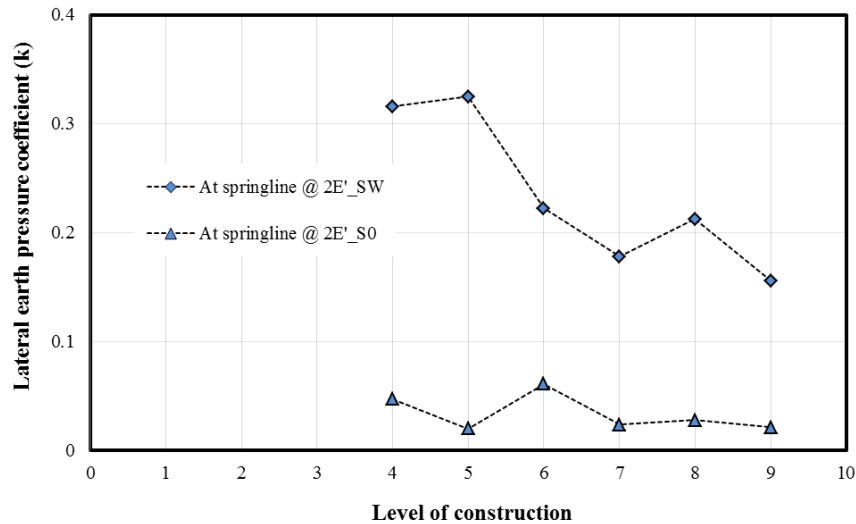
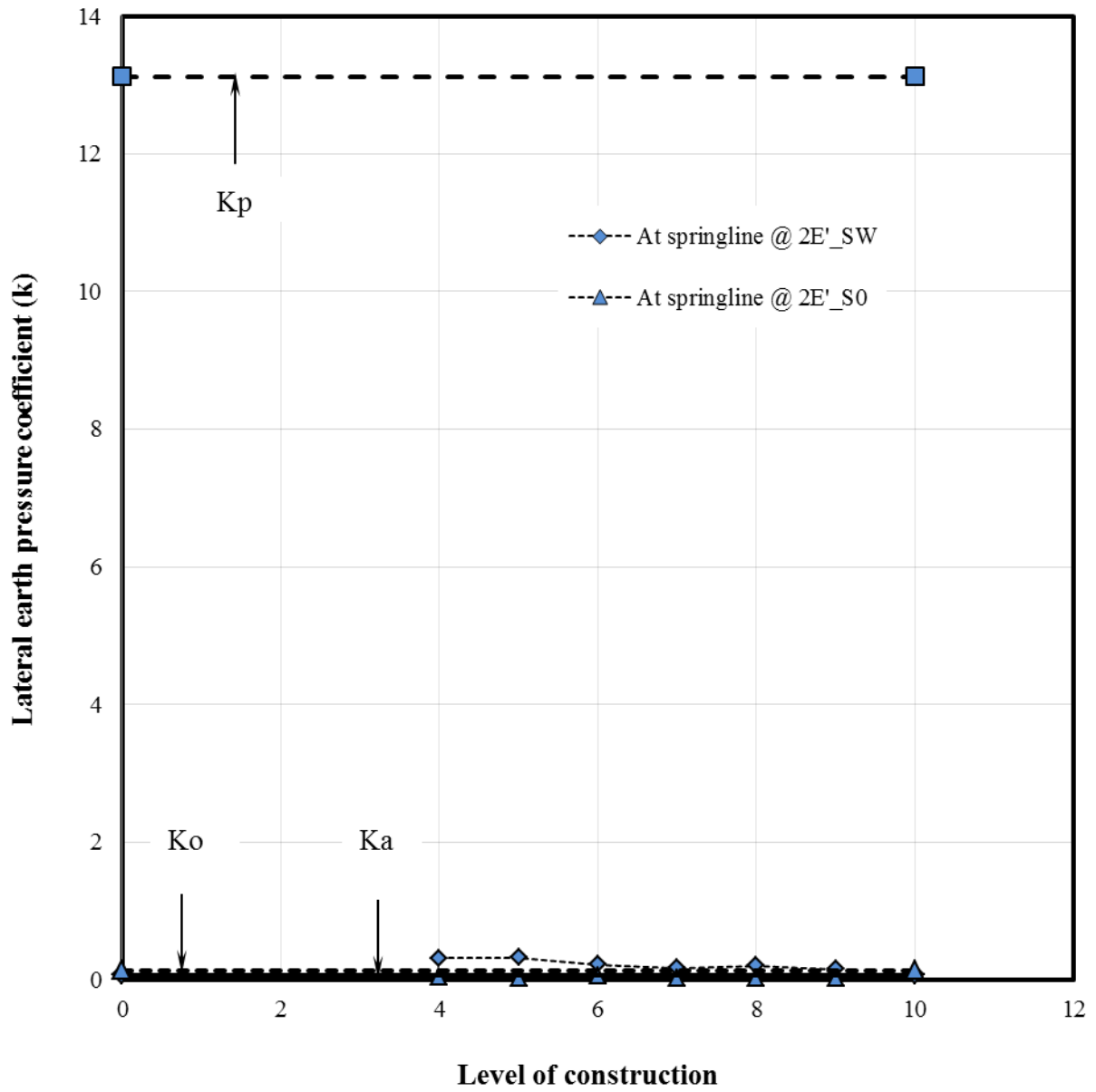


FIGURE 6.15 Measured lateral and overburden pressures at the springline in Test Section B



(a) Lateral earth pressure coefficient at the springline

FIGURE 6.16 Lateral earth pressure coefficients (K) at the springline in Test Section B



(b) Comparison to the active, at rest, and passive lateral earth pressure coefficients

FIGURE 6.16 Lateral earth pressure coefficients (K) at the springline in Test Section B

(continued)

Comparison and Summary

The earth pressures measured around the pipe in the field against the levels of construction had similar trends to the earth pressures measured around the pipe in the laboratory tests. However, the vertical pressures recorded by the pressure cells fixed at the invert (E_{10}) varied from negative in Test 1 to very high values relative to other pressure cells around the pipes in Test 3 (in the laboratory test) and in Test Section A in the field test. As discussed above in **SECTION 6.1.1**, the negative values at the invert were due to the lifting of the pipe because of the compaction at the haunch of the pipe whereas high pressures at the invert were due to the concentrated load at the invert along the pipe run because of possibly non-uniform bedding. Therefore, to reduce the concentrated stress at the invert of SRHDPE pipes, the 2007 KDOT Pipe and Culvert Specifications practice of not compacting the middle 33% of the bedding material is appropriate. In addition, the uplifting of SRHDPE pipes can be reduced by compacting backfills lightly up to the springline.

The VAFs varied from 1.00 to 1.41 for all the backfills both in the laboratory and field tests. As described by McGrath (1998), the SRHDPE pipe behaved similarly to a corrugated steel pipe based on the vertical arching factor range obtained in the tests and the hoop stiffness of the pipes. In addition, the calculated VAFs were found to be close to no-slip or in between no-slip to full-slip Burns and Richard solutions (**EQUATIONS 2.2** and **2.3**). Therefore, the SRHDPE pipe should be designed based on a no-slip condition to be conservative for the VAF value.

The lateral earth pressure coefficients (K) for both laboratory and field tests were the highest at level 4 (i.e., when the fill height reached the crown of the pipe) and then decreased to a value close to the coefficient K_0 . The higher values of the coefficients (K), when the

construction levels were close to the pipe, may be due to the effect of the compaction on the pipe. Therefore, it can be concluded that the lateral pressure generated by the backfill soil should be represented by a combination of lateral earth force due to the backfill and a force generated by the compaction effort during the backfilling.

6.1.2 Deflection Results

Laboratory Tests

Test 1. The deflections of the pipe (or the changes in the inside diameters) against the levels of construction are shown in **FIGURE 6.17**. The pipe exhibited peak deflections during the backfilling. When the backfill height was at the same elevation with the pipe crown, the vertical diameter was increased by an average of 0.27 in. (1.14%) while the horizontal diameter was reduced by an average of 0.26 in. (-1.10%). When the compaction of the lifts was above the pipe crown, the vertical diameter started decreasing and the horizontal diameter started increasing as the compaction commenced further. At the end of the construction of the test section, the net increase in the vertical diameter and the decrease in the horizontal diameter (ΔD_{VC} and ΔD_{HC}) were 0.20 in. (0.86%) and 0.21 in. (0.89%), respectively. The vertical deflection of the pipe (ΔD_{VC}) was approximately equal to horizontal deflection (ΔD_{HC}) during the installation of the pipe as shown in **FIGURE 6.18**. During the initial backfilling, the pipe started being lifted upward until the backfilling reached the crown and then started moving downward as the compaction continued. The pipe was lifted by a maximum of 1.23 in. during the initial backfilling.

The peak deflection calculated using **EQUATION 2.10** proposed by Masada and Sargand (2007) was 1.28 %, which was close to the measured peak deflection (1.14%). The

lateral pressure (P_c) generated by the rammer compaction for the sand backfill as 0.39 psi/in. was selected from **TABLE 2.4** to calculate the peak deflection. The lateral earth pressure coefficient at rest (K_o) was calculated as $K_o = 1 - \sin \phi$, where ϕ is the friction angle of 37° . The horizontal deflection of the pipe (ΔD_{HC}) measured during the backfilling was also compared with the Iowa formula using **EQUATION 2.8** as shown in **FIGURE 6.19**. The bedding constant (k) of 0.1, the VAF of 1.26 (calculated in **SECTION 5.1.1**), the unit weight of the sand (113 pcf), and the modulus of elasticity of 2,027 psi were used to calculate the horizontal deflection (ΔD_{HC}). In the horizontal deflection calculation, the effect of the compaction effort on the pipe during the installation was ignored because of the unknown pressure increase caused by the compaction equipment during the installation of the pipe. The measured horizontal deflections (ΔD_{HC}) were higher than the calculated. The higher horizontal deflections might not include the effect of the compaction effort during the installation in the vertical deflection calculation.

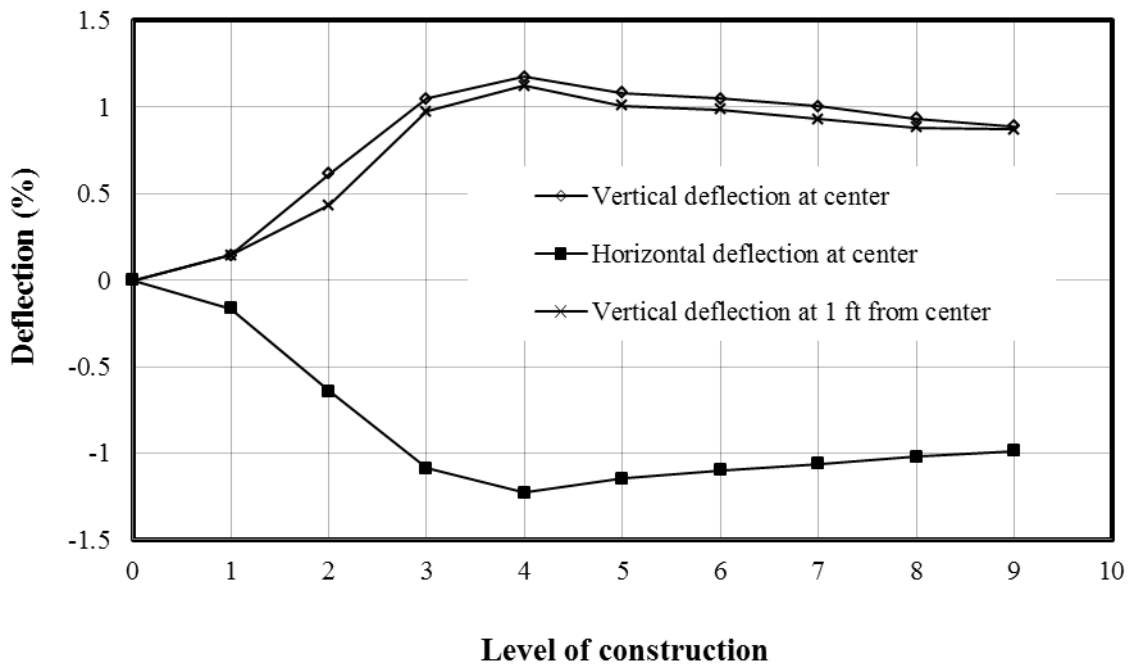


FIGURE 6.17 Measured deflections of the pipe during the installation in Test Section 1

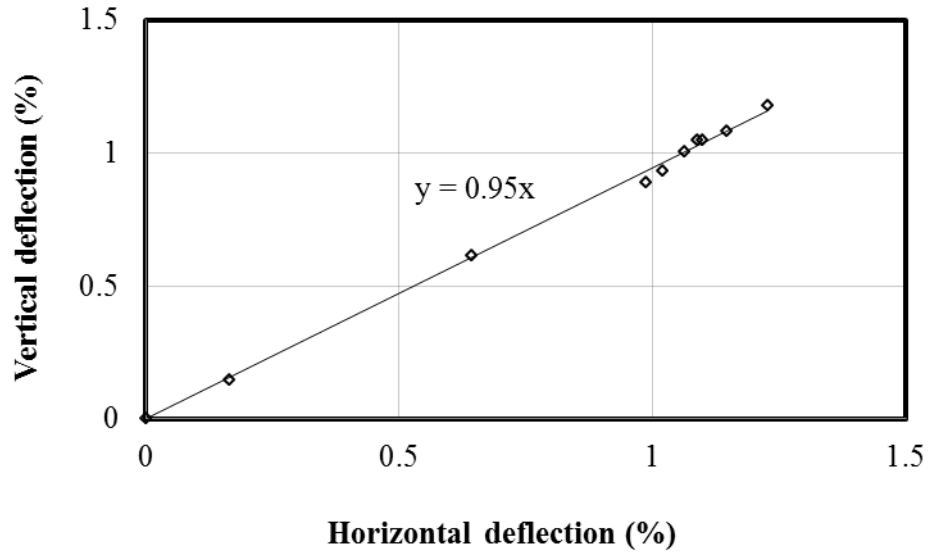


FIGURE 6.18 Relations between the measured vertical and horizontal deflections during the installation in Test Section 1

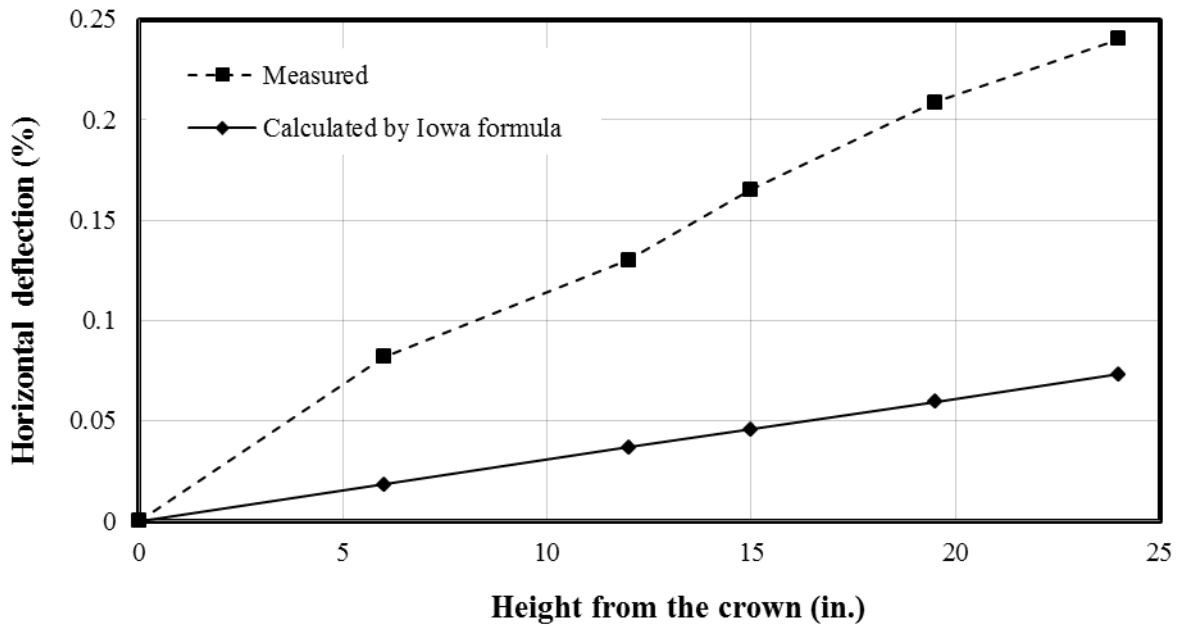


FIGURE 6.19 Comparison of the measured and calculated horizontal deflections by the Iowa formula in Test Section 1

Test 3. The deflections of the pipe (or the changes in the inside diameters) against the levels of construction are shown in **FIGURE 6.20**. Similar to the pipe installed with the sand as the backfill, the pipe exhibited peak deflections during backfilling. When the backfill height was at the same elevation with the pipe crown, the vertical diameter (ΔD_{VC}) was increased by an average of 0.050 in. (0.21%) while the horizontal diameter (ΔD_{HC}) was reduced by an average of 0.057 in. (-0.24%). When the backfilling was above the pipe crown, the vertical diameter (ΔD_{HV}) started decreasing and the horizontal diameter (ΔD_{HC}) started increasing as the backfilling commenced further. At the end of the construction of the test section, the net decrease in the vertical diameter and the increase in the horizontal diameter (ΔD_{VC} and ΔD_{HC}) were 0.007 in. (-0.03%) and 0.014 in. (0.06%), respectively. The ratio of the vertical deflection of the pipe to the horizontal deflection ($\Delta D_{VC} / \Delta D_{HV}$) was equal to 0.85 on average during the installation of the pipe as shown in **FIGURE 6.21**. The pipe was not lifted up during the initial backfilling by dumping the crushed stone (CS-I).

The peak deflection calculated using **EQUATION 2.10** proposed by Masada and Sargand (2007) was 0.08 %, which was lower to the measured peak deflection of 0.21%. The Masada and Sargand (2007) equation underestimated the peak deflection. The lateral earth pressure coefficient at rest (K_o) calculated as $K_o = 1 - \sin \phi$, where ϕ is the friction angle with the value of 54° , was used to calculate the peak deflection. The horizontal deflection measured (ΔD_{HC}) during the backfilling was also compared with the Iowa formula using **EQUATION 2.8** as shown in **FIGURE 6.22**. The bedding constant (K) of 0.1, a VAF of 1.26 (calculated in **SECTION 5.1.1**), the unit weight of the crushed stone, and the modulus of elasticity (1,125 psi) were used to calculate the horizontal deflection. The calculated horizontal deflections (ΔD_{HC}) were close to the measured deflections.

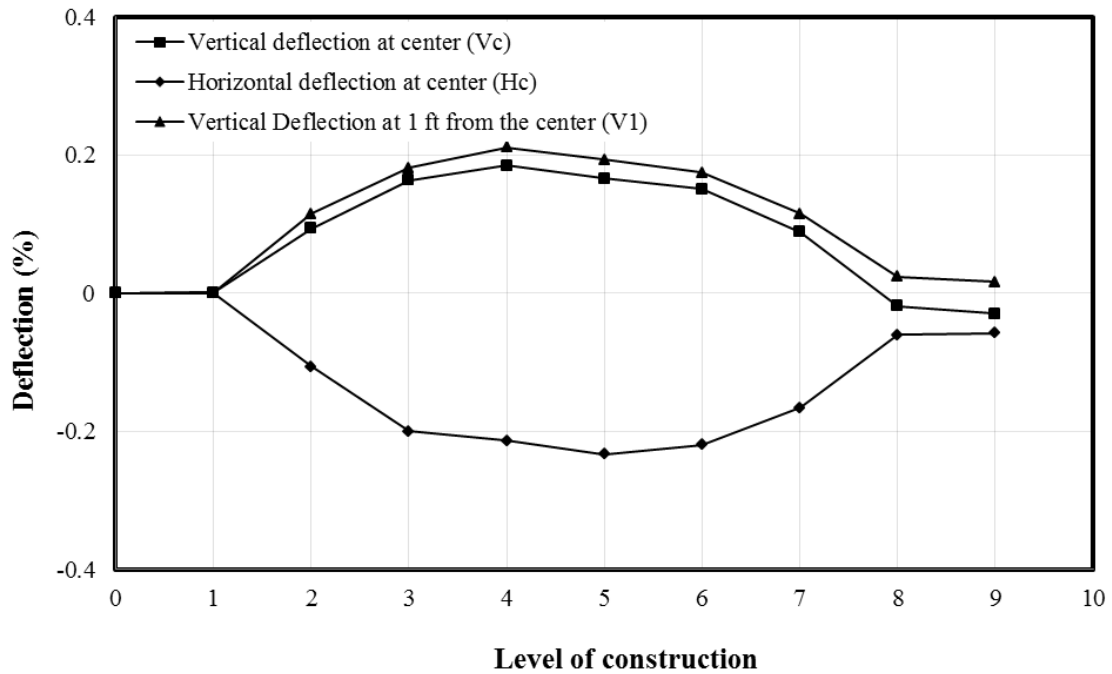


FIGURE 6.20 Measured deflections of the pipe during the installation in Test Section 3

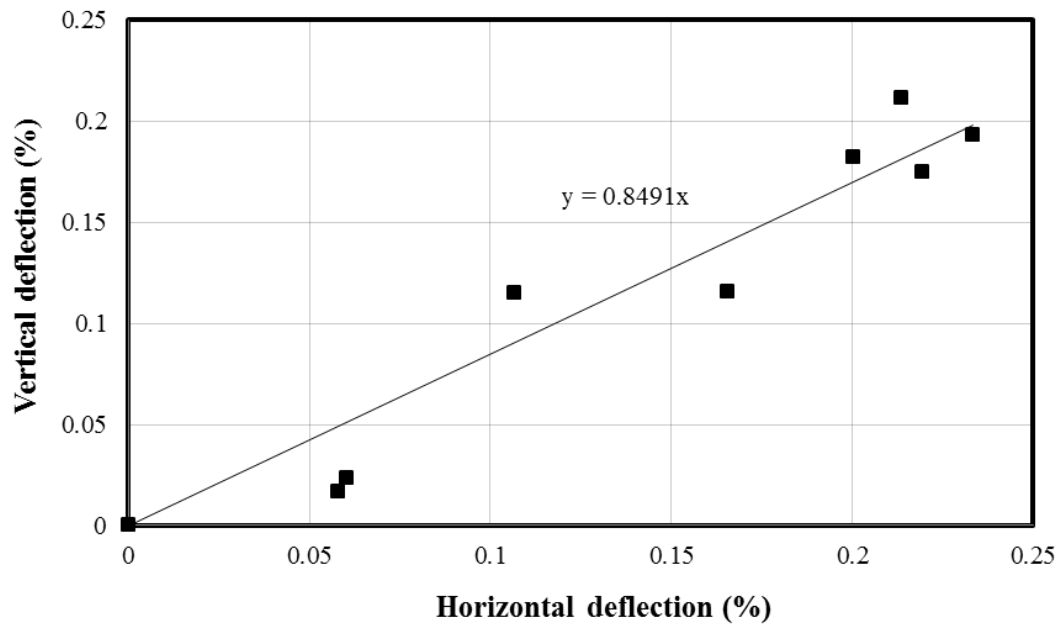


FIGURE 6.21 Relations between the measured vertical and horizontal deflections during the installation in Test Section 3

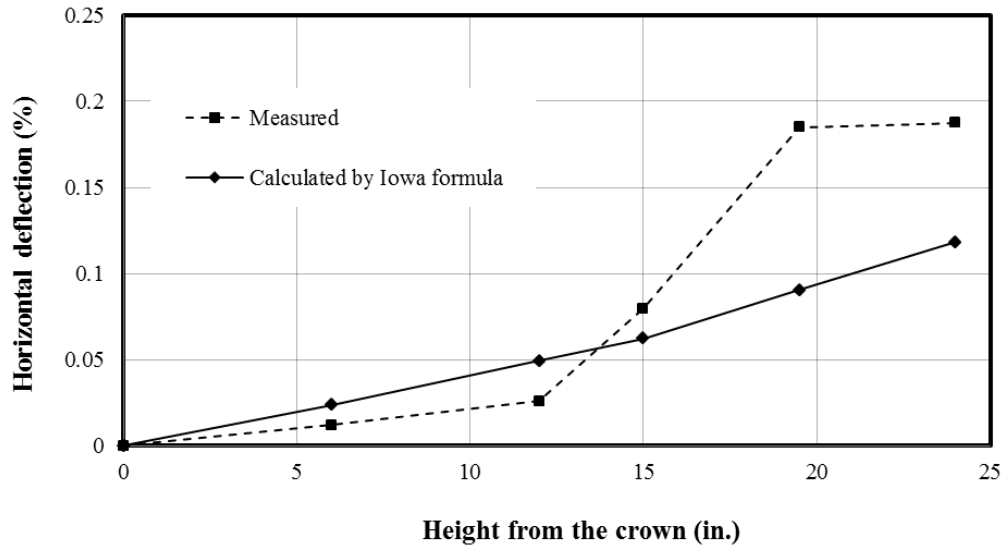


FIGURE 6.22 Comparison of the measured and calculated horizontal deflections by the Iowa formula in Test Section 3

Field Installation Test

Section A. The deflections of the pipe (or the changes in the inside diameters) against the levels of construction in Test Section A of the field test had similar behavior to the deflections of the pipes in the laboratory tests. The pipe exhibited peak deflections during the backfilling as shown in **FIGURE 6.23**. When the backfill height was at the same elevation with the pipe crown, the vertical diameter (ΔD_{VC}) was increased by an average of 0.15 in. (0.41%) while the horizontal diameter (ΔD_{HC}) was reduced by an average of 0.20 in. (-0.56%). When the compaction of the lifts was above the pipe crown, the vertical diameter (ΔD_{VC}) started decreasing and the horizontal diameter (ΔD_{HC}) started increasing as the compaction commenced further. At the end of the construction of the test section, the net decreases in the vertical and horizontal diameters (ΔD_{VC} and ΔD_{HC}) were 0.0015 in. (-0.0044%) and 0.095 in. (0.269%), respectively. The vertical deflection of the pipe (ΔD_{VC}) was approximately equal to horizontal deflection (ΔD_{HC}) during the backfilling up to the pipe crown as shown in **FIGURE 6.24**.

The peak deflection calculated using **EQUATION 2.10** proposed by Masada and Sargand (2007) was 1.37 %, which was higher to the measured peak deflection (0.43%). The lateral pressure (P_c) generated by the rammer compaction for the sand backfill as 0.39 psi/in. was selected from **TABLE 2.4** even for the AB-3-II to calculate the peak deflection. The contribution of the backfill cohesion to the peak deflection was neglected. The horizontal deflection of the pipe (ΔD_{HC}) measured during the backfilling was also compared with the horizontal deflection calculated using the Iowa formula, **EQUATION 2.8**, as shown in **FIGURE 6.25**. The bedding constant (k) of 0.1, the VAF of 1.20 (calculated in **SECTION 6.1.1.1**), the unit weight of the AB-3-II aggregate (136 pcf), and the modulus of elasticity of 2,675 psi were used to calculate the horizontal deflection (ΔD_{HC}). In the horizontal deflection calculation, the effect of the compaction effort on the pipe during the installation was ignored because of the unknown pressure increase caused by the compaction equipment during the installation of the pipe. The measured horizontal deflections (ΔD_{HC}) were higher than the calculated. The higher horizontal deflections might not include the effect of the compaction effort during the installation in the horizontal deflection calculation.

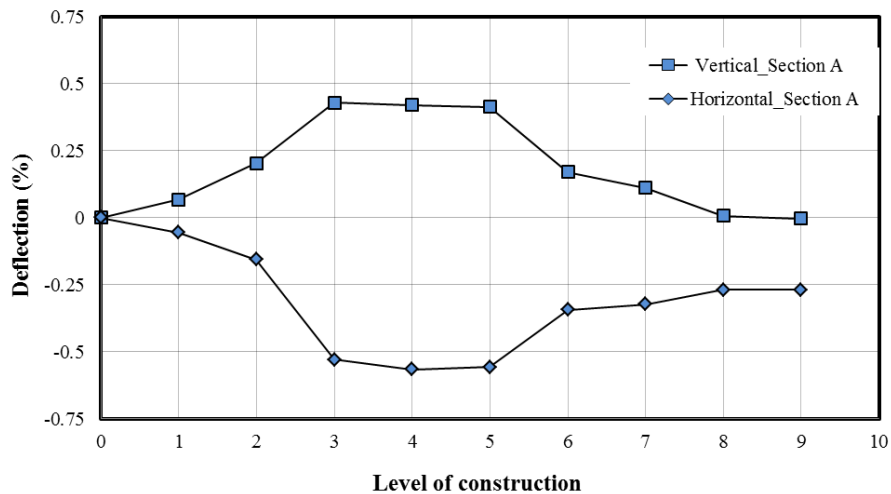


FIGURE 6.23 Measured deflections of the pipe during the installation in Test Section A

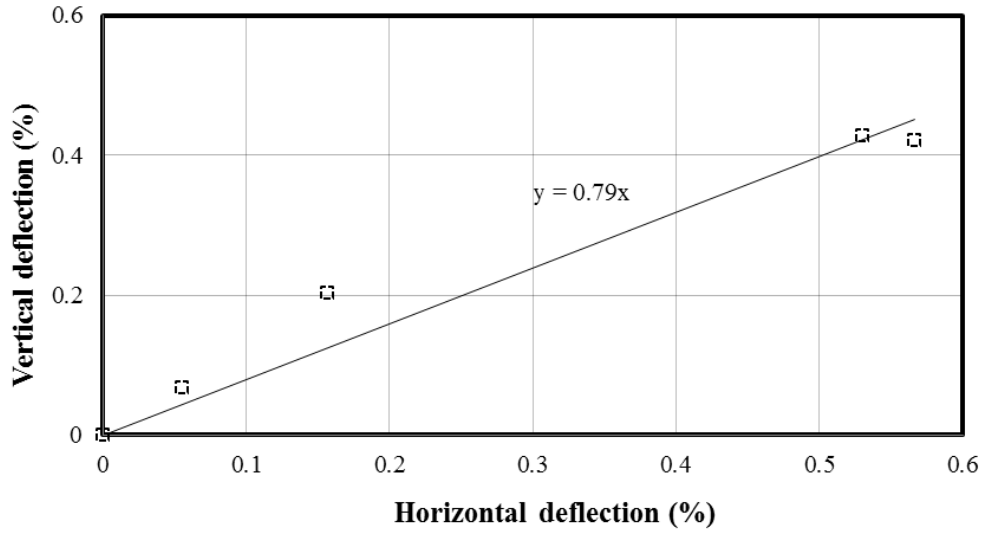


FIGURE 6.24 Relations between the measured vertical and horizontal deflections during the installation in Test Section A

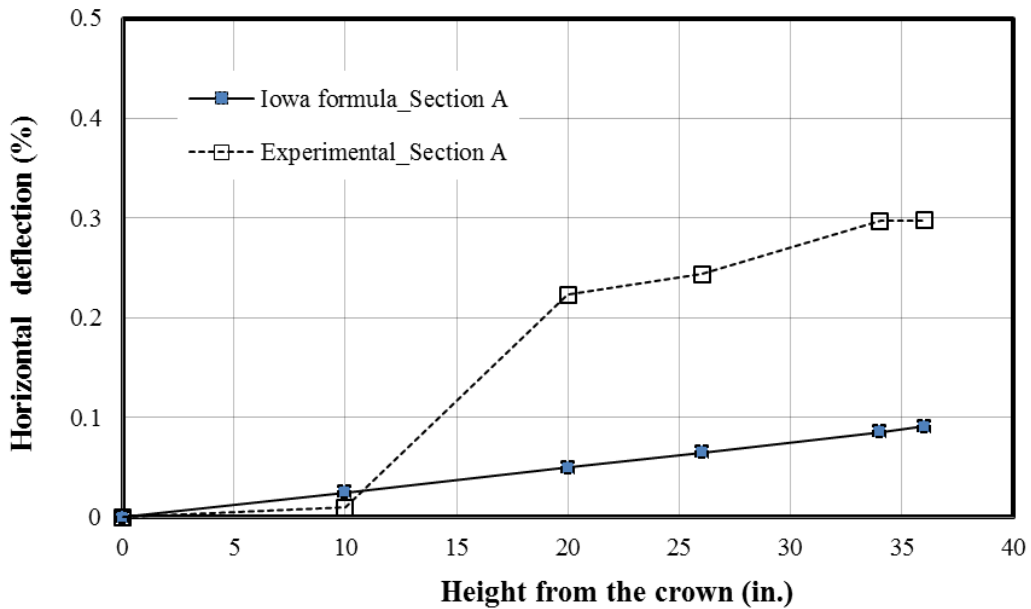


FIGURE 6.25 Comparison of the measured and calculated horizontal deflections by the Iowa formula in Test Section A

To investigate the damage caused by the compactors and construction vehicles to the pipe, the data were continuously recorded once the pipe was placed in the trench. The

displacement transducers which were instrumented to measure the deflections of the pipe were selected to collect the response of the pipe during the construction of the test sections. The data sample interval of 10 msec was set on the transducers to read the immediate response of the pipe. The response of the pipe using other sensors such as the pressure cells and the strain gages were collected at 1 minute intervals. During the installation of the pipe, the maximum deflections of the pipe caused by the tamping hammer, Multiequip MT65H, were noticed during the backfill compaction at the shoulder as shown in **FIGURE 6.26** and during the compaction of the soil cover above the crown of the pipe (discussed earlier). **FIGURE 6.26** shows that the tamping hammer produced an immediate decrease in the horizontal diameter of around 0.23% and an increase in the vertical diameter of 0.19 %. The deformation response of the pipe was also collected when the smooth wheel vibratory roller, 2005 model Hamm HD13, was run above the top of the pipe before placing the HMA base as shown in **FIGURE 6.27**. The maximum immediate decrease in the vertical diameter of 0.08 % was measured.

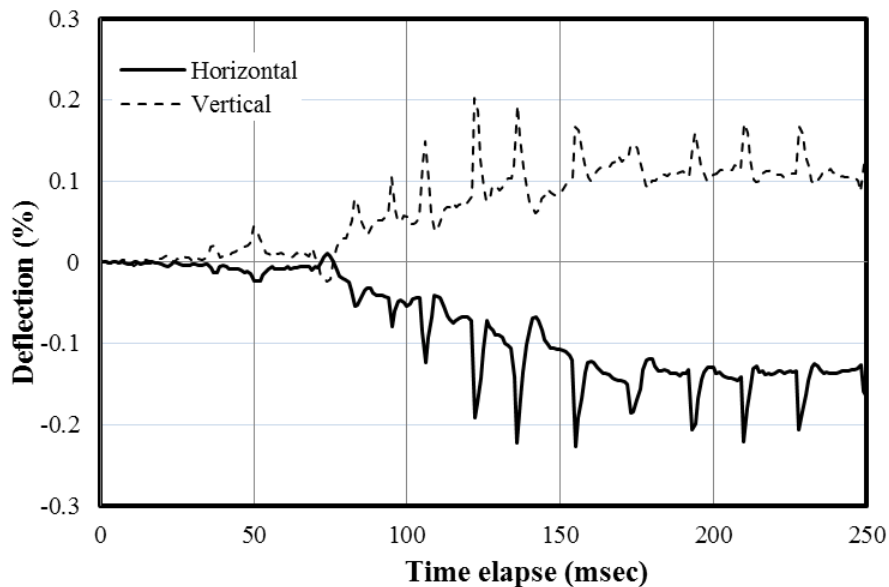


FIGURE 6.26 Deflection produced by the tamping hammer during the compaction at the pipe shoulder in Test Section A

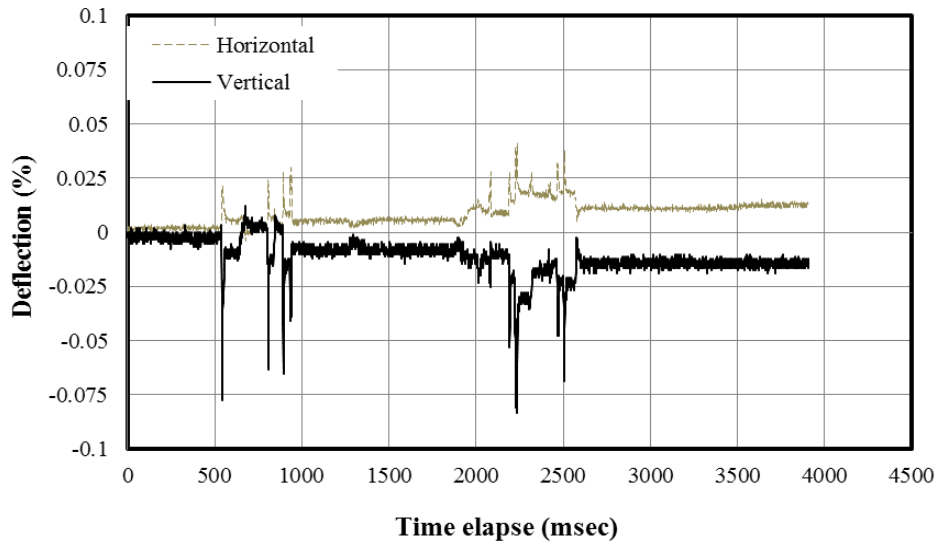


FIGURE 6.27 Deflection produced by the smooth wheel vibratory roller during the compaction before placing the HMA base in Test Section A

Section B. The deflections of the pipe during the backfilling of the pipe exhibited peak deflection similar to the deflections in all both laboratory and field tests discussed above and are shown in **FIGURE 6.28**. When the backfill height was at the same elevation with the pipe crown, the vertical diameter (ΔD_{VC}) was increased by an average of 0.3 in. (0.85%) while the horizontal diameter (ΔD_{HC}) was reduced by an average of 0.30 in. (-0.87%). When the compaction of the lifts was above the pipe crown, the vertical diameter (ΔD_{VC}) started decreasing and the horizontal diameter (ΔD_{HC}) started increasing as the compaction commenced further. At the end of the construction of the test section, the net increase in the vertical diameter and the decrease in the horizontal diameter (ΔD_{VC} and ΔD_{HC}) were 0.11 in. (0.30%) and 0.13 in. (-0.89%), respectively. The vertical deflection of the pipe (ΔD_{VC}) was approximately equal to the horizontal deflection (ΔD_{HC}) during the installation of the pipe as shown in **FIGURE 6.29**.

The peak deflection calculated using **EQUATION 2.10** proposed by Masada and Sargand (2007) was 0.37 %, which was lower than the measured peak deflection (0.87%). The lateral pressure (P_c) generated by the vibratory plate compactor for the crushed stone (CS-II) backfill as 0.0.6 psi/in. was selected from **TABLE 2.4** to calculate the peak deflection. The lateral earth pressure coefficient at rest (K_o) was calculated as $K_o = 1 - \sin \phi$, where ϕ is the friction angle of 52.4^0 . The horizontal deflection (ΔD_{HC}) of the pipe measured during the backfilling was also compared with the horizontal deflection using the Iowa formula, **EQUATION 2.8**, as shown in **FIGURE 6.30**. The bedding constant (k) of 0.1, the VAF of 1.10 (calculated in **SECTION 6.1.1.2b**), the unit weight of the crushed stone CS-II (97 pcf), and the modulus of subgrade reaction of 3,780 psi were used to calculate the horizontal deflection (ΔD_{HC}). In the horizontal deflection calculation, the effect of the compaction effort on the pipe during the installation was ignored because of the unknown pressure increase caused by the compaction equipment during the installation of the pipe. The measured horizontal deflections (ΔD_{HC}) were higher than the calculated. The higher horizontal deflections might not include the effect of the compaction effort during the installation in the horizontal deflection calculation.

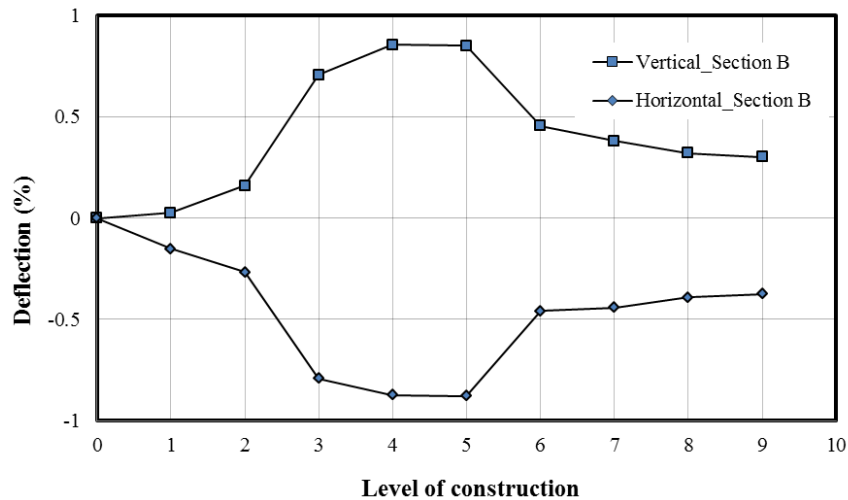


FIGURE 6.28 Measured deflections of the pipe during the installation in Test Section B

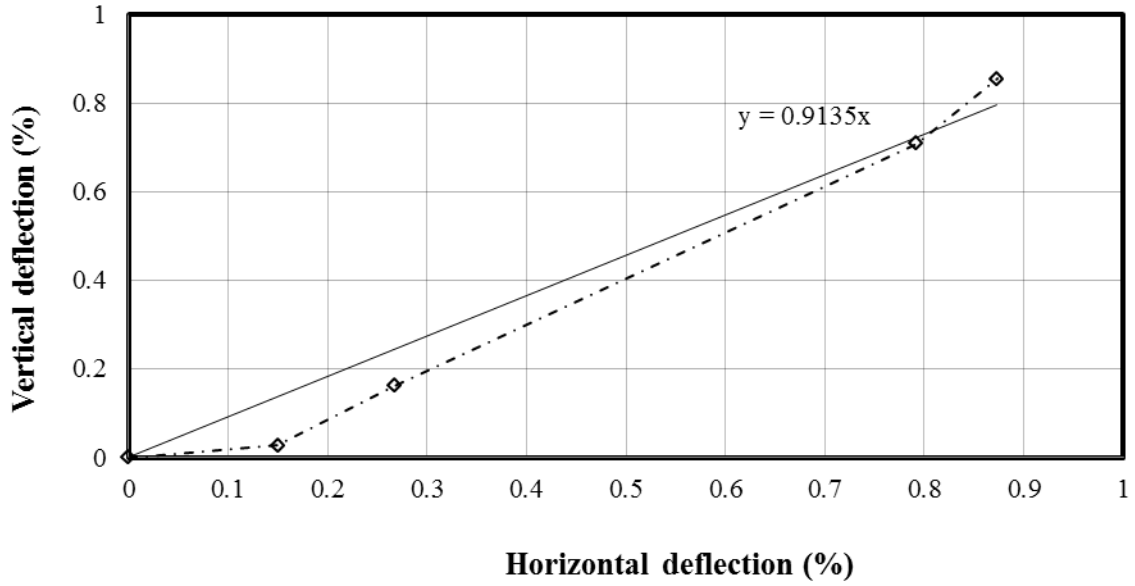


FIGURE 6.29 Relations between the measured vertical and horizontal deflections during the installation in Test Section B

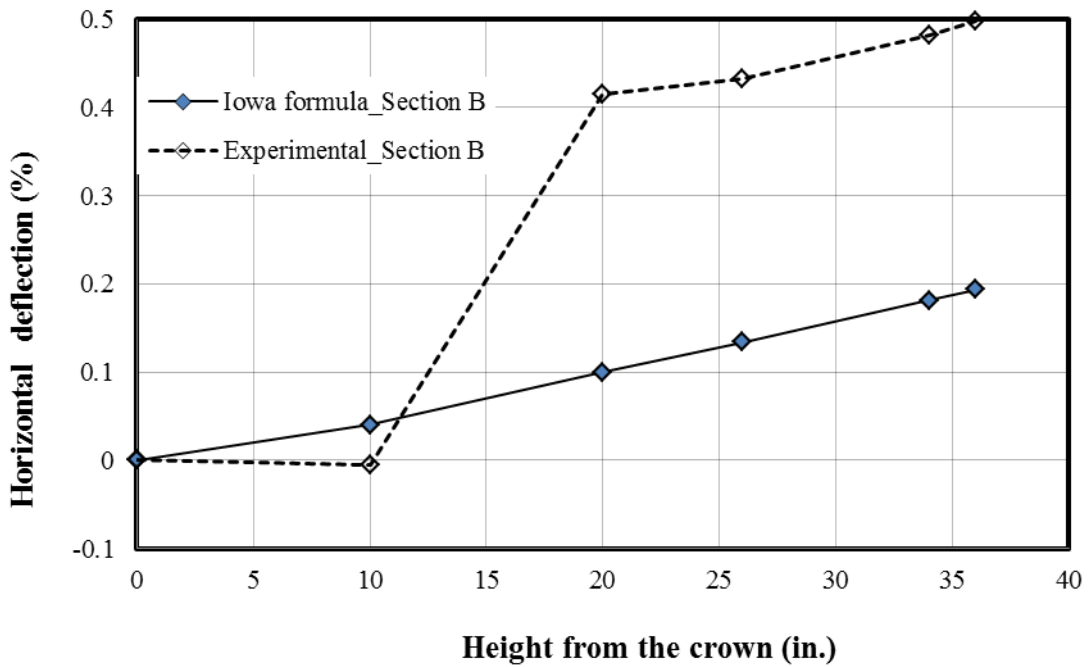


FIGURE 6.30 Comparison of the measured and calculated horizontal deflections by the Iowa formula in Test Section B

To investigate the damage caused by the compactors and construction vehicles to the pipe in Test Section B, the data were continuously recorded as described above for Test Section A. During the installation of the pipe, the maximum deflections of the pipe caused by the vibratory plate compactor, Wacker WP1550AW, were also noticed during the backfill compaction at the shoulder as shown in **FIGURE 6.31** and during the compaction of the soil cover above the crown of the pipe (discussed above). **FIGURE 6.31** shows that the deflection produced by the vibratory plate compactor in Test Section B was less than that produced by the tamping hammer in Test Section A. This indicates that the vibratory plate compactor was less severe to the pipe as compared to the tamping hammer. The deformation response of the pipe was also collected when the smooth wheel vibratory roller, 2005 model Hamm HD13, was run above the top of the pipe before placing the HMA base as in **FIGURE 6.32**. The maximum immediate decrease in the vertical diameter of 0.083 % was measured during the compaction using the smooth wheel vibratory roller.

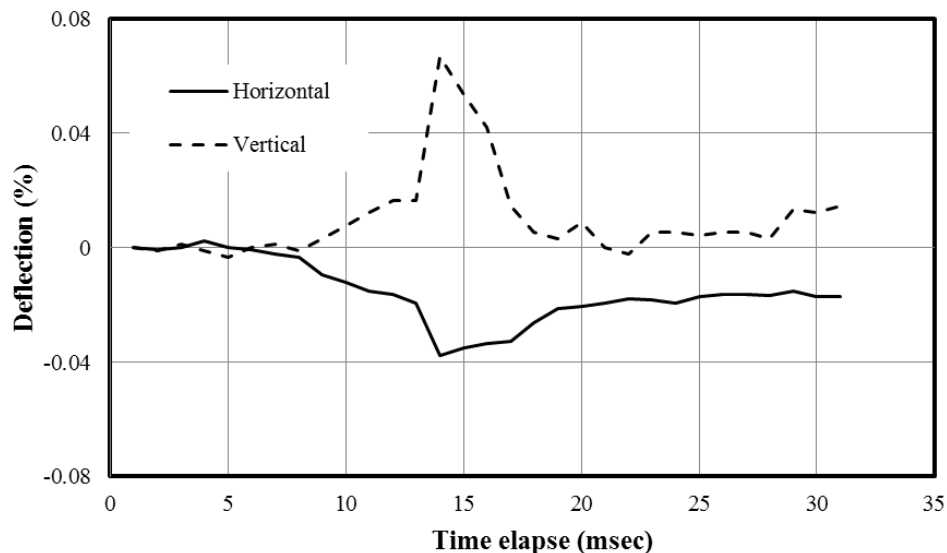


FIGURE 6.31 Deflection produced by the vibratory plate compactor during the compaction at the pipe shoulder in Test Section B

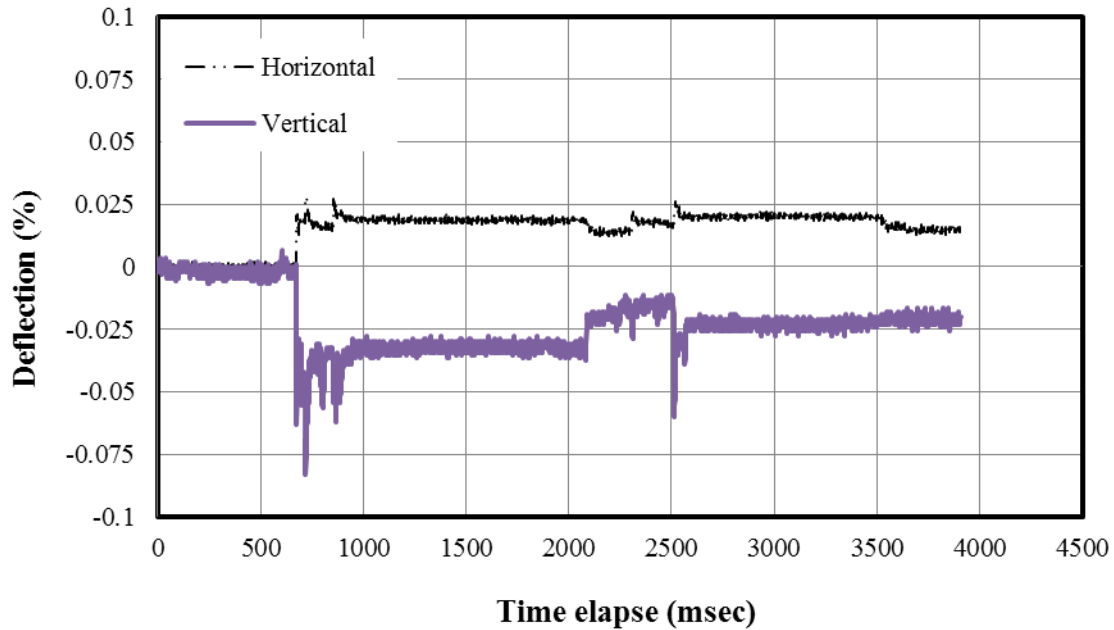


FIGURE 6.32 Deflection produced by the smooth wheel vibratory roller during the compaction before placing the HMA base in Test Section B

Comparison and Summary

The deflections of the pipe were monitored during the installation with various backfills, such as the KR sand, crushed stone (Dumped and compacted), and the AB-3-II aggregate, and during compaction using the vibratory plate compactor and the tamping hammer both in the laboratory and field tests. **FIGURE 6.33** shows the deflection of the pipe for all the tests conducted in both laboratory and field. The deflections of the pipe for all installation conditions showed the similar behavior with peaking vertical deflections when the backfills reached the pipe crown. The compaction of the soil cover directly on the top of the pipe was allowed in all installation cases for the first layer of soil above the pipe crown to prevent the damage on the pipes due to the compaction equipment. After the compaction of a first layer soil above the pipe crown, the section layer was then compacted even directly above the pipe crown. This is the

reason in **FIGURE 6.33** that there was a decrease in the vertical deflections and an increase in the horizontal deflections after the construction level 4. In other words, the forces induced by the compaction equipment directly above the pipe crown produced the changes in the diameters of the pipe. The highest deflections of 1.17 % to diameter occurred when the KR sand, which was used as backfill, was compacted at 70 % relative density using the tamping hammer in the laboratory test. The deflection produced in the field test with the crushed stone (CS-II) as backfill compacted at 89 % relative density showed the second highest deflection of the pipe. In addition, the immediate deflection of the pipe under the compaction equipment, such as the vibratory plate compactor and the tamping hammer, and construction vehicles in the field including the excavator, the bobcat, the smooth wheel vibratory roller, and the dumped truck etc. were measured and it was found that the deflections on the pipe were not significant as described in **SECTION 6.1.1** (see **FIGURES 6.26, 6.27, 6.31, and 6.32**). The deflection produced by the dumped truck was discussed in **SECTION 6.2** later. The deflections produced in all installation cases for the SRHDPE pipe were much less than the permissible deflection of 7.5 % according to the KDOT pipe and culvert specification (2007) for the polyethylene and polyvinyl chloride pipe.

The peak deflections, calculated using **EQUATION 2.10** proposed by Masada and Sargand (2007) with the lateral pressure generated by the compaction equipment from McGrath et al. (1999), were found to be unconservative for most of the installation cases as discussed above. **FIGURE 6.34** shows the comparison of the calculated and measured horizontal deflections of the pipe during the installation both in the laboratory and field tests. The measured horizontal deflections were higher than those calculated using the Iowa formula (**EQUATION 2.8**). The higher horizontal deflections might not include the effect of the

compaction effort applied during the installation in the horizontal deflection calculation as discussed in SECTION 6.1.2. The above statement may be true since the measured deflections of the pipe were increased sharply as the fill height reached approximately 10 in. (from the pipe crown) at which the backfill soils above the crown were compacted with the compaction equipment directly above the pipe crown.

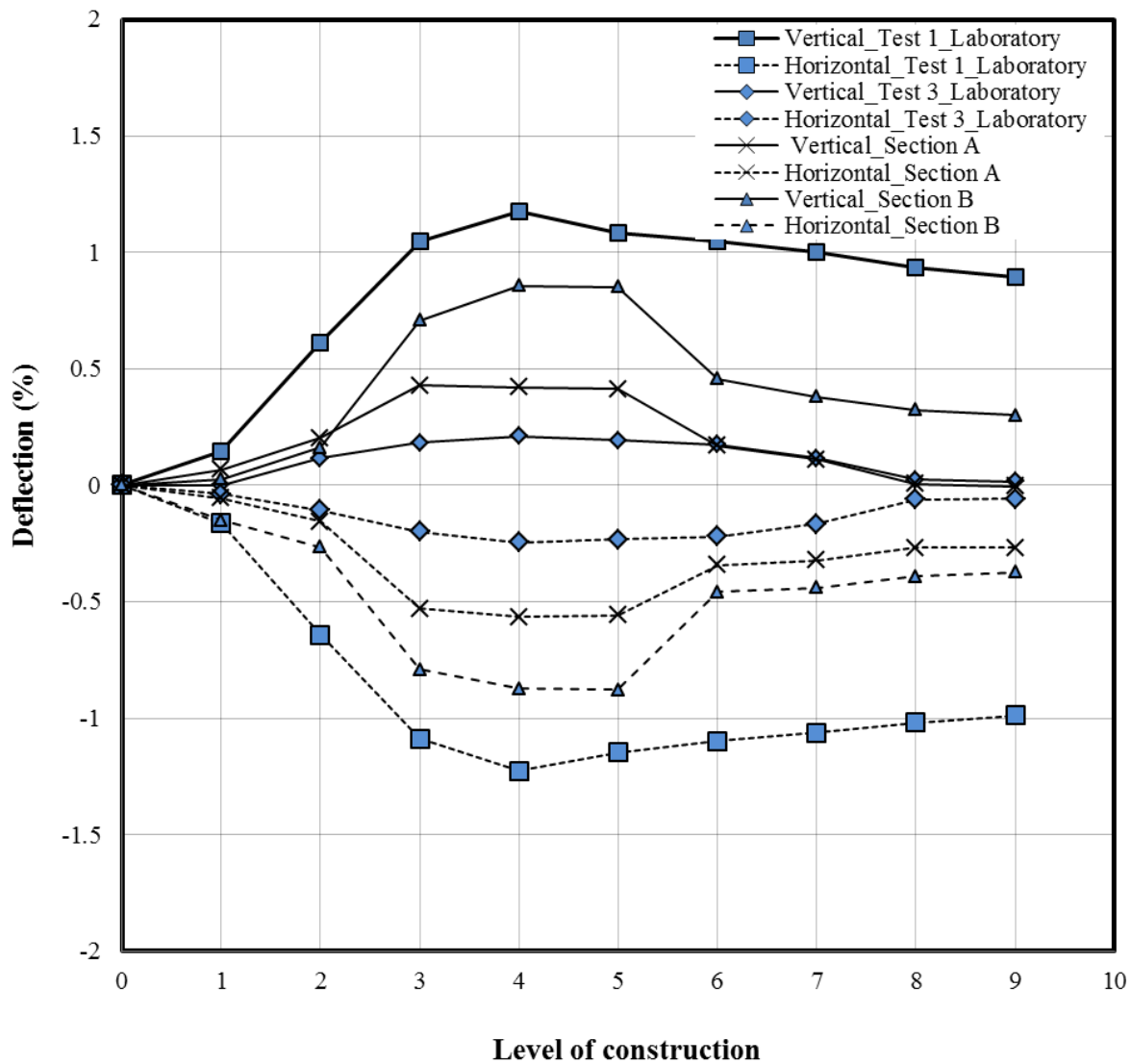


FIGURE 6.33 Comparison of the measured deflections of the SRHDPE pipes during the installation

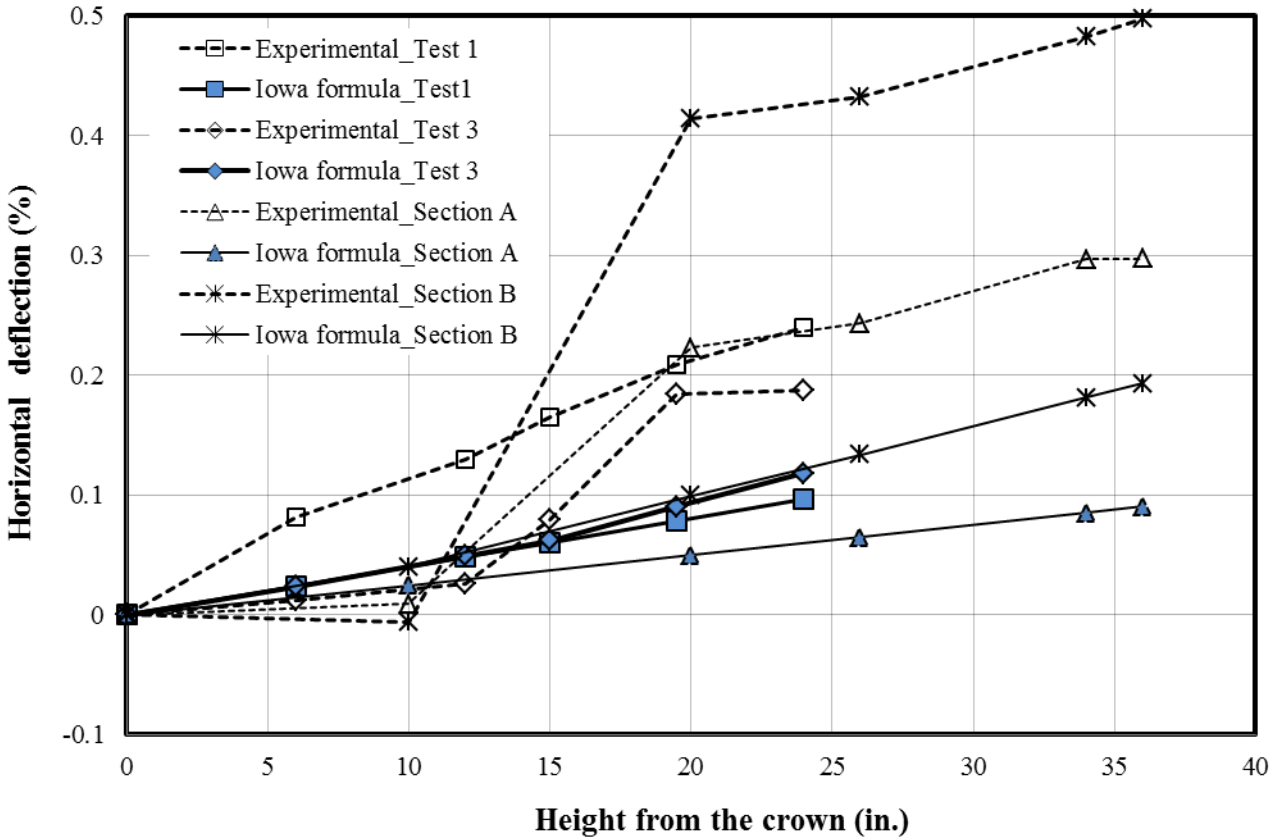


FIGURE 6.34 Comparison of calculated and measured horizontal deflections of the SRHDPE pipes during the installation

6.1.3 Strain Data

Most of the strain gages fixed on the steel and plastic surfaces of the pipe at various locations both in laboratory and field tests performed well. All the measured strain values on the plastic material were adjusted according to Brachman et al. (2008) as described earlier in **SECTION 3.1.1**. Positive values are tensile strains while negative values are compressive strains.

Laboratory Tests

Most of the strain gages used in laboratory tests performed well during the installation of the pipe except the strain gage G'_{SR1} in Test 1 and the strain gages, G_{CR1} , G_{SR2} , and G'_{SR1} in Test 3.

Test 1. The adjusted strains according to Brachman et al. (2008) are plotted against the levels of construction in **FIGURES 6.35 to 6.37**.

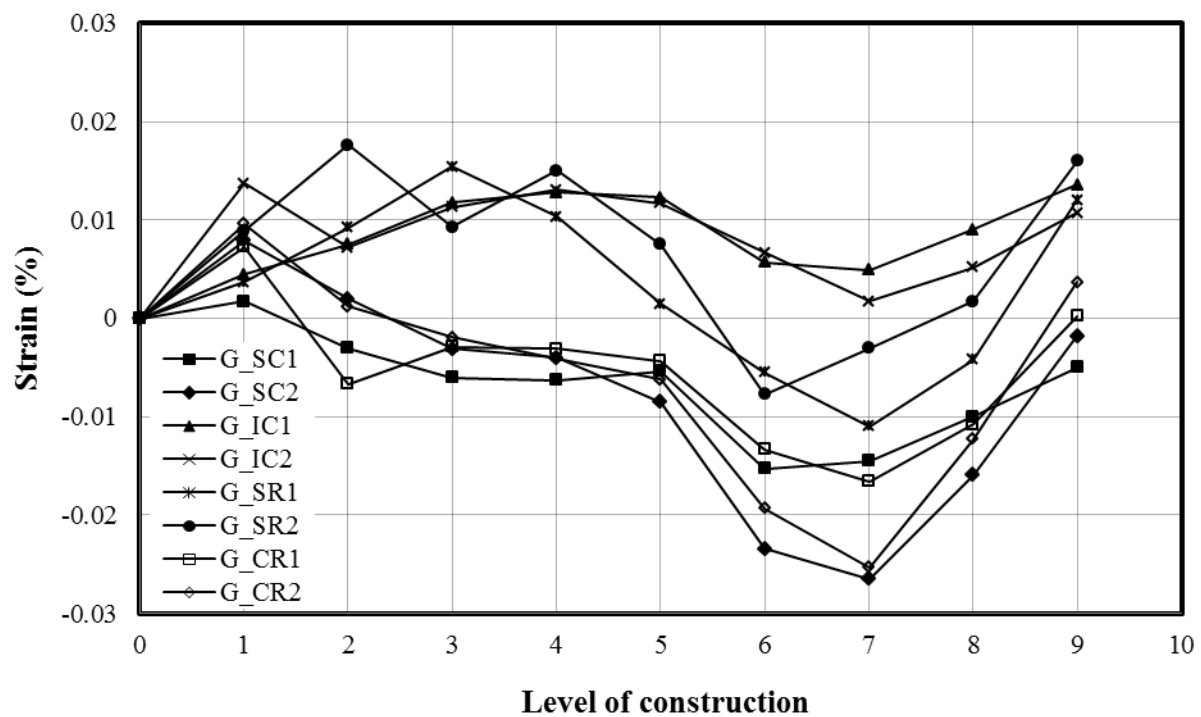


FIGURE 6.35 Measured strains on the steel surface during the installation in Test Section 1

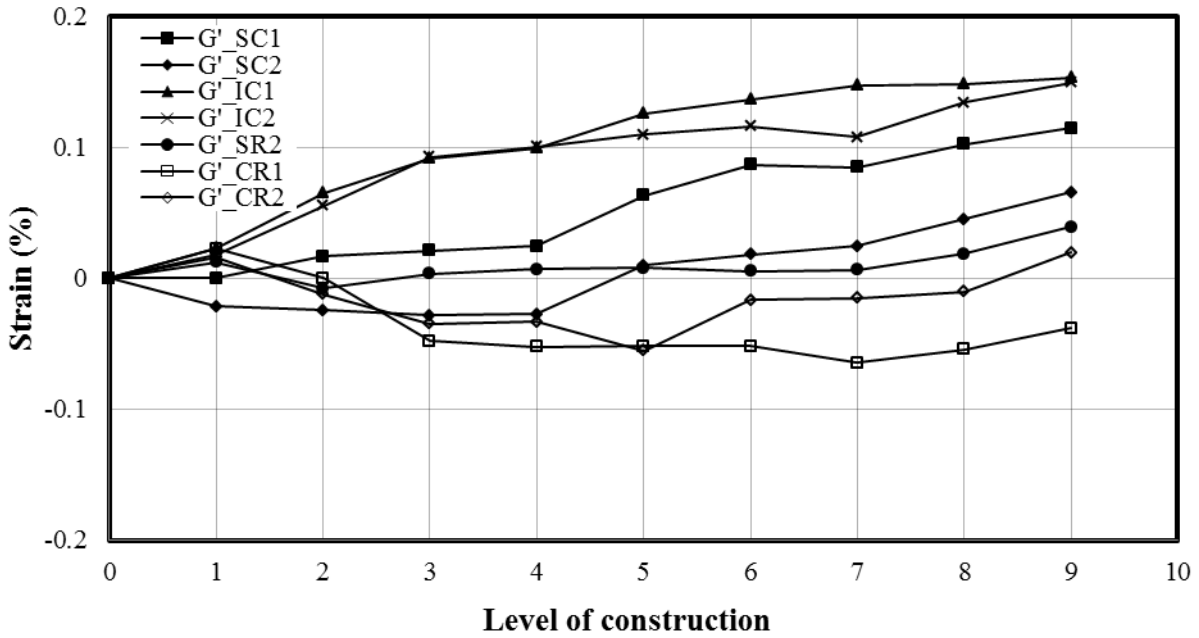


FIGURE 6.36 Measured strains on the plastic ribs during the installation in Test Section 1

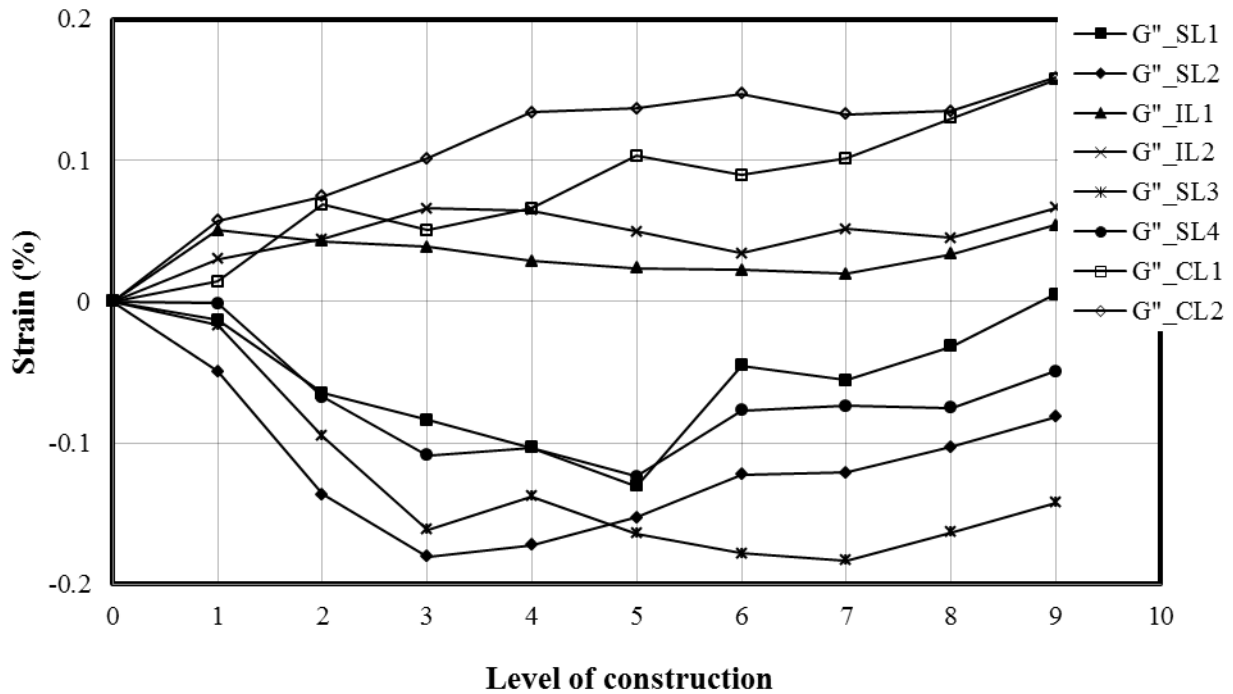


FIGURE 6.37 Measured strains on the plastic at inside and outside pipe wall during the installation in Test Section 1

The circumferential and radial strains developing on the steel of the pipe are shown in **FIGURE 6.35**. The strain gages, G_{SC1} and G_{SC2} at the springline and G_{CR1} and G_{CR2} at the crown, showed an increase in compressive strains, while the strain gages G_{IC1} and G_{IC2} at the invert and G_{SR1} and G_{SR2} at the springline showed increasing strain values until the backfill reached the pipe crown (i.e. Level 4 of construction). All strain gages then showed an increase in compressive strains up to three more layers of compaction (i.e. up to Level 7 of compaction). After that, all strain gages measured increasing tensile strains. The maximum radial strain of 0.0026% (G_{CR1} , compressive strain) and the maximum circumferential strain of 0.0027% (G_{SC2} , compressive strain) developed during the installation. The strain gages fixed on both sides of a steel rib at any particular location (for example, G_{SC1} and G_{SC2} at the springline at the rib), gave similar values (i.e. there was no sudden change in strain values). This result indicates that the out-of-plane buckling of the steel ribs observed during the parallel plate load tests at a high level of load did not occur during the installation of the pipe.

FIGURE 6.36 shows the circumferential and radial strains on the plastic at the ribs against the levels of construction. The strains developing on the plastic were higher in magnitude than the strains on the steel. Most of the strain gages showed an increase in tensile strains with the level of construction, but the strain gages G'_{CR1} and G'_{CR2} had an increase in the compressive strains until the backfill was at the same level with the pipe crown. The maximum tensile strain of 0.15% was recorded during the installation.

The strains measured by the strain gages on the plastic wall inside and outside are shown in **FIGURE 6.37**. All strain gages showed an increase in tensile strains after compaction up to the springline (i.e. Level 2 of construction). The strain gages affixed on the pipe inside walls experienced more tensile strains than those on the outside walls. The magnitudes of the strains

on the pipe walls were higher than the strains on the steel and the plastic at the ribs. The maximum tensile strain of 0.17% (G''_{CL2}) was recorded on the pipe wall during the installation.

Test 3. The adjusted strains according to Brachman et al. (2008) are plotted against the levels of construction in **FIGURES 6.38** to **6.40**.

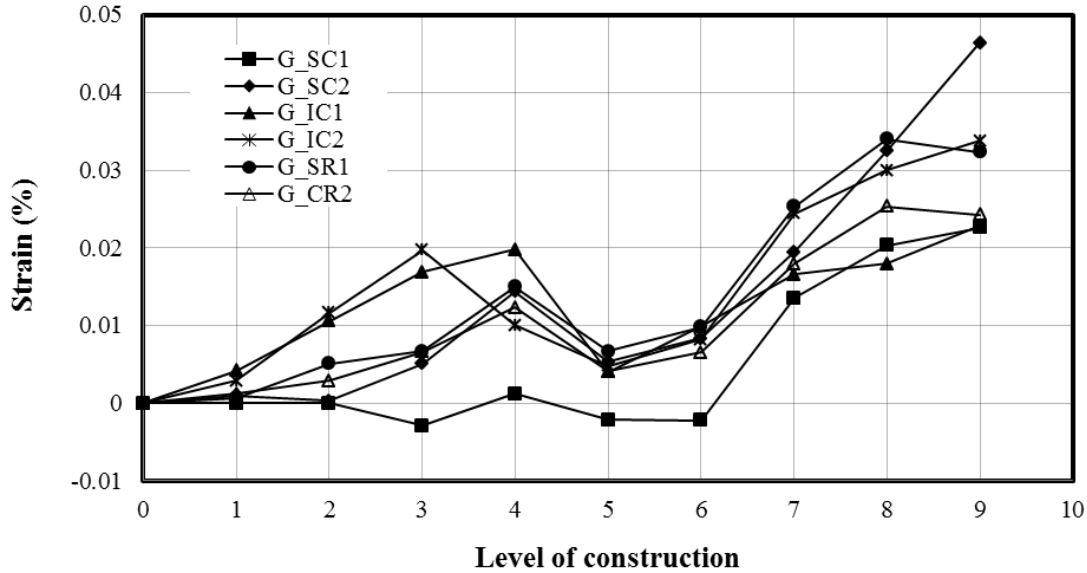


FIGURE 6.38 Measured strains on the steel during the installation in Test Section 3

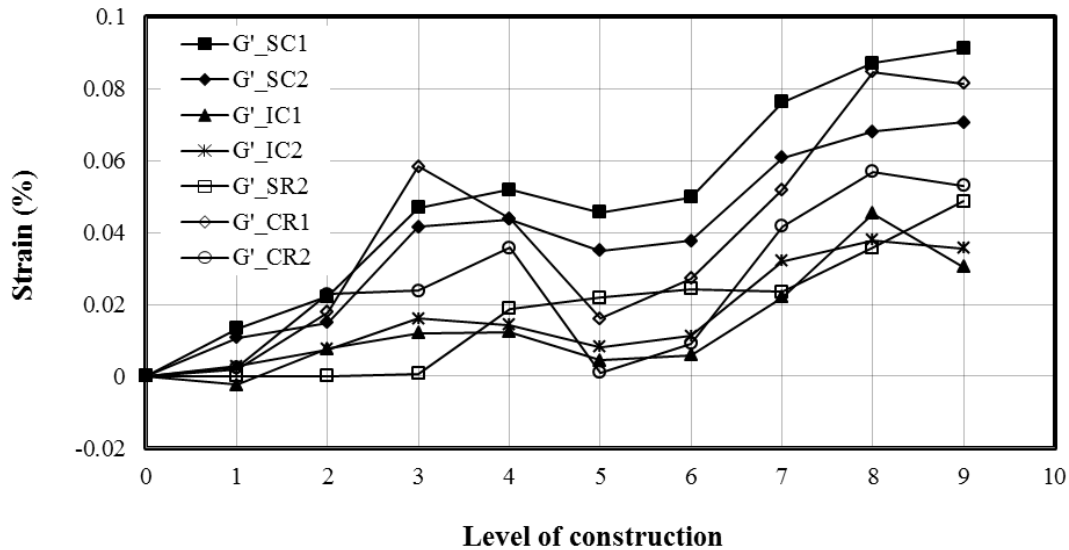


FIGURE 6.39 Measured strains on the plastic ribs during the installation in Test Section 3

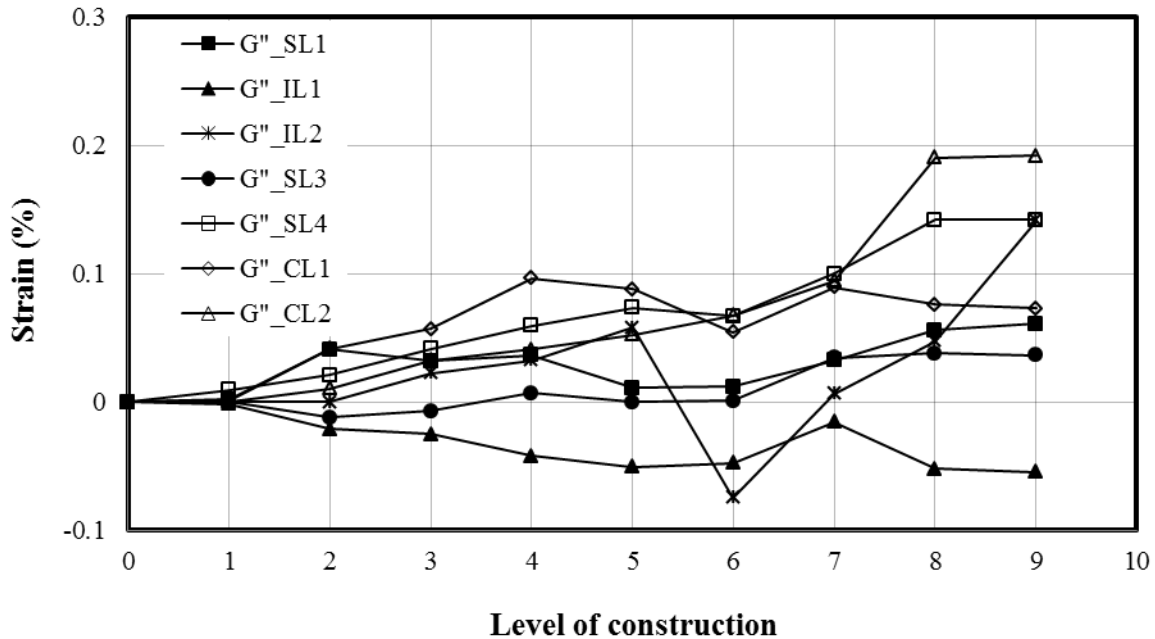


FIGURE 6.40 Measured strains on the plastic at inside and outside pipe wall during the installation in Test Section 3

The circumferential and radial strains developing on the steel of the pipe are shown in **FIGURE 6.38**. Most of the strain gages showed increasing strains until the backfill reached the pipe crown (i.e. Level 4 of construction). There were some decreases in the strains from Levels 4 to 6 of construction. After Level 6, all the strain gages had an increasing trend in the measured strains. The maximum circumferential strain of 0.043% (G_{SC2} , tensile strain) developed during the installation. The strain gages fixed on both sides of a steel rib at any particular location (for example, G_{SC1} and G_{SC2} at the springline at the rib), gave similar strain values (i.e., there was no sudden change in the strain values). This result indicates that the out-of-plane buckling of the steel ribs observed during the parallel plate load tests at a high level of load did not occur during the installation of the pipe.

FIGURE 6.39 shows the circumferential and radial strains on the plastic at the ribs against the levels of construction. The strains developing on the plastic were higher in the magnitude than the strains on the steel. Most of the strain gages showed an increase in the tensile strains with the level of construction. The maximum tensile strain of 0.063% was recorded during the installation.

The strains measured by the strain gages on the plastic wall inside and outside the pipe are shown in **FIGURE 6.40**. All the strain gages showed an increase in the tensile strains. The strain gages affixed on the pipe inside walls experienced more tensile strains than those on the outside walls. The magnitudes of the strains on the pipe walls were higher than the strains on the steel and the plastic cover at the ribs. The maximum tensile strain of 0.19% (G''_{CL2}) was recorded on the pipe wall during the installation.

Field Installation Test

Most of the strain gages (47 out of 52 strain gages) used in this test performed well during the installation of the pipe except the strain gages, G_{SR2} , G''_{SL1} , G''_{CL5} , and G''_{SL1} , fixed in Test Section A and the strain gage, G_{SR1} , fixed in Test Section B. All strain gages which did not work during the installation of the pipe were fixed later and started working for the long-term monitoring of the pipe. The long-term performance data were not presented in this study.

Section A. The adjusted strains according to Brachman et al. (2008) are plotted against the levels of construction in **FIGURES 6.41 to 6.43.**

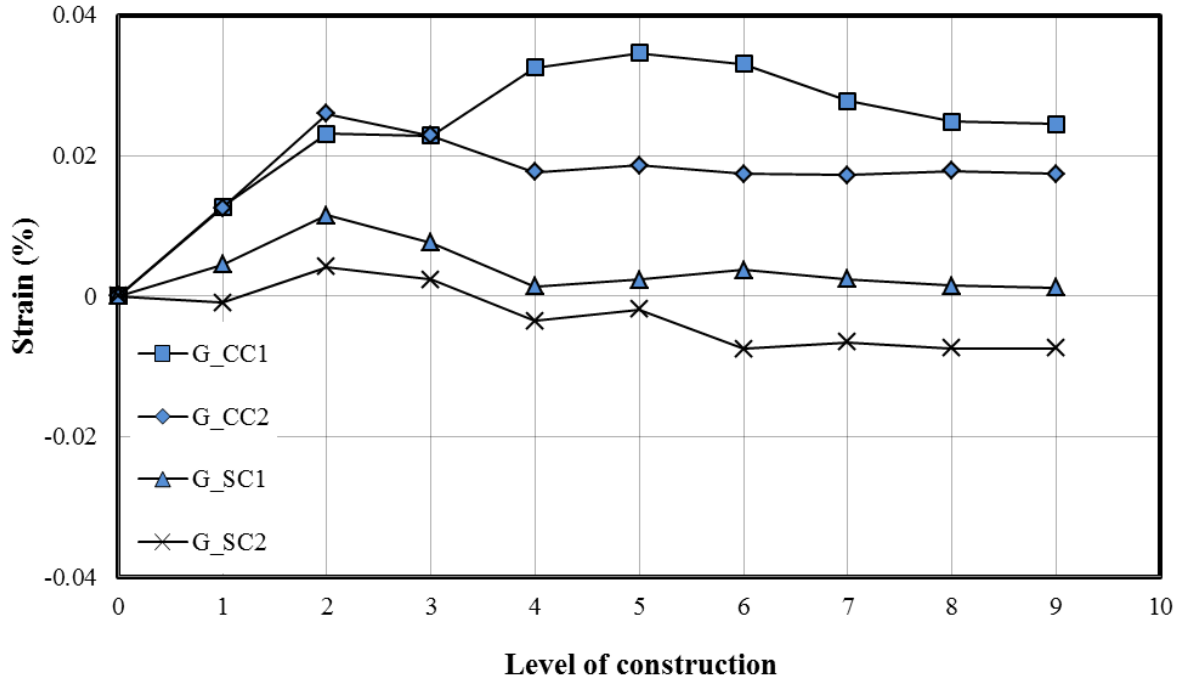


FIGURE 6.41 Measured strains on the steel surface during the installation in Test Section A

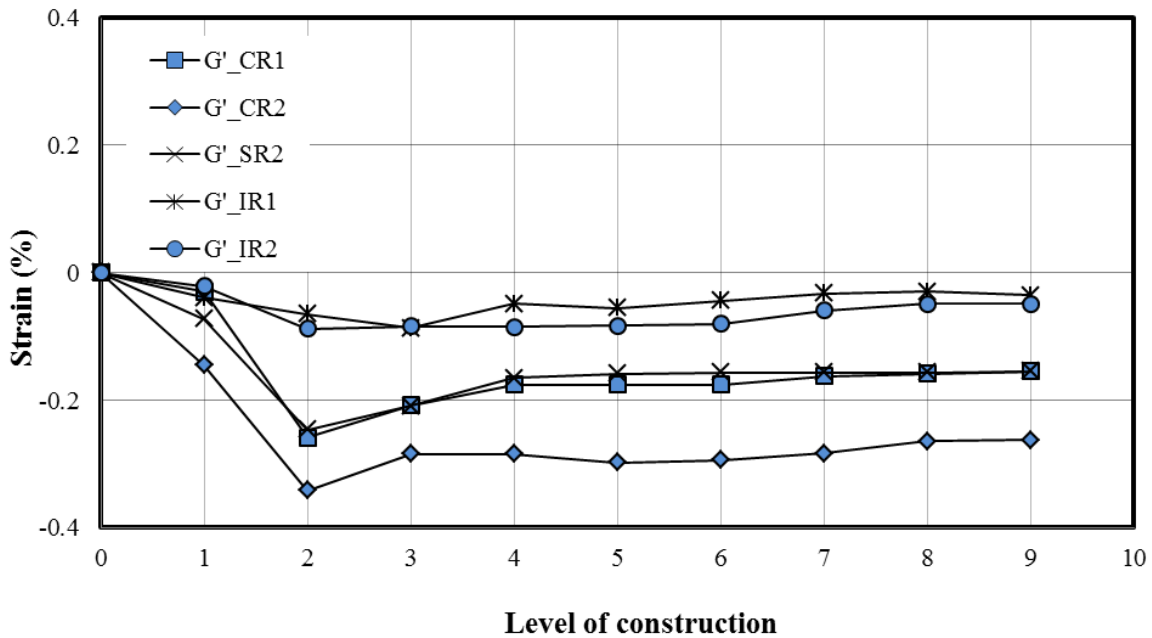
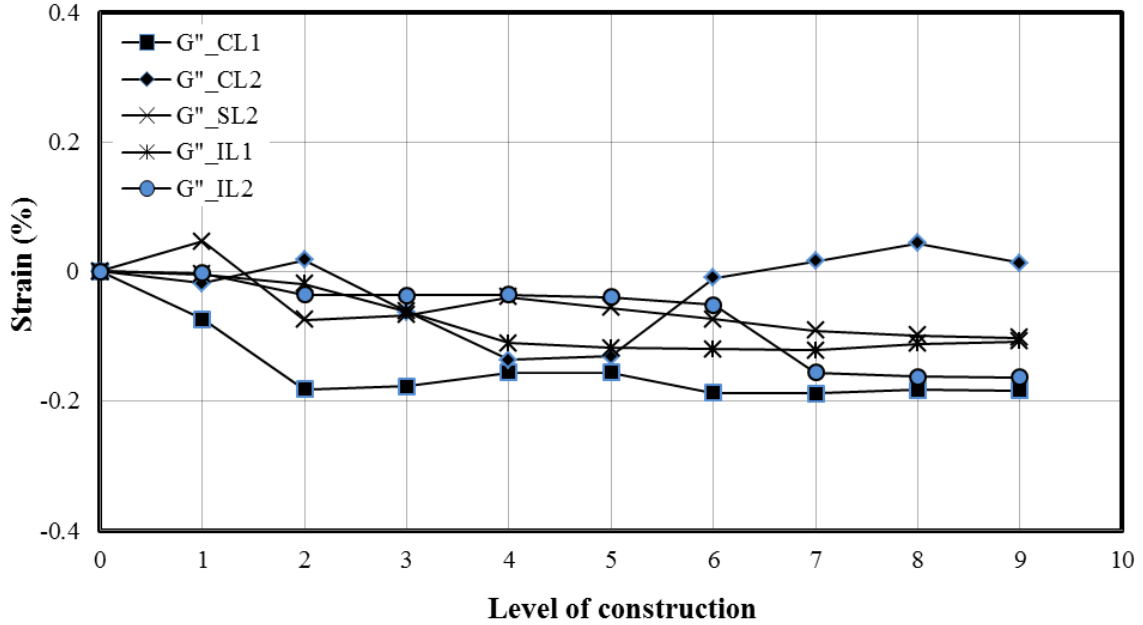
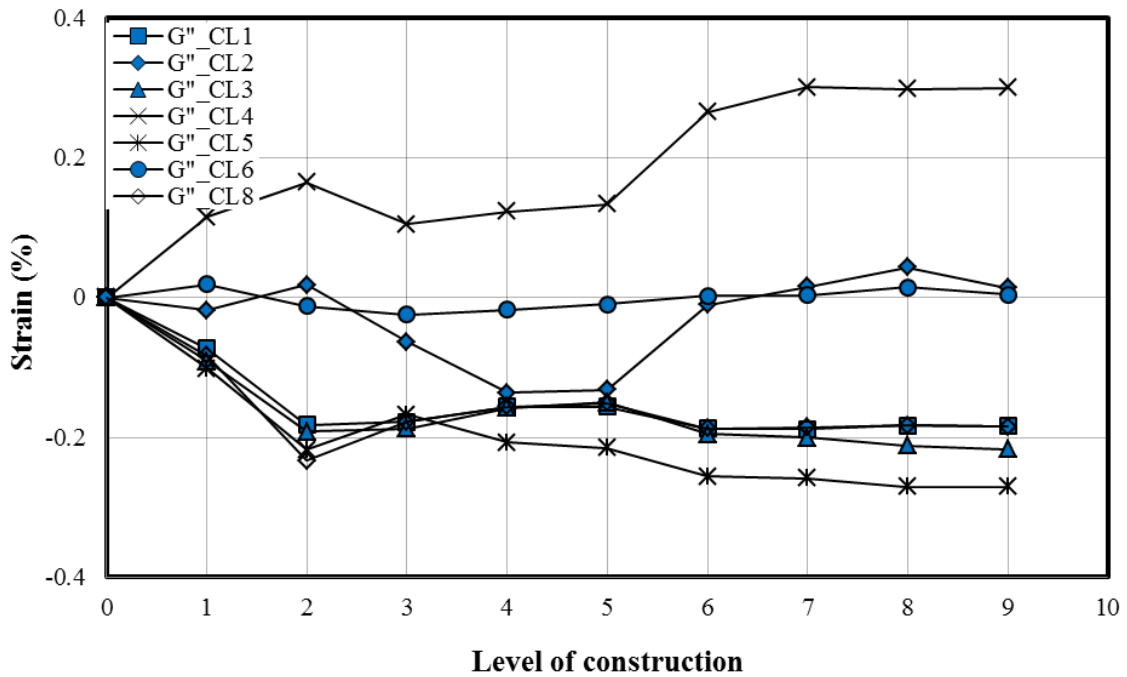


FIGURE 6.42 Measured strains on the plastic ribs during the installation in Test Section A



(a) Strains on plastic beneath the wheel path



(b) Strains on plastic away from the wheel path to centerline of the roadway

FIGURE 6.43 Measured strains on the plastic at inside and outside pipe wall during the installation in Test Section A

The circumferential strains (**FIGURE 6.41**) developing on the steel of the pipe in the field in Test Section A had similar values to the strains on the steel in the laboratory tests. The strain gages, G_{SC1} and G_{SC2} at the springline and G_{CC1} and G_{CC2} at the crown, showed an increase in tensile strains until the backfill reached the pipe springline (i.e., Level 2 of construction). All strain gages (except G_{CC1}) showed an increase in compressive strains with the increase in soil lifts. Strain gage G_{CC1} showed the increase in tensile strains up to Level 5 of construction. After that, strain gage G_{CC1} indicated the increase in the compressive strains. The maximum circumferential strain of 0.034% (G_{CC1} , tensile strain) and the maximum circumferential strain of 0.007% (G_{SC2} , compressive strain) developed during the installation. The strain gages fixed on both sides of a steel rib at any particular location (for example, G_{SC1} and G_{SC2} at the springline at the rib), gave similar values (i.e. there was no sudden change in strain values). This result indicates that the out-of-plane buckling of the steel ribs observed during the parallel plate load tests at a high level of load did not occur during the installation of the pipe.

FIGURE 6.42 shows the radial strains on the plastic at the ribs against the levels of construction. The strains developing on the plastic were higher in magnitude than the strains on the steel. All strain gages showed an increase in compressive strains until the backfill was at the springline (i.e., Level 2 of construction) and started increasing in tensile strains with the increase in soil lifts. A maximum compressive strain of 0.34 % was recorded during the installation.

The strains measured by the strain gages on the plastic wall inside and outside are shown in **FIGURE 6.43**. **FIGURE 6.43a** shows the strains at the crown, springline, and invert of the pipe under the wheel path whereas **FIGURE 6.43b** shows the strains at the pipe crown at various locations from the pipe crown to the centerline of the roadway. Most of the strain gages affixed on the pipe outside experienced the increase in compressive strains whereas most of the strain

gages on the pipe inside experienced the increase in tensile strains after the backfill was at the springline (i.e., Level 2 of construction). The strain gages affixed on the pipe inside walls experienced more tensile strains than those on the outside walls. The magnitudes of the strains on the pipe walls were higher than the strains on the steel and higher than or close to the plastic at the ribs. The maximum tensile strain of 0.3% (G''_{CL4}) was recorded on the pipe wall during the installation.

Section B. The adjusted strains according to Brachman et al. (2008) are plotted against the levels of construction in **FIGURES 6.44 to 6.46**.

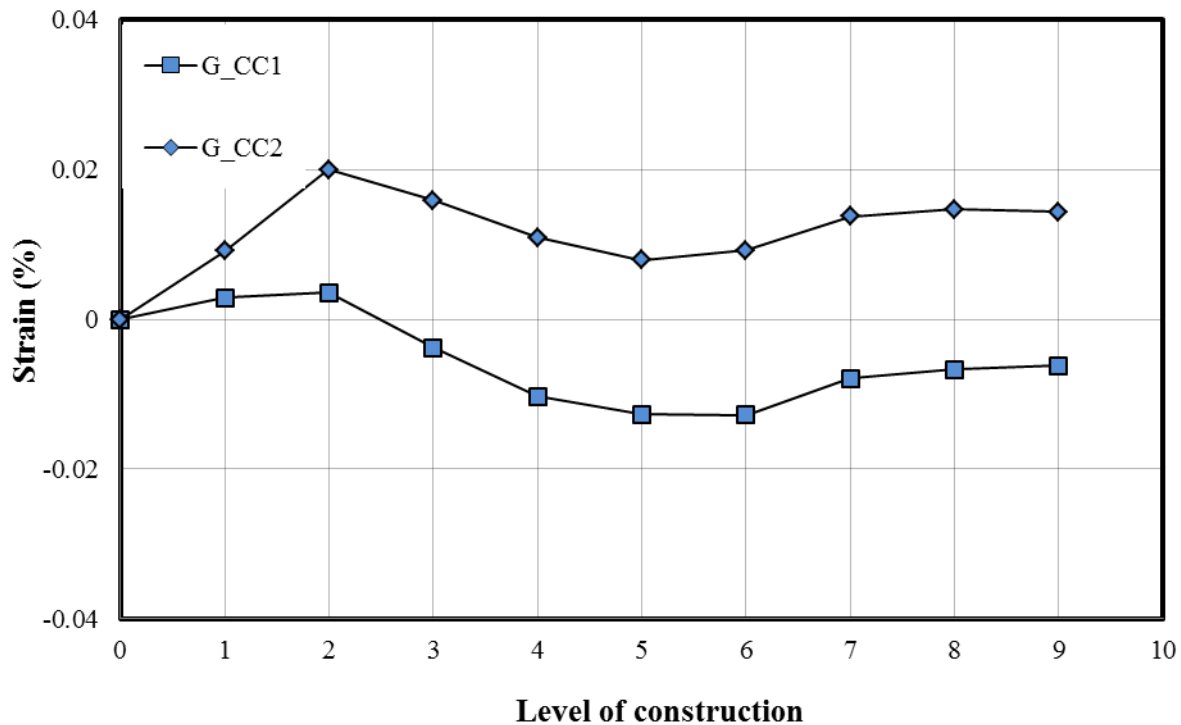


FIGURE 6.44 Measured strains on the steel during the installation in Test Section B

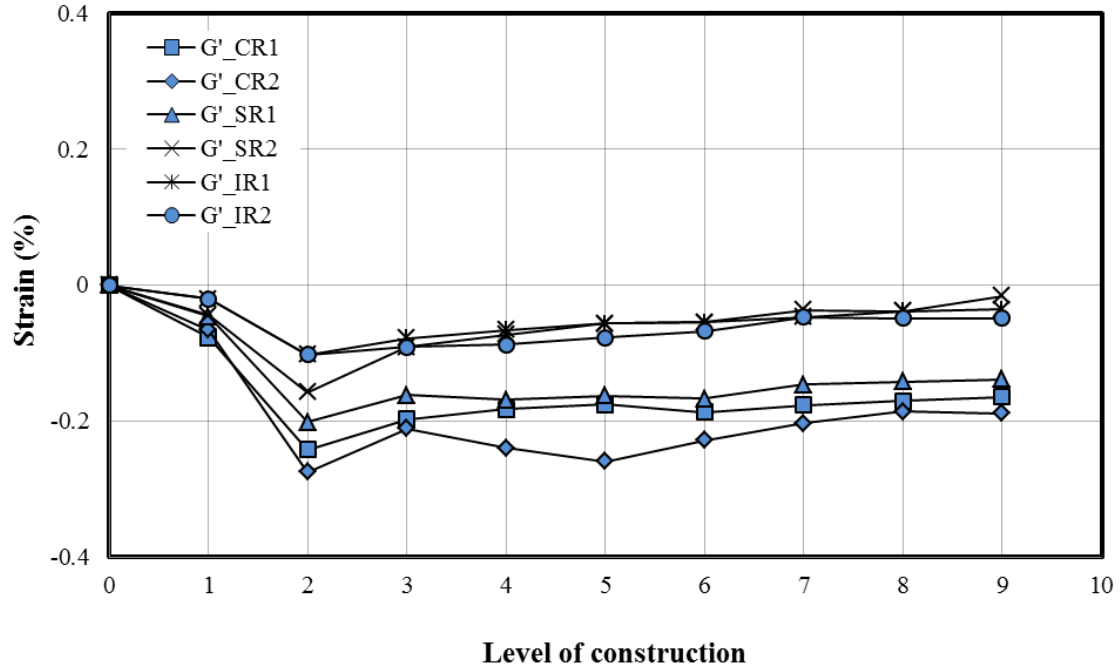
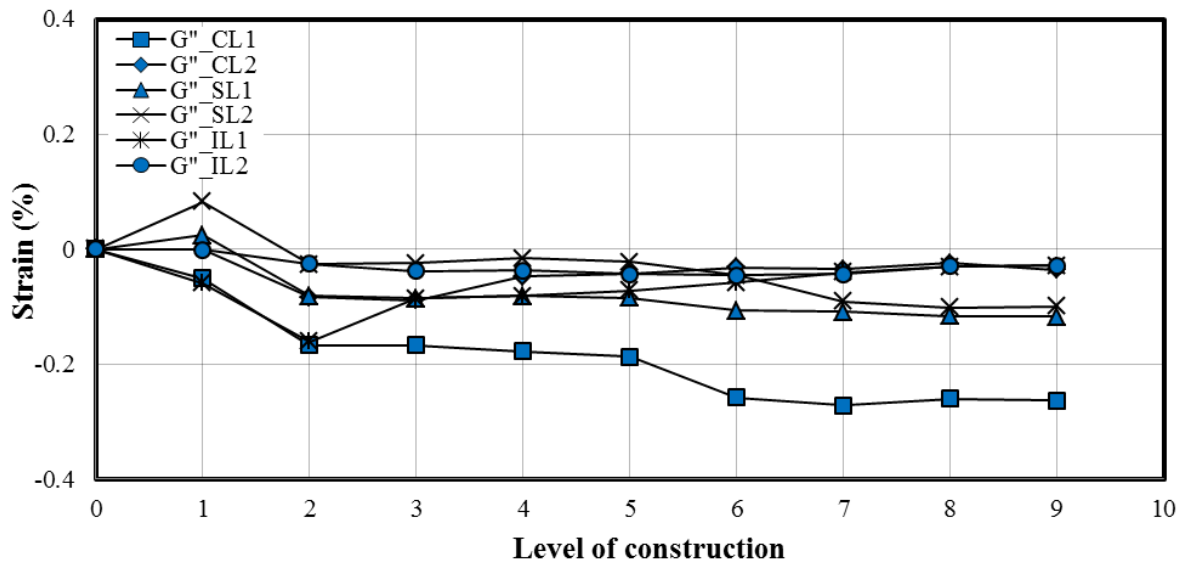
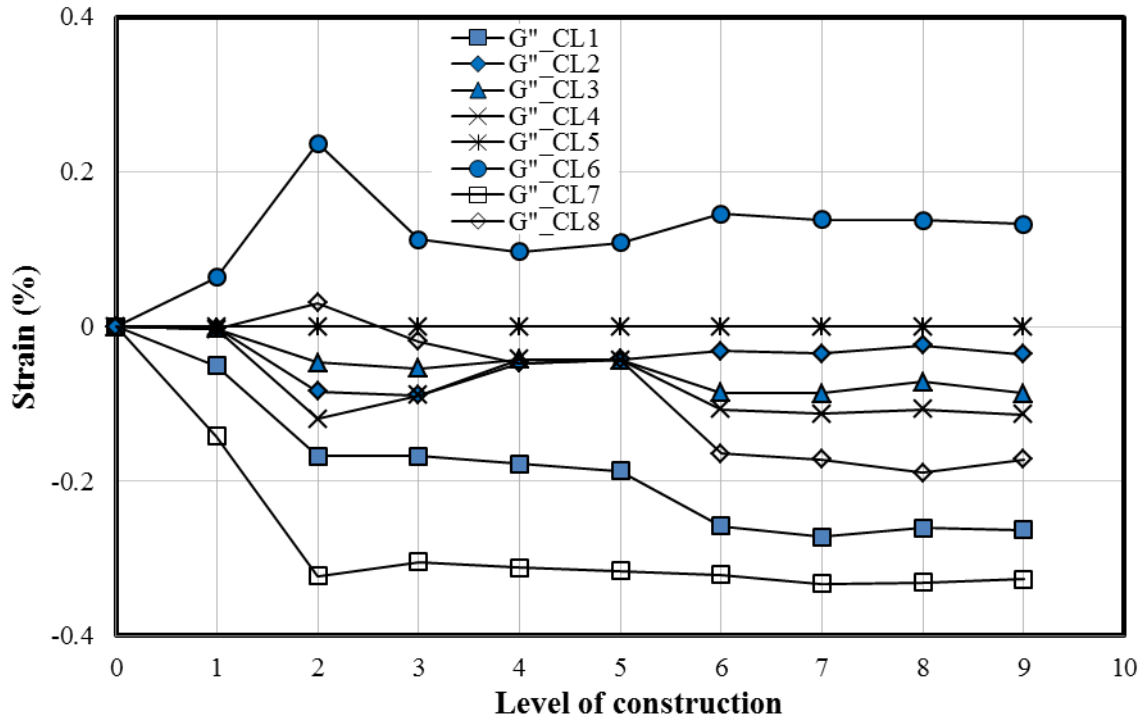


FIGURE 6.45 Measured strains on the plastic ribs during the installation in Test Section B



(a) Strains on plastic beneath the wheel path

FIGURE 6.46 Measured strains on the plastic at inside and outside pipe wall during the installation in Test Section B



(b) Strains on plastic away from the wheel path to centerline of the road way

FIGURE 6.46 Measured strains on the plastic at inside and outside pipe wall during the installation in Test Section B (continued)

The circumferential strains (**FIGURE 6.44**) developing on the steel of the pipe in the field in Test Section B had similar values to the strains on the steel in the laboratory and field (Test Section A) tests. The strain gages, G_{CC1} and G_{CC2} at the crown, showed an increase in tensile strains until the backfill reached the pipe springline (i.e., Level 2 of construction). All strain gages showed a decrease in compressive strains up to the top of the pipe and an increase in tensile strains with soil lifts as the construction commenced further. The maximum

circumferential strain of 0.02% (G_{CC2} , tensile strain) and the maximum circumferential strain of 0.012% (G_{CC1} , compressive strain) developed during the installation.

FIGURE 6.45 shows the radial strains on the plastic at the ribs against the levels of construction and the strains were similar to the strains obtained on the plastic ribs for the laboratory and field (Test Section A) tests. The strains developing on the plastic were higher in magnitude than the strains on the steel. All strain gages showed an increase in compressive strains until the backfill was at the springline (i.e., Level 2 of construction) and started increasing in tensile strains with the increase in soil lifts. A maximum compressive strain G'_{CR2} of 0.27 % was recorded during the installation

The strains measured by the strain gages on the plastic wall inside and outside are shown in **FIGURE 6.46**. **FIGURE 6.46a** shows the strains at the crown, springline, and invert of the pipe under the wheel path whereas **FIGURE 6.46b** shows the strain at the pipe crown at various locations from the pipe crown to the centerline of the roadway. Most of the strain gages affixed on the pipe outside experienced an increase in compressive strains whereas most of the strain gages on the pipe inside experienced an increase in tensile strains after the backfill was at the springline (i.e., Level 2 of construction). The strain gages affixed on the pipe inside walls experienced more tensile strains than those on the outside walls. The magnitudes of the strains on the pipe walls were higher than the strains on the steel and higher than or close to the plastic at the ribs. The maximum strain of 0.32% (G''_{CL7} , tensile strain) was recorded on the pipe wall during the installation.

6.2 Static Loading Test Results

To evaluate the performance of SRHDPE pipes in a ditch under a shallow cover for traffic loading, loads were applied on the pipe both in the laboratory and field tests. For the laboratory tests, simulated traffic loads were applied using the loading plate of 1 ft. in diameter as described in **SECTION 4.2**. For the field test, the dump truck, 2004 International 7400 6x4, was used to apply the static construction vehicle load as described in **SECTION 5.4**.

For both laboratory static plate loading and the field construction vehicle loading tests, the earth pressures around the pipe, the deflections of the pipe, and the strains on the pipe. The settlements of the loading plate were measured for the laboratory tests only). Their results are presented in the subsequent sections.

6.2.1 Settlement of Loading Plate

Laboratory Tests

Test 1. **FIGURE 6.47** shows the settlements of the loading plate against the applied pressures during loading and unloading. The total settlement of the loading plate was 0.163 in. at the applied pressure of 80 psi, which is the typical tire pressure of a highway truck. This total settlement consisted of an elastic deformation of 0.063 in. and a permanent deformation of 0.1 in. based on the unloading curve. Using the initial slope of the pressure-settlement curve, the elastic modulus of the test section (E_s) was calculated using **EQUATION 6.2** as 5,068 psi.

$$E_s = 0.79 d (1 - \nu^2) \frac{P}{\delta} \quad 6.2$$

where E_s = the elastic modulus of the test section, ν = the Poisson's ratio (a typical value of 0.33 was used), p = the applied pressure on the elastic range, and δ = the settlement of the loading plate at p .

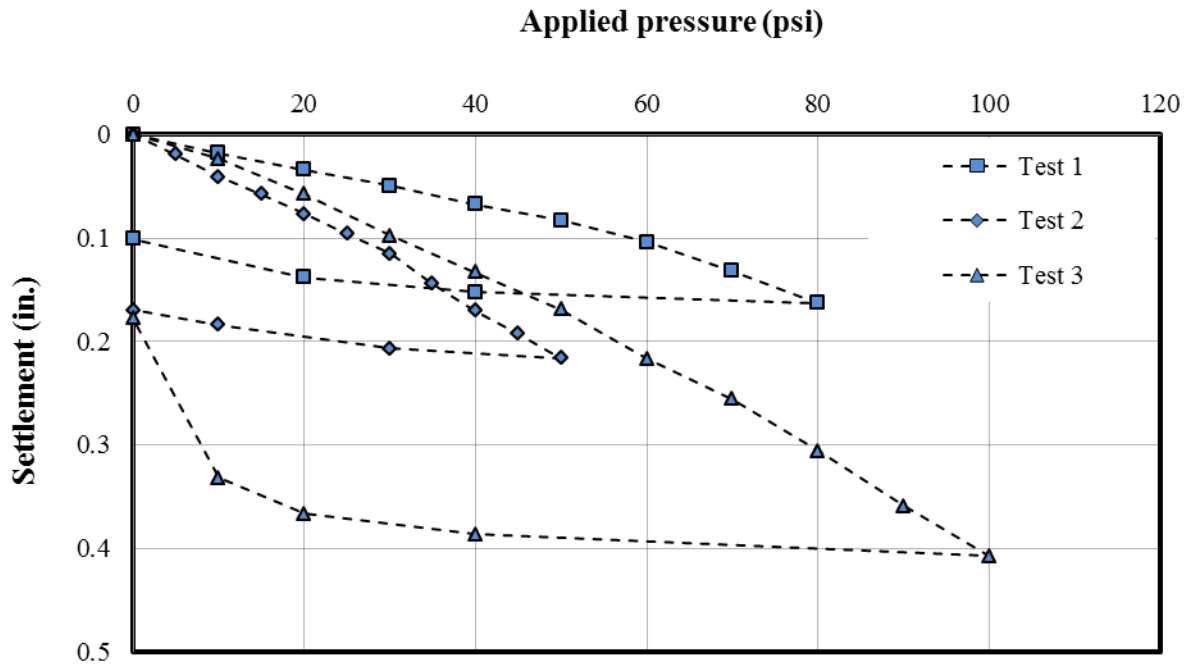


FIGURE 6.47 Settlement of the loading plate versus applied pressure under static loads

Test 2. The total settlement of the loading plate in Test 1 was 0.215 in. at the applied pressure of 50 psi, as shown in **FIGURE 6.47**. This total settlement consisted of an elastic deformation of 0.045 in. and a permanent deformation of 0.17 in. Based on the initial slope of the pressure-settlement curve, the elastic modulus of the test section (E_s) was calculated using **EQUATION 6.2** as 2,214 psi.

Test 3. The total settlement of the loading plate in Test 3 was 0.40 in. at the applied pressure of 100 psi, as shown in **FIGURE 6.47**. This total settlement consisted of an elastic deformation of 0.18 in. and a permanent deformation of 0.22 in. Based on the initial slope of the pressure-

settlement curve, the elastic modulus of the test section (E_s) was calculated using **EQUATION 6.2** as 2,500 psi.

FIGURE 6.47 shows that Test 1 had the smallest settlement while the Test 2 had the largest settlement among all three tests. The reason Test 1 had the smallest settlement is that the section in Test 1 had a well-compacted sand and a stiff AB-3-I aggregate as the base course. In Test 2, Kansas River sand was used as the base course and was weaker or less stiff than the AB-3-I aggregate. In Test 3, however, the crushed stone (CS-I) in the trench was not compacted; therefore, it deformed more than the compacted sand.

6.2.2 Earth Pressure Results

The distribution of earth pressures around the pipe due to the applied static load was measured using the earth pressure cells. The earth pressures discussed in this section are those induced by the applied load only. In other words, the measured earth pressures during the pipe installation were excluded.

Laboratory Tests

Test 1. FIGURE 6.48 shows the measured earth pressures around the pipe against the pressures applied on the loading plate. The earth pressure cell placed at the pipe crown (E_{C0}) showed the highest earth pressure on the pipe. The earth pressure at the crown under the applied pressure of 80 psi was approximately 11 psi. The vertical earth pressure at 6 in. away from the center (E_{C6}) was 0.43 to 0.5 times that at the pipe crown (E_{C0}). The horizontal pressure at the pipe springline (E_{S0}) was 0.32 times the vertical earth pressure at the crown (E_{C0}). The ratio of the horizontal pressure at the springline (E'_{S0}) to that at the shoulder (E'_{SH0}) was 1.3 to 1.5. The higher

horizontal pressure at the springline (E'_{s0}) as compared with that at the shoulder (E'_{sh0}) is attributed to the additional lateral pressure applied by the pipe at the springline level due to more outward deflection of the pipe.

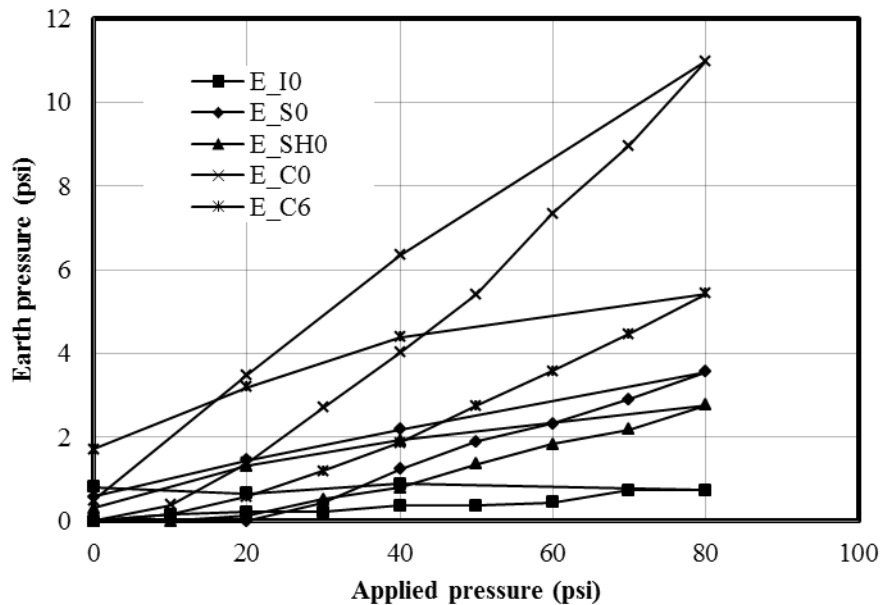


FIGURE 6.48 Measured earth pressures around the pipe in Test 1

Test 2. **FIGURE 6.49** shows the measured earth pressures versus the applied pressures. The earth pressure cell at the pipe crown (E_{C6}) showed the highest earth pressure on the pipe. The earth pressure at the crown under the applied pressure of 50 psi was approximately 7.3 psi. The vertical earth pressure at 6 in. away from the center (E_{C6}) was 0.62 to 0.67 times that at the pipe crown (E_{C0}). The horizontal pressure at the pipe springline (E'_{s0}) was 0.32 times the vertical earth pressure at the crown (E_{C0}). The ratio of the horizontal pressure at the springline (E'_{s0}) to the pressure at the shoulder (E'_{sh0}) was 1.16 to 1.30. This result is attributed to the additional lateral pressure applied by the pipe at the springline level due to more outward deflection of the pipe.

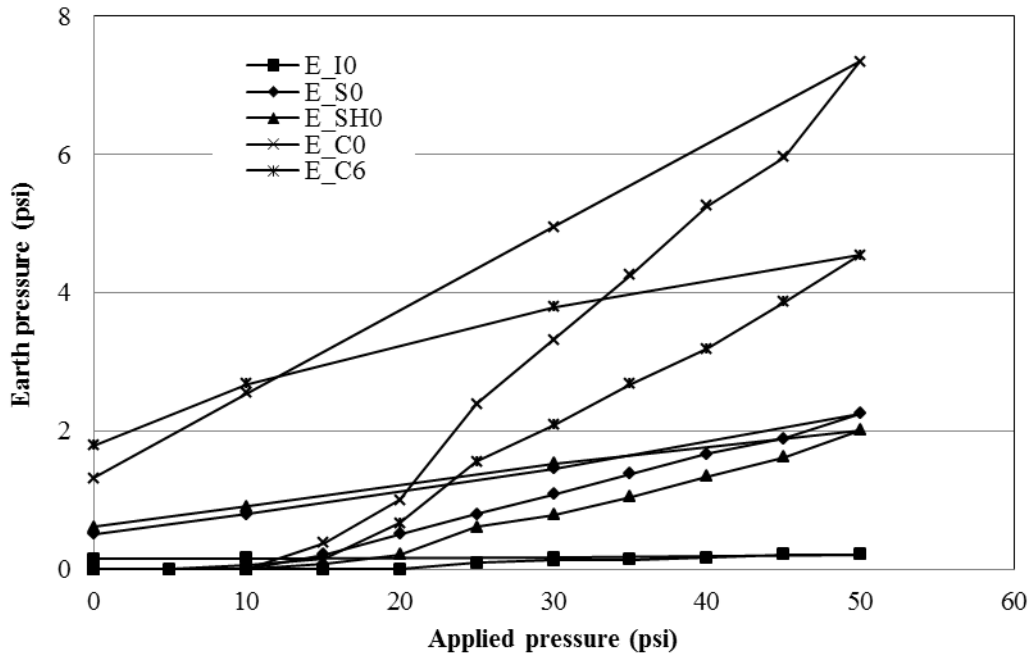


FIGURE 6.49 Measured earth pressures around the pipe in Test 2

Test 3. **FIGURES 6.50** and **6.51** show the measured earth pressures by the earth pressure cell (E_{IF}) at the base course and backfill interface and nine other earth pressure cells around the pipe at different applied pressures, respectively. **FIGURE 6.50** shows the measured interface pressures were close to those calculated using the chart developed by Huang (1969) when the applied pressure was less than 60 psi. However, for pressures higher than 60 psi, the measured earth pressures were higher than those calculated pressures because of the stress concentration on the pipe crown in the test. In the calculation, the elastic moduli of 1,125 and 5,280 psi (determined in **SECTIONS 3.2.2** and **3.2.3**) were used for the crushed stone (CS-I) backfill and the AB-3-I base course, respectively. **FIGURE 6.51** shows that the pressures recorded by the earth pressure cell (E_{C6}) placed at 6 in. away from the pipe crown were the highest during loading. The earth pressure at the crown (E_{C0}) under the applied pressure of 100 psi was

approximately 7.35 psi. The earth pressure cells at the crown and 1 ft away from the crown (i.e., E_{C0} and E_{C12}) showed approximately the similar earth pressures during loading. The vertical earth pressure at 6 in. away from the center (E_{C6}) was 1.2 to 1.5 times that at the pipe crown (E_{C0}). During loading, the highest lateral earth pressure was at the shoulder of the pipe. The highest pressures may be due to the relatively higher outward deflection of the pipe at the shoulder than the deflection at the springline and at the haunch. The horizontal earth pressure at the shoulder (E'_{SH0}) was 0.33 to 0.36 times that at the pipe crown (E_{C0}). The ratio of the horizontal pressure at the springline (E'_{S0}) to that at the shoulder (E'_{SH0}) was 3.23 to 4.2.

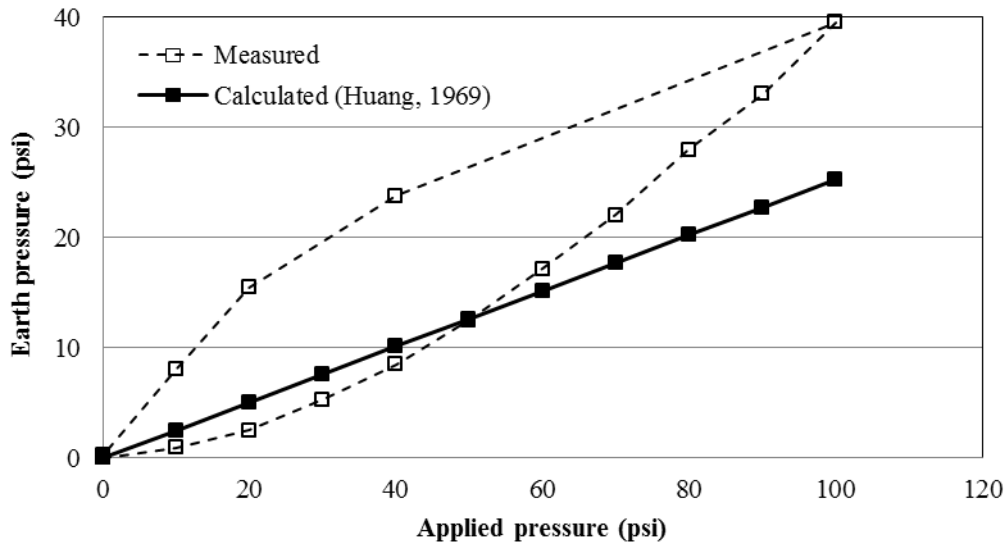


FIGURE 6.50 Measured and calculated earth pressure (E_{IF}) at the backfill-base course interface in Test 3

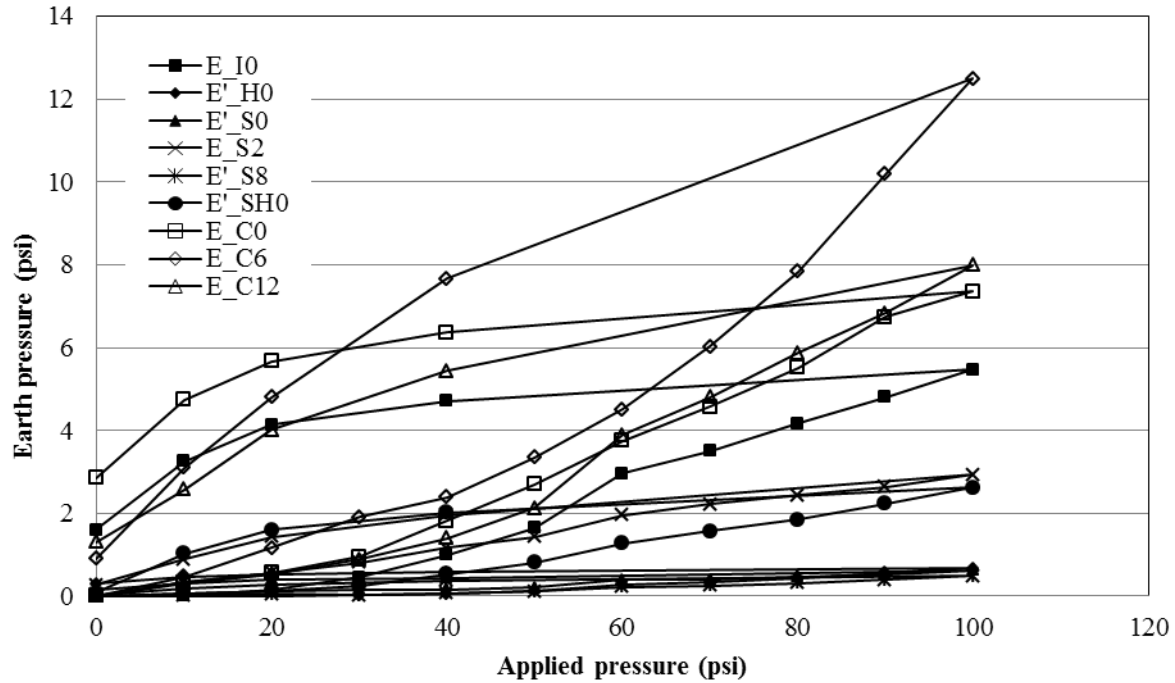


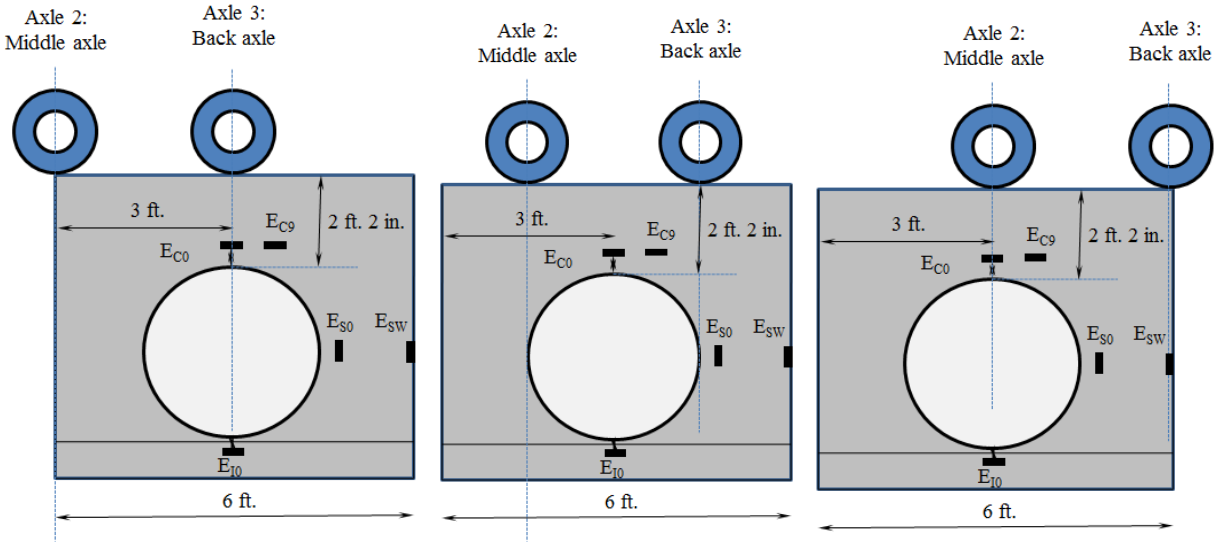
FIGURE 6.51 Measured earth pressures around the pipe in Test 3

Field Test

Before placing the HMA base material, the dump truck of 13.72 tons (empty) loaded with HMA base course material of 15.2 tons was used as the test truck. As discussed in **SECTION 5.5**, the contact area calculated for each rear wheel load of 5.25 tons with the tire pressure of 120 psi was found to be 87.5 in.². The static truck load was applied on both western and eastern test sections (Sections A and B) with three different loading configurations: (a) back axle above the pipe crown, (b) back axle at the center between the pipe crown and the trench wall, and (c) middle axle above the pipe crown. For each loading step, the truck was kept for a while till all readings from the displacement transducers that were attached inside the pipe to measure the changes in diameter of the pipe were stable.

Test Section A. **FIGURE 6.52** shows the positions of the truck wheels when the truck loads were applied on Test Section A. **FIGURE 6.53** shows the measured earth pressures around the pipe against the time elapse both in Test Sections A and B with the truck loadings. When the truck load was applied directly above the instrumented section (Section 2) close to the centerline on Test Section A, there were no or little changes in the earth pressures around the pipe at the instrumented section (Section 3) of the pipe in Test Section B. It showed that the truck load applied above the instrumented section close to the centerline of the roadway (Section 2) in Test Section A had no or negligible effects on the instrumented section (Section 3) close to the centerline of the roadway in Test Section B.

When the back axle was placed above the crown (**FIGURE 6.52a**), the pressure cells placed at the crown, $1E_{C0}$ and $2E_{C0}$, in Sections 1 and 2 on the western test section (Section A) recorded the equal highest vertical earth pressures of 10.03 psi. The vertical earth pressure at 12 in. away from the center ($2E_{C12}$) was 3.71 psi, which was 0.37 times the pressure at the pipe crown ($2E_{C0}$). The horizontal pressure at the pipe springline ($2E'_{s0}$) was 0.16 times the vertical earth pressure at the crown ($2E_{C0}$). The ratio of the horizontal pressure at the springline ($2E'_{s0}$) to that at the trench wall ($2E'_{sw}$) was 1.32. The vertical earth pressure at the invert ($2E_{I0}$) was 1.51 psi, which was 0.15 times the pressure at the pipe crown ($2E_{C0}$). When the back axle between the pipe crown and trench wall (**FIGURE 6.52b**) and the middle axle above the pipe crown (**FIGURE 6.52c**) were applied, there were not much variations (little higher) in the earth pressures measured around the pipe from those measured with the back axle above the pipe crown (**FIGURE 6.52a**) as shown in **FIGURE 6.53**.



(a) Back axle over the crown (b) Back axle in between the crown and trench wall (c) Middle axle over the crown

FIGURE 6.52 Axle loads on the pipe in Test Section A

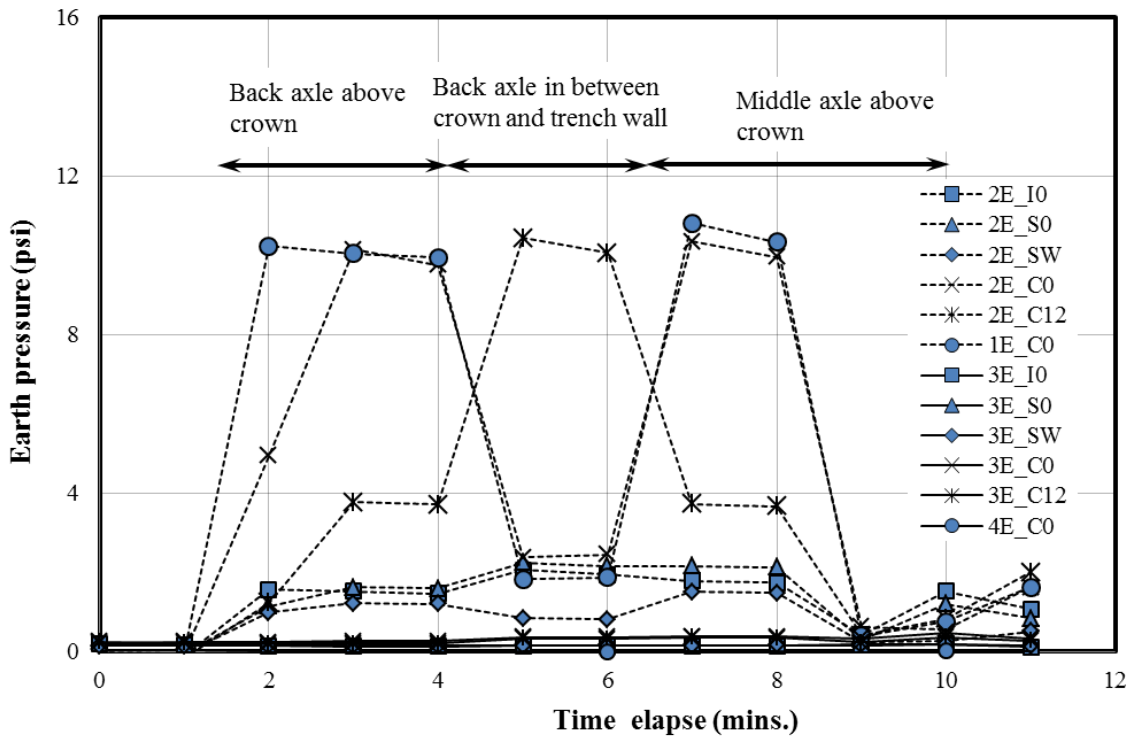


FIGURE 6.53 Measured earth pressures around the pipe under truck loading on Test Section A

Test Section B. **FIGURE 6.54** shows the positions of the wheels when the truck loads were applied on Test Section B. In Test Section B, when the back axle was applied between the pipe crown and the trench wall (**FIGURE 6.54a**), the middle axle was on the surrounding soil whereas in Test Section A, the middle axle was on the trench (**FIGURE 6.52b**). It made the loading configuration different in Test Section B from Test Section A when the back axle was applied between the pipe crown and trench wall. **FIGURE 6.55** shows the measured earth pressures around the pipe against the time elapse in both Test Sections A and B with the truck loadings. When the truck load was applied on Test Section B, there were no or little changes in the pressures measured around the pipe at the instrumented section (Section 2) of the pipe in Test Section A. It showed that the truck load applied on Test Section B had no or negligible effects on the pipe in Test Section A.

When the back axle was placed between the pipe crown and the trench wall (**FIGURE 6.54a**), the pressure cell $3E_{C12}$ placed at 12 in. away from the pipe crown in Section 3 on Test Section B recorded the highest vertical earth pressures of 8.18 psi. The vertical earth pressure at the pipe crown $3E_{C0}$ showed 0.97 psi. When the back axle was placed above the crown (**FIGURE 6.54b**), the earth pressures measured around the pipe in Test Section B were similar to those obtained with the back axle above the crown in Test Section A. The pressure cells placed at the crown, $4E_{C0}$ and $3E_{C0}$, in Sections 4 and 3 on the eastern test section (Section B) recorded the highest pressures of 8.91 and 8.35 psi, respectively. The vertical earth pressure at 12 in. away from the center ($3E_{C12}$) was 5.01 psi, which was 0.6 times the pressure on the pipe crown ($3E_{C0}$). The horizontal earth pressure at the pipe springline ($3E'_{s0}$) was 0.11 times the vertical earth pressure on the crown ($3E_{C0}$). The ratio of the horizontal pressure at the springline ($3E'_{s0}$) to that at the trench wall ($3E'_{sw}$) was 1.16. The vertical earth pressure at the invert ($3E_{I0}$)

was 1.04 psi, which was 0.12 times the pressure on the pipe crown ($3E_{C0}$). For the middle axle above the pipe crown (**FIGURE 6.54c**), the earth pressure distribution around the pipe was similar to that for the back axle applied above the crown (**FIGURE 6.54b**).

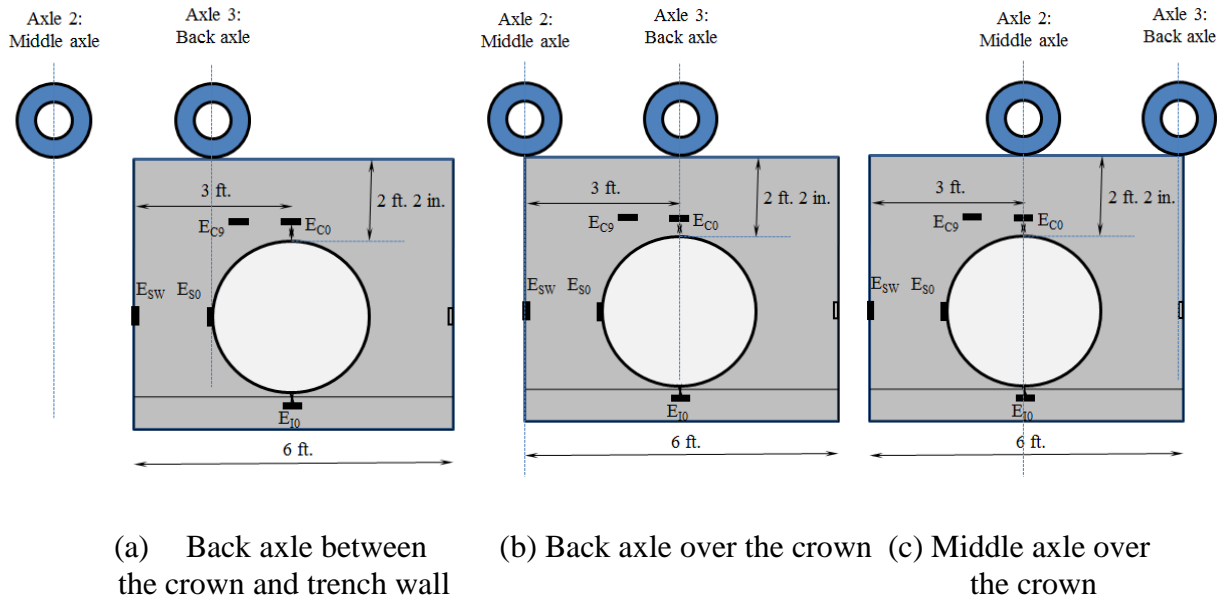


FIGURE 6.54 Axle loads on the pipe in Test Section B

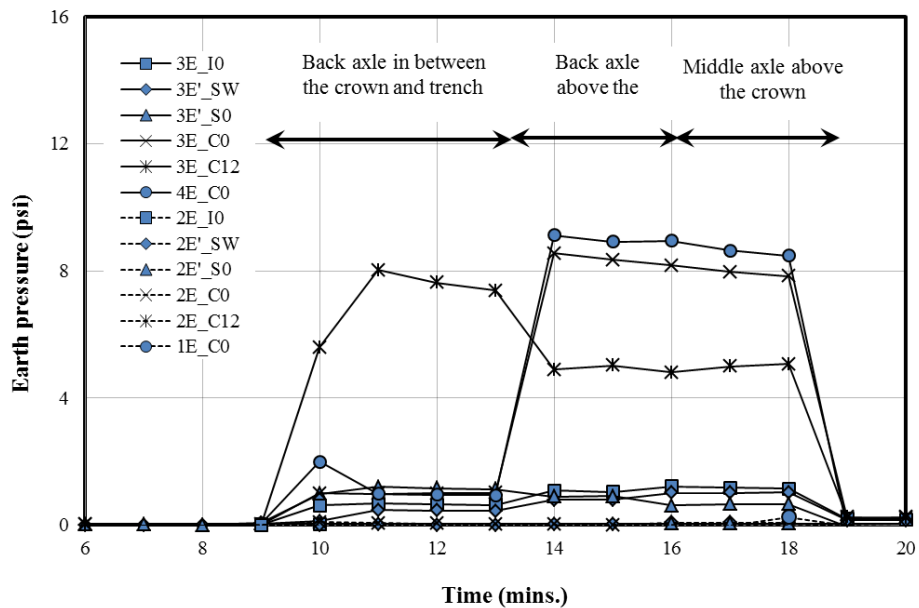


FIGURE 6.55 Measured earth pressures around the pipe under truck loading on Test Section B

Comparison of test results

Laboratory Tests. FIGURE 6.56 shows the comparison of the earth pressure distributions around the pipe in Test 1 (with the AB-3-I base course and the KR sand backfill) and Test 2 (with the KR sand as the base course and the backfill). The measured earth pressures in Test 1 were less than those in Test 2, with the exception of the earth pressures measured at the invert (E_{I0}). Their differences were even more pronounced at the higher applied pressure. The lower earth pressures around the the pipe in Test 1 were due to the higher distribution of the pressures by the stiff AB-3-I base course than the sand base course.

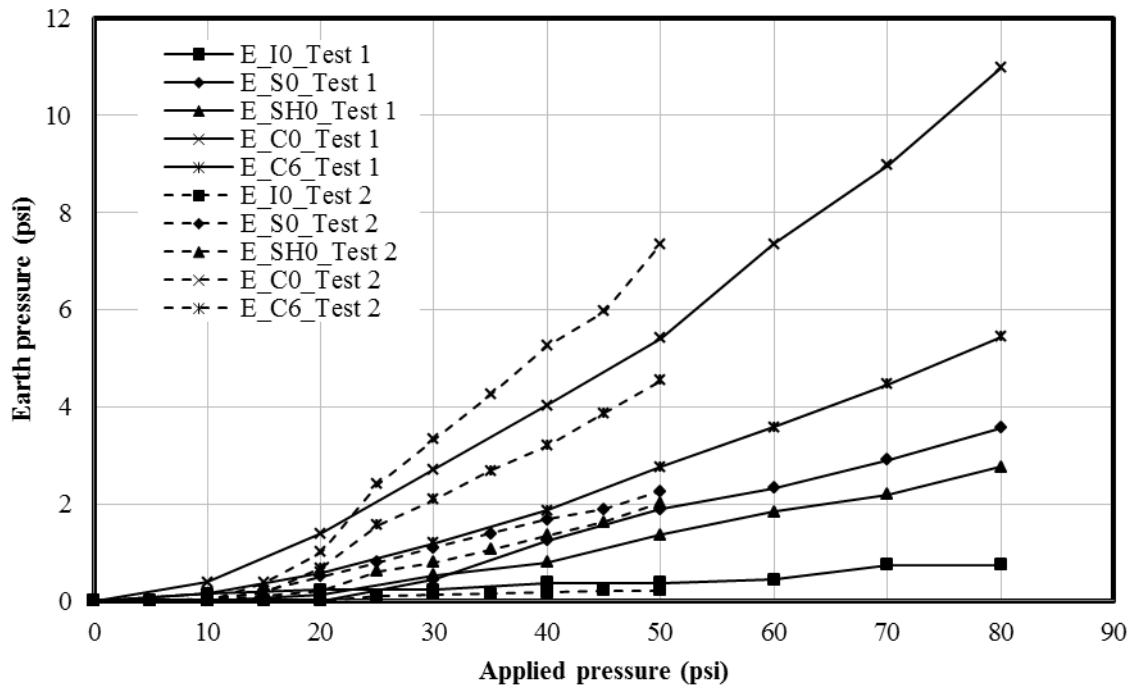


FIGURE 6.56 Measured earth pressures around the pipe in Test 1 and Test 2

FIGURE 6.57 shows the comparison of the measured earth pressures around the pipe for two different backfills: the Kansas River sand in Test 1 and the crushed stone (CS-I) in Test 3.

The vertical earth pressures on the crown (E_{C0}) were higher than those (E_{C6}) at 6 in. away from the crown in Test 1 whereas the earth pressures on the crown (E_{C0}) were lower than those (E_{C6}) in Test 3. Similarly, the horizontal earth pressures at the springline (E'_{S0}) were lower than those (E'_{SH0}) at the shoulder in Test 3 while the horizontal earth pressures at the springline (E'_{S0}) were higher than those (E'_{SH0}) at the shoulder in Test 1. The earth pressure cell at the invert (E_{I0}) showed a higher earth pressure in Test 3 than that in Test 1 because the pipe was lifted up in Test 1 as discussed in **SECTION 6.1.1** but there was little or no lift-up of the pipe in Test 3 during backfilling.

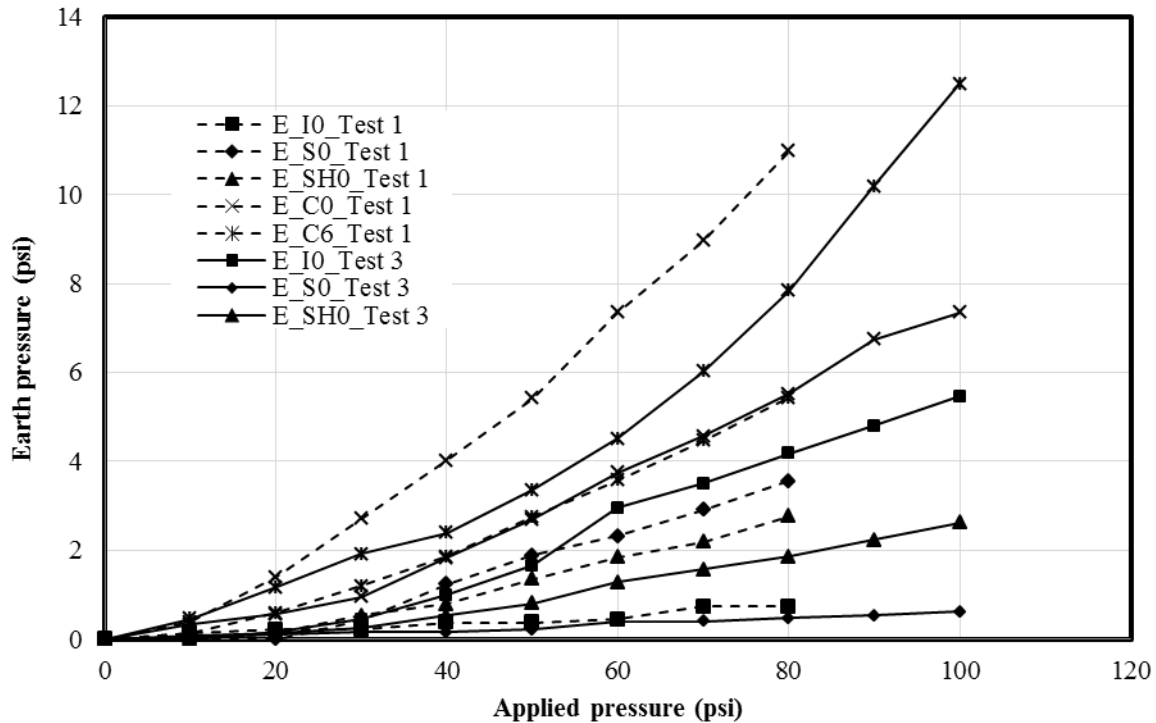


FIGURE 6.57 Measured earth pressures around the pipe in Test 1 and Test 3

The vertical earth pressures on the top of the pipe under the applied static load in each test were calculated using the simplified distribution method (AASHTO, 2007) and the approach

proposed by Giroud and Han (2004) (as discussed in **SECTION 2.1**). The moduli of elasticity of the Kansas River (KR) sand, the crushed stone (CS-I), and the AB-3-I aggregate needed for the calculation of the earth pressures were determined from the small plate loading tests (see **SECTIONS 3.2.2** and **3.2.3**). The calculated earth pressures are then compared with the average pressures of E_{C0} , E_{C6} , and E_{C12} measured on the top of the pipe in **FIGURE 6.58**. The measured pressures on the crown of the pipe were close to those calculated using the Giroud and Han (2004) method as compared with the simplified distribution method (AASHTO, 2007).

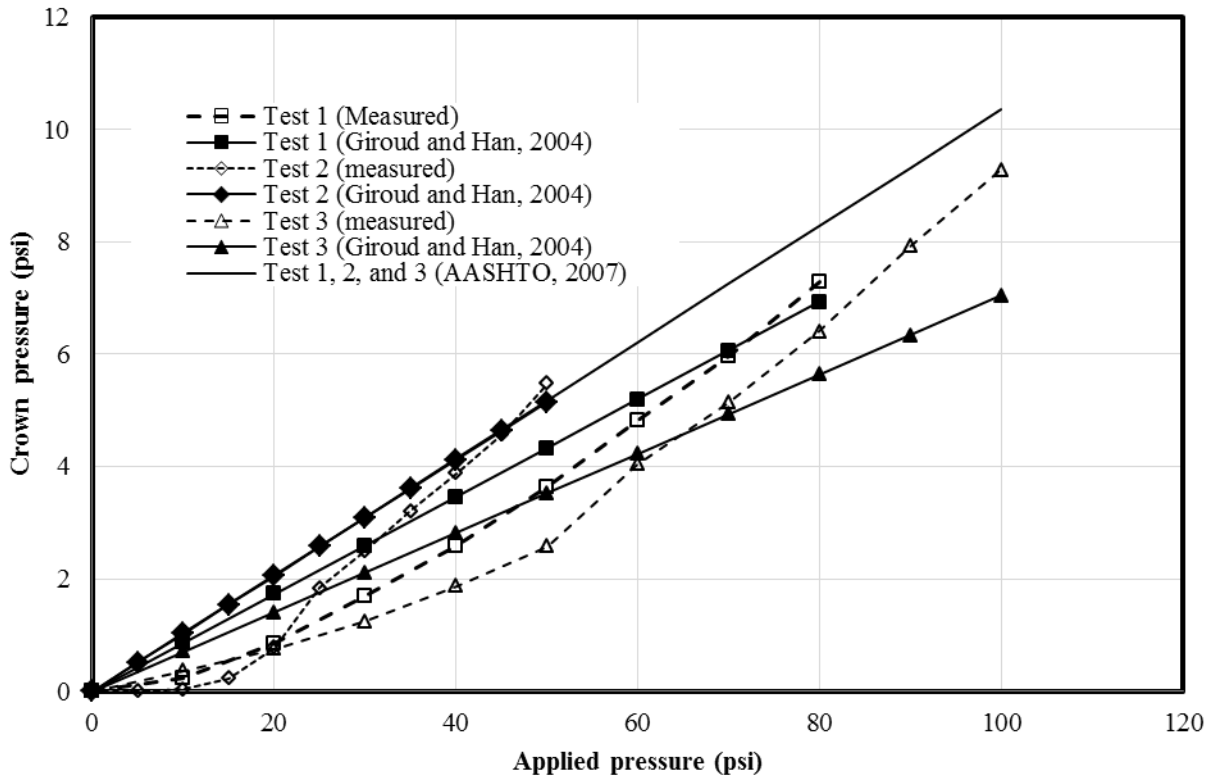


FIGURE 6.58 Comparison of the measured crown pressures with the 2007 AASHTO LRFD Bridge Design Specifications and the Giroud and Han (2004) methods

In Tests 1 and 2, the pressure cell E_{S2} was not placed to measure the vertical pressure at the springline. The pressure cell (E_{S2}) at the springline was added at 2 in. away from the pipe

surface in Test 3 and the measured earth pressure was used to calculate the coefficient of lateral earth pressure (K). **FIGURE 6.59** shows the coefficient of lateral earth pressure at the springline (K), which was calculated from the measured horizontal pressure at the springline (E'_{s0}) divided by the measured vertical pressure measured at the springline (E_{S2}). The average coefficient of lateral earth pressure at the springline (K) was approximately 0.2. Similarly, the coefficients of lateral earth pressure at the shoulder and the haunch were calculated by the measured horizontal pressures E'_{SH0} and E'_{H0} divided by the measured vertical pressures by E_{S2} . **FIGURE 6.60** shows the calculated coefficients at the shoulder, the springline, and the haunch as compared with the theoretical coefficients of lateral earth pressure, K_a , K_o , and K_p , calculated using the friction angle of the crushed stone of 54° . The calculated coefficients (K) at the springline and the haunch from the measured pressures were close to the lateral earth coefficient at rest K_o . However, the calculated coefficient at the shoulder (K) from the measured pressures was 0.70, which was higher than the lateral earth coefficient at rest K_o .

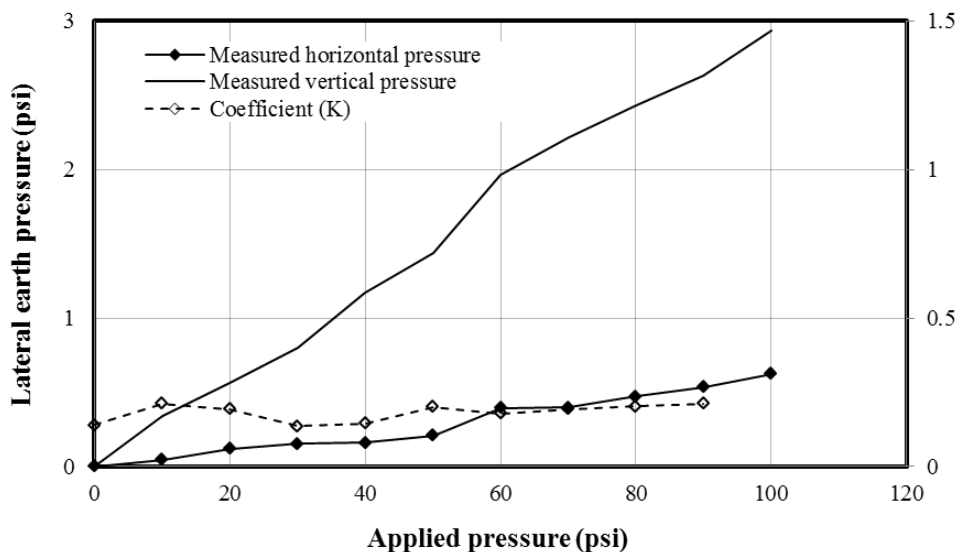


FIGURE 6.59 Calculated lateral earth pressure coefficients (K) at the springline from the measured pressures in Test 3

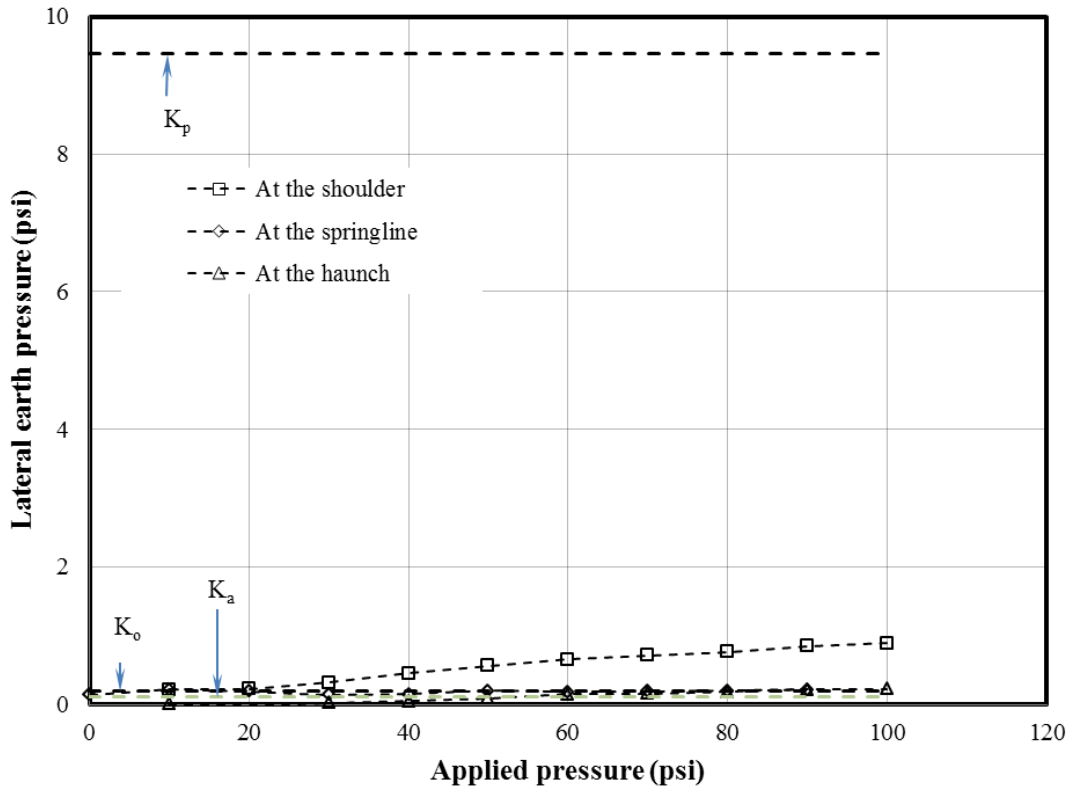


FIGURE 6.60 Comparison of the lateral earth pressure coefficients (K) at the shoulder, springline, and haunch in Test 3

Field Test. TABLE 6.1 shows the comparison of the earth pressure distributions around the pipe in Test Section A (with the AB-3-II aggregate as backfill) and Test Section B (with the crushed stone CS-II as backfill). When the truck load was applied with the back and middle axles over the pipe crown in Test Sections A and B, the measured earth pressures around the pipe in Test Section A were higher than those in Test Section B except the earth pressure at 12 in. away from the pipe ($3E_{C12}$). For example, the earth pressures at the crown ($3E_{C0}$) in Test Section B were lower than those in Test Section A whereas the earth pressures at 12 in. from the crown of the pipe ($3E_{C0}$) in Test Section A were higher than those in Test Section B. These variations may be

due to a wider distribution of the applied truck load caused by the stiff crushed stone (CS-II) used in Test Section A than that of the AB-3-II aggregate used in Test Section B. When the back axle was applied between the crown and the trench wall, the earth pressure distributions around the pipe were not directly comparable between Test Section A and Test Section B because of the different loading configurations (see **FIGURE 6.52b** and **FIGURE 6.54a** for loading configurations).

TABLE 6.1 Comparison of the earth pressures (psi) measured around the pipe in the field test

Sections	Positions	Symbols	Back axle at the crown	Back axle in between the crown and trench wall	Middle axle at the crown
Section A	Crown	1E _{C0}	9.95	1.87	10.33
		2E _{C0}	9.75	2.45	9.95
		2E _{C12}	3.72	10.06	3.66
	Springline	2E _{SW}	1.20	0.82	1.48
		2E _{S0}	1.60	2.16	2.13
	Invert	2E _{I0}	1.47	1.95	1.74
Section B	Crown	4E _{C0}	8.91	0.96	8.64
		3E _{C0}	8.35	0.99	7.96
		3E _{C12}	5.02	7.63	4.99
	Springline	3E _{SW}	0.79	0.45	1.02
		3E _{S0}	0.91	1.15	0.66
	Invert	3E _{I0}	1.04	0.64	1.17

The vertical earth pressures on the top of the pipe at the location of the pressure cells were calculated using the Foster and Ahlvin (1954) pressure distribution under a uniformly loaded circular area under the applied truck load in each test and compared with the earth pressures measured by the pressure cells as shown in **TABLE 6.2**. The calculated pressures on

the pipe crown (E_{C0}) in Test Section A were lower than the measured pressures; however, the calculated pressures at 12 in. away from the pipe crown (E_{C12}) in Test Section A (with the AB-3-II aggregate as backfill) were higher than the measured pressures. This may be due to the concentration of the applied load on the crown of the pipe in Test Section A. On the other hand, the calculated earth pressures on the crown and at 12 in. away from the crown (E_{C0} and E_{C12}) were close to the earth pressures measured by the pressure cells in Test Section B (with the crushed stone CS-II as backfill). The concentration of the pressures at the crown in Test Section A as compared with that in Test Section B may be due to the relatively lower stiffness of the AB-3-II aggregates in Test Section A than that of the crushed stone CS-II in Test Section B.

The vertical earth pressures on the top of the pipe under the applied truck load with back and middle axles above the crown in each test were also calculated using two approximate methods: the simplified distribution method (AASHTO, 2007) and the approach proposed by Giroud and Han (2004) (as discussed in **SECTION 2.1**). The moduli of elasticity of the AB-3 aggregate needed for the calculation of the earth pressures were determined from the small plate loading test (see **SECTIONS 3.2.2**). When the truck axle load was applied directly above the pipe crown, the pressure induced by the second axle load (at 3 ft. distance apart) on the top of the pipe was found to be very small using the Foster and Ahlvin (1954) pressure distribution under a uniformly loaded circular area. For example, when the back axle was applied above the pipe crown (**FIGURE 6.54b**), the pressure on the pipe crown due to the middle axle load was found to be 0.24 psi, which was considered small or negligible. Therefore, in the calculation of the earth pressures on the top of the pipe using the approximate methods, the effect of the second axle load was neglected. The calculated earth pressures are then compared with the average earth pressures of E_{C0} and E_{C12} measured on the top of the pipe in **TABLE 6.3**. The measured

pressures at the crown of the pipe were close to those calculated using the Giroud and Han (2004) method as compared with the simplified distribution method (AASHTO, 2007).

TABLE 6.2 Comparison of the measured and calculated (Foster and Ahlvin, 1954) earth pressures (psi) around the pipe in the field test

Sections	Location	Back axle at the crown		Back axle in between the crown and trench wall		Middle axle at the crown	
		Measured	Calculated	Measured	Calculated	Measured	Calculated
Section A	1E _{C0}	9.95	8.82	1.87	4.16	10.33	8.82
	2E _{C0}	9.75	8.82	2.45	4.16	9.95	8.82
	2E _{C12}	3.72	4.8	10.06	9.08	3.66	5.82
Section B	4E _{C0}	8.91	8.82	0.96	2.08	8.64	8.82
	3E _{C0}	8.35	8.82	0.99	2.08	7.96	8.82
	3E _{C12}	5.02	5.82	7.63	8.58	4.99	4.8

TABLE 6.3 Comparison of the average measured crown pressures (psi) with the 2007 AASHTO LRFD Bridge Design Specifications and Giroud and Han (2004) methods

Section	Back axle at the crown		
	Measured	AASHTO (2007)	Giroud and Han (2004)
Section A	6.7	9.2	8.9
Section B	6.7	9.2	9.2
	Middle axle at the crown		
Section A	6.8	9.2	8.9
Section B	6.5	9.2	9.2

Summary

The earth pressures measured around the pipe in the field tests had similar trends to the earth pressures measured around the pipe in the laboratory tests. From the laboratory and field tests, it was found that the stiffer materials in the soil cover above the pipe crown resulted in the lower pressures around the pipe. The pressures measured on the pipe crown were predicted well by the available theories and the approximate methods. The Giroud and Han (2004) method accurately predicted the vertical earth pressure on the top of the pipe induced by the applied load on the surface both in the laboratory and in the field when there were two layers of different soils above the pipe crown. The 2007 AASHTO LRFD Bridge Design Specifications slightly over-predicted the vertical earth pressure in the test sections with two layers of different soils above the crown.

6.2.3 Pipe Deflection Results

Laboratory Tests

Test 1. The deflections of the pipe (or the changes of the inside diameters) against the applied pressures from Test 1 are shown in **FIGURE 6.61**. As the load increased, the vertical diameter of the pipe (ΔD_V) decreased while the horizontal diameter of the pipe (ΔD_H) increased. **FIGURE 6.61** also shows that the horizontal deflection of the pipe (ΔD_H) was less than the vertical deflection (ΔD_V). When the applied pressure was 80 psi, the decrease in the vertical diameter and the increase in the horizontal diameter at the center of the pipe section (ΔD_{VC} and ΔD_{HC}) were 0.035 in. (0.147% of the initial diameter) and 0.021 in. (0.89% of the initial diameter), respectively. The vertical deflections at the center of the pipe (ΔD_{VC}) were 1.60 to 1.67 times the horizontal deflections at the center of the pipe (ΔD_{HC}), and 2.00 to 2.55 times the vertical deflections at 1 ft. from the center of the test pipe (ΔD_{V1}).

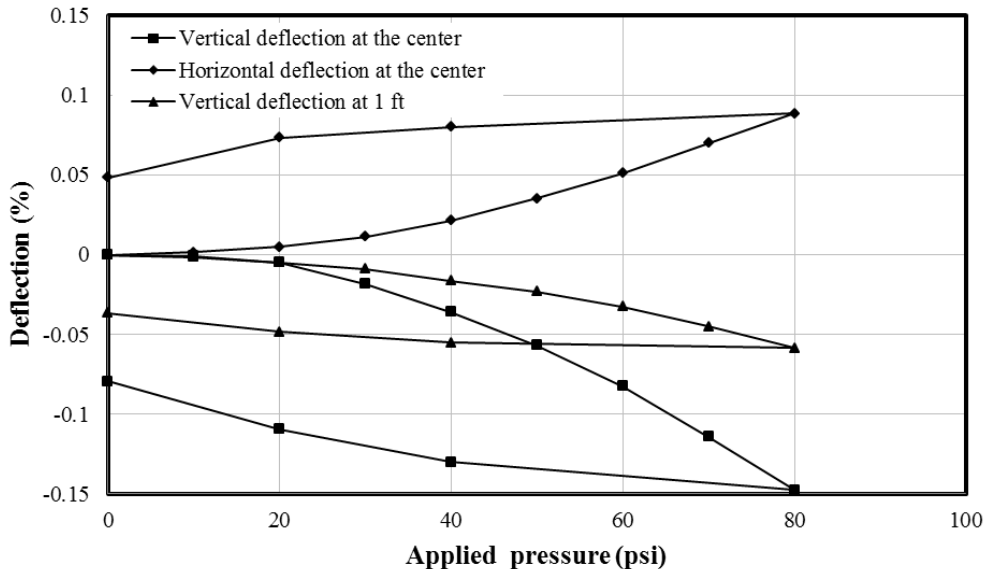


FIGURE 6.61 Deflections of the pipe under the static load in Test 1

Test 2. FIGURE 6.62 shows the deflections of the pipe against the applied pressures from Test 2. When the applied pressure was 50 psi, the decrease in the vertical diameter and the increase in the horizontal diameter at the center of the pipe section (ΔD_{VC} and ΔD_{HC}) were 0.017 in. (0.07% of the initial diameter) and 0.008 in. (0.035% of the initial diameter), respectively. The vertical deflections at the center of the pipe (ΔD_{VC}) were 1.60 to 1.67 times the horizontal deflections at the center of the pipe (ΔD_{HC}), and 3.5 to 3.9 times the vertical deflections at 1 ft. from the center of the test pipe (ΔD_{V1}).

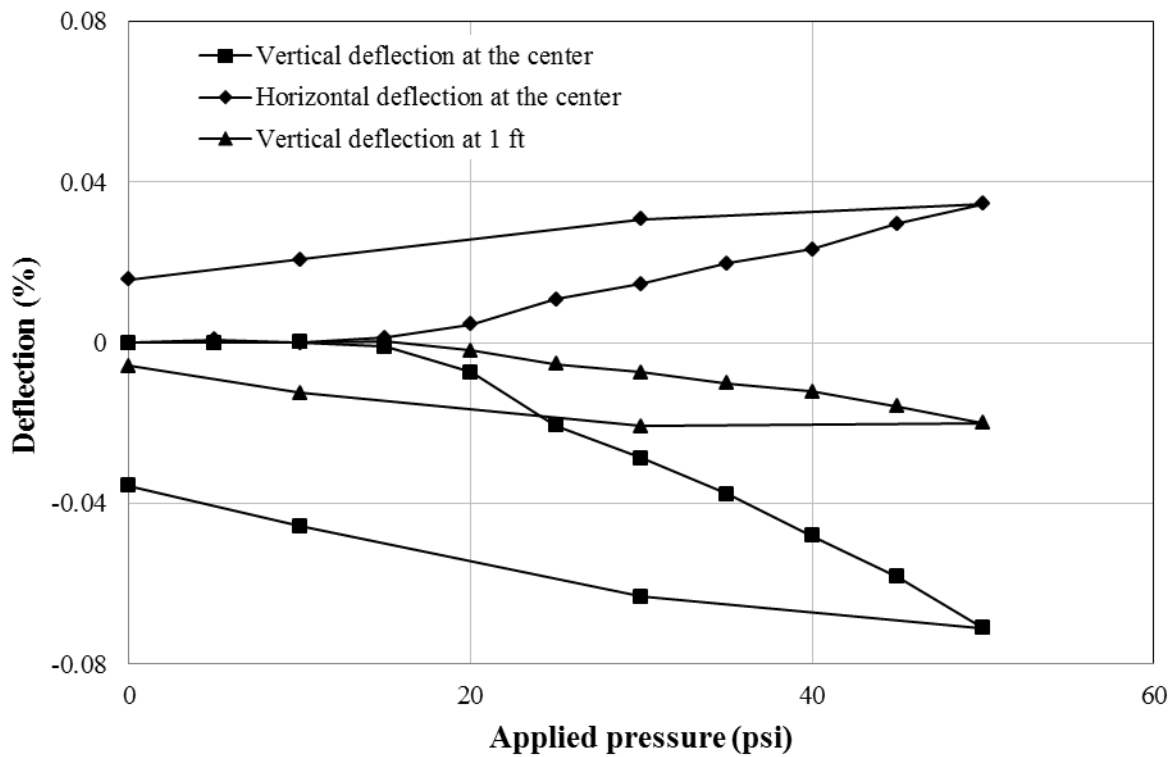


FIGURE 6.62 Deflections of the pipe under the static load in Test 2

Test 3. FIGURE 6.63 shows the deflections of the pipe against the applied pressures from Test 3. When the applied pressure was 100 psi, the decrease in the vertical diameter and the increase in the horizontal diameter at the center of the pipe section (ΔD_{VC} and ΔD_{HC}) were 0.081 in. (0.34% of the initial diameter) and 0.050 in. (0.21% of the initial diameter), respectively. The vertical deflections at the center of the pipe (ΔD_{VC}) were approximately 1.64 times the horizontal deflections at the center of the pipe (ΔD_{HC}), and 1.53 times the vertical deflections at 1 ft from the center of the test pipe (ΔD_{V1}).

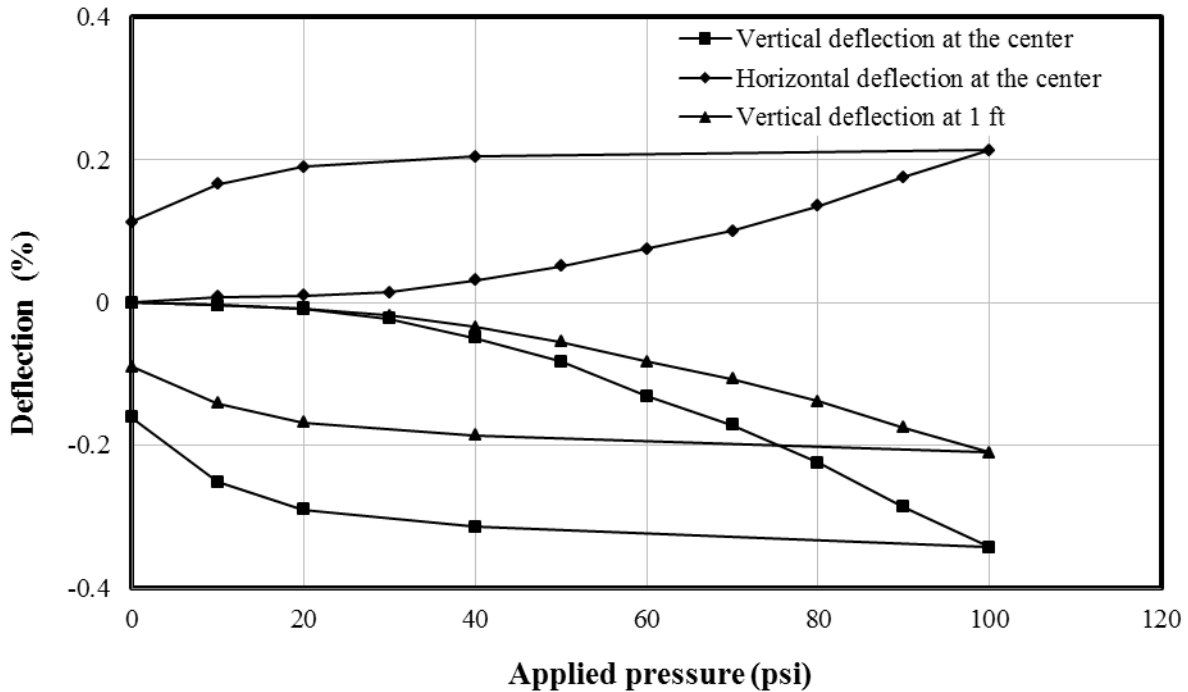


FIGURE 6.63 Deflections of the pipe under the static load in Test 3

Field Test

Test Section A. The deflections of the pipe (or the changes of the inside diameters) with truck axle loadings against the time elapse both in Test Sections A and B are shown in FIGURE 6.64.

When the truck load was applied directly above the instrumented section (Section 2) close to centerline on Test Section A, there were no or little changes in diameters of the pipe in the instrumented section (Section 3) of the pipe in Test Section B. It is shown that the truck load applied above the instrumented section close to the centerline of the roadway (Section 2) in Test Section A had no or negligible effects on the instrumented section (Section 3) close to the centerline of the roadway in Test Section B.

When the truck load was applied above the pipe, the vertical diameter of the pipe (ΔD_V) decreased while the horizontal diameter of the pipe (ΔD_H) increased. **FIGURE 6.60** also shows that the horizontal deflection of the pipe (ΔD_H) was less than the vertical deflection (ΔD_V). The maximum deformation of the pipe was pronounced when the middle axle load was applied above the pipe crown. The deflections of the pipe occurred with the middle axle above the pipe crown was slightly higher or close to those when the back axle was above the pipe crown. The back axle placed between the pipe crown and the trench wall deflected the pipe less as compared with those obtained under the back and middle axles above the pipe crown. When the middle axle was placed above the pipe crown, the decrease in the vertical diameter and the increase in the horizontal diameter of the pipe in Test Section A (ΔD_V and ΔD_H) were 0.071 in. (0.20% of the initial diameter) and 0.028 in. (0.08% of the initial diameter), respectively. The vertical deflections of the pipe (ΔD_V) were 2.53 times the horizontal deflections of the pipe (ΔD_H). After the completion of the static loading, the truck was run over the pipe at slow speed and the deflections of the pipe were even higher than those at the static truck loading as shown in **FIGURE 6.64**. The decrease in the vertical diameter and the increase in the horizontal diameter of the pipe in Test Section A (ΔD_V and ΔD_H) were 0.088 in. (0.24% of the initial diameter) and 0.039 in. (0.11% of the initial diameter) when the truck was run at the slow speed, respectively.

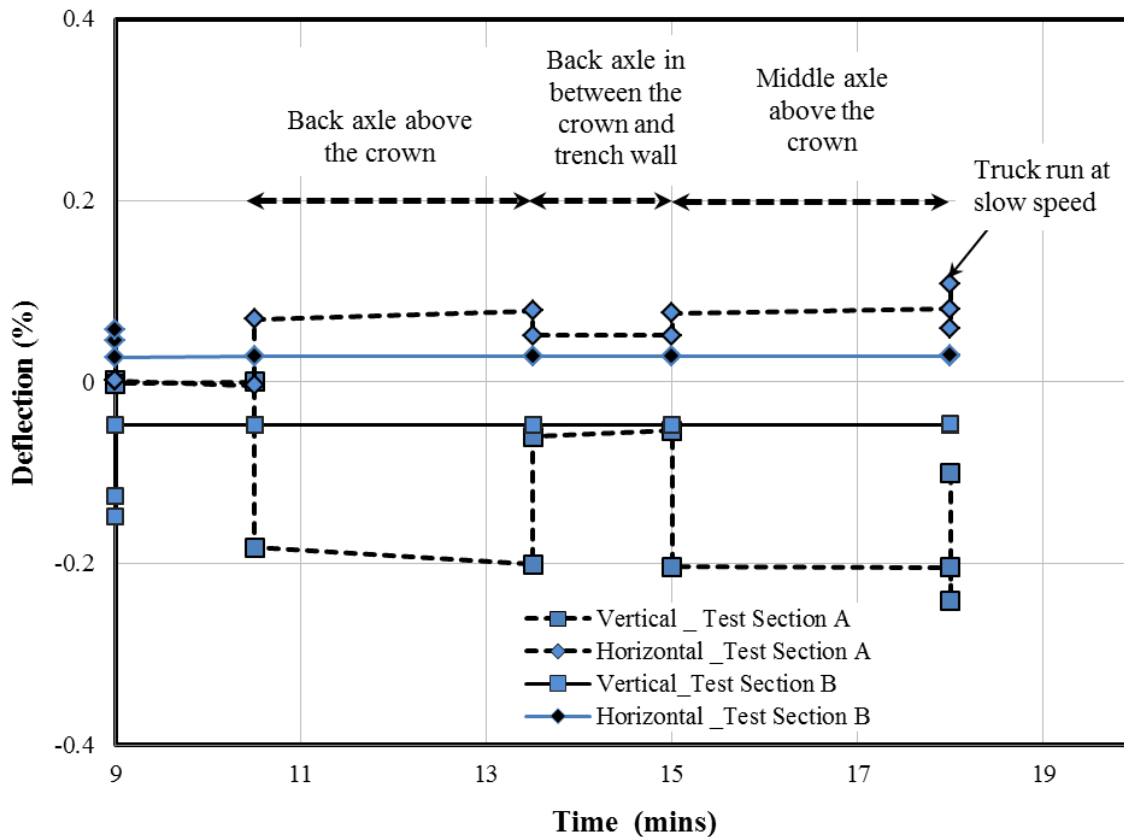


FIGURE 6.64 Deflections of the pipe under the truck loading in Test Section A

Test Section B. The deflections of the pipe (or the changes of the inside diameters) with the truck axle loadings against the time elapse both in Test Sections A and B are shown in **FIGURE 6.65**. The deflection of the pipe in Test Section B was similar to that in Test Section A. When the truck load was applied on Test Section B, there were no or little changes in diameters of the pipe in Test Section A.

The maximum deflection of the pipe was pronounced when the back axle was placed above the pipe crown. The deflection of the pipe occurring with the back axle above the crown was slightly higher or close to that when the middle axle was above the pipe crown. The back axle placed between the pipe crown and the trench wall deflected the pipe less as compared with those obtained under the back and middle axles above the pipe crown. When the back axle was

placed above the pipe crown, the decrease in the vertical diameter and the increase in the horizontal diameter of the pipe in Test Section B (ΔD_V and ΔD_H) were 0.05 in. (0.14% of the initial diameter) and 0.016 in. (0.045% of the initial diameter), respectively. The vertical deflections of the pipe (ΔD_V) were 3.22 times the horizontal deflections at the center of the pipe (ΔD_{HC}). After the completion of the static loading, the truck was run over the pipe at slow speed and the deflections of the pipe were even slightly higher than those at the static truck loading as shown in **FIGURE 6.65**. The decrease in the vertical diameter and the increase in the horizontal diameter of the pipe in Test Section A (ΔD_{VC} and ΔD_{HC}) were 0.053 in. (0.15% of the initial diameter) and 0.02 in. (0.057% of the initial diameter) when the truck was run at slow speed, respectively.

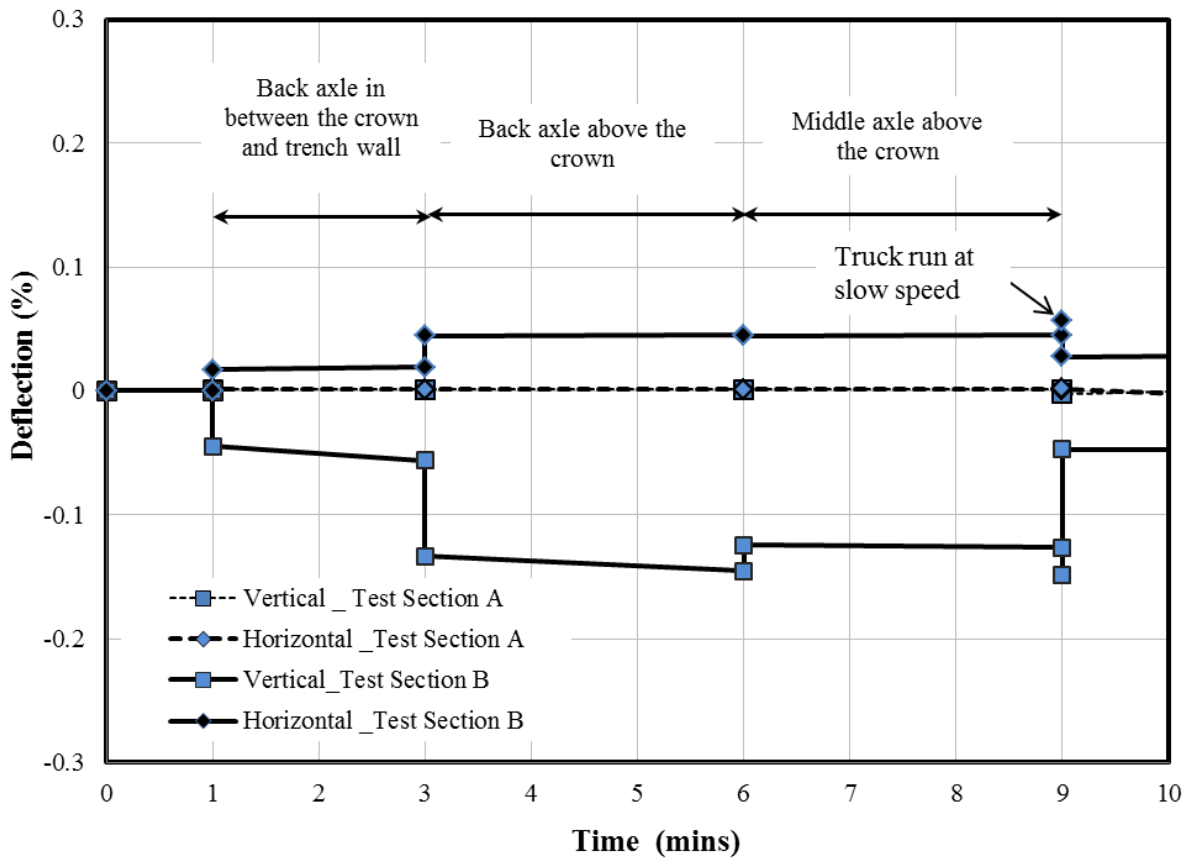


FIGURE 6.65 Deflections of the pipe under the truck loading in Test Section B

Comparison of test results

Laboratory Tests. FIGURE 6.66 shows the comparison of the deflection of the pipe in Test 1 (with the AB-3-I base course and the KR sand backfill) and Test 2 (with the KR sand as the base course and the backfill). The measured vertical deflections at the center of the pipe (ΔD_{VC}) in Test 1 were smaller than those deflections in Test 2. However, the measured horizontal deflections at the center (ΔD_{HC}) and the vertical deflections measured at 1 ft. longitudinally away from the center of the pipe (ΔD_{V1}) were nearly the same in both tests. The differences in the vertical deflections in Tests 1 and 2 resulted from the wider distribution of the load by the stiffer AB-3-I base course in Test 1 than that in Test 2.

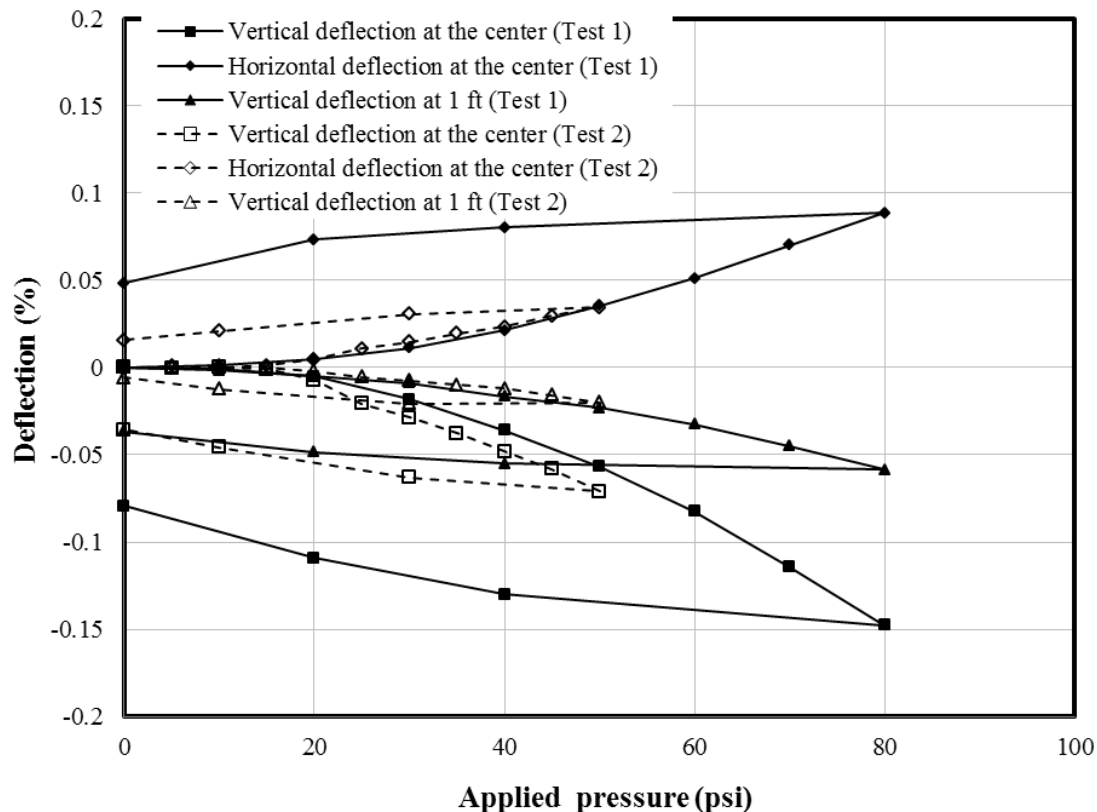


FIGURE 6.66 Comparison of the deflections of the pipe in Tests 1 and 2

FIGURE 6.67 shows the comparison of the measured deflections of the pipe in Test 1 (with the KR sand backfill) and Test 3 (with the crushed stone CS-I backfill). The measured deflections of the pipe in Test 1 were smaller than those in Test 3. The reason for Test 3 to have larger deflections is that the crushed stone CS-II (dumped) had a lower modulus of elasticity than the Kansas River sand (well compacted). The lower modulus of the crushed aggregate (CS-II) caused more load concentrated on the pipe.

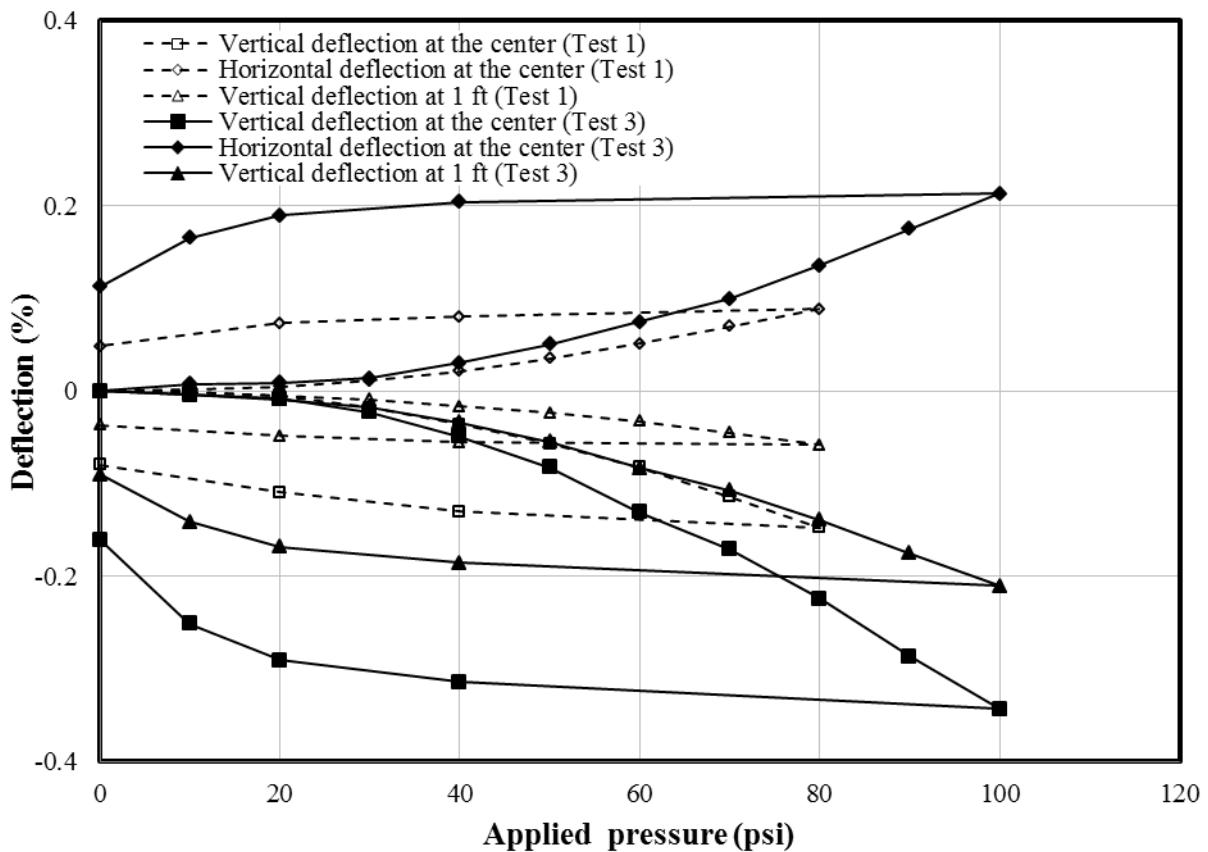


FIGURE 6.67 Comparison of the deflections of the pipe in Tests 1 and 3

FIGURE 6.68 shows the relationship between the vertical and horizontal deflections at the center of the pipe during loading. The ratio of the vertical to horizontal deflection ($\Delta D_{VC}/\Delta D_{HC}$) was approximately 1.64 in Tests 1 and 3 whereas the ratio was approximately 2.0 in Test 2. The ratios of the vertical to horizontal deflection ($\Delta D_{VC}/\Delta D_{HC}$) at the center of the pipe under the buried conditions were higher than those for the pipe tested in air (i.e., 1.25). The higher ratios under the buried conditions were due to the resistance of the backfill against the horizontal deflections of the pipe.

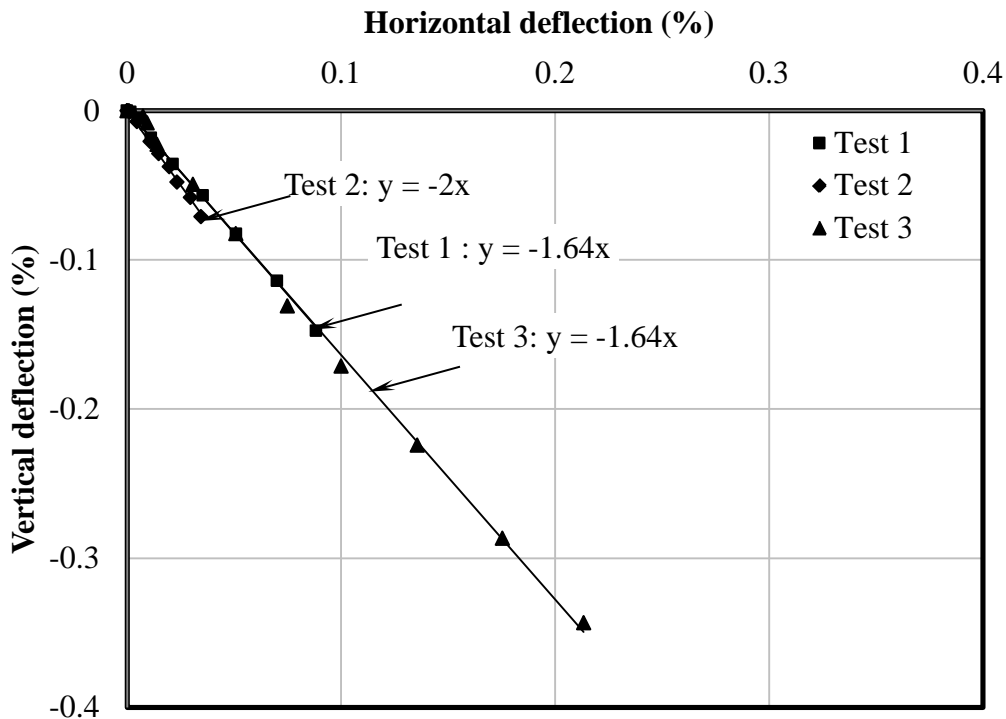


FIGURE 6.68 Relation between the horizontal and vertical deflections at the center of the pipe

FIGURE 6.69 shows the measured horizontal deflections during loading as compared with the calculated horizontal deflections using the Iowa formula (i.e., **EQUATION 2.8**). The

calculation of the horizontal deflections at the center of the pipe were based on the bedding constant (k) of 0.1, the earth pressure on the crown (i.e., live load), the moduli of subgrade reaction of 4,500 psi for the Kansas River sand and 2,500 psi for the crushed stone CS-I. The moduli of the subgrade reaction for the Kansas River sand and the crushed stone CS-I were determined using EQUATIONS 2.14 and 2.15 from the modulus of elasticity described in SECTION 3.2.2. The earth pressures on the crown were calculated using the Giroud and Han (2004) method (see FIGURE 6.58). It is shown that the Iowa formula over-predicted the deflections of the pipe during loading in all tests.

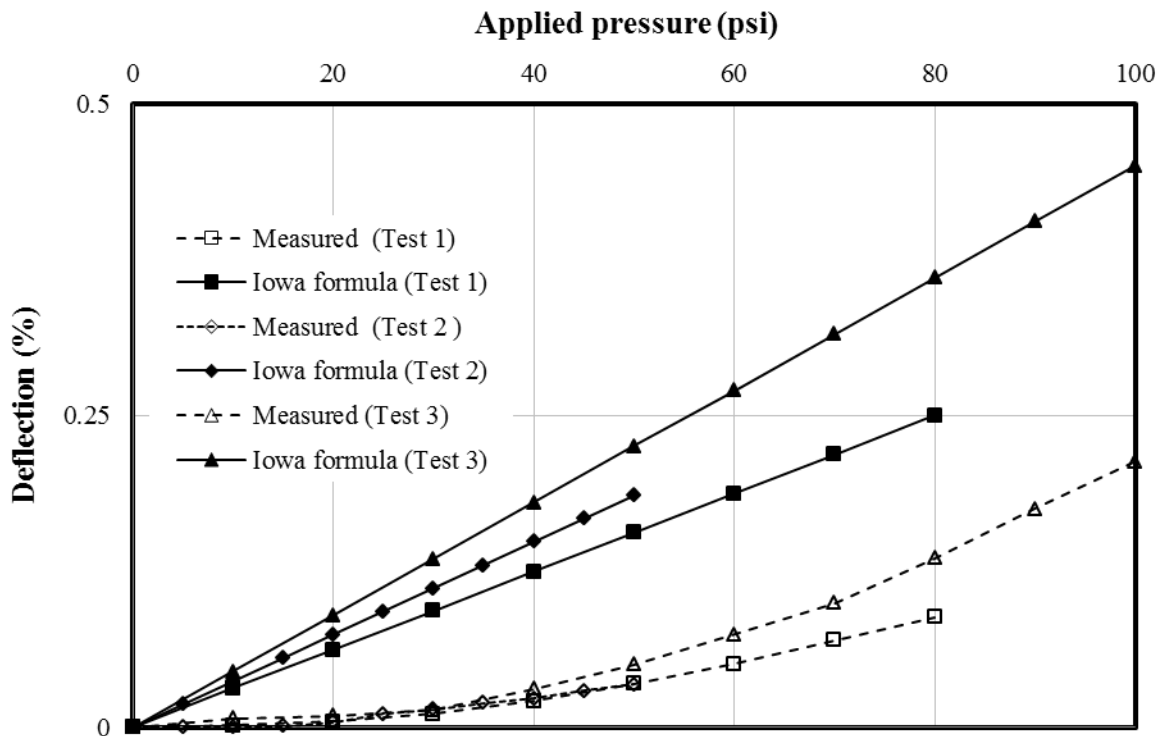


FIGURE 6.69 Comparison of the measured and calculated vertical deflections by the Iowa formula

Field Tests. TABLE 6.4 shows the comparison of the deflections of the pipe in Test Section A (with the AB-3-II aggregate as backfill) and Test Section B (with the crushed stone CS-II as backfill). For the truck load applied with the back or middle axle over the pipe crown, the measured deflections of the pipe in Test Section A were higher than those in Test Section B. These variations may be due to a wider distribution of the applied truck load caused by the stiff crushed stone (CS-II) used in Test Section B than that of the AB-3-II aggregate used in Test Section A. When the back axle was applied between the crown and the trench wall, the deflections of the pipe were not directly comparable between Test Section A and Test Section B because of the different loading configurations (see FIGURE 6.52b and FIGURE 6.54a for loading configurations). The vertical to horizontal deflection ratios ($\Delta D_V/\Delta D_H$) for the pipe varied from 2.55 to 3.22 when the back and middle axles were placed above the pipe and are presented in TABLE 6.4.

TABLE 6.4 Comparison of the deflections of the pipe

Sections	Symbols (unit)	Back axle at the crown	Back axle in between the crown and trench wall	Middle axle at the crown	Moving truck load
Section A	ΔD_V (in.)	0.201	0.053	0.204	0.244
	ΔD_H (in.)	0.078	0.051	0.080	0.173
	Ratio	2.570	1.030	2.550	1.410
	ΔD_H (in.) (calculated)	0.191	0.169	0.1936	-
Section B	ΔD_V (in.)	0.145	0.056	0.126	0.148
	ΔD_H (in.)	0.045	0.019	0.045	0.057
	Ratio	3.220	2.940	2.800	2.590
	ΔD_H (calculated)	0.375	0.332	0.379	-

TABLE 6.4 also shows the calculated horizontal deflections (ΔD_H) using the Iowa formula (i.e., **EQUATION 2.8**). The calculation of the horizontal deflections (ΔD_H) of the pipe under the truck load in Test Sections A and B were based on the bedding constant (k) of 0.1, the earth pressure on the crown (i.e., applied truck load), and the moduli of subgrade reaction of 5,950 psi for the compacted AB-3-II aggregate and 3,700 psi for the compacted crushed stone (CS-II). The moduli of the subgrade reaction for the AB-3-II aggregate and the crushed stone (CS-II) were determined using **EQUATIONS 2.14** and **2.15** from the modulus of elasticity described in **SECTION 3.2.2**. The average values of the measured earth pressures on the crown (E_{C0}) and at 12 in. away from the crown (E_{C12}) were calculated (**TABLE 6.3**) and used for the deflection calculation. It is shown that the Iowa formula over-predicted the deflections of the pipe during loading in all applied truck loading.

Summary

The deflections of the pipe for various backfill materials with different compaction efforts under the simulated traffic load in the laboratory and the construction vehicle in the field were measured. The deflections of the pipe were less for the pipe with the high stiff backfills. The maximum vertical deflections to the pipe diameter in the laboratory were: 0.15% with 4.52 tons applied load in Test 1, 0.055% with 2.826 tons in Test 2, and 0.34 % with 5.36 tons in Test 3 while the ratios in the field were: 0.2% with 5.25 tons in Test Section A and 0.145 % with 5.25 in Test Section B. The deflections measured in Test 1 (with the compacted KR sand as backfill and the 9 in. AB-3 aggregate base on the top) in the laboratory and in Test Sections A (with the compacted AB-3-II as both backfill and soil cover) and Section B (with the compacted crushed stone CS-II and the 6 in. AB-3 aggregate base on the top) in the field were close to each other.

Test 3 in the laboratory and Test Section B in the field both used the crushed stone (CS) as the backfill materials with the AB-3 aggregate on the top of the crushed stone soil cover (see **FIGURE 4.2** and **5.2** for the test sections). The higher vertical deflection (0.34 %) in Test 3 in the laboratory as compared with the deflection (0.145%) in Test Section B in the field showed that the compaction had the obvious influence for the performance of the SRHDPE pipes. From the above deflection values it is clear that that the pipe did not deflect excessively with the compacted soils as backfill. The deflections produced in all loading cases for the SRHDPE pipe were much smaller than the permissible deflection of 7.5 % according to the KDOT pipe and culvert specification (2007) for the polyethylene and polyvinyl chloride pipe during installation.

The horizontal deflections calculated using the Iowa formula **EQUATION 2.7** were found to be conservative for all test sections both in the laboratory and field. The Iowa formula for the prediction of the horizontal deflection of a buried pipe derived by the Spangler (1941) was found to be un-conservative for stiff pipes and conservative for flexible pipes. In addition, the Iowa formula was derived only to predict the horizontal deflection of pipe assuming that the vertical and horizontal deflections would be approximately equal in magnitude. However, the literature (Masada 1996) indicates that the vertical deflection would be higher than the horizontal deflection in most installation conditions. Therefore, the relation **EQUATION 2.10** proposed by the Masada (2000) for the prediction of the vertical deflection was checked to make sure the applicability in the SRHDPE pipe. The ratio of the vertical to horizontal deflection ($\Delta D_V/\Delta D_H$) was calculated from the measured deflections both in the laboratory and field tests and compared with the ratio calculated using **EQUATION 2.10 in TABLE 6.5**. The moduli of subgrade reaction of 4,500 psi for the Kansas River sand in Tests 1 and 2, 2,500 psi for the crushed stone CS-I (uncompacted) in Test 3, 5,950 psi for the compacted AB-3-II aggregate in Test Section A,

and 3,700 psi for the compacted crushed stone (CS-II) in Test Section B were used to calculate the horizontal to vertical deflection ratio using **EQUATION 2.10**. The good agreement in the measured and calculated ratios suggests that the relation provided by the Masada (2000) can be used to predict the vertical deflection of the pipe with known horizontal deflection.

TABLE 6.5 Horizontal to vertical deflection ratio

Tests		Horizontal to vertical ration	
		From measured data	Masada (2000)
Laboratory	Test 1	1.64	1.98
	Test 2	2.00	1.98
	Test 3	1.64	1.54
Field	Section A	2.56	2.30
	Section B	3.01	2.1

6.2.4 Strain Results

Laboratory Tests

Test 1. The circumferential and radial strains on the steel of the pipe are shown in **FIGURE 6.70**. The strain gages, G_{SC1} and G_{SC2} at the springline and G_{IC1} and G_{IC2} at the invert in the circumferential direction, showed an increase in the compression strains, while G_{SR1} and G_{SR2} at the springline and G_{CR1} and G_{CR2} on the crown in the radial direction showed an increase in the tensile strains under the applied pressures. The maximum circumferential strain of 0.0034% (G_{SC1} , compressive strain) and the maximum radial strain of 0.0031% (G_{SR2} , tensile strain) developed at the maximum plate load. The strain gages fixed on both sides of the steel rib at any particular location gave similar values (i.e., there were no sudden changes in the strain values). This result indicates that the out-of-plane buckling of the steel ribs observed during the parallel plate load tests at a high level of load did not occur during the static loading. The maximum strains, which were observed at the springline in the circumferential direction, are compared with the calculated values in **FIGURE 6.71**. The strains on the steel were calculated assuming the pipe carried all the applied loads on the top of the pipe (i.e., neglecting the side resistance from the fill at the springline). The calculated strains were higher than the measured strains.

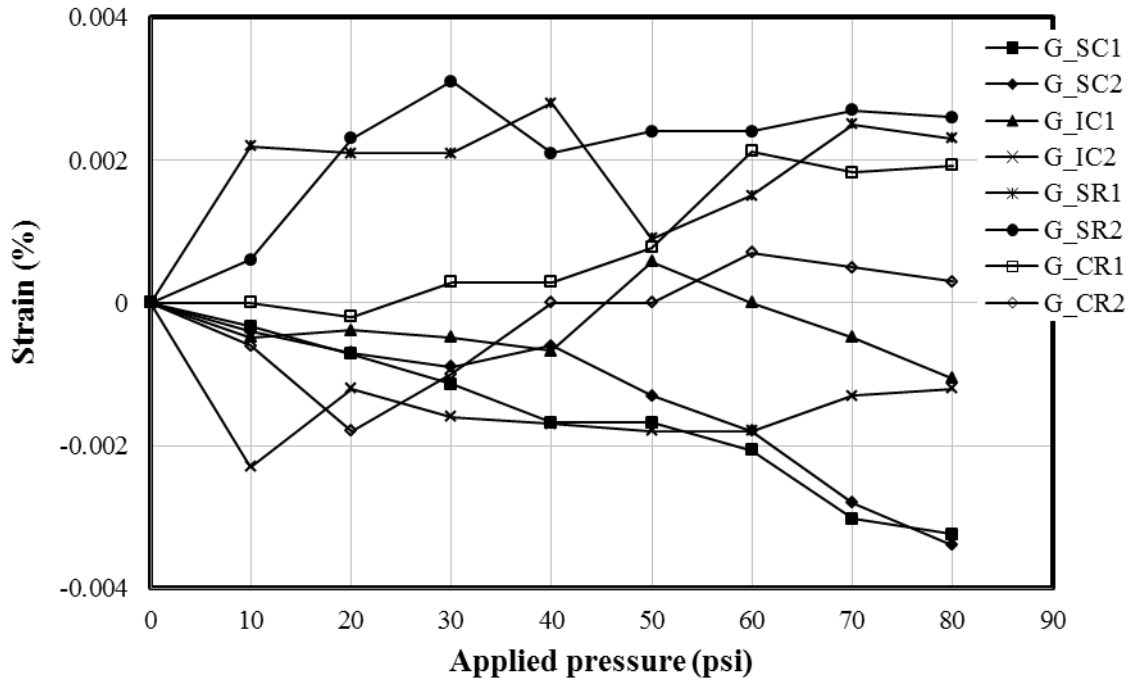


FIGURE 6.70 Measured strains on the steel ribs in Test 1

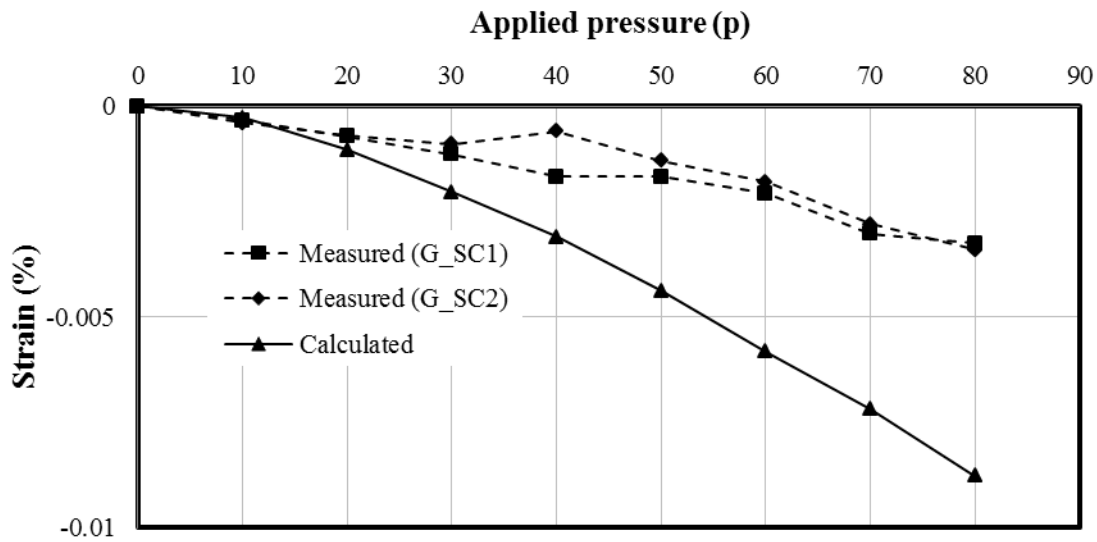


FIGURE 6.71 Measured and calculated strains on the steel ribs at the springline in the circumferential direction

FIGURE 6.72 shows the circumferential and radial strains on the plastic at ribs against the applied static pressures. The strains developing in most locations on the plastic were higher in magnitude than those strains on the steel. Most of the strain gages showed an increase in tensile strains with an increase of the pressures except the strain gage G'_{CR1} which had an increase in compressive strains. During the static loading test, strain gages G'_{SR2} and G'_{CR1} on the plastic rib in the radial direction at the springline and the crown showed the maximum tensile strain of 0.014% and the maximum compressive strain of 0.013%, respectively.

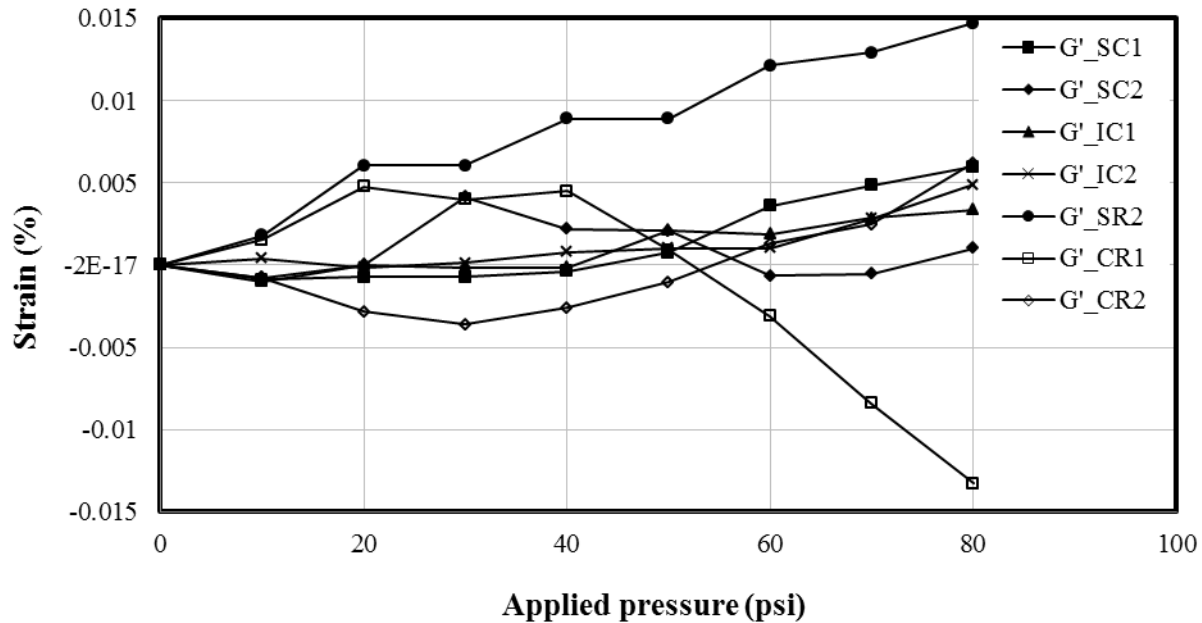


FIGURE 6.72 Measured strains on the plastic at ribs in Test 1

To calculate the strain in the plastic cover on the steel rib, the problem was simplified by assuming the load transfer mechanism as shown in **FIGURE 6.73**. Neglecting the arching effect and the friction between the plastic cover and the steel rib, all the load applied on an area between two ribs have to be carried by the plastic cover on the two ribs based on the vertical equilibrium. Since the maximum earth pressures and the strains (on the plastic) during static

loading was observed on the top of the pipe at the crown, the strains on the plastic cover at the ribs in the radial direction at the pipe crown were calculated and were compared with the measured strains. **FIGURE 6.74** shows the comparison between the measured and calculated strains in the plastic cover on the rib at the pipe crown. The calculated strains were higher than the measured strains.

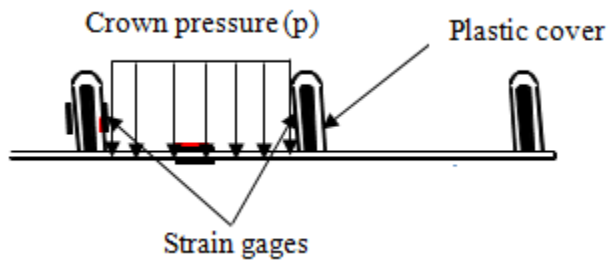


FIGURE 6.73 Simplified load transfer mechanism

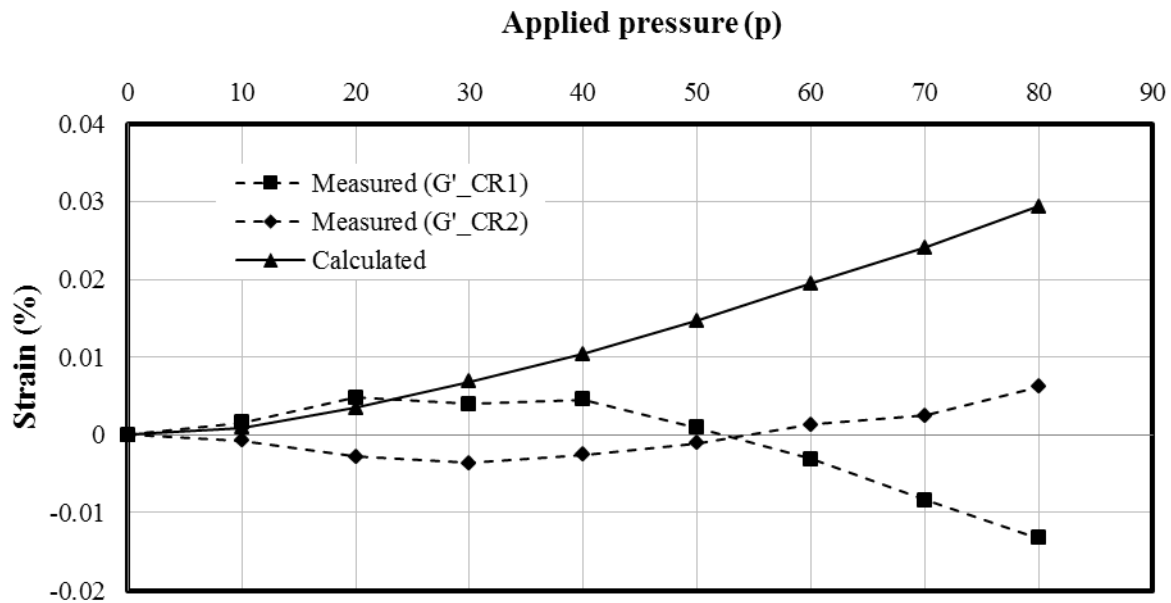


FIGURE 6.74 Measured and calculated strains on the plastic cover at the rib at the pipe crown in the radial direction in Test 1

FIGURE 6.75 shows the strains measured by the strain gages on the plastic wall inside and outside the pipe. The magnitudes of the strains on the pipe walls were higher than the strains on the steel and the plastic at the ribs. Most strain gages showed an increase in the tensile strains with an increase of the applied pressures except the strain gage G''_{SL3} , which had an increase in the compressive strains under the applied pressures. The maximum tensile strain of 0.13% was recorded by the strain gage G''_{CL1} while the maximum compressive strain of 0.023% was recorded by the strain gage G''_{SL3} under the applied static pressure of 80 psi. The strain gages on the pipe valley experienced the tensile strains and those on the inside wall had more tensile strains than those on the outside wall. This behavior of the valley wall on strain values indicates that the valley wall may have the combined bending and membrane effects. A numerical model is needed to investigate the load transfer mechanism of the plastic wall (i.e., the valley) further.

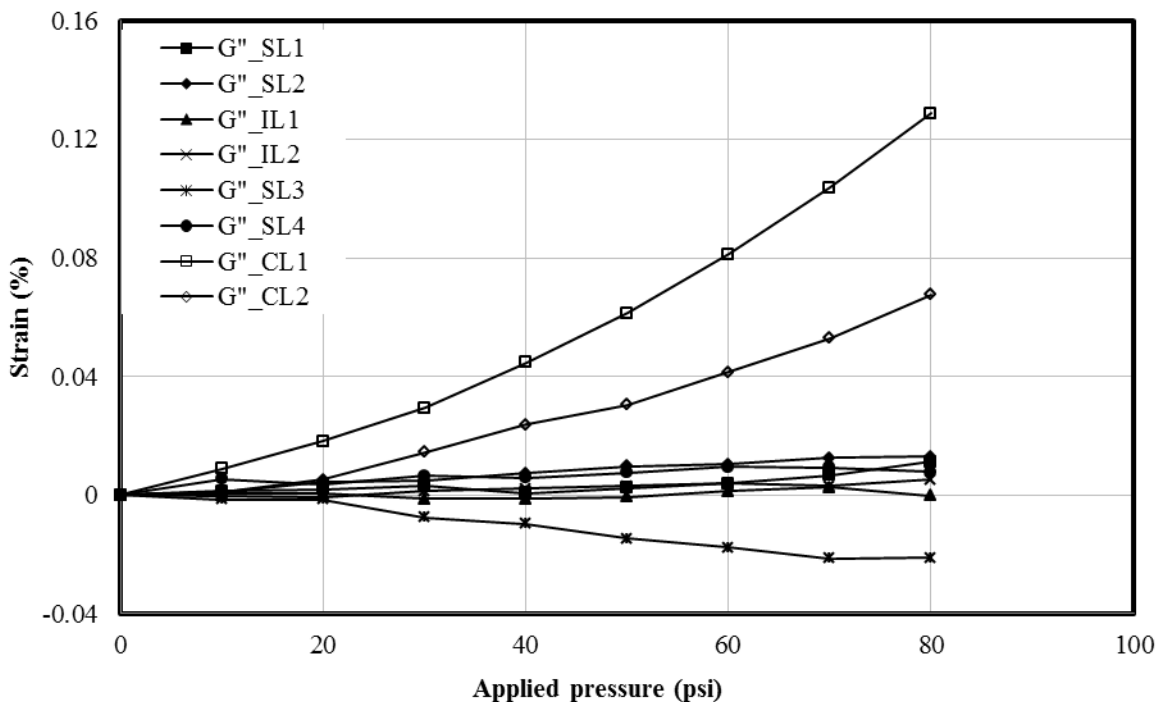


FIGURE 6.75 Measured strains on the inside and outside plastic wall of the pipe in Test 1

Test 2 . The circumferential and radial strains on the steel of the pipe are shown in **FIGURE 6.76**. Most strain gages showed an increase in the compressive strains with an increase of the static pressures except the strain gage G_{CR1} at the crown in the radial direction. The maximum circumferential strain of 0.0032% (G_{SC2} , compressive strain) and the maximum radial strain of 0.0007% (G_{CR1} , tensile strain) developed at the maximum applied static pressure. The strain gages on both sides of the steel rib at any particular location gave similar strain values (i.e., there was no sudden change in the strain values). This result indicates that the out-of-plane buckling of the steel ribs observed during the parallel plate load tests at a high level of load did not occur during static loading. **FIGURE 6.77** shows the comparison of the measured and calculated strains on the steel at the springline in the circumferential direction using the simplified load transfer mode proposed for Test 1.

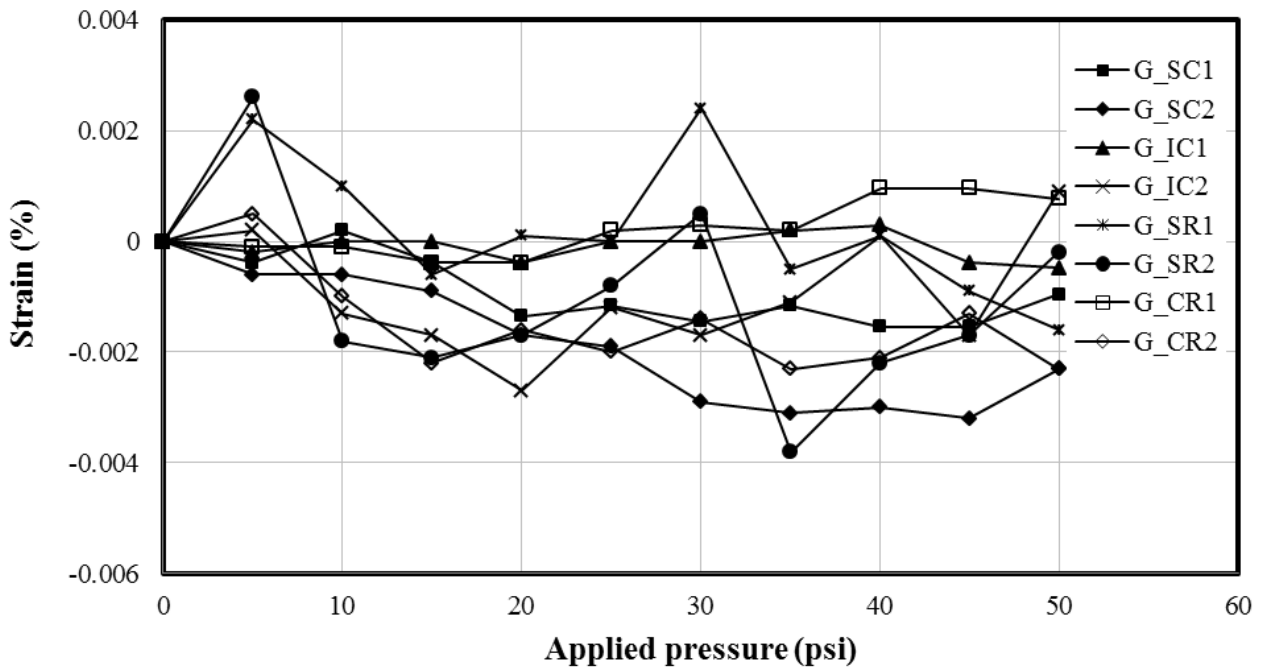


FIGURE 6.76 Measured strains on the steel ribs in Test 2

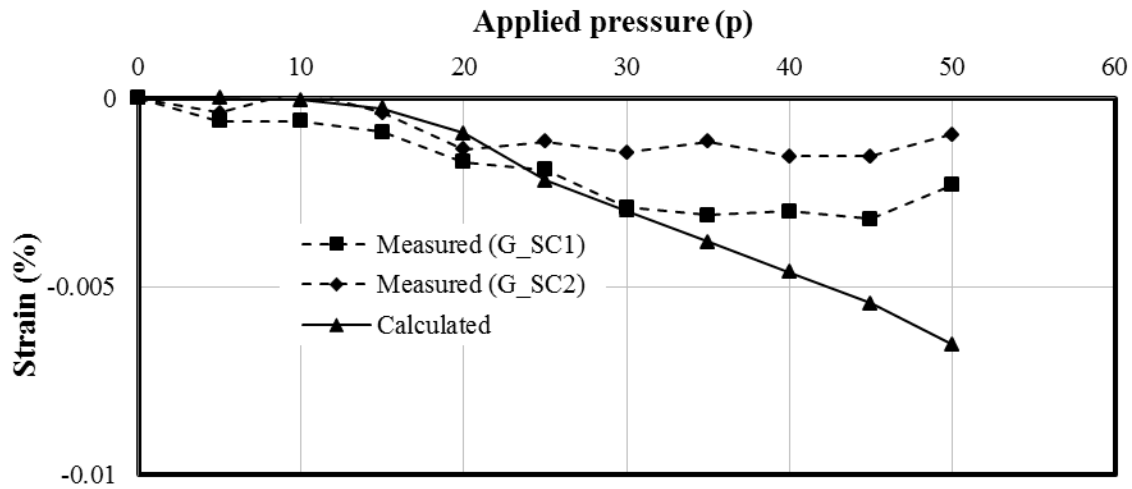


FIGURE 6.77 Measured and calculated strains on the steel at the springline in the circumferential direction in Test 2

FIGURE 6.78 shows the circumferential and radial strains on the plastic cover on the ribs against the applied static pressures. The strains measured at most locations on the plastic cover were higher than those on the steel. The maximum circumferential strain of 0.0061% (G'_{SC2} , compressive strain) and the maximum radial strain of 0.0098% (G'_{CR2} , tensile strain) developed during loading. **FIGURE 6.79** shows the comparison of the measured and calculated strains in the plastic cover on the ribs at the pipe crown.

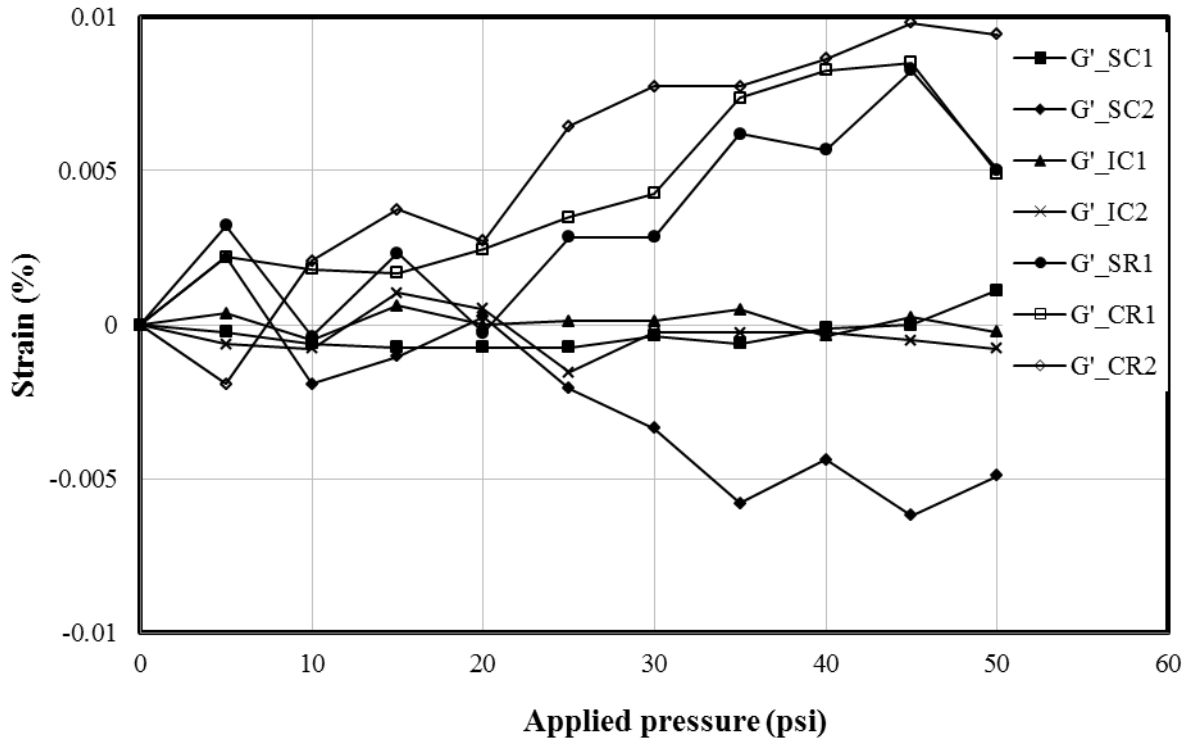


FIGURE 6.78 Measured strains on the plastic cover at the ribs in Test 2

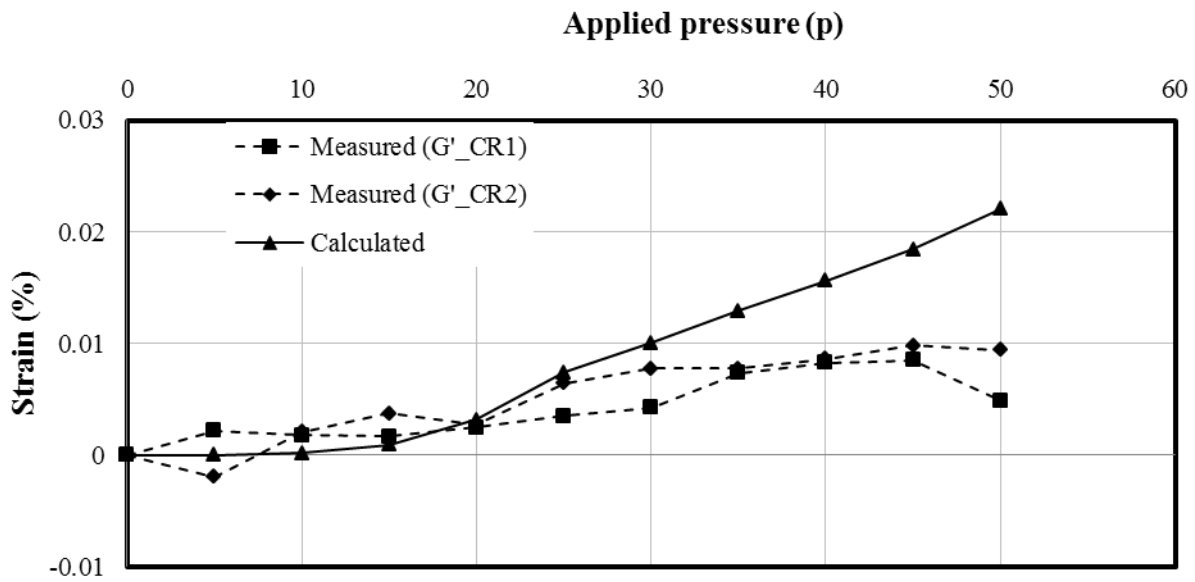


FIGURE 6.79 Measured and calculated strains on the plastic cover at the rib at the pipe crown in the radial direction in Test 2

The strains measured by the strain gages on the inside and outside plastic walls are shown in **FIGURE 6.80**, which indicates that the magnitudes of the strains on the pipe walls were higher than those on the steel rib and the plastic cover. The strain gages on the inside wall of the pipe experienced more tensile strains than those on the outside wall. Most strain gages showed an increase in the tensile strains with an increase of the applied pressures except the strain gage G''_{SL3} , which had an increase in the compressive strains under the applied static pressures. The strain gage G''_{CL1} at the crown measured the maximum tensile strain of 0.07% while the strain gage G''_{SL3} at the springline measured the maximum compressive strain of 0.019% during static loading.

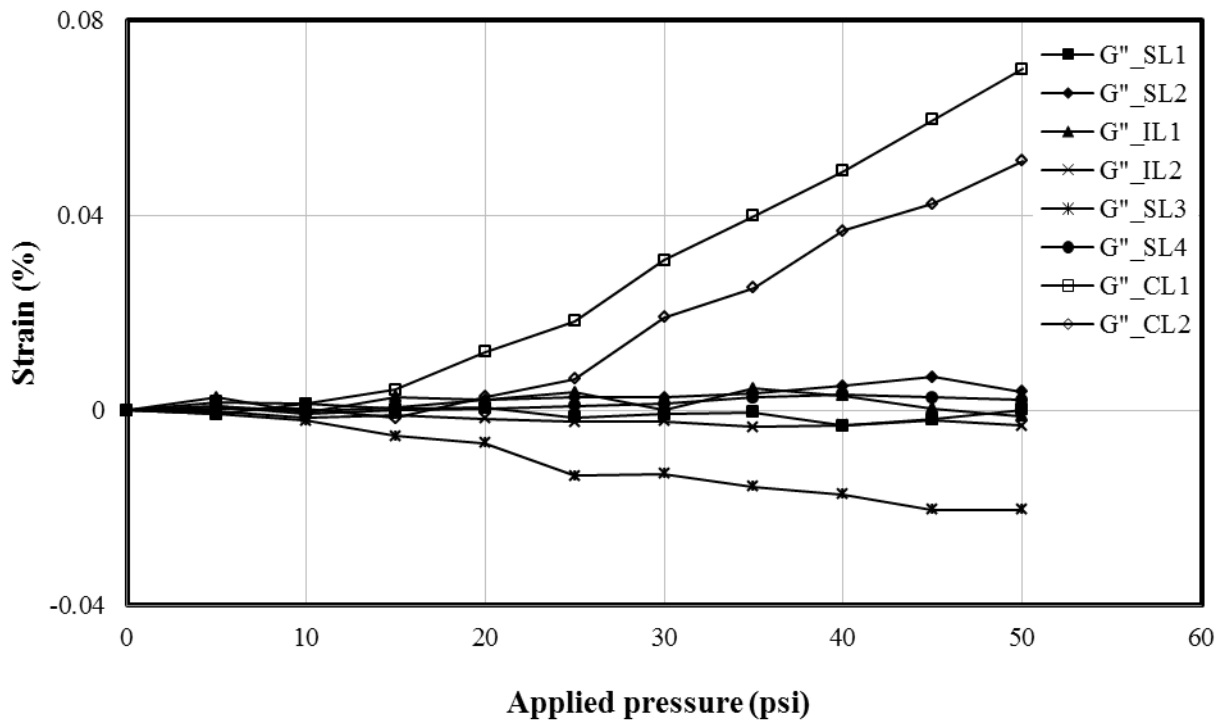


FIGURE 6.80 Measured strains on the inside and outside plastic walls of the pipe in Test 2

Test 3. The circumferential and radial strains on the steel of the pipe are shown in **FIGURE 6.81**. The strain gages, G_{SC1} and G_{SC2} at the springline and G_{IC1} and G_{IC2} at the invert in the circumferential direction, showed an increase in the compression strains while G_{SR1} at the springline and G_{CR2} at the crown in the radial direction showed an increase in the tensile strains under the applied static pressures. The maximum circumferential strain of 0.020% (G_{SC1} , compressive strain) and the maximum radial strain of 0.011% (G_{CR2} , tensile strain) developed during static loading. The strain gages on both sides of the steel rib at any particular location gave similar values (i.e., there was no sudden change in the strain values). This result indicates that the out-of-plane buckling of the steel ribs observed during the parallel plate load tests at a high level of load did not occur during static loading. **FIGURE 6.82** shows the comparison of the measured and calculated strains in the steel rib at the pipe crown.

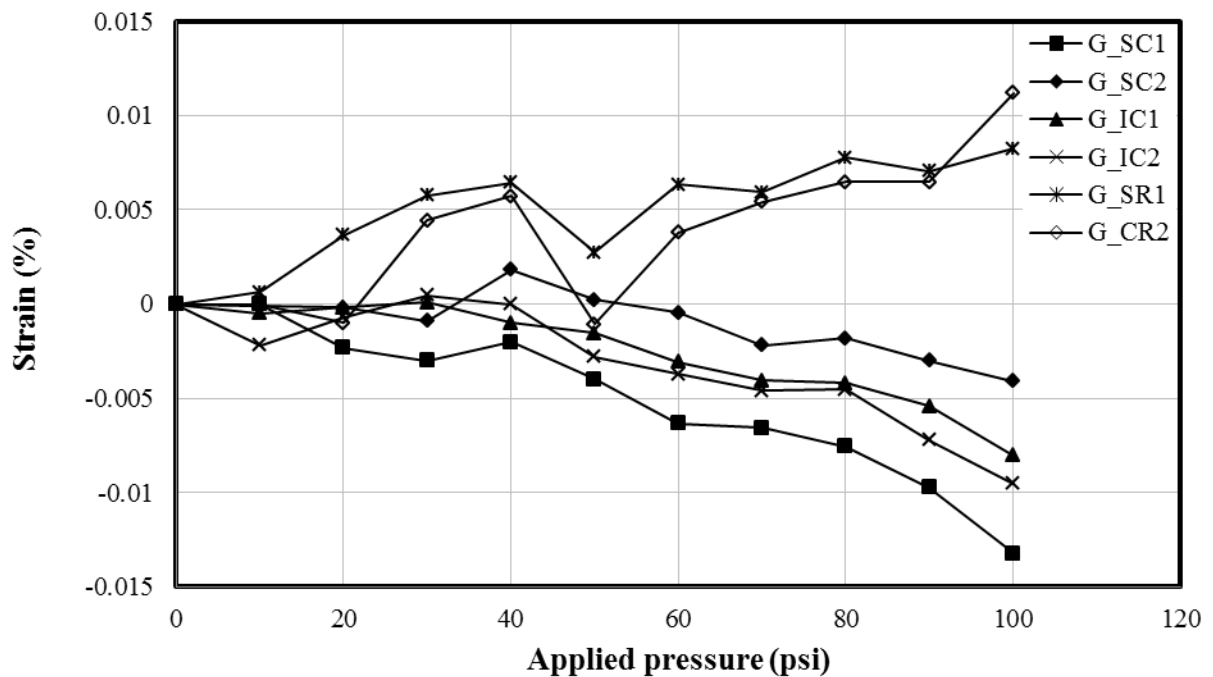


FIGURE 6.81 Measured strains on the steel ribs in Test 3

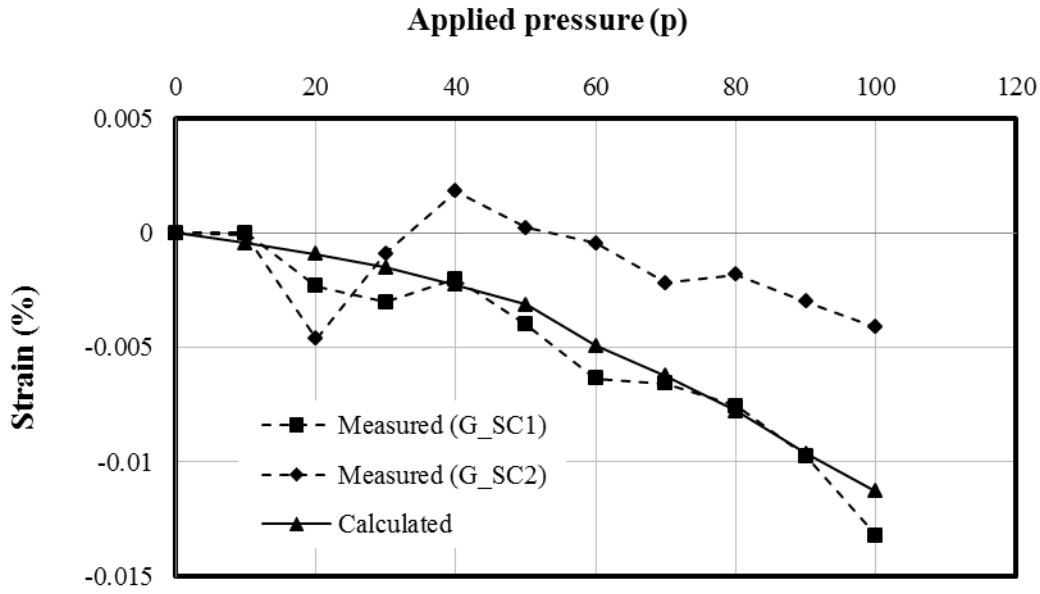


FIGURE 6.82 Measured and calculated strains on the steel rib at the springline in the circumferential direction in Test 3

FIGURE 6.83 shows the circumferential and radial strains on the plastic cover at the ribs against the applied static pressures. The strains measured at most locations on the plastic cover were higher in magnitude than those on the steel. The maximum circumferential strain of 0.19% (G'_{IC1} , tensile strain) and the maximum radial strain of 0.07% (G'_{CR1} , tensile strain) developed during static loading. **FIGURE 6.84** shows the comparison of the measured and calculated strains in the plastic cover on the ribs at the pipe crown.

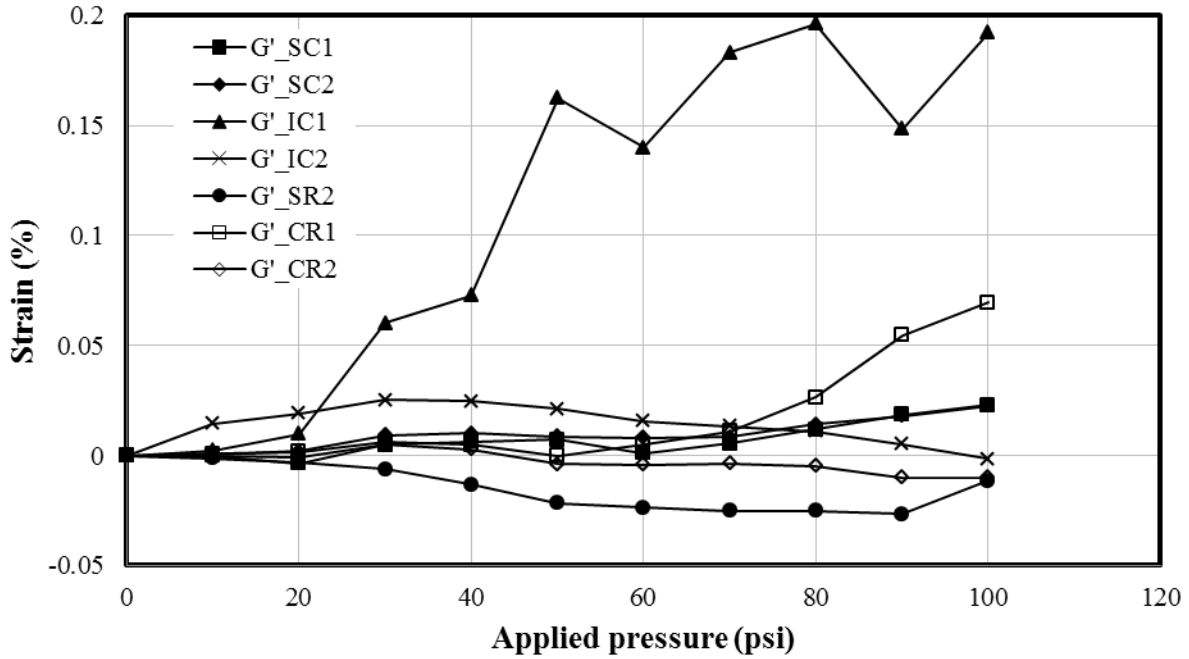


FIGURE 6.83 Measured strains on the plastic cover at the ribs in Test 3

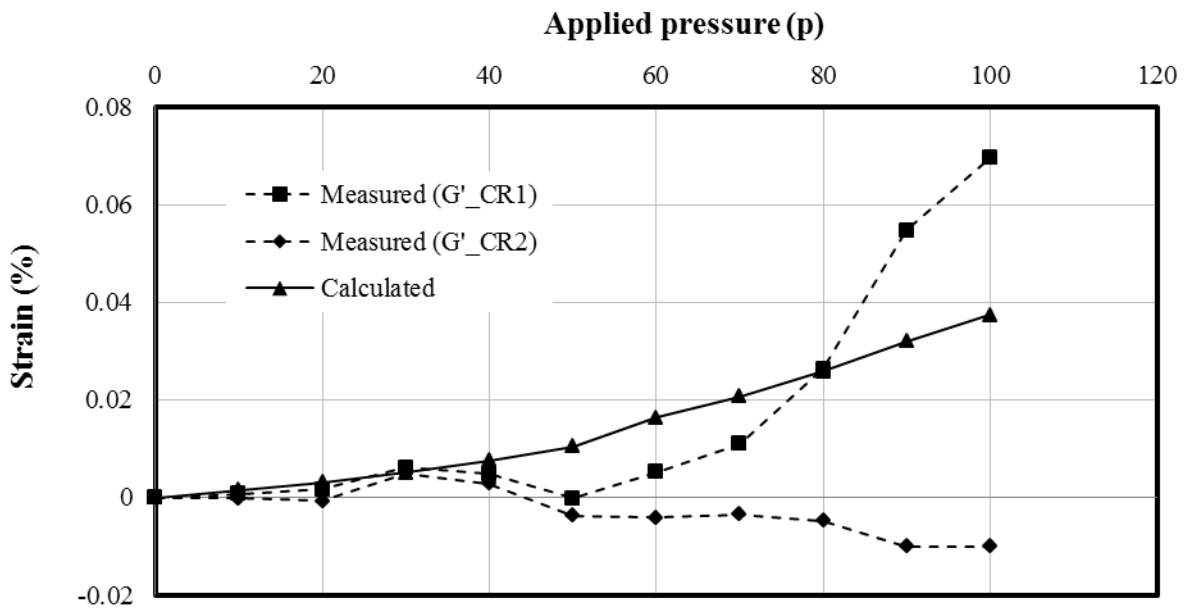


FIGURE 6.84 Measured and calculated strains on the plastic cover at the ribs at the pipe crown in the radial direction in Test 3

The strains measured by the strain gages on the inside and outside plastic walls are shown in **FIGURE 6.85**, which indicates that the magnitudes of the strains on the pipe walls were higher than those on the steel and the plastic cover at the ribs. The strain gages on the pipe inside walls experienced more tensile strains than those on the outside walls. Most strain gages showed an increase in the tensile strains with an increase of the applied static pressures except the strain gages G''_{SL2} and G''_{SL4} , which had an increase in the compressive strains under the applied pressures. The maximum tensile strain of 0.360% was recorded by the strain gage G''_{CL1} at the crown while the maximum compressive strain of 0.054% was recorded by the strain gage G''_{SL4} at the springline during static loading.

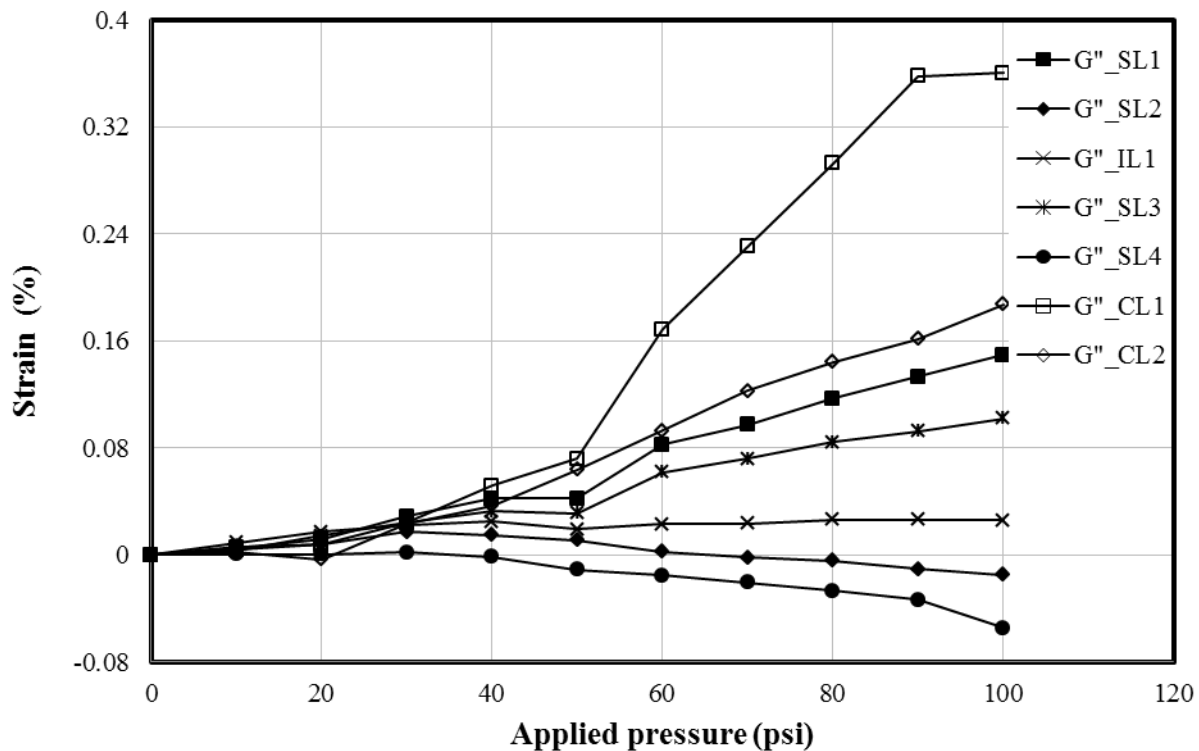


FIGURE 6.85 Measured strains on the inside and outside plastic wall of the pipe in Test 3

Field Test

Test Section A. The adjusted strains according to Brachman et al. (2008) are plotted against the time elapse when the truck load was applied as shown in **FIGURES 6.86 to 6.88**.

Since the maximum strains at the steel ribs recorded in the laboratory tests were in the circumferential direction at the pipe crown and springline, the strain gages were only placed in the circumferential direction at the pipe crown and springline in the field test. The strains measured on the steel at the ribs are shown in **FIGURE 6.86**. All strain gages, G_{SC1} and G_{SC2} at the springline and G_{CC1} and G_{CC2} at the crown in the circumferential direction, showed an increase in the compression strains under the applied truck load. The maximum circumferential strain of 0.0115 % (G_{CC1} , compressive strain) was recorded at the steel rib in the pipe crown when the middle axle was placed above the pipe crown. The strain gages at the steel rib in the springline showed the maximum circumferential strain of 0.00416 % (G_{SC2} , compressive strain) when the middle axle was above the pipe crown. For the back axle placed above the pipe crown, the measured strains were close or slightly lower than those recorded for the middle axle placed above the pipe crown. The strain gages fixed on both sides of the steel rib at any particular location gave similar values (i.e., there were no sudden changes in the strain values). This result indicates that the out-of-plane buckling of the steel ribs observed during the parallel plate load tests at a high level of load did not occur during the truck loading. The maximum strains, which were observed at the springline in the circumferential direction, are compared with the calculated values in **TABLE 6.6**. The strains on the steel were calculated assuming the pipe carried all the applied loads on the top of the pipe (i.e., neglecting the side resistance from the fill at the springline). The calculated strains were higher than the measured strains.

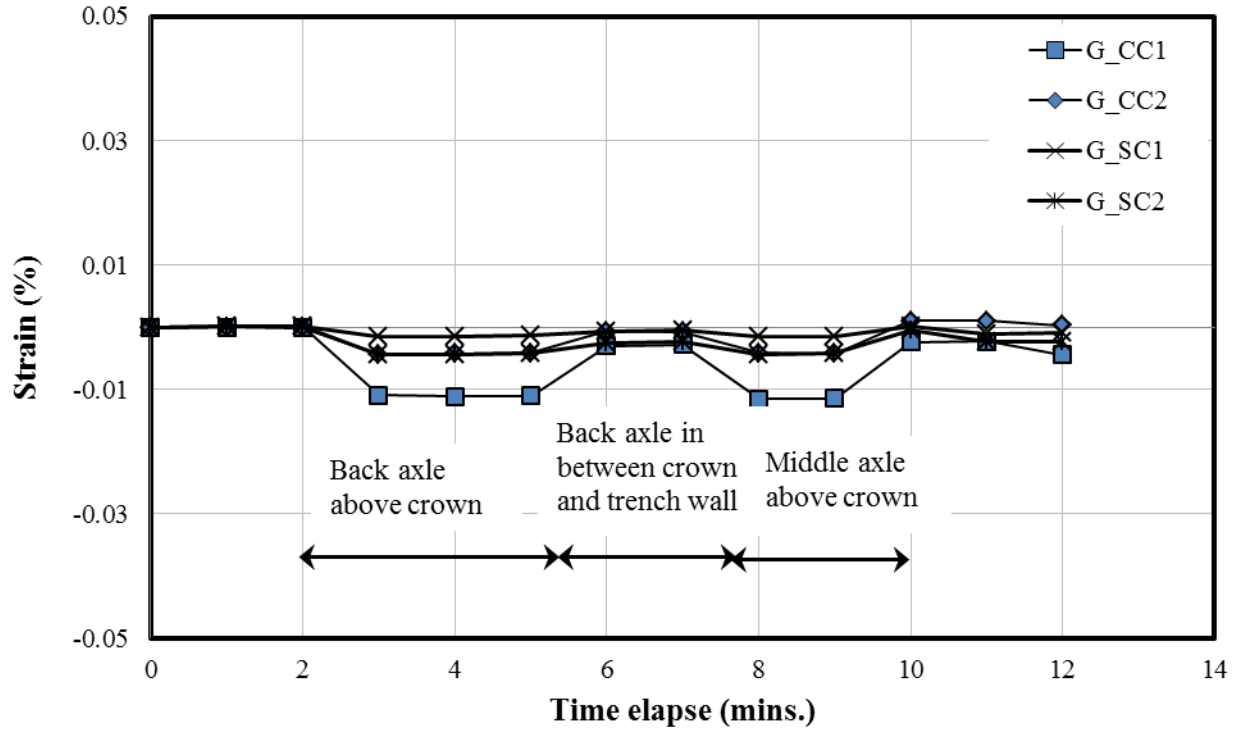


FIGURE 6.86 Measured strains on the steel ribs in Test Section A

TABLE 6.6 Comparison of the calculated and measured strains of the pipe in the field

Sections	Symbols		Back axle at the crown	Back axle in between the crown and trench wall	Middle axle at the crown
Section A	G_SC	Calculated	-0.01093	-0.0096	-0.01106
		Measured	-0.004360	0.0025	0.00416
	G'_CR	Calculated	0.03960	0.0351	0.04010
		Measured	0.032100	0.0124	0.03800
Section B	G_SC	Calculated	-0.010800	-0.00693	-0.010500
		Measured	N/A	N/A	N/A
	G'_CR	Calculated	0.039440	0.02530	0.038200
		Measured	0.03800	0.033	0.037100

FIGURE 6.87 shows the radial strains on the plastic cover at the ribs against the applied truck load. The strains developing on the plastic were higher in magnitude than the strains on the steel. Most of the strain gages showed an increase in tensile strains. The maximum radial strain on the plastic surface at the rib occurred at the pipe crown under the truck loadings. The maximum radial strain of 0.0369 % (G'_{CR1} , tensile strain) was recorded at the plastic rib in the pipe crown when the middle axle was placed above the pipe crown. The strain gages on the plastic at the plastic rib in the pipe springline and invert showed the maximum radial strains of 0.0195 % (G'_{SR1} , tensile strain) and 0.0143% (G'_{IR1} , tensile strain), respectively when the middle axle was above the pipe crown. For the back axle placed above the pipe crown, the measured strains were close or slightly lower than those recorded for the middle axle placed above the pipe crown. The strain gages fixed on both sides of the steel rib at any particular location gave similar values (i.e., there were no sudden changes in the strain values). This result indicates that the out-of-plane buckling of the steel ribs observed during the parallel plate load tests at a high level of load did not occur during the truck loading.

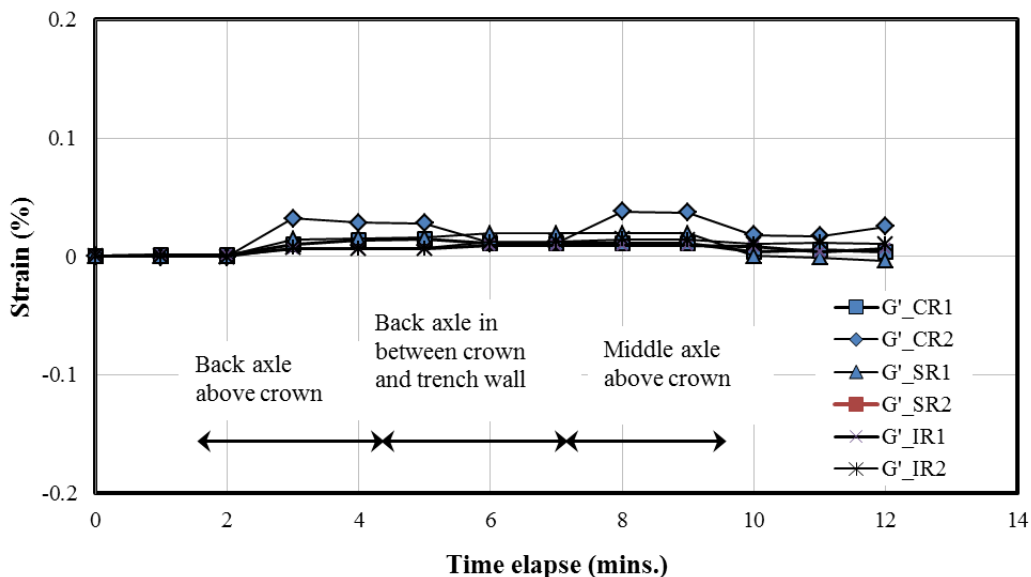
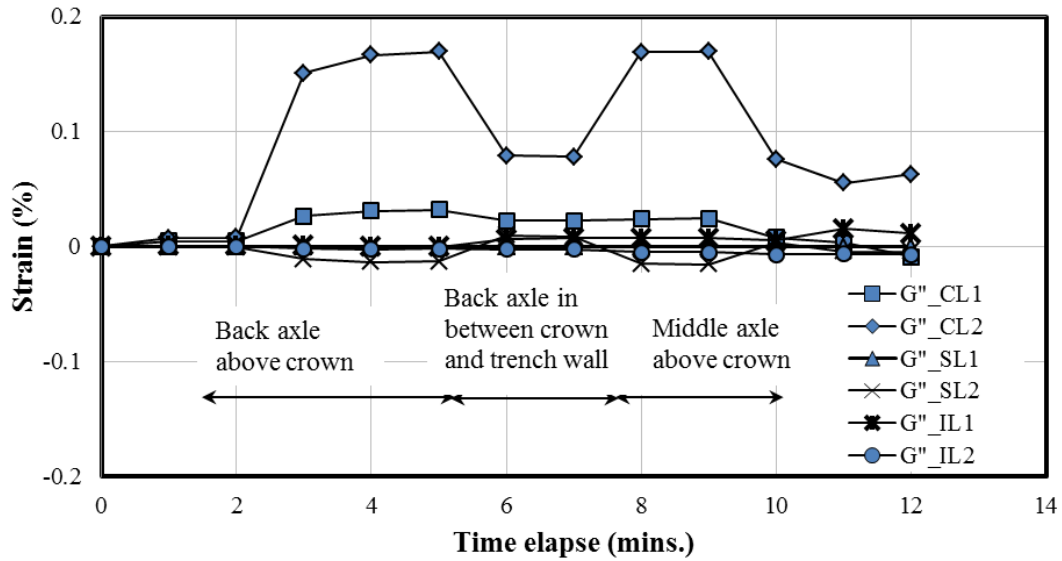


FIGURE 6.87 Measured strains on the plastic at ribs in Test Section A

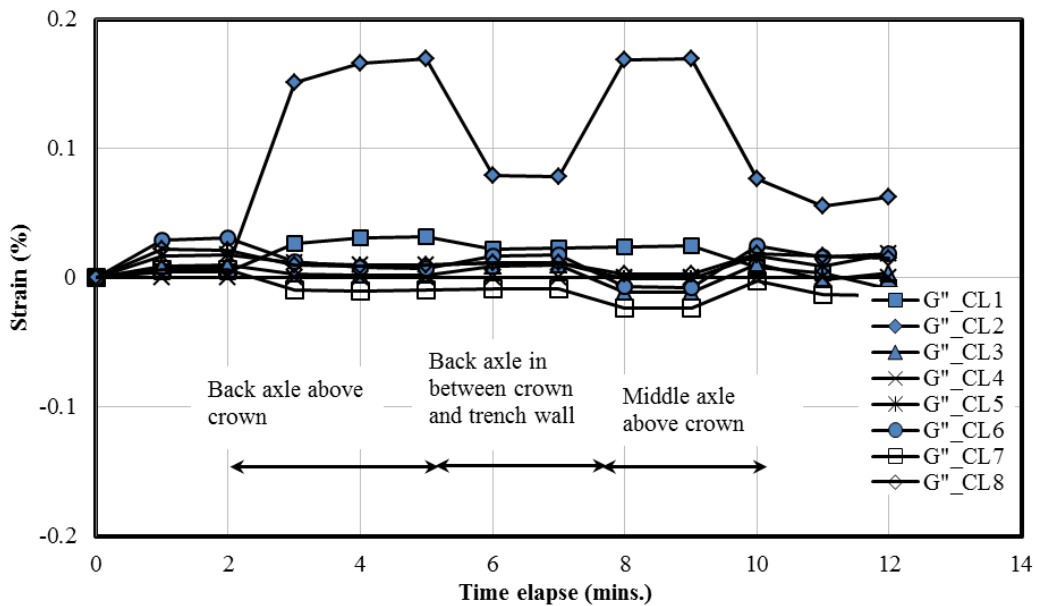
To calculate the strain in the plastic cover on the steel rib, the problem was simplified by assuming the load transfer mechanism as shown in **FIGURE 6.73**. Since the maximum earth pressures and the strains (on the plastic) during the truck loading was observed on the top of the pipe at the crown, the strains on the plastic cover at the ribs in the radial direction at the pipe crown were calculated and compared with the measured strains. The comparison between the measured and calculated strains in the plastic cover on the rib at the pipe crown is presented in **TABLE 6.5**. The calculated strains were close to the measured strains when the back or middle axle was applied above the pipe crown. The measured strains at the plastic cover at the plastic rib in the crown were lower than the calculated strains for the back axle between the crown and the trench wall.

FIGURE 6.88 shows the strains measured by the strain gages on the plastic wall inside and outside the pipe. The magnitudes of the strains on the pipe walls were higher than the strains on the steel and plastic at the ribs. **FIGURE 6.88a** shows the strains measured by the strain gages at the instrumented section (Section 2) close to the centerline of the roadway beneath the truck wheel path. The maximum strains were recorded at the pipe crown. At the pipe crown, both strain gages placed on the plastic inside and outside the pipe showed the tensile strain. This indicates that the plastic pipe wall could behave as the membrane element. However, the strain gage affixed on the plastic inside showed the higher tensile strain than the strain recorded by the strain gage on the plastic outside. This also indicates that the plastic wall between the ribs behaves as a beam element. Therefore, from above two findings it is clear that the plastic pipe wall had the combined action of bended beam and tensioned membrane. The strains on the plastic wall at the invert and springline were small as compared with those recorded on the pipe crown. The maximum tensile strain of 0.169% was recorded by the strain gage G''_{CL2} under the

back axle load above the pipe crown. A numerical model is needed to investigate the load transfer mechanism of the plastic wall (i.e., the valley) further.



(a) Strains on plastic beneath the wheel path



(b) Strains on plastic away from the wheel path to centerline of the road way

FIGURE 6.88 Measured strains on the inside and outside plastic walls of the pipe in Test

Section A

FIGURE 6.89 shows the strains measured by the strain gages on the plastic wall inside and outside at the crown against the distance of the strain gages from the instrumented section (Section 2) in Test Section A (see **FIGURE 5.7** for the locations of the strain gages). The strains measured along the longitudinal direction of the pipe at different distances from the instrumented section showed the similar behavior for all three configurations of the truck loading. The maximum strains at the pipe wall were recorded at the instrumented section beneath the applied truck axle. These maximum strains may be due to the concentration of the truck axle load on the pipe crown beneath the point of application of the axle load. The strains measured on the outside plastic wall along the pipe run were lower than those measured inside on the plastic wall to a distance of approximately 36 in. from the instrumented section. After the distance of 36 in. along the pipe run, the strains on the outside wall were measured higher than those on the inside wall. The maximum strains of 0.125 % (G''_{CL2} , tensile strain) and 0.024 % (G''_{CL2} , tensile strain) were recorded during the truck loadings.

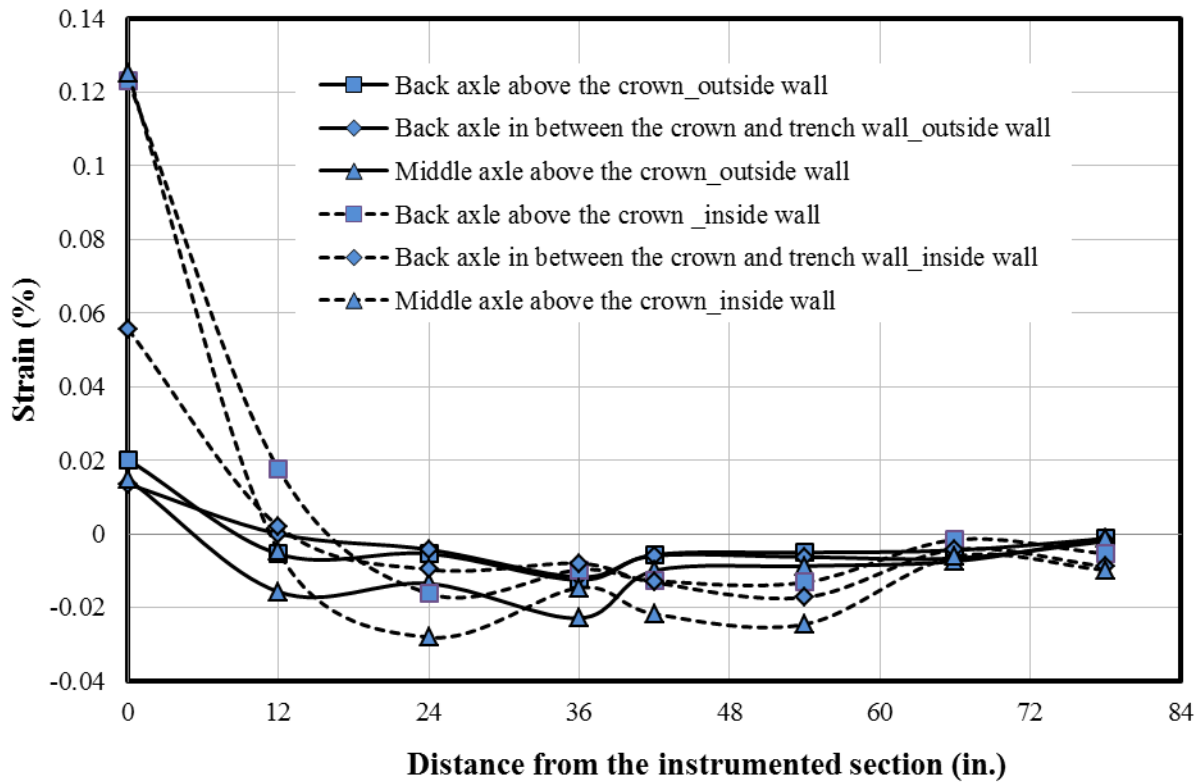


FIGURE 6.89 Measured strains on the inside and outside plastic walls of the pipe in Test Section A

Test Section B. The measured strains from the strain gages attached on the plastic surface of the pipe at the instrumented section (Section 3) of Test Section B were adjusted according to Brachman et al. (2008) and are plotted against the time elapse during the truck loading as shown in **FIGURES 6.90** to **6.91**.

Two strain gages attached on the steel at the pipe springline did not work during the installation of the pipe. Two strain gages, G_{CC1} and G_{CC2} at the crown in the circumferential direction, showed an increase in the compression strain under the applied truck load as shown in **FIGURE 6.90**. The maximum circumferential strain of 0.00378 % (G_{CC1} , compressive strain)

was recorded at the steel rib in the pipe crown when the back axle was placed above the pipe crown. For the middle axle placed above the pipe crown, the measured strains were close or slightly lower than those recorded for the back axle placed above the pipe crown. The strain gages fixed on both sides of the steel rib at any particular location gave similar values (i.e., there were no sudden changes in the strain values). The calculated strains at the springline in the circumferential direction are presented in **TABLE 6.5**. The strains on the steel were calculated and are described in **SECTION 6.2.4**.

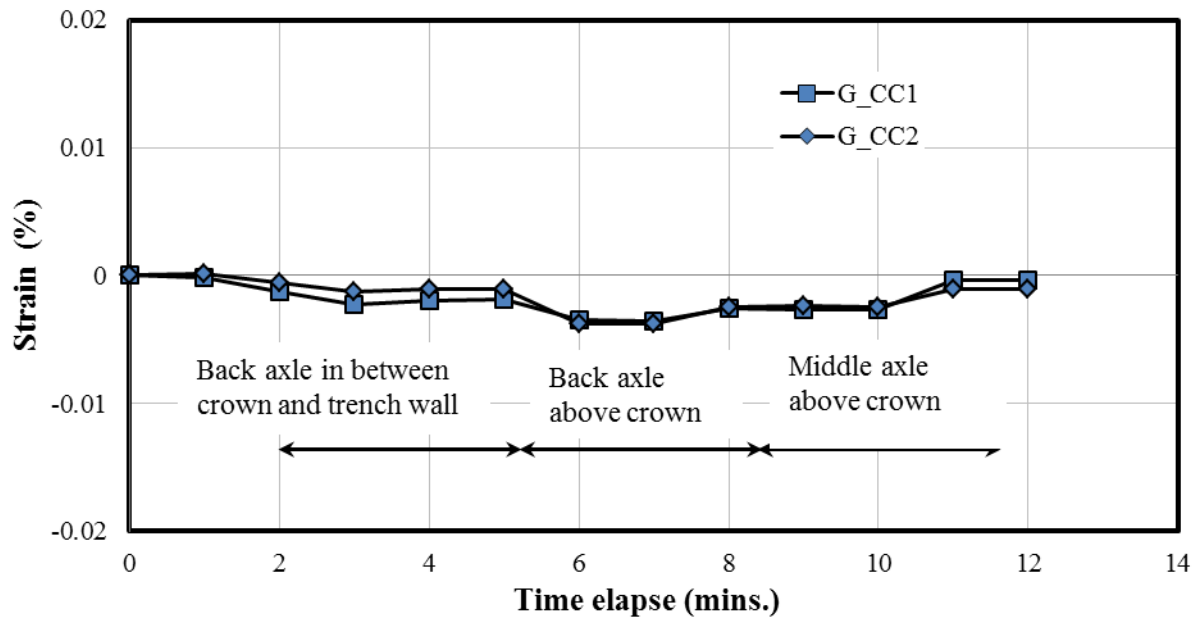


FIGURE 6.90 Measured strains on the steel ribs in Test Section B

FIGURE 6.91 shows the radial strains on the plastic cover at the ribs against the applied truck load. The strains developing on the plastic were higher in magnitude than the strains on the steel. Most of the strain gages showed an increase in tensile strains except the strain gage G'_{IR2} at the pipe invert. The maximum radial strains on the plastic cover at the ribs occurred at the

pipe crown under the truck loadings. The maximum radial strain of 0.037 % (G'_{CR2} , tensile strain) was recorded on the plastic cover at the rib in the pipe crown when the middle axle was placed above the pipe crown. The strain gages on the plastic cover at the rib in the pipe springline and invert showed the maximum radial strains of 0.0113 % (G'_{SR2} , tensile strain) and 0.0168 % (G'_{IR1} , tensile strain), respectively when the middle axle was above the pipe crown. For the back axle placed above the pipe crown, all measured strains were close or slightly lower than those recorded for the middle axle placed above the pipe crown. The strain gages fixed on both sides of the steel rib at any particular location gave similar values (i.e., there were no sudden changes in the strain values).

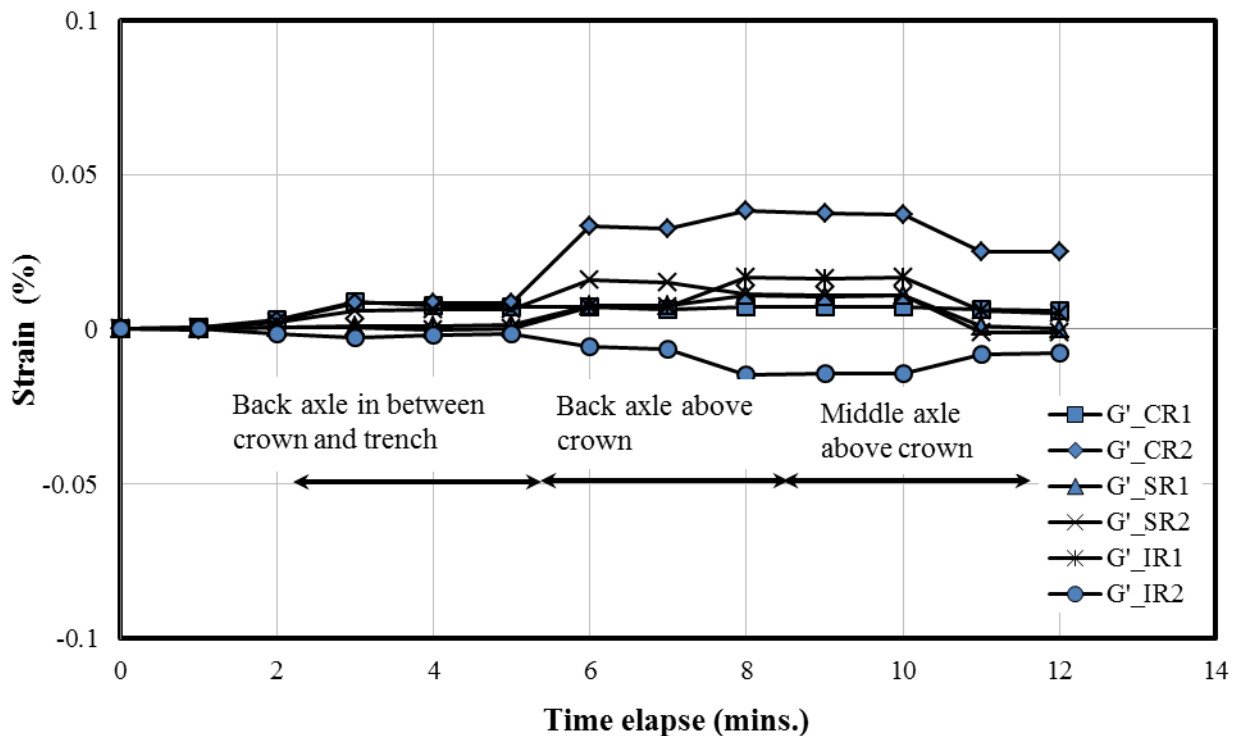
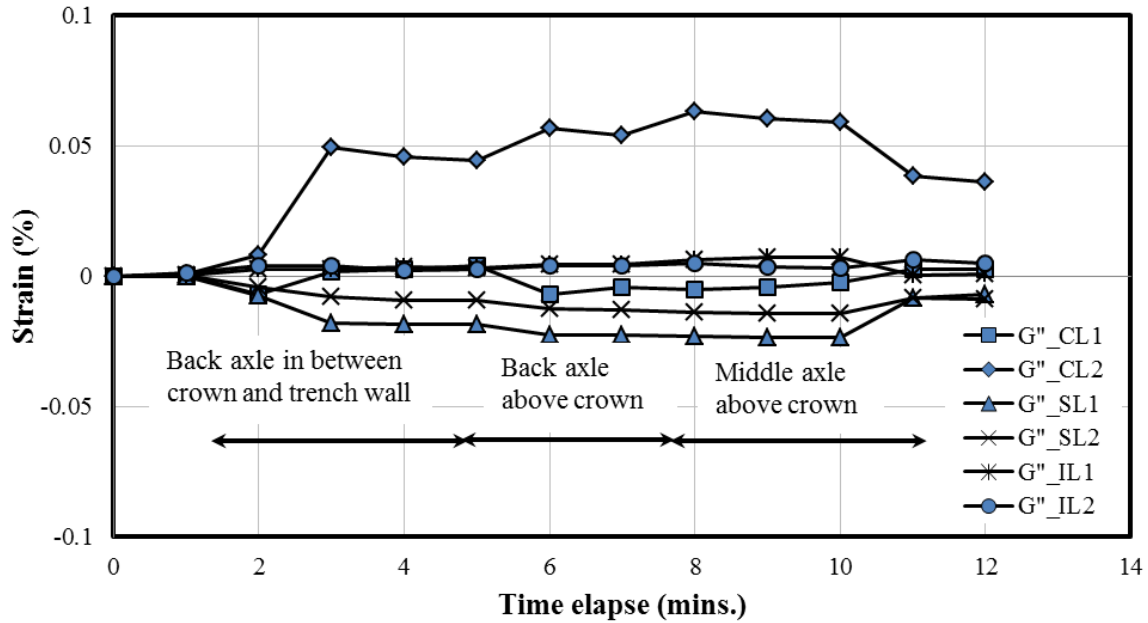


FIGURE 6.91 Measured strains on the plastic at ribs in Test Section B

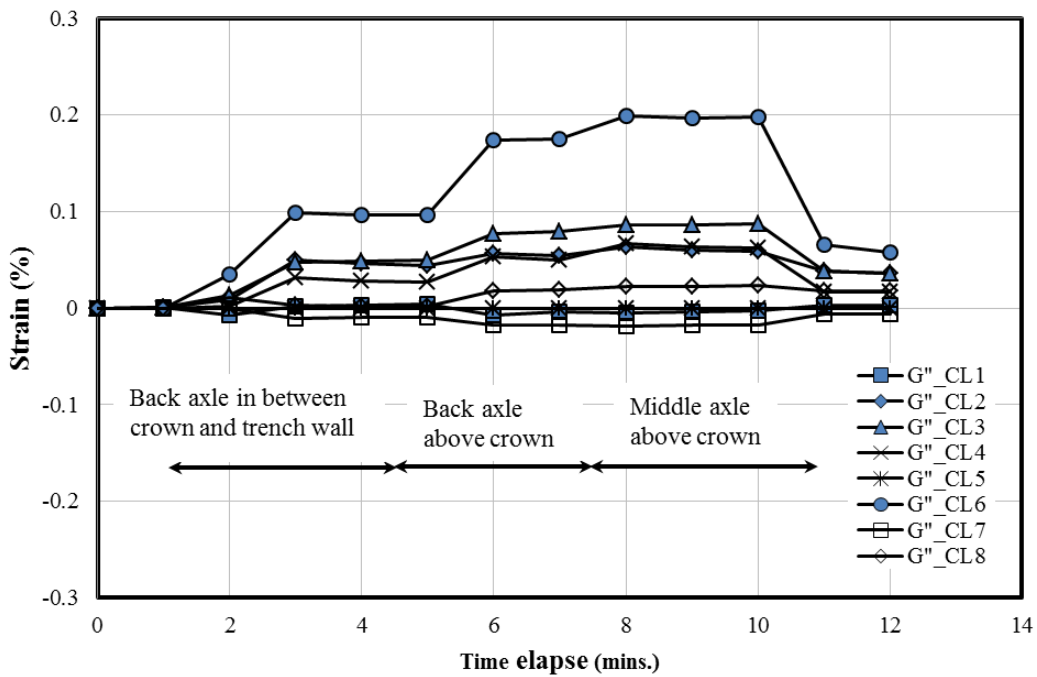
The maximum earth pressures and the strains (on the plastic) during the truck loading were observed on the top of the pipe at the crown. Therefore, the strains on the plastic cover at

the ribs in the radial direction at the pipe crown were calculated using the suggested load transfer mechanism as described **SECTION 6.2.4** and compared with the measured strains as provided in **TABLE 6.5**. The calculated strains were close to the measured strains when the back or middle axle was applied above the pipe crown. The measured strains were lower than the calculated strains at the plastic cover at the rib on the crown for the back axle between the crown and trench wall.

FIGURE 6.92 shows the strains measured by the strain gages on the plastic wall inside and outside the pipe. The magnitudes of the strains on the pipe walls were higher than the strains on the steel and plastic at the ribs. **FIGURE 6.92a** shows the strains measured by the strain gages at the instrumented section (Section 3) close to the centerline of the roadway beneath the truck wheel path in Test Section B. The maximum strains were recorded at the pipe crown. The strains on the plastic wall at the invert and springline were small as compared with those recorded on the pipe crown. The maximum tensile strain of 0.0063 % was recorded by the strain gage G_{CL2} under the middle axle load above the pipe crown. At the pipe crown, the strain gages placed on the plastic inside showed the tensile strains whereas the strain gages placed outside the pipe showed the compressive strains under the truck loadings. However the magnitude of the strains were higher in the strain gages attached on the pipe outside than those on the pipe inside. Most of the strain gages placed on the plastic wall between the ribs showed the similar behavior to the strain gages attached at the pipe crown beneath the applied truck loadings as shown in **FIGURE 6.92**. This indicates that the plastic pipe wall had the combined beam and tensioned membrane effect. A numerical model is needed to investigate the load transfer mechanism of the plastic wall (i.e., the valley) further.



(a) Strains on plastic wall (i.e., valley) beneath the wheel path



(b) Strains on plastic wall (i.e., valley) away from the wheel path to centerline of the roadway

FIGURE 6.92 Measured strains on inside and outside plastic wall of the pipe in Test Section B

FIGURE 6.93 shows the strains measured by the strain gages on the plastic wall inside and outside at the crown against the distance of the strain gages from the instrumented section (Section 3) in Test Section B. The strains measured along the longitudinal direction of the pipe run at different distances from the instrumented section showed the similar behavior for all three configurations of the truck loading. The strains measured by the strain gages of Test Section B showed the maximum strains were not close to the instrumented section below the point of application of the axle load (as recorded in Test Section A) but approximately 24 in. away from the instrumented section. The measured strains were uniform near the instrumented section. Similar to Test Section A, the measured strains were higher on the inside pipe wall than those on the outside to a distance of approximately 36 in. After the distance of approximately 36 in., the higher strains were measured on the outside pipe wall than those on the inside pipe wall. These may result from the concentration of the truck axle load at the pipe crown beneath the point of application of the axle load. The strains measured on the outside plastic wall along the pipe run were lower than those measured inside on the plastic wall to a distance of approximately 36 in. from the instrumented section. After the distance of 36 in. along the pipe run, the strains on the outside wall were measured higher than those on the inside wall. The maximum strains of 0.153 % (G''_{CL6} , tensile strain) and 0.037 % (G''_{CL6} , compressive strain) were recorded during the truck loadings.

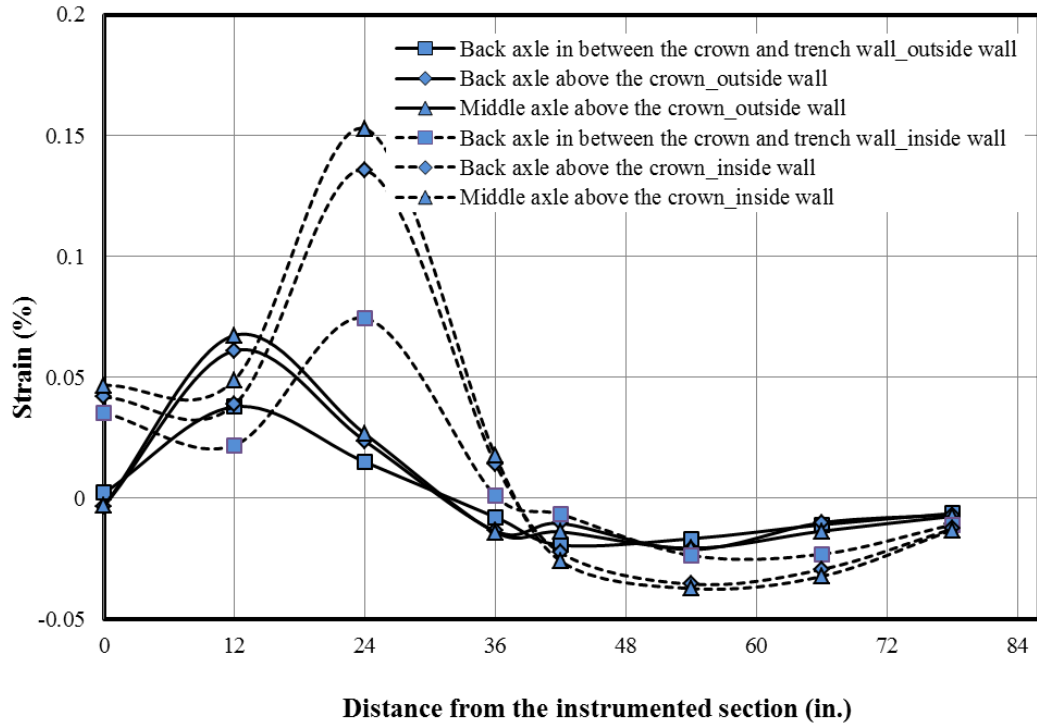


FIGURE 6.93 Measured strains on the inside and outside plastic walls of the pipe in Test Section B

Comparison of test results and summary

Strain gages were attached on both steel and plastic surfaces of the test specimens to measure the local strain developments in the SRHDPE pipes. The strains on the steel and plastic obtained in both laboratory and field tests under the applied static loadings were discussed in **SECTION 6.2.3**. This section presents the comparison of the magnitude and trend of the strains on the steel ribs and plastic cover of the pipe for all tests. Since a large number of strain gages were used in each test, only the strain gages which showed the maximum values were taken for the comparison. From the above discussion in **SECTION 6.2.3**, it was found that the strains on the steel were the maximum in the circumferential direction at the springline while the strains on the plastic at the ribs and at the pipe wall (i.e., valley) between the ribs were the maximum at the

pipe crown in most cases. Therefore, the strains at the springline in the circumferential direction for the steel ribs and the strains at the pipe crown for the plastic were selected for the comparison of the strains.

Laboratory Tests. FIGURE 6.94 shows the comparison of the strains on the steel ribs of the pipe measured in Test 1 (with the AB-3-I base course and the KR sand backfill), Test 2 (with the KR sand base course and the backfill), and Test 3 (with the AB-3-I base course and the crushed stone CS-I backfill). At the rib in the springline, the measured circumferential strains on the steels had similar trends (the compressive strain increased with the increasing applied load) for all three tests. The highest measured strain on the steel among all the tests was 0.013%, which was less than the strain limit of 0.28% calculated at the yield point of the steel as $\epsilon = F_y/E$ (where F_y is the yield strength of the steel (80 ksi) and E is the Young's modulus of elasticity of the steel (29,000 ksi)).

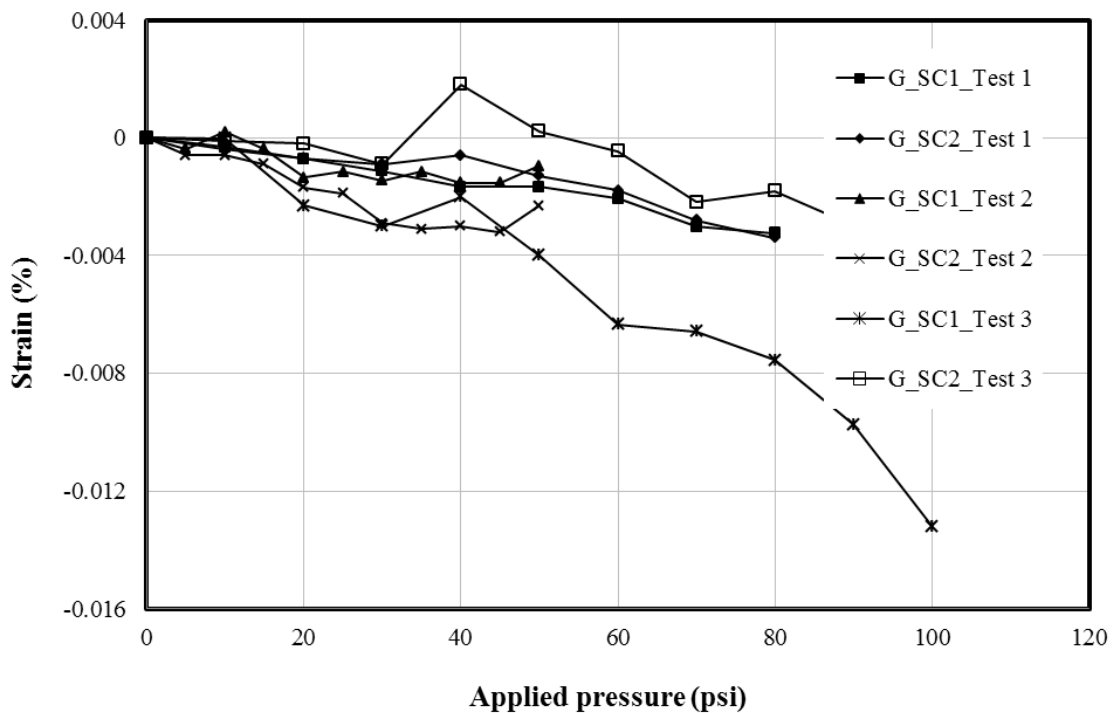


FIGURE 6.94 Comparison of the strains measured on steel in the laboratory tests.

FIGURE 6.95 shows the comparison of the strains on the plastic cover at the ribs at the pipe crown measured in all three laboratory tests. Most of the strain gages showed an increase in the tensile strains with an increase of the applied pressures. **FIGURE 6.96** shows the comparison of the strains on the plastic cover at the pipe wall (i.e., valley) at the pipe crown measured in all three laboratory tests. The highest measured strain on the plastic during the installation and loading among all the tests was 0.069%, which was within the permissible limit of 5% (the 2007 AASHTO LRFD Bridge Design Specifications).

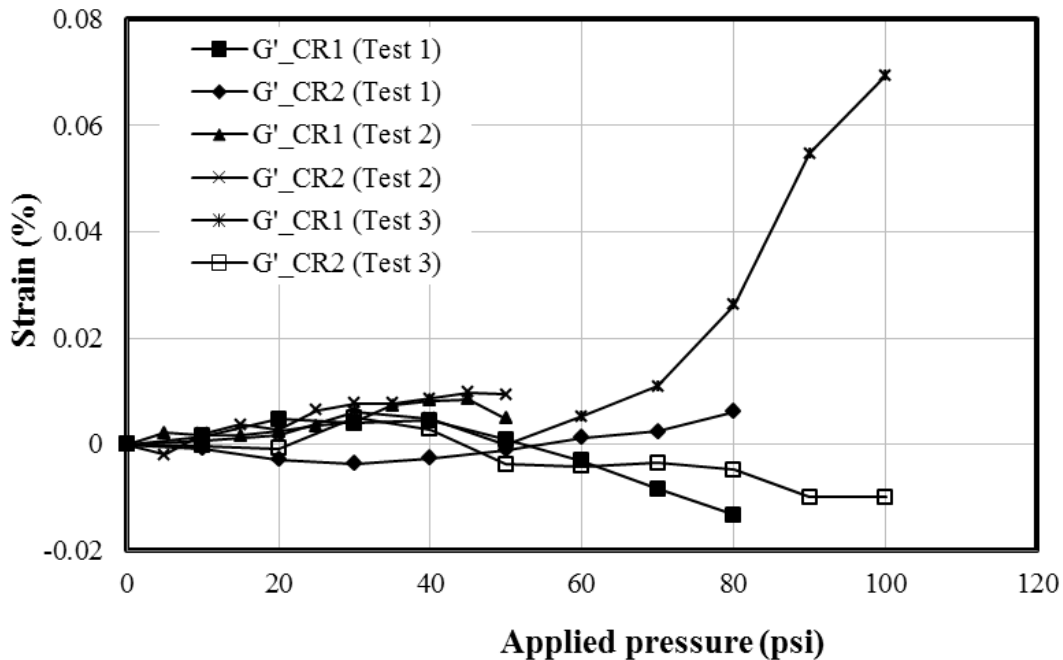


FIGURE 6.95 Comparison of the measured strains on the plastic cover at the ribs in the laboratory tests.

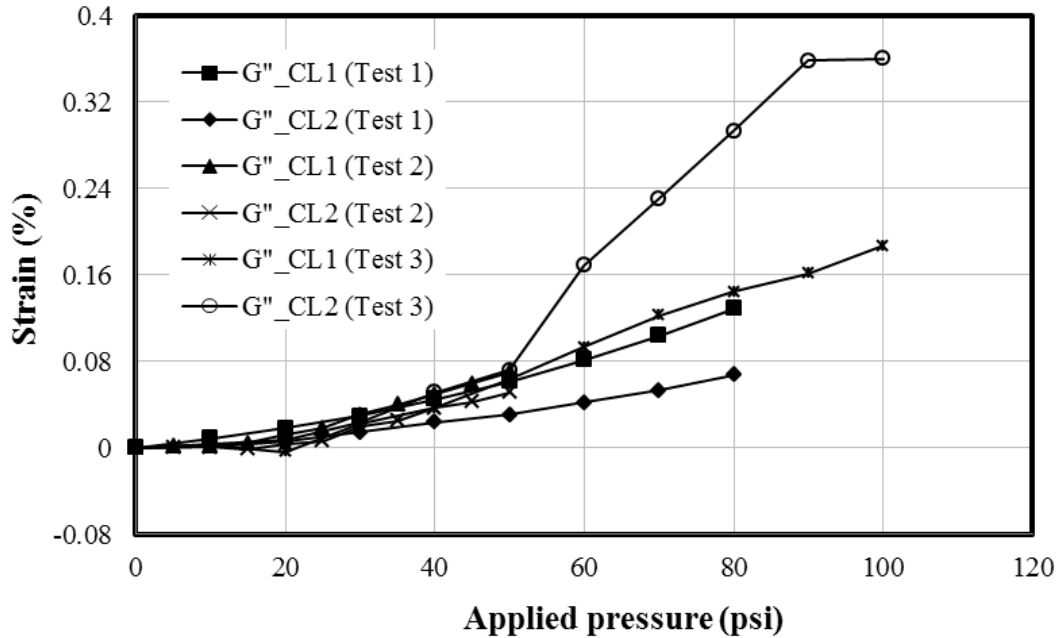


FIGURE 6.96 Comparison of the strains measured outside and inside the pipe at the valley between ribs.

FIGURE 6.97 shows the comparison of the strains measured on the steel at the springline and on the plastic cover at the ribs and pipe walls at the pipe crown in all three laboratory tests. The strains measured on the steel at the springline in the circumferential were compressive whereas all the strains measured on the plastic were tensile in most cases. The strains on the plastic cover at the pipe walls were higher than those measured on the plastic cover at the ribs and on the steel.

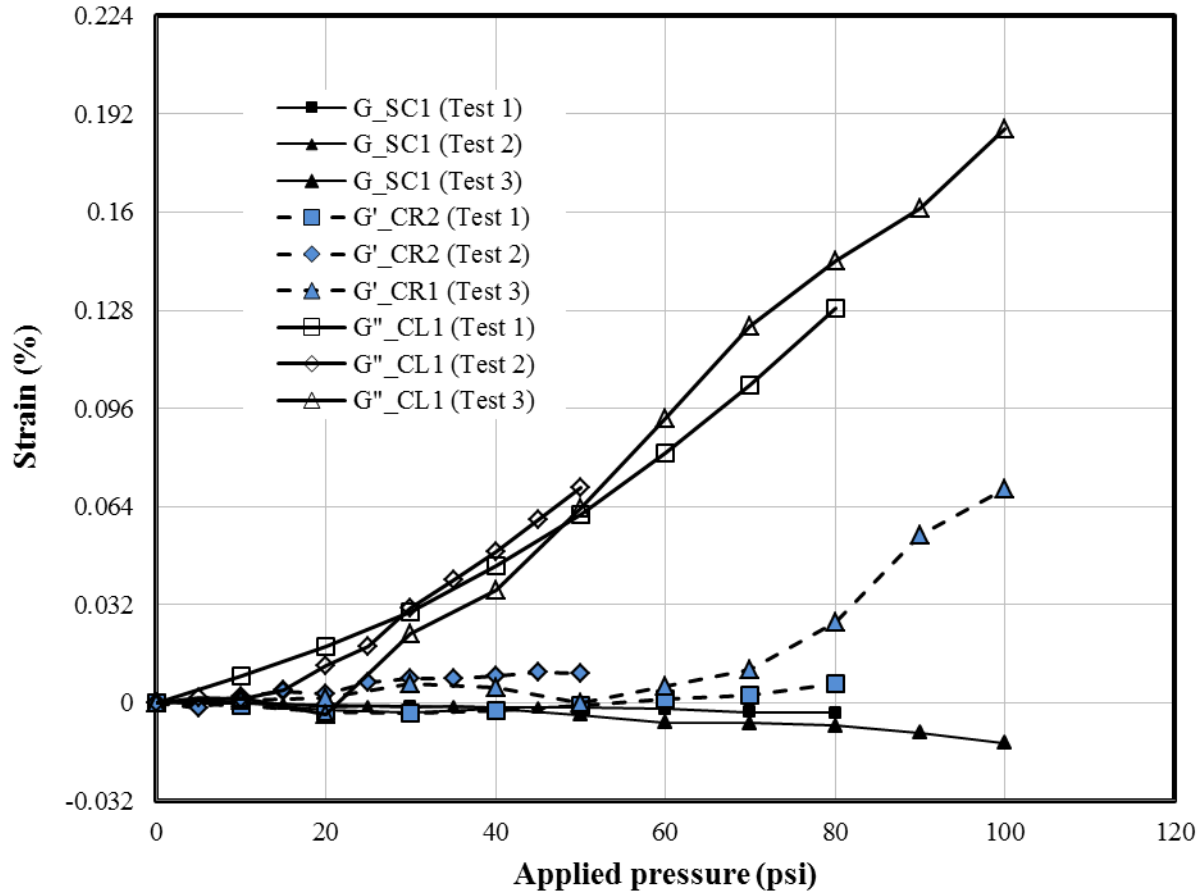


FIGURE 6.97 Comparison of the strains measured on the steel and plastic in the laboratory tests.

Field Test. **FIGURE 6.98** shows the comparison of the strains measured in the field test on the steel at the springline and on the plastic cover at the ribs and pipe walls at the pipe crown in Test Section A (with the AB-3-II backfill and base course) and in Test Section B (with the crushed stone CS-II backfill and the top 6 in AB-3-II aggregate). The measured strains on the steel and plastic cover in the field test had the same trends as those obtained on the measured strains in the laboratory tests. The magnitudes of the strains both in the laboratory and field tests were nearly equal for both steel and plastic. The strains measured in the field test were found to be well below the permissible values for both steel and plastic of the pipe.

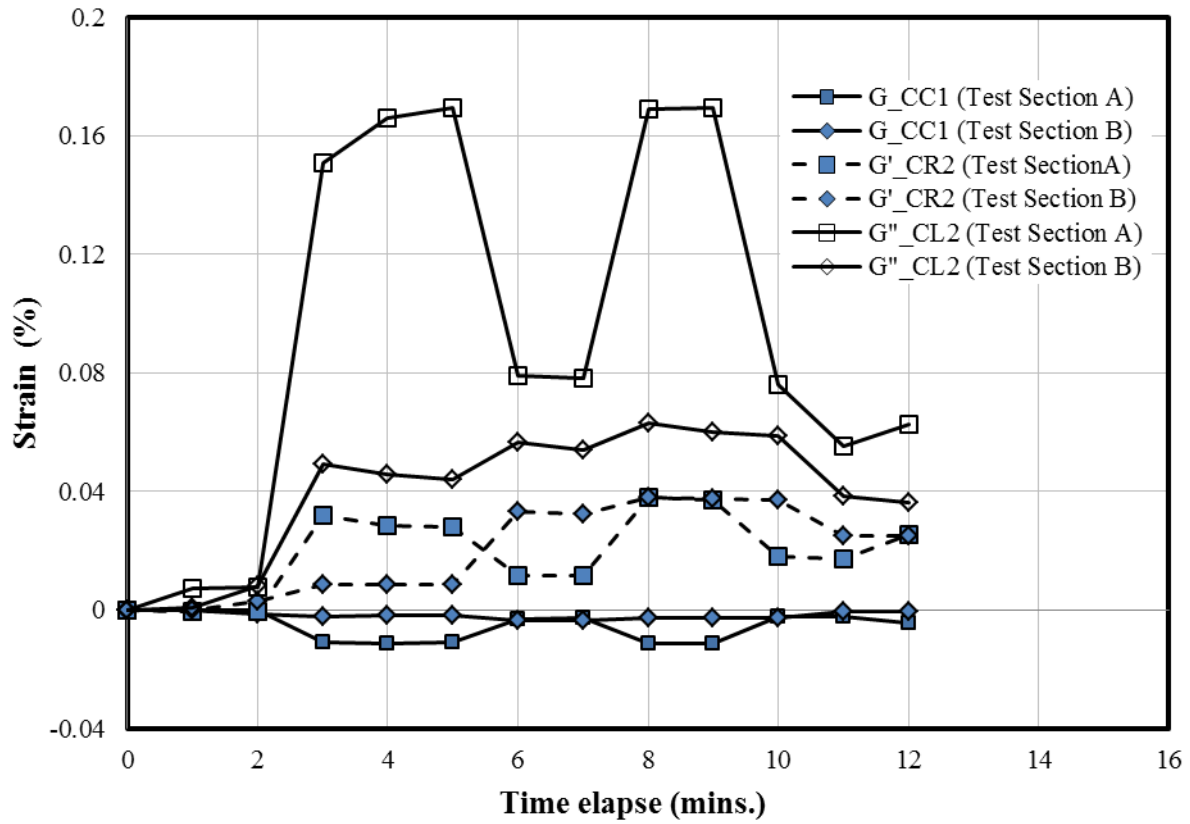


FIGURE 6.98 Comparison of the strains measured on the steel and plastic in the laboratory tests.

6.3 Cyclic Plate Loading Test Results

After the static plate loading tests, cyclic loads, as described in **SECTION 4.1.2**, were applied on each test section in the laboratory. The vertical deformation of the loading plate, the earth pressures around the pipe, the deflections of the pipe, and the strains experienced in the pipe were monitored and are presented in the subsequent sections.

6.3.1 Vertical Deformation of the Loading Plate

The vertical deformations of the loading plate against the applied cyclic pressures in Tests 1, 2, and 3 are shown in **FIGURES 6.99, 6.100, and 6.101**, respectively. It is shown that the test sections with the AB-3-I base course in Tests 1 and 3 had more elastic rebound than that with the KR sand base course in Test 2. The settlement of the loading plate under cyclic loading is the permanent deformation of the plate after unloading in the load cycle. **FIGURE 6.102** shows the comparison of the settlements of the loading plate for all the tests under both static and cyclic loadings. **TABLE 6.7** shows the load step, the number of load cycles, and the permanent deformation of the loading plate for each load step in Tests 1, 2, and 3. The permanent deformation was higher in Test 2 because the KR sand was used as the base course instead of the AB-3-I aggregate. Even though Tests 1 and 3 had the same base course (i.e., 9 in. thick AB-3-I aggregate), the permanent deformation was higher in Test 3 than in Test 1 because the crushed stone (CS-I) in Test 3 was dumped in place without any compaction.

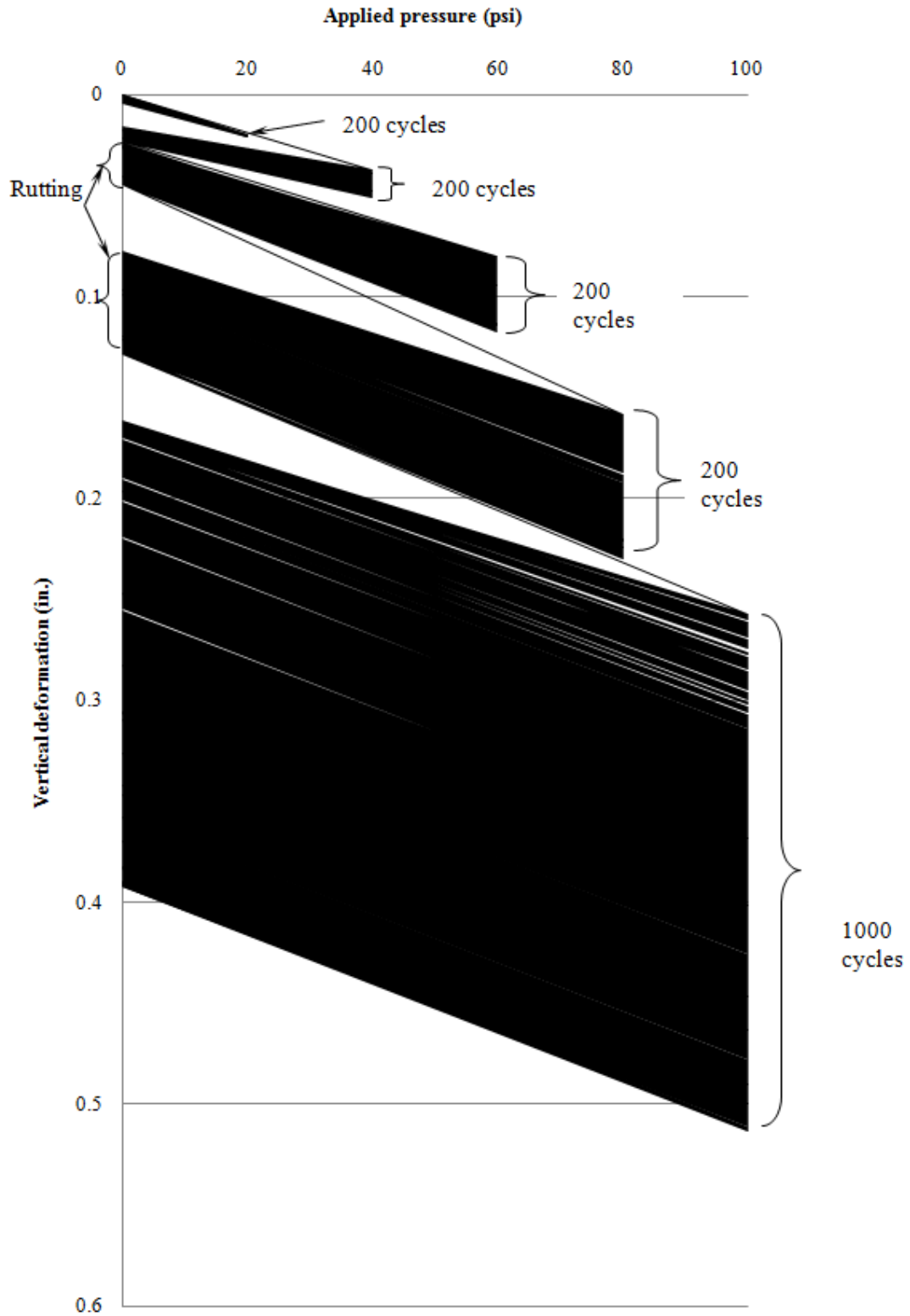


FIGURE 6.99 Vertical deformation of the loading plate under cyclic loading in Test 1

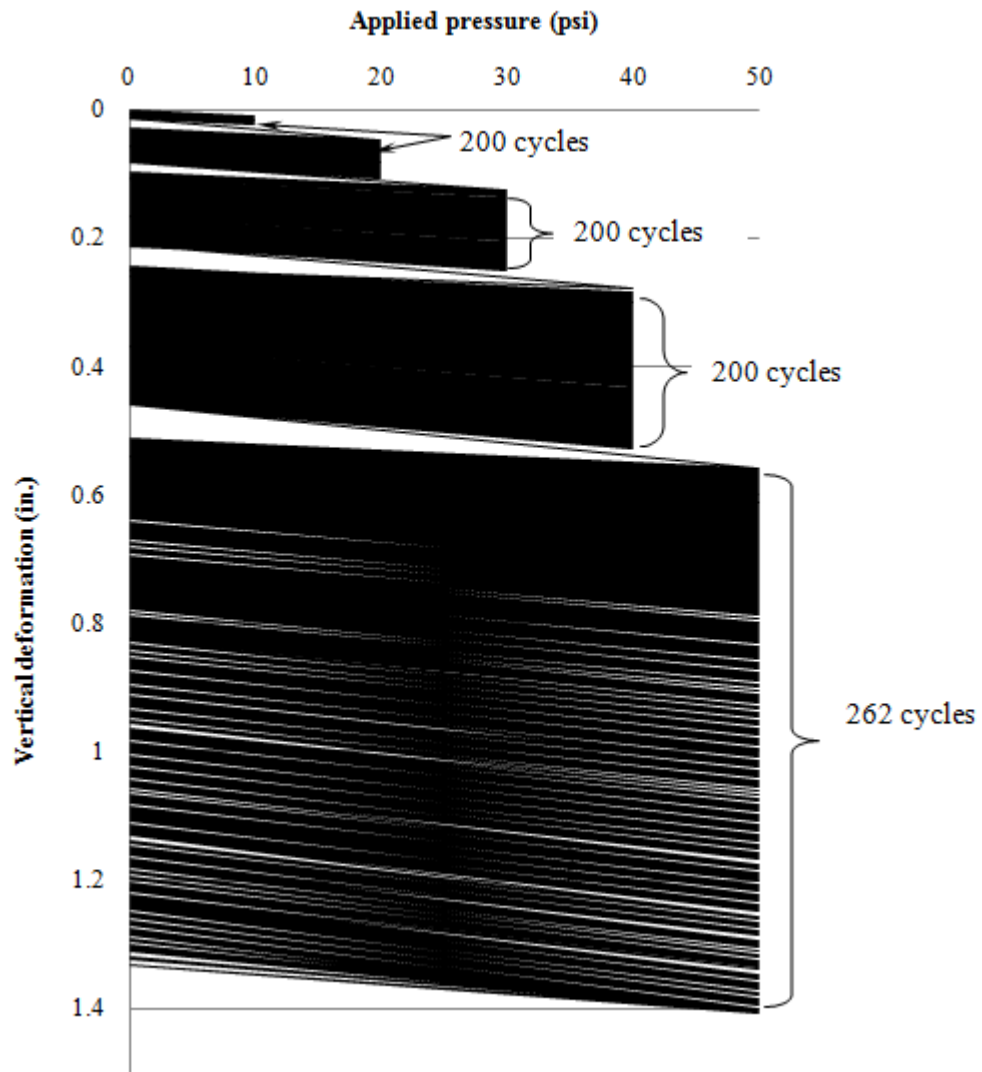


FIGURE 6.100 Vertical deformation of the loading plate under cyclic loading in Test 2

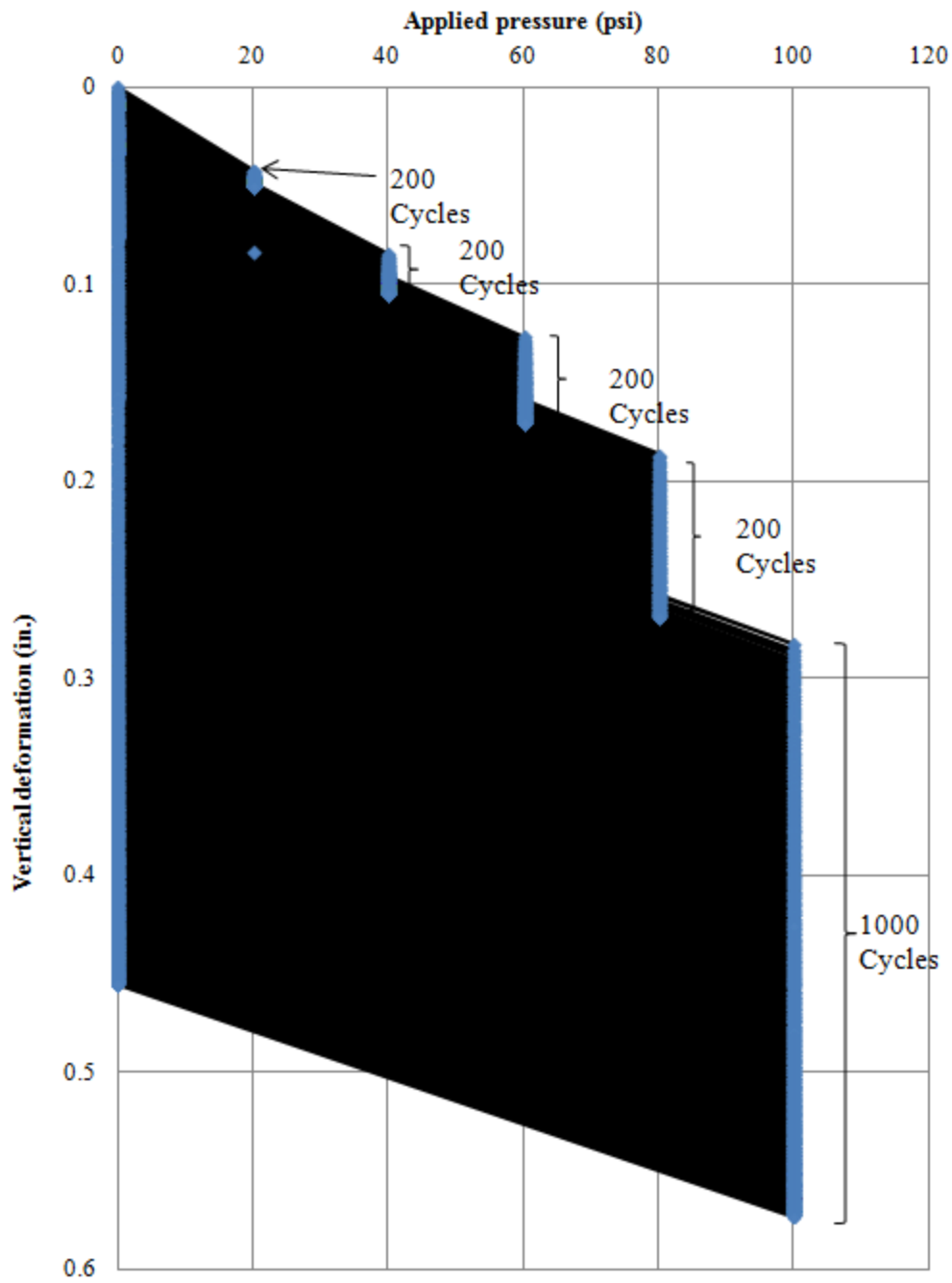


FIGURE 6.101 Vertical deformation of the loading plate under cyclic loading in Test 3

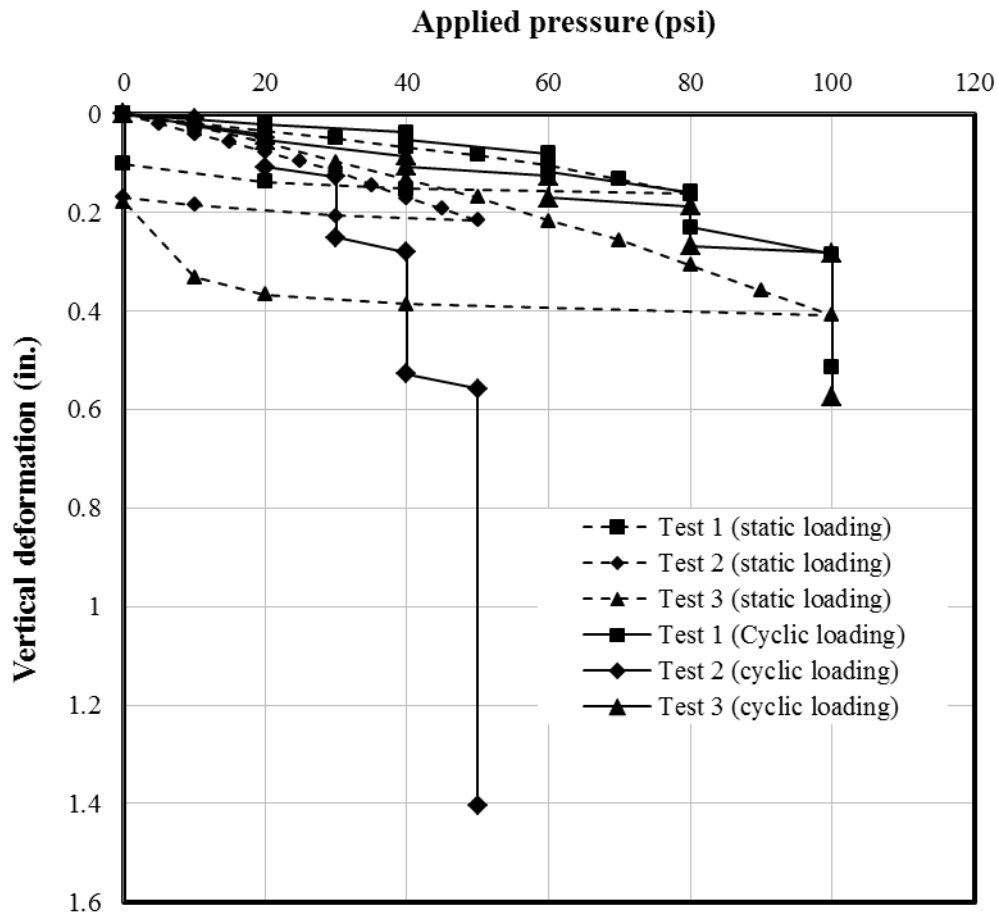


FIGURE 6.102 Vertical deformations of the loading plate under static and cyclic loadings

TABLE 6.7 Permanent deformations

Loading Step	Applied pressure (psi)		Cycles		Permanent deformation (in.) (due to each load step)		
	Test 1 and 3	Test 2	Test 1 and 3	Test 2	Test 1	Test 2	Test 3
1	0-20	0-10	200	200	0.005	0.015	0.011
2	0-40	0-20	200	200	0.008	0.04	0.019
3	0-60	0-30	200	200	0.020	0.11	0.040
4	0-80	0-40	200	200	0.050	0.215	0.080
5	0-100	0-50	1000	260	0.227	0.818	0.296

6.3.2 Maximum Earth Pressure Results

The maximum earth pressures measured by the earth pressure cells during each loading step were induced by cyclic loading only. In other words, the earth pressures induced during installation and static loading were not included. These cyclic earth pressure results are discussed in this section.

Test 1

FIGURE 6.103 shows the measured maximum earth pressures against the applied cyclic pressures in all the loading steps in Test 1. The earth pressure cell on the pipe crown (E_{C6}) showed the highest earth pressure on the pipe. The maximum earth pressure measured on the crown (E_{C0}) at the end of 1,000 cycles of the final load step (0 to 100 psi) was approximately 12 psi. The vertical earth pressure at 6 in. away from the center (E_{C6}) was 0.55 to 0.67 times that on the pipe crown (E_{C0}). The maximum horizontal pressure at the pipe springline (E'_{s0}) was 0.3 to 0.4 times the maximum vertical earth pressure at the crown (E_{C0}). The ratio of the maximum horizontal pressure at the springline (E'_{s0}) to that at the shoulder (E'_{sh0}) was 1.25 to 1.5.

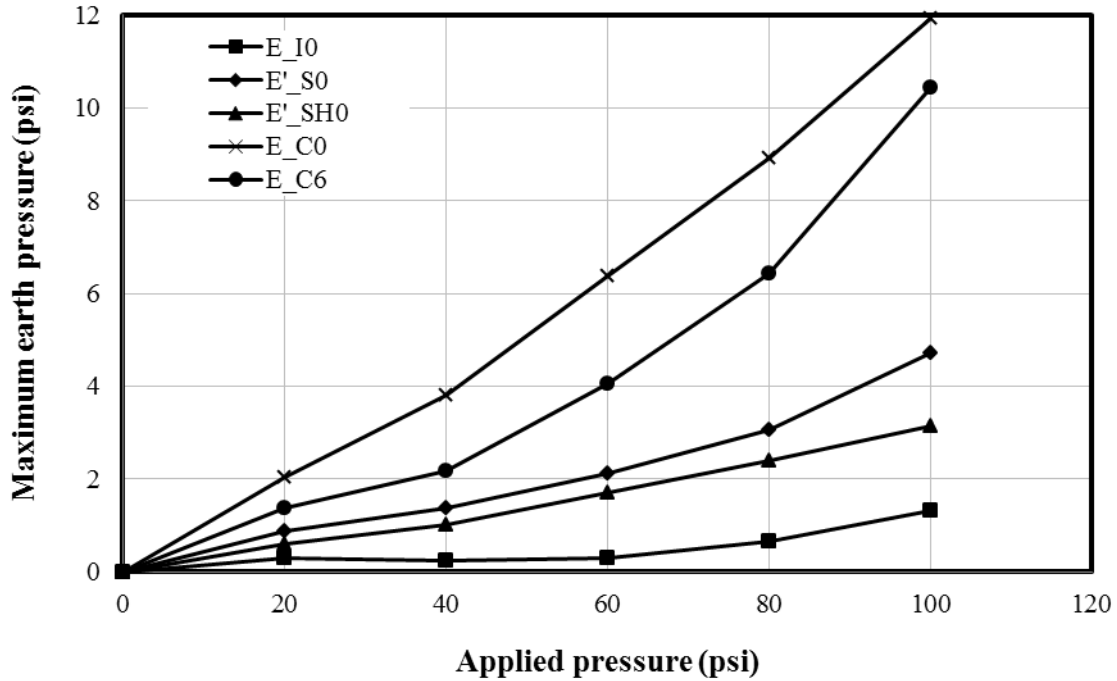


FIGURE 6.103 Measured maximum earth pressures around the pipe under cyclic loading in Test

1

Test 2

FIGURE 6.104 shows the measured maximum earth pressures against the applied cyclic pressures in all the loading steps in Test 2. The earth pressure cell on the pipe crown (E_{C0}) showed the highest earth pressure on the pipe. The maximum earth pressure measured on the crown (E_{C0}) at the end of 260 cycles of the final load step (0 to 50 psi) was approximately 5.83 psi. The maximum vertical earth pressure at 6 in. away from the center (E_{C6}) was 0.60 to 0.70 times that on the pipe crown (E_{C0}). The maximum horizontal earth pressure at the pipe springline (E'_{S0}) was 0.3 to 0.45 times the maximum vertical earth pressure at the crown (E_{C0}). The ratio of the maximum horizontal earth pressure at the springline (E'_{S0}) to that at the shoulder (E'_{SH0}) was 1.1 to 1.46.

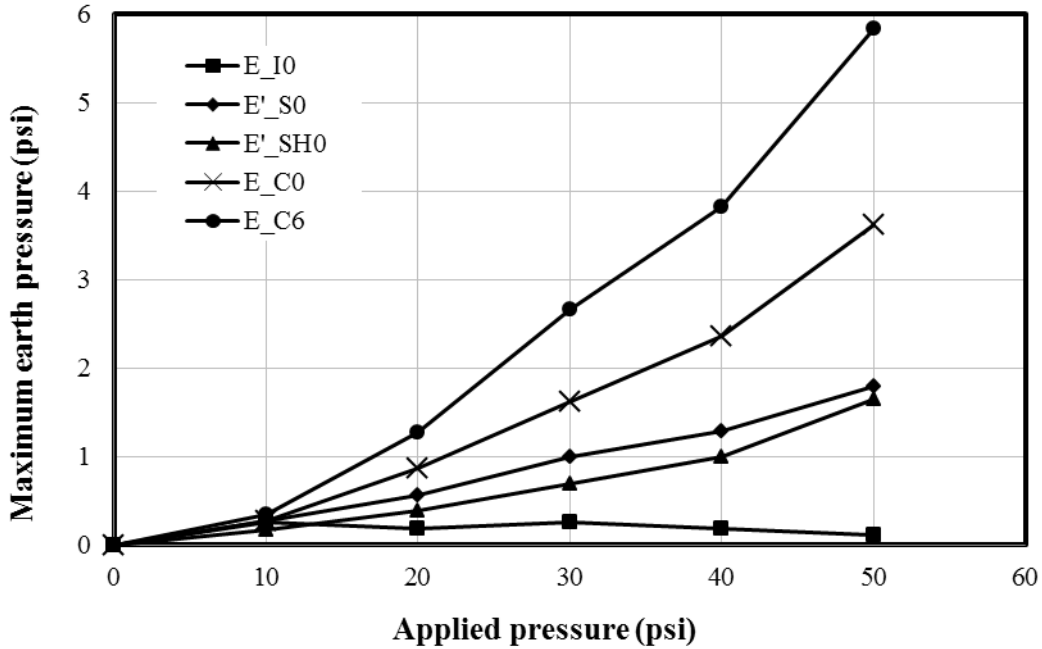


FIGURE 6.104 Measured maximum earth pressures around the pipe under cyclic loading in Test

2

Test 3

FIGURES 6.105 and **6.106** show the maximum earth pressures recorded by the earth pressure cell (E_{IF}) at the base course and backfill interface and nine other earth pressure cells around the pipe against the applied cyclic pressures in different loading steps. **FIGURE 6.106** shows that the maximum earth pressures recorded by the earth pressure cell (E_{C6}) at 6 in. away from the pipe crown were the highest during loading. The maximum earth pressure measured on the crown (E_{C0}) at the end of 1,000 cycles of the final load step (0 to 100 psi) was approximately 8 psi. The maximum vertical earth pressure at 6 in. away from the center (E_{C6}) was mostly 1.5 to 2 times that on the pipe crown (E_{C0}). The maximum horizontal earth pressures at the pipe springline (E'_{S0} and E'_{S8}) were 0.04 to 0.10 times the maximum vertical earth pressure at the

crown (E_{CO}). The ratio of the maximum horizontal earth pressure at the springline (E'_{S0}) to that at the shoulder (E'_{SH0}) was 0.16 to 0.22.

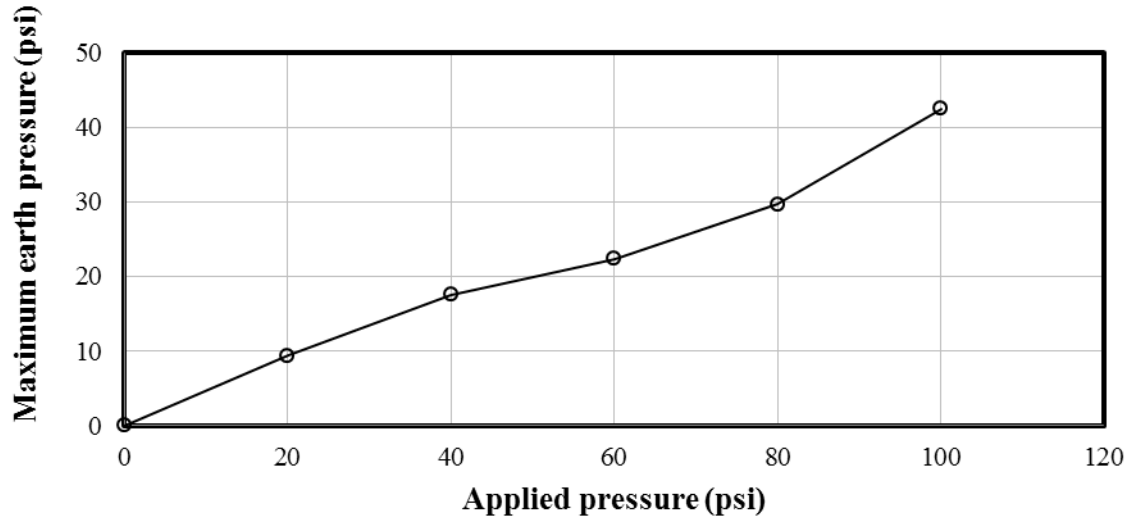


FIGURE 6.105 Measured maximum earth pressure at the backfill-base course interface in Test 3

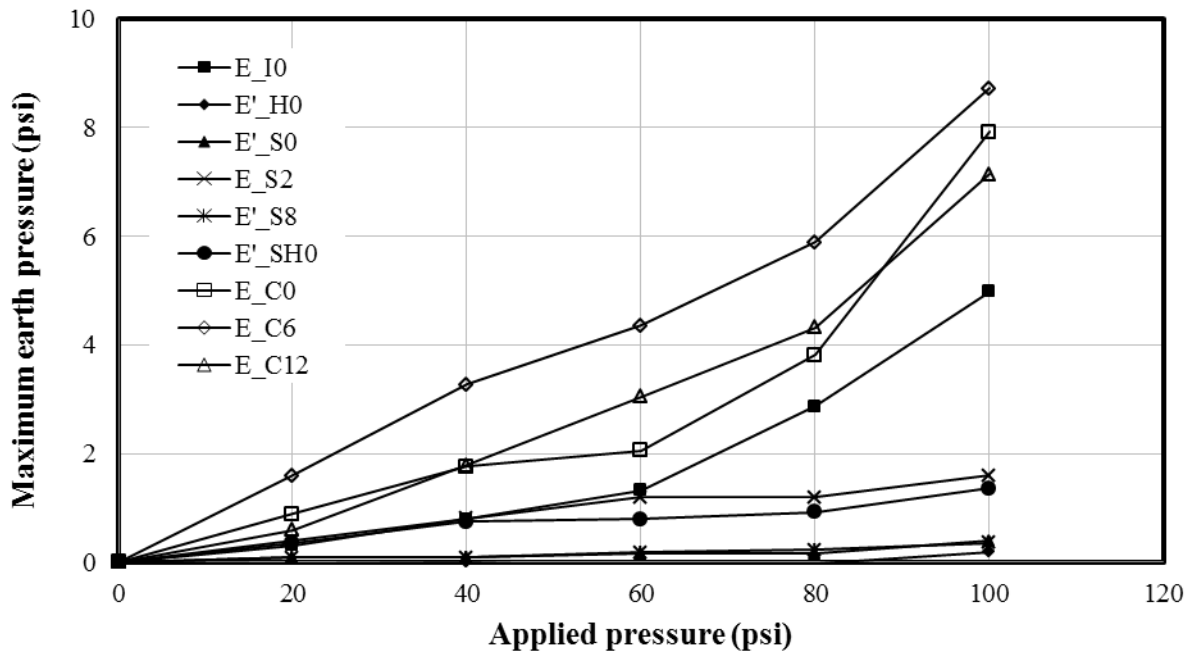


FIGURE 6.106 Measured maximum earth pressures around the pipe under cyclic loading in Test 3

Comparison of test results and Summary

FIGURE 6.107 shows the comparison of the maximum earth pressure distributions around the pipe in Test 1 (with the AB-3-I base course and the KR sand backfill) and Test 2 (with the KR sand backfill and the base course). The maximum earth pressures around the pipe were lower in Test 2 than those in Test 1 at low applied pressures. As the applied pressure was increased, the differences became smaller. At the high applied pressures, the maximum earth pressures around the pipe were higher in Test 2 than in Test 1.

FIGURE 6.108 shows the comparison of the maximum earth pressure distributions around the pipe for two different backfills: the KR sand in Test 1 and the crushed stone CS-I in Test 3. The maximum earth pressures around the pipe were higher in Test 1 than in Test 3. The maximum vertical earth pressures on the crown (E_{C0}) were higher than those at 6 in. away from the crown (E_{C6}) in Test 1. However, the maximum earth pressures on the crown (E_{C0}) were lower than those (E_{C6}) in Test 3. Similarly, the maximum horizontal earth pressures at the springline (E'_{s0}) were lower than those (E'_{sh0}) at the shoulder in Test 3. However, the maximum horizontal earth pressures at the springline (E'_{s0}) were higher than those earth pressures at the shoulder (E'_{sh0}) in Test 1. The earth pressure cell at the invert (E_{I0}) showed the higher earth pressure in Test 3 than that in Test 1 because the pipe was lifted up in Test 1 as discussed in **SECTION 6.1.1**, but there was little or no lift-up of the pipe in Test 3 during backfilling.

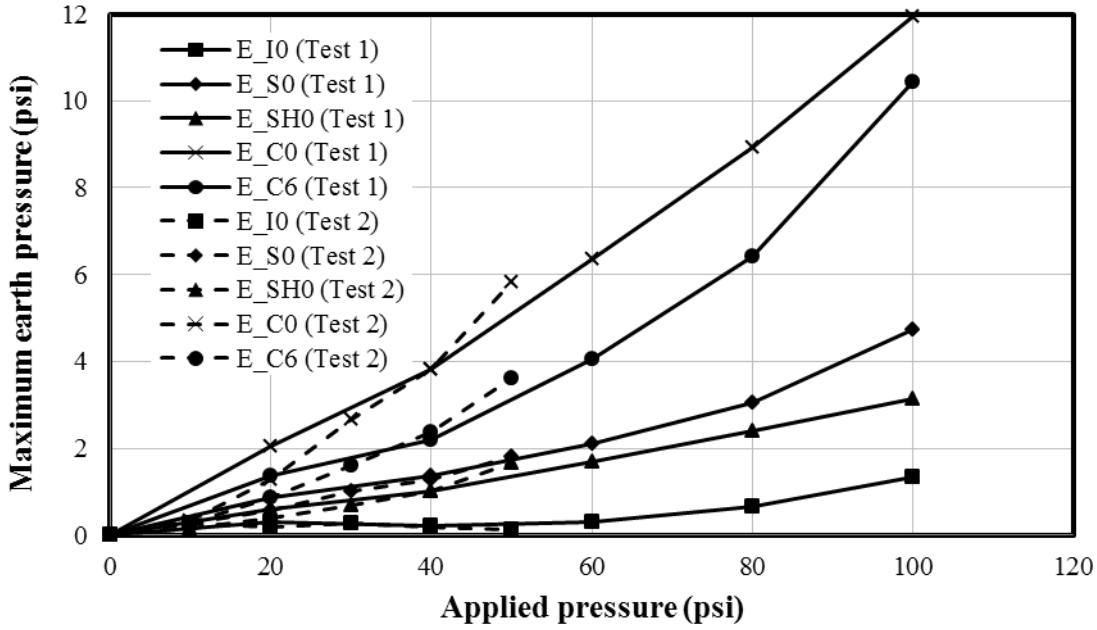


FIGURE 6.107 Comparison of the maximum earth pressures around the pipe under cyclic loading in Tests 1 and 2

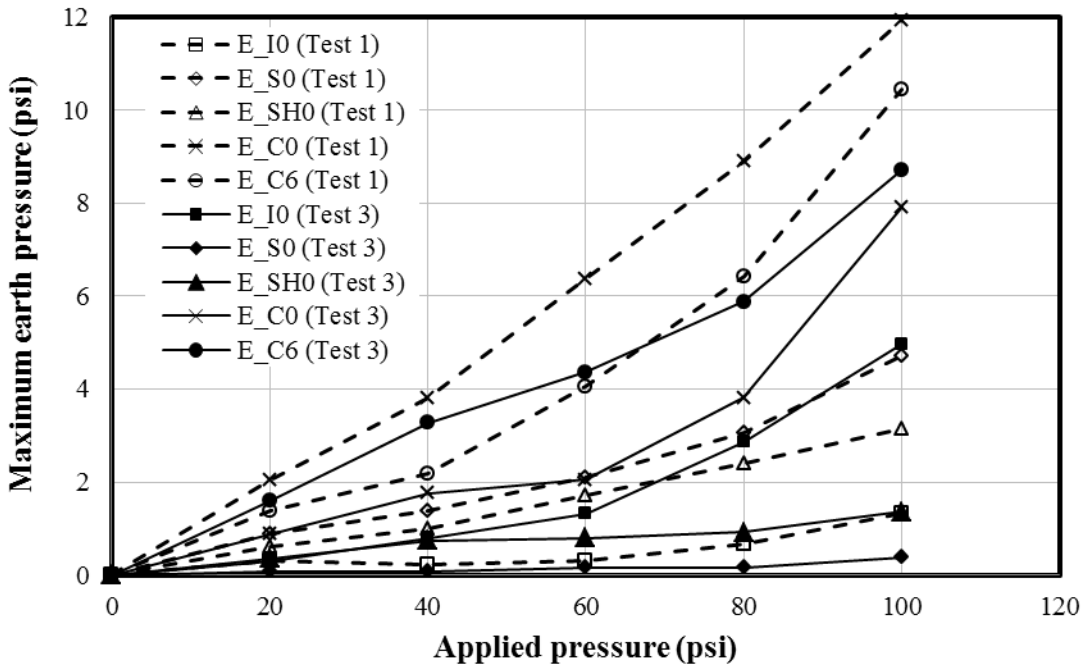


FIGURE 6.108 Comparison of the maximum earth pressures around the pipe under cyclic loading in Tests 1 and 3

6.3.3 Pipe Deflection Results

Test 1

The maximum deflections of the pipe (or the changes in the inside diameters) against the applied cyclic pressures are shown in **FIGURE 6.109**. The maximum deflection of the test pipe illustrates that the vertical diameter of the pipe (ΔD_{VC}) decreased while the horizontal diameter of the pipe (ΔD_{HC}) increased as the load increased. The maximum vertical deflection at the center of the pipe (ΔD_{VC}) was approximately 1.5 to 2 times the maximum horizontal deflection (ΔD_{HC}) at the same pipe section and 2.5 to 3 times the maximum vertical deflection at 1 ft longitudinally from the center of the test pipe. The maximum decrease in the vertical diameter (ΔD_{VC}) and the maximum increase in the horizontal diameter at the center of the pipe (ΔD_{HC}) at the end of 1,000 cycles of the final load step (0 to 100 psi) was 0.055 in. (0.23% of the initial diameter) and 0.027 in. (0.11% of the initial diameter), respectively.

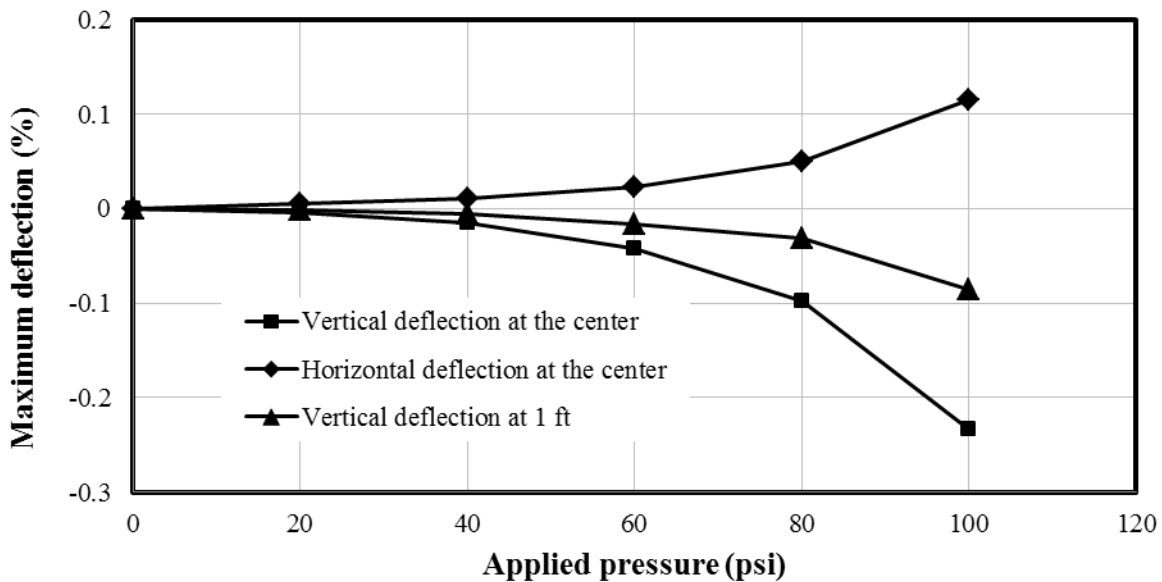


FIGURE 6.109 Maximum deflections of the pipe under cyclic loading in Test 1

Test 2

The maximum deflections of the pipe (or the changes in the inside diameters) against the applied cyclic pressures are shown in **FIGURE 6.110**. The maximum vertical deflection at the center of the pipe (ΔD_{VC}) was approximately 1.26 to 1.8 times the maximum horizontal deflection (ΔD_{VC}) at the same pipe section, and 1.75 to 3.1 times the maximum vertical deflection at 1 ft longitudinally from the center of the test pipe (ΔD_{V1}). The maximum decrease in the vertical diameter (ΔD_{VC}) and the maximum increase in the horizontal diameter (ΔD_{VC}) at the center of the pipe at the end of 260 cycles of the final load step (0 to 50 psi) were 0.0098 in. (0.042% of the initial diameter) and 0.0054 in. (0.023% of the initial diameter), respectively.

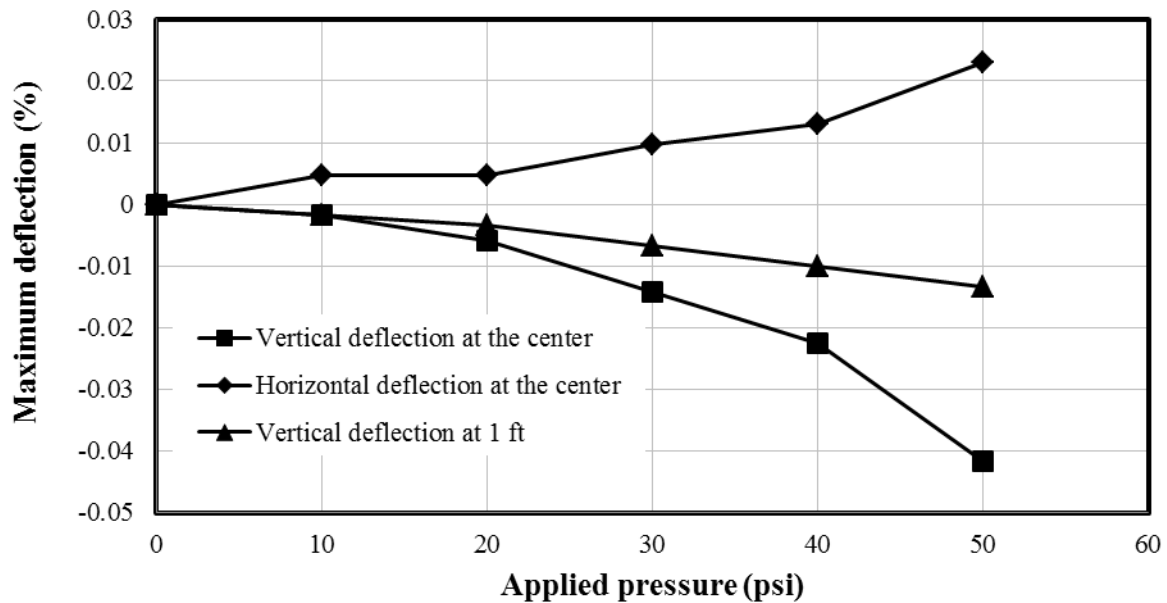


FIGURE 6.110 Maximum deflections of the pipe under cyclic loading in Test 2

Test 3

The maximum deflections of the pipe (or the changes in the inside diameters) against the applied cyclic pressures are shown in **FIGURE 6.111**. The maximum vertical deflection at the center of the pipe (ΔD_{VC}) was approximately 1.5 to 2 times the maximum horizontal deflection at the same pipe section (ΔD_{HC}) and 1.4 to 2.0 times the maximum vertical deflection at 1 ft longitudinally from the center of the test pipe (ΔD_{V1}). The maximum decrease in the vertical diameter (ΔD_{VC}) and the maximum increase in the horizontal diameter at the center of the pipe (ΔD_{HC}) at the end of 1,000 cycles of the final load step (0 to 100 psi) was 0.066 in. (0.28% of the initial diameter) and 0.040 in. (0.17% of the initial diameter), respectively.

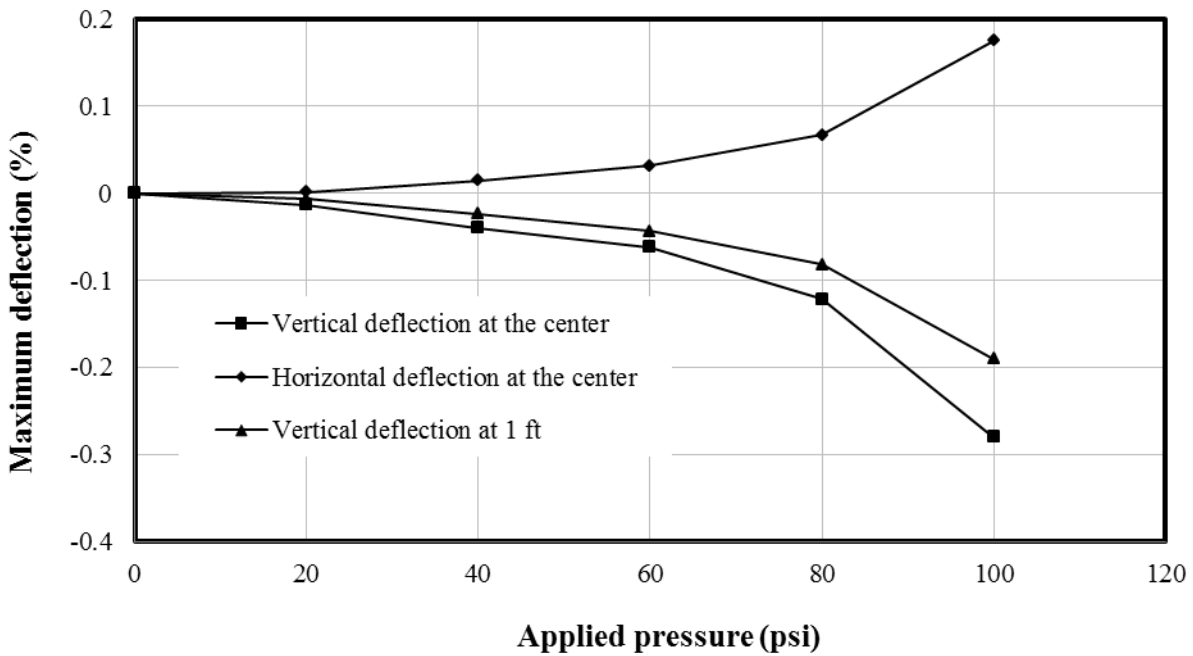


FIGURE 6.111 Maximum deflections of the pipe under cyclic loading in Test 3

Comparison of test results

FIGURE 6.112 shows the comparison of the maximum deflections of the pipe in Test 1 (with the AB-3-I base course and the KR sand backfill) and Test 2 (with the KR sand as the base course and the backfill). The measured maximum deflections at the center of the pipe (Δ_{VC} and Δ_{HC}) in Test 1 were less than those in Test 2.

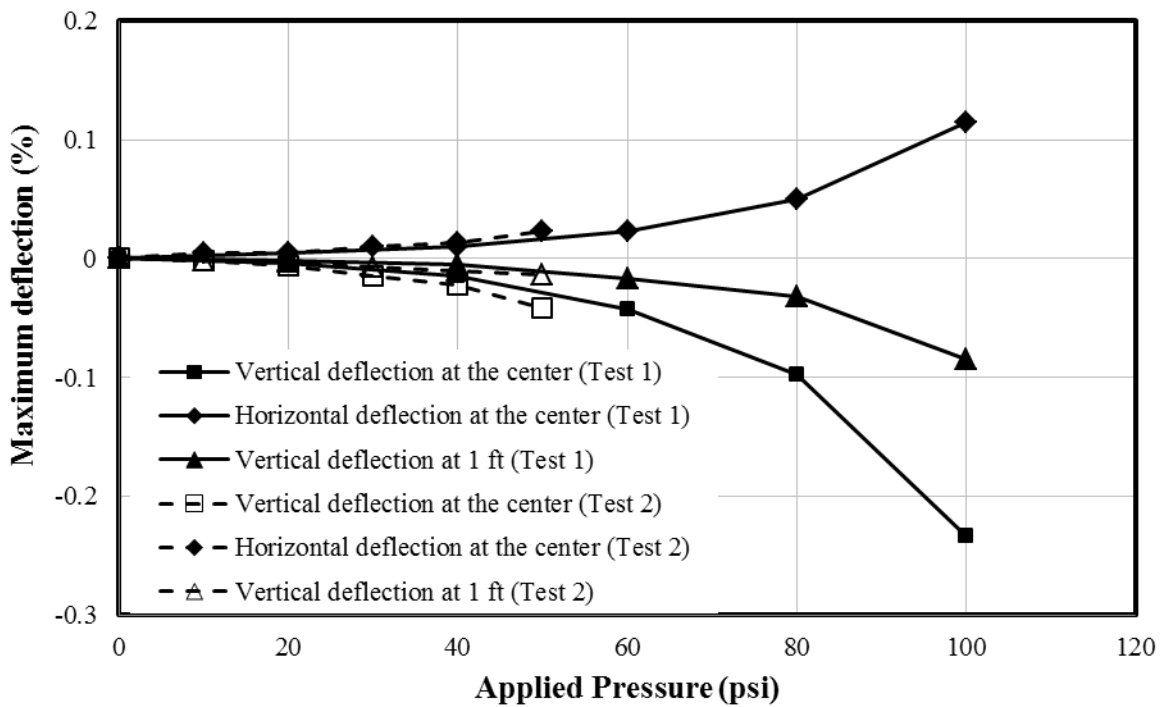


FIGURE 6.112 Comparison of the maximum deflections of the pipe under cyclic loading in Tests 1 and 2

FIGURE 6.113 shows the comparison of the maximum deflections of the pipe in Test 1 (with the KR sand backfill) and Test 3 (with the crushed stone CS-I backfill). The measured

maximum deflections of the pipe in Test 1 were less than those in Test 3 because the crushed stone CS-I in Test 3 was dumped without any compaction.

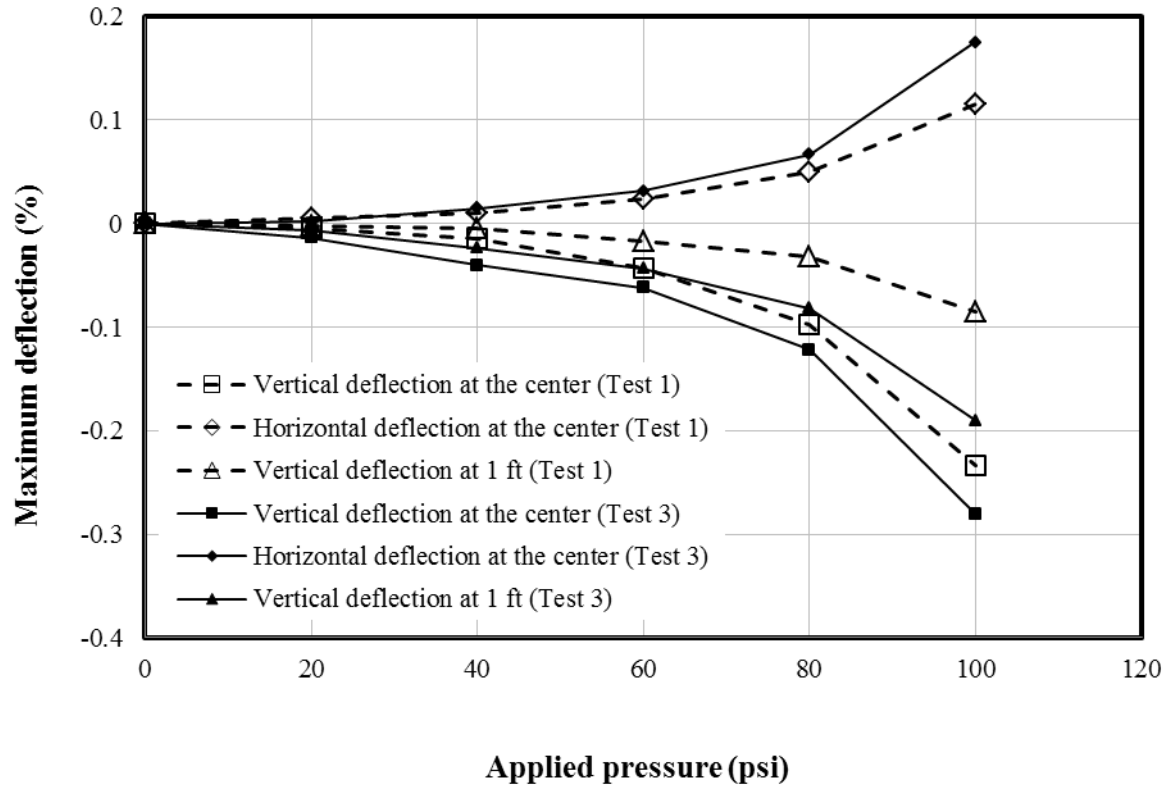


FIGURE 6.113 Comparison of the maximum deflections of the pipe under cyclic loading in Tests 1 and 3

FIGURE 6.114 shows the relationship between the maximum vertical and maximum horizontal deflections at the center of the pipe during loading. The ratio of the vertical to horizontal deflection ($\Delta D_{VC}/\Delta D_{HC}$) was approximately 1.64 in Tests 2 and 3 while the ratio was approximately 2.0 in Test 1. The ratios of the vertical to horizontal deflection ($\Delta D_{VC}/\Delta D_{HC}$) at the center of the pipe under the buried conditions were higher than that of the pipe tested in air

(i.e., 1.25). The higher ratios under the buried conditions were due to the resistance of the backfill against the horizontal deflections (ΔD_{HC}).

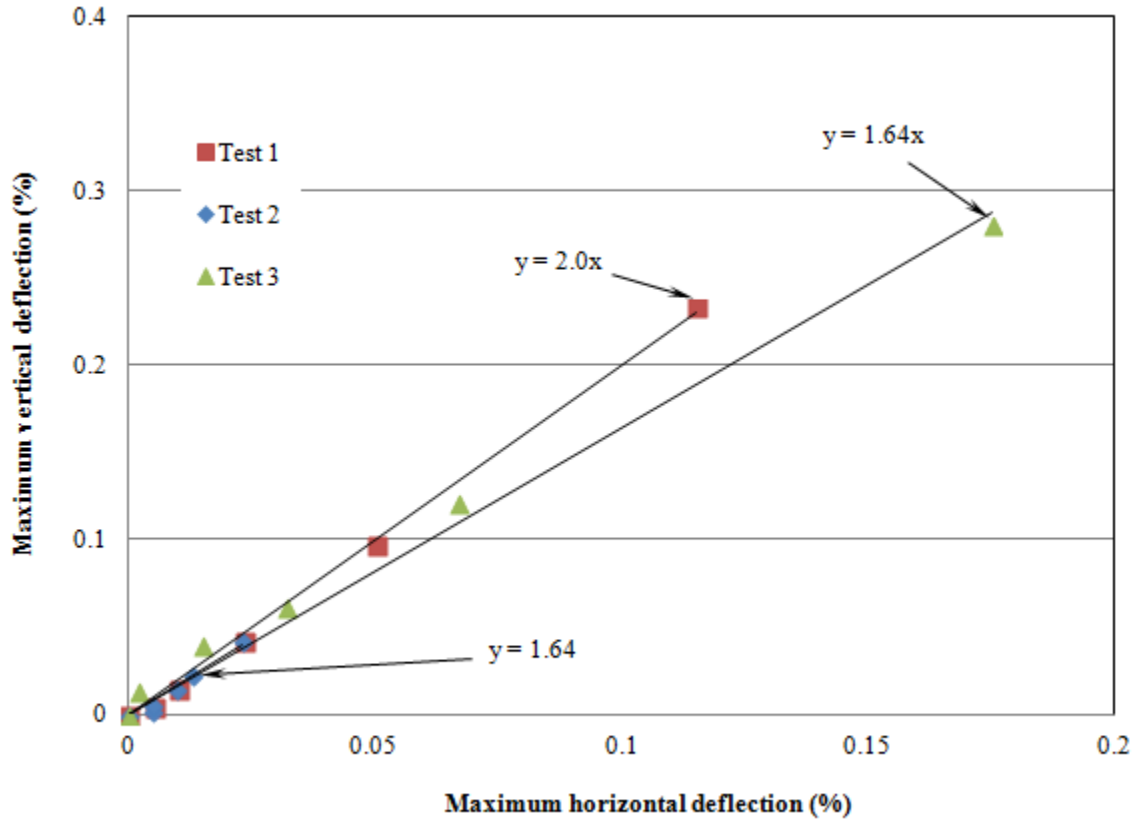


FIGURE 6.114 Relationship between the maximum horizontal and vertical deflections at the center of the pipe under cyclic loading

6.3.4 Strain Results

Test 1

The maximum circumferential and radial strains on the steel of the pipe at different loading steps are shown in **FIGURE 6.115**. Strain gage G_{SC1} at the springline and G_{IC2} at the

invert gave higher maximum strains in the circumferential direction than other strain gages on the steel. Strain gage G_{SC1} showed the maximum circumferential tensile strain of 0.0069% at the springline while strain gage G_{IC2} had a maximum circumferential compressive strain of 0.0053% at the invert.

FIGURE 6.116 shows the maximum circumferential and radial strains on the plastic cover at the ribs against the applied cyclic pressures. The maximum strains measured at most locations on the plastic cover were higher in magnitude than the maximum strains on the steel. Most of the strain gages showed an increase of tensile strains with an increase of the applied cyclic pressures except strain gage G'_{CR1} , which indicated an increase of compressive strains. Strain gage G'_{SC2} on the plastic cover at the rib at the springline in the circumferential direction showed a maximum tensile strain of 0.048% and strain gage G_{CRI} had a maximum compressive strain of 0.015%.

FIGURE 6.117 shows the maximum strains measured by strain gages $G1''$ to $G8''$ on the inside and outside plastic walls. **FIGURES 6.115** to **6.117** indicate that the plastic walls between the steel ribs experienced the highest strains among other components of the pipe wall. The maximum tensile strain of 0.17% at strain gage G''_{CL1} and the maximum compressive strain of 0.025% at strain gage G''_{SL1} were measured on the outside plastic wall (valley) at the end of 1,000 cycles of the final load step (0 to 100 psi).

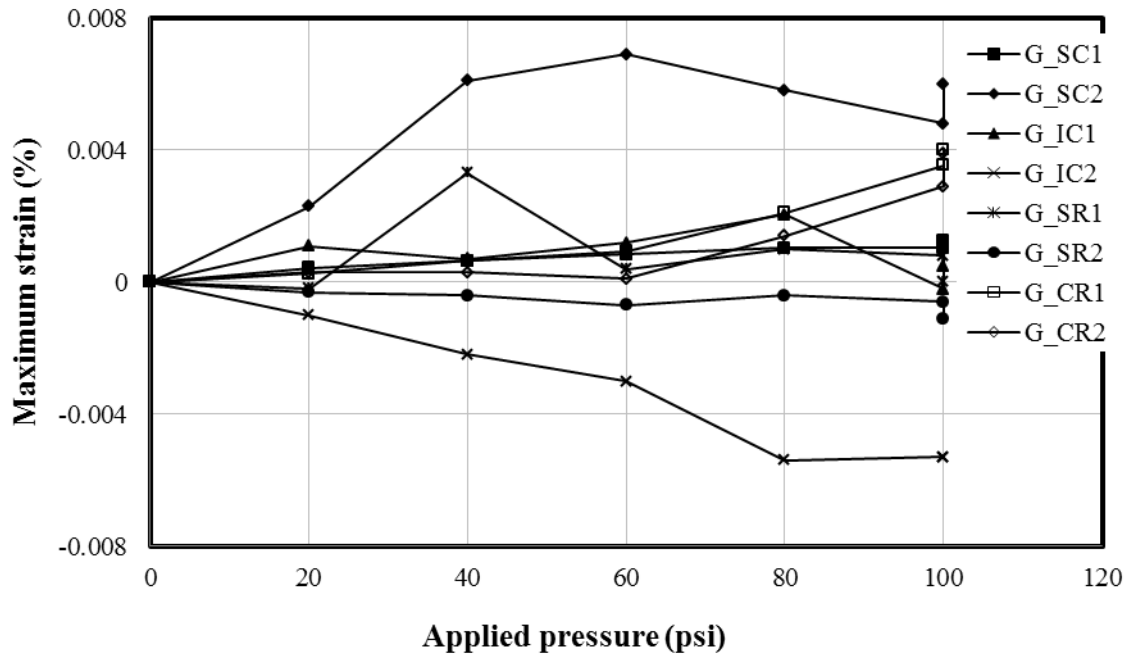


FIGURE 6.115 Measured maximum strains on the steel under cyclic loading in Test 1

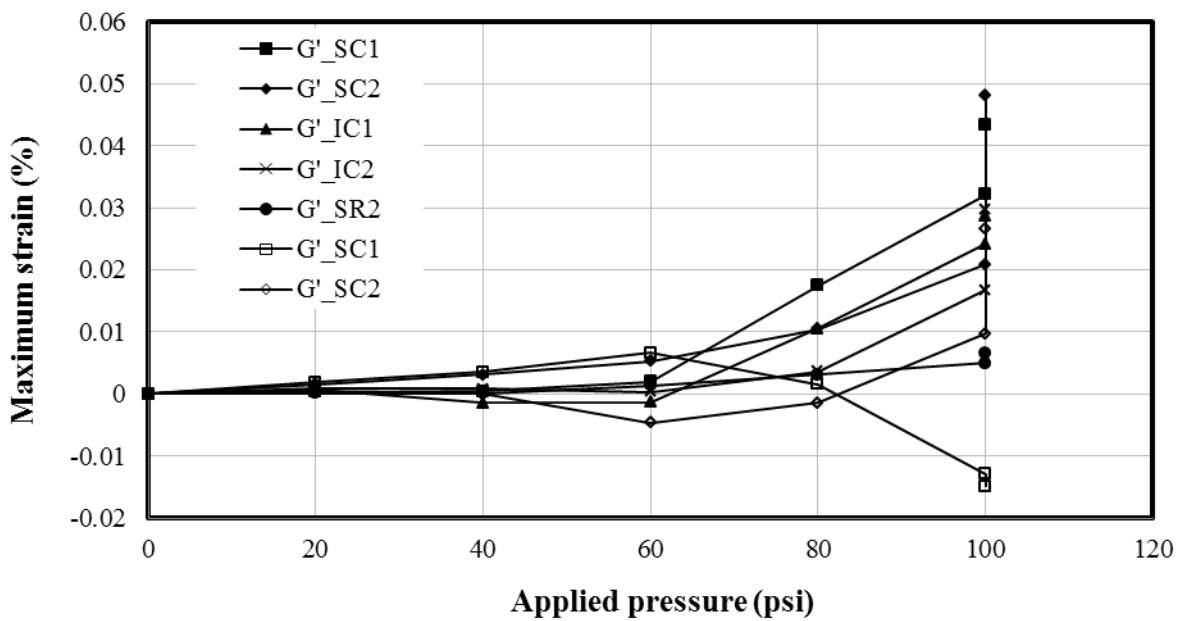


FIGURE 6.116 Measured maximum strains on the plastic cover at ribs under cyclic loading in

Test 1

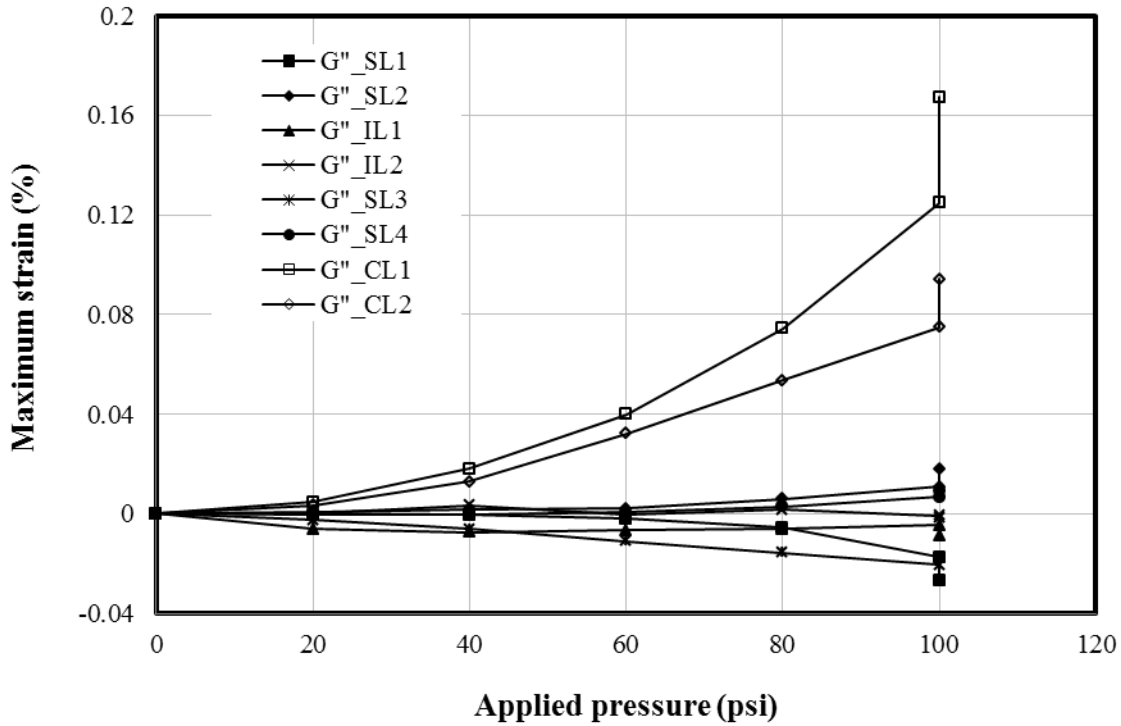


FIGURE 6.117 Measured maximum strains on the inside and outside walls of the pipe during cyclic loading in Test 1

Test 2

The maximum circumferential and radial strains on the steel of the pipe are shown in **FIGURE 6.118**. Most of the strain gages showed an increase in tensile strains under the applied cyclic pressures. However, strain gages, G_{SR1} and G_{SR2} at the springline and G_{CR1} and G_{CR2} at the crown in the radial direction, showed compressive strains at the lower cyclic loading step and tensile strains at the higher loading step. Strain gage G_{IC2} on the steel at the invert in the circumferential direction measured a maximum tensile strain of 0.0027% at the end of 260 cycles of the final loading step (0 to 50 psi).

FIGURE 6.119 shows the maximum circumferential and radial strains on the plastic cover at the ribs against the applied cyclic pressures. Most of the strain gages showed an increase in tensile strains under the applied pressures. Strain gage G_{SR2} showed a maximum tensile strain of 0.0083% at the end of 260 cycles of the final load step (0 to 50 psi).

The maximum strains measured by the strain gages on the inside and outside plastic walls are plotted in **FIGURE 6.120**, which indicates that the plastic walls between the steel ribs experienced the highest strains among all the components of the pipe wall. Strain gages G_{SL1} to G_{SL4} showed small strains as compared with those measured by strain gages G_{CL1} and G_{CL2} at the crown. The maximum tensile strain measured by strain gage G_{CL1} was 0.041% and the maximum compressive strain measured by strain gage G_{SL3} was 0.013% at the end of 1000 cycles of the final load step (0 to 100 psi).

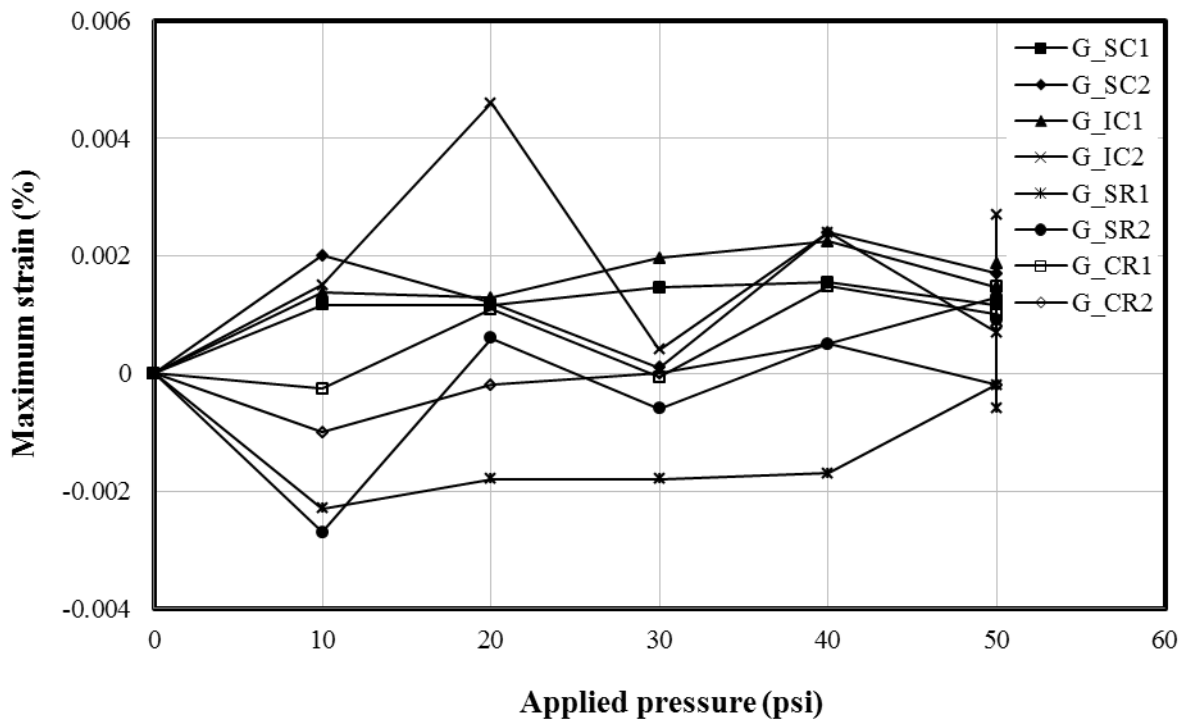


FIGURE 6.118 Measured maximum strains on the steel under cyclic loading in Test 2

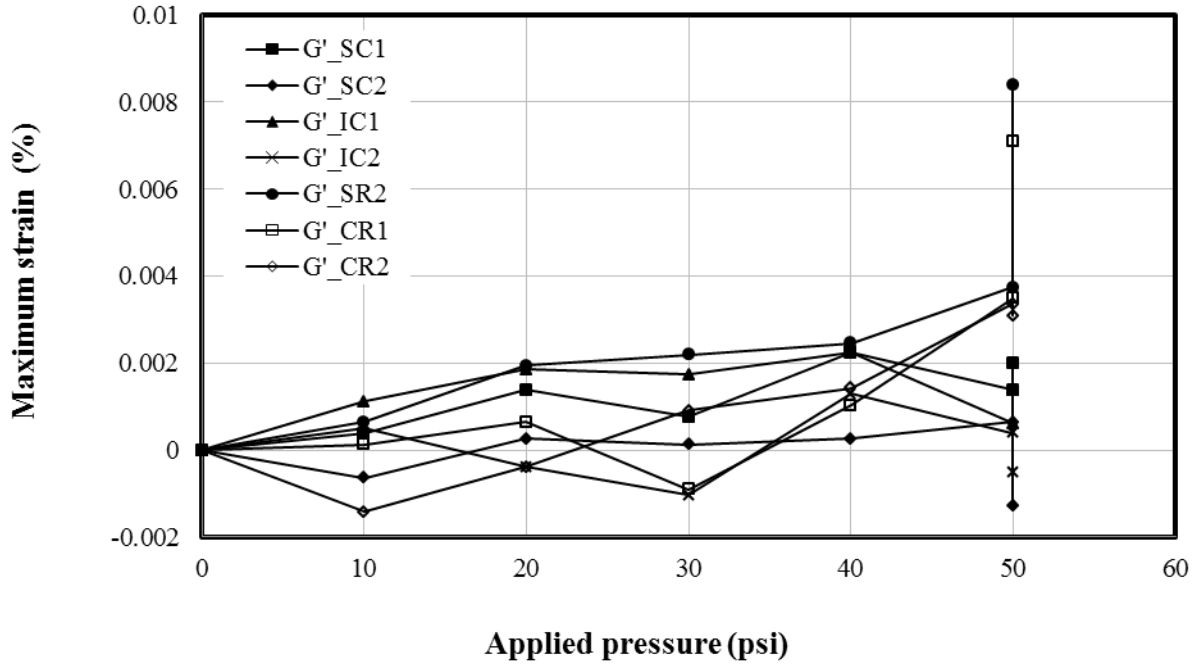


FIGURE 6.119 Measured maximum strains on the plastic cover at the ribs under cyclic loading in Test 2

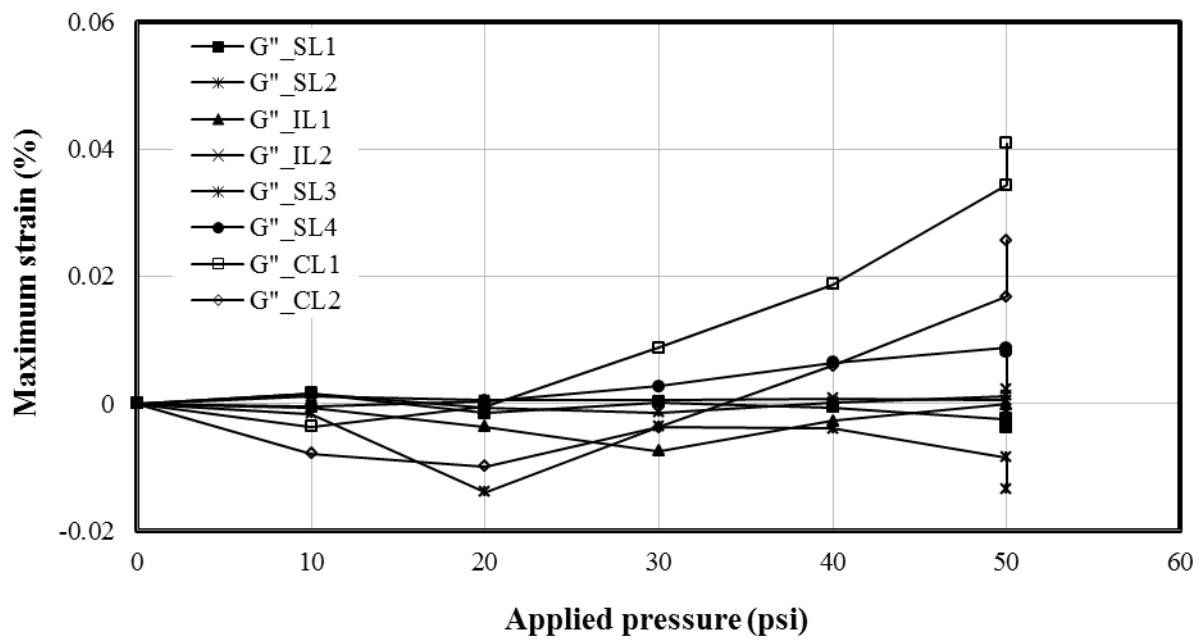


FIGURE 6.120 Measured maximum strains on the inside and outside plastic walls of the pipe during cyclic loading in Test 2

Test 3

The maximum circumferential and radial strains on the steel of the pipe are shown in **FIGURE 6.121**. Most of the strain gages showed an increase in tensile strains under the applied cyclic pressures. Strain gage G_{sC2} on the steel at the invert in the circumferential direction showed a maximum tensile strain of 0.016% at the end of 1000 cycles of the final load step (0 to 100 psi).

FIGURE 6.122 shows the maximum circumferential and radial strains on the plastic cover at the rib against the applied cyclic pressures. Strain gage G'_{CR1} showed the maximum tensile strain of 0.053% at the end of 1,000 cycles of the final load step (0 to 100 psi).

The strains measured by strain gages on the inside and outside plastic walls are plotted in **FIGURE 6.123**, which indicates that the plastic walls between the steel ribs experienced the highest strains among all the components of the pipe wall. The maximum tensile strain measured by strain gage G''_{CL1} was 0.2% and the maximum compressive strain measured by strain gage G''_{SL1} was 0.0063% at the end of 1000 cycles of the final load step (0 to 100 psi).

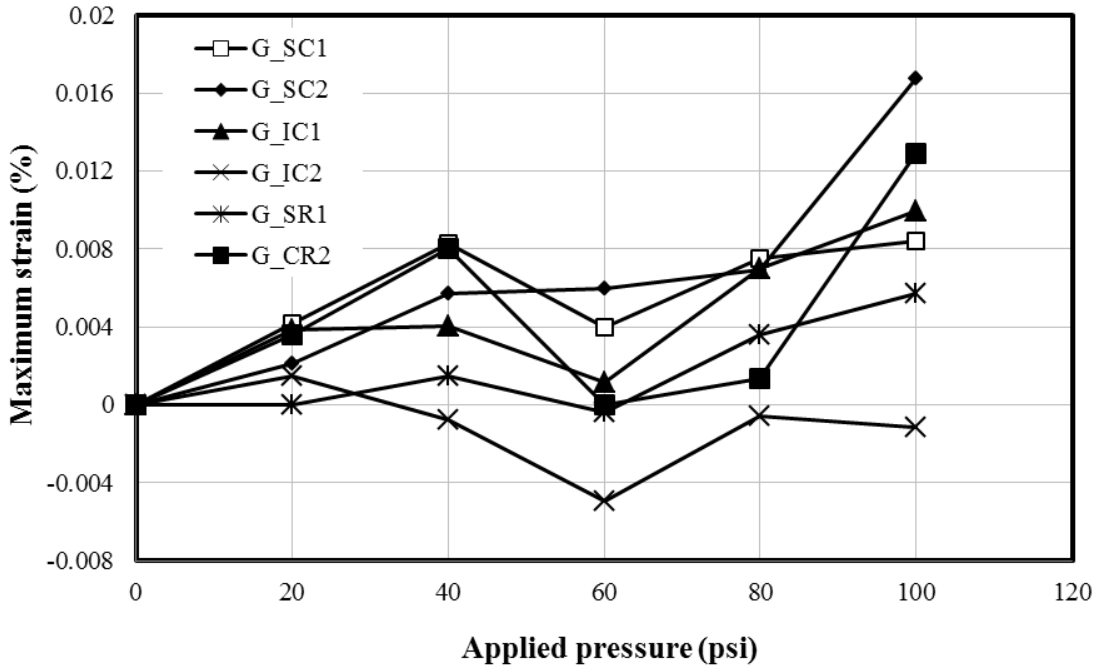


FIGURE 6.121 Measured maximum strains on the steel under cyclic loading in Test 3

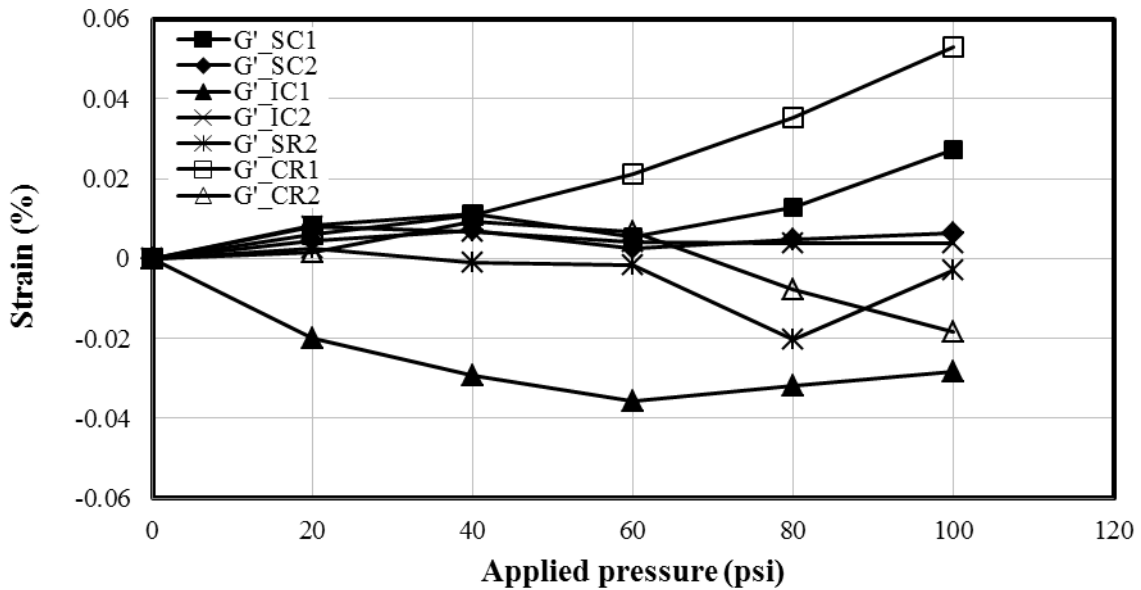


FIGURE 6.122 Measured maximum strains on the plastic cover at the ribs under cyclic loading in Test 3

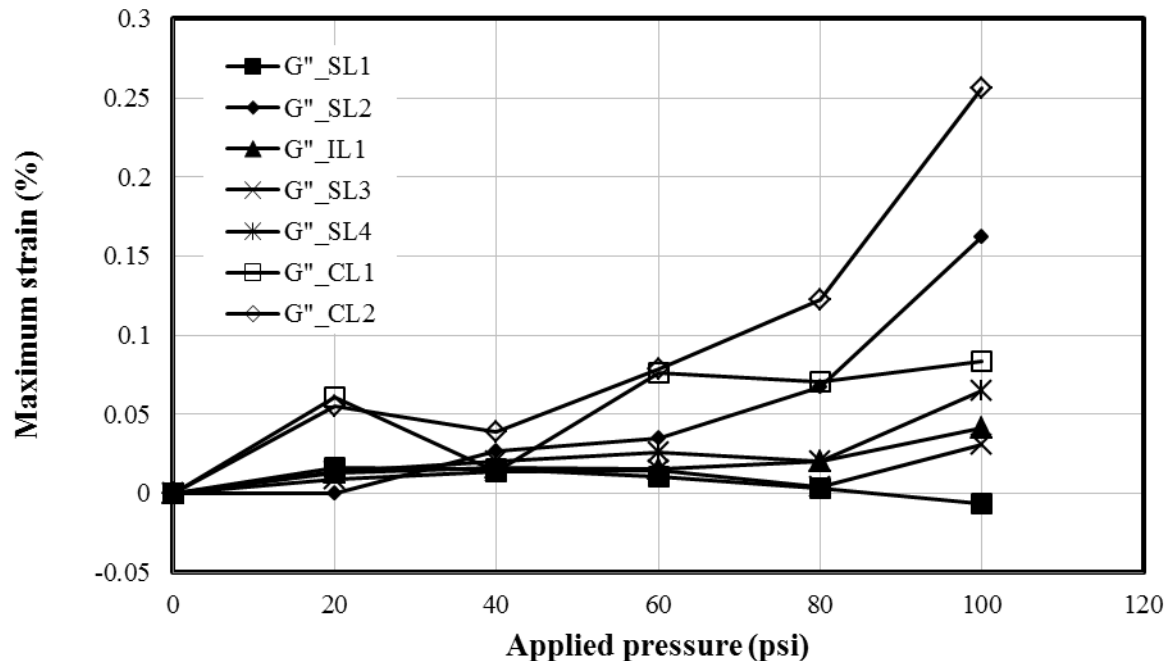


FIGURE 6.123 Measured maximum strains on the inside and outside pipe walls of the pipe under cyclic loading in Test 3

6.3.5 Comparison of Static and Cyclic Test Results

Earth Pressure Results

FIGURES 6.124, 6.125, and 6.126 indicate that the measured earth pressures around the pipe under static loading were higher than the maximum earth pressures under cyclic loading in Test 1, Test 2, and Test 3, respectively. The measured earth pressures around the pipe due to the applied static and cyclic loads for each test were normalized by the measured crown pressures for each loading step. The ratios of these normalized pressures around the pipe are presented in **TABLE 6.8**. The ratios of the measured earth pressures under static and cyclic loads in both Test 1 (with the AB-3-I base course and the KR sand backfill) and Test 2 (with the KR sand base course and backfill) were similar. However, the ratios of the measured earth pressures in Tests 1

and 2 (with the KR sand backfill) were different from those in Test 3 (with the crushed stone CS-I backfill). In Tests 1 and 2, the highest earth pressures were recorded at the crown of the pipe (E_{C0}) while in Test 3, the highest earth pressures were at 6 in. away from the crown of the pipe (E_{C6}). The earth pressure at the invert (E_{I0}) showed higher pressure in Test 3 than that in Tests 1 and 2 because the pipe was lifted up in Tests 1 and 2 as discussed in **SECTION 6.1.1** during the compaction of the backfill, but there was little or no lift-up of the pipe in Test 3 during backfilling.

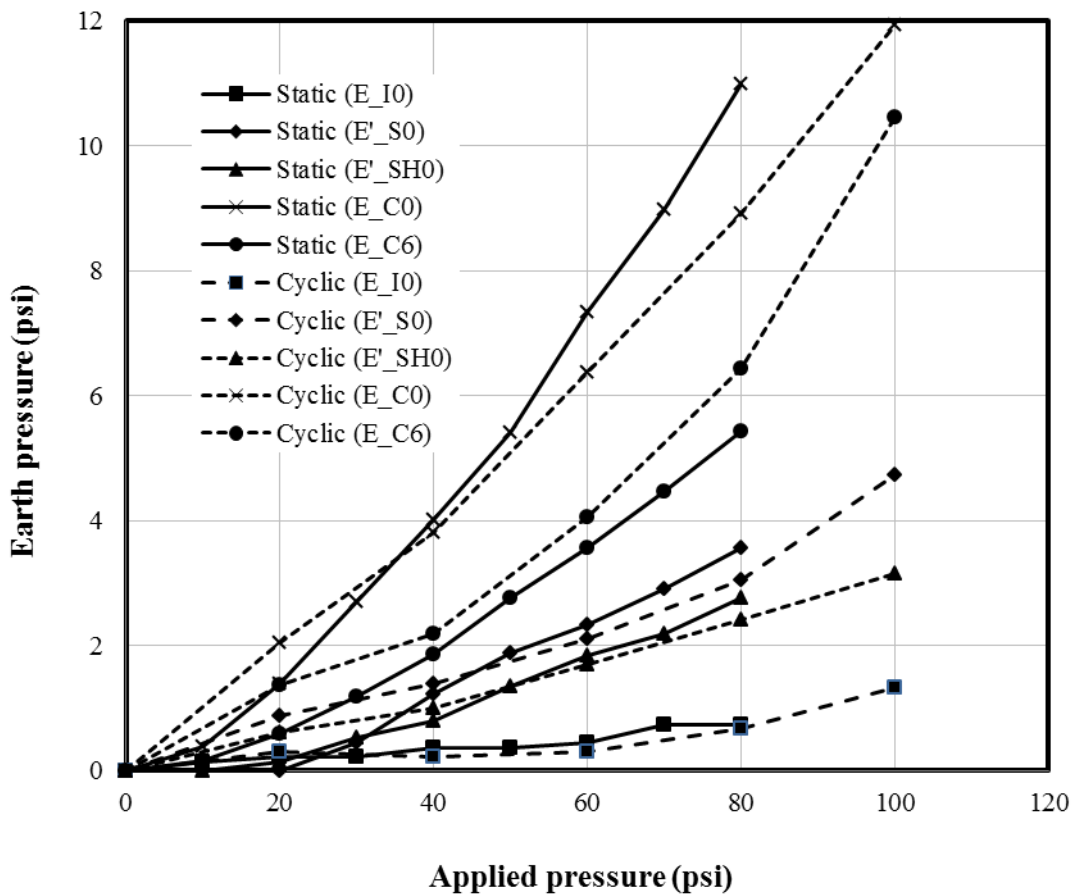


FIGURE 6.124 Comparison of the measured earth pressures around the pipe under static and cyclic loads in Test 1

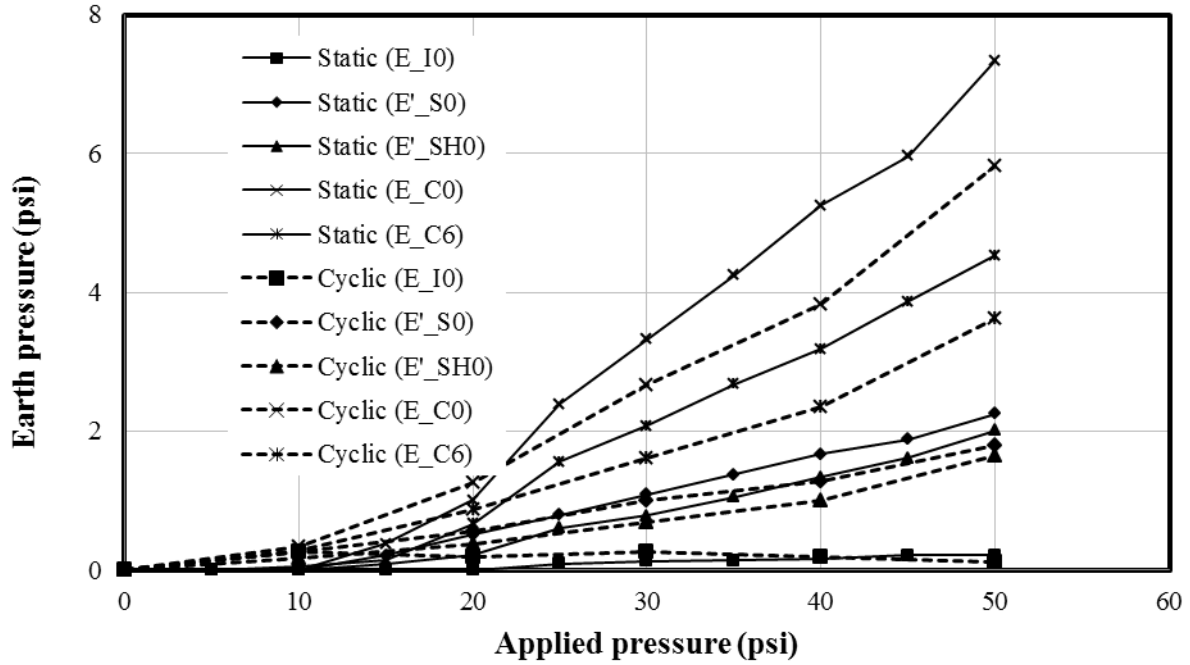


FIGURE 6.125 Comparison of the earth pressures around the pipe under static and cyclic loads in Test 2

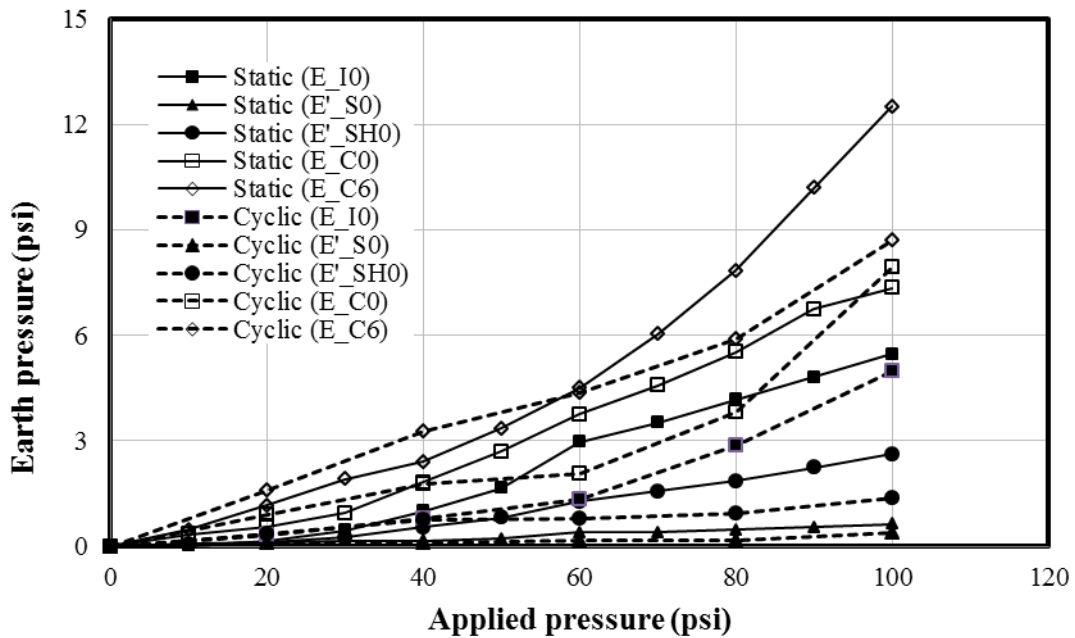


FIGURE 6.126 Comparison of the earth pressures around the pipe under static and cyclic loads in Test 3

TABLE 6.8 Comparisons of the earth pressures around the pipe and the deflections of the pipe

		Vertical to horizontal deflection ratio	$E_{T0}:E_{S0}:E_{SH0}:E_{C0}:E_{C6}$
In Air		1.25	-
Test 1	Installation	0.95	-
	Static	1.64	0.075:0.32:0.24:1:0.50
	Cyclic	2	0.075:0.36:0.27:1:0.70
Test 2	Installation	-	-
	Static	2	0.035:0.32:0.25:1:0.63
	Cyclic	1.64	0.077:0.36:0.27:1:0.63
Test 3	Installation	0.85	-
	Static	1.64	0.70:0.08:0.30:1:1.38
	Cyclic	1.64	0.62:0.05:0.30:1:1.65

Pipe Deflection Results

FIGURES 6.127, 6.128, and 6.129 indicate that the measured deflections of the pipe under static loading were higher than those under cyclic loading in Test 1, Test 2, and Test 3, respectively. The ratio of the vertical to horizontal deflection at the center of the test pipe for each test is shown in **TABLE 6.8**. When the pipe was tested by the parallel plate test in air, the ratio was 1.25. However, the ratio was higher than 1.25 when the pipe was tested in a buried condition under a shallow depth under both static and cyclic loads. This is because the backfill soil minimized the outward movement of the pipe at the springline. The ratios of the vertical to horizontal deflection of the pipe under the buried condition were almost the same for all tests under static and cyclic load tests, ranging from 1.64 to 2.0. During the installation of the test pipe, the ratios were 0.95 in Test 2 (with the KR sand backfill) and 0.85 in Test 3 (with the crushed stone CS-I backfill).

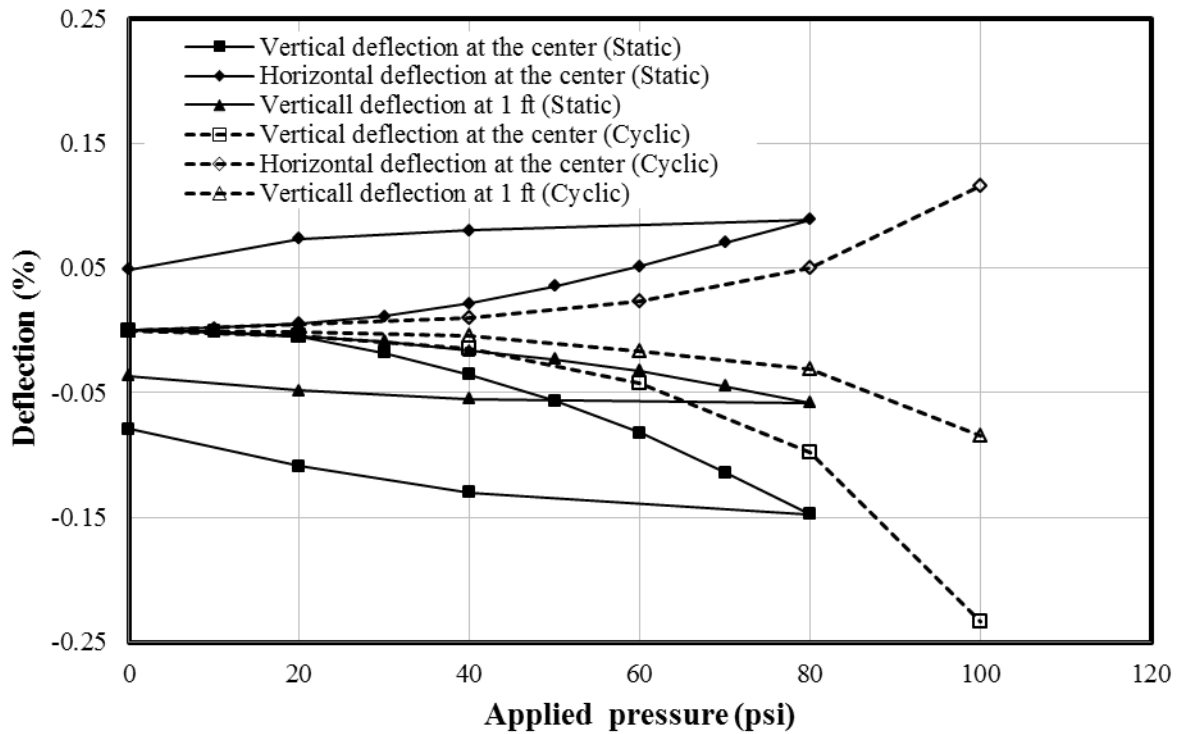


FIGURE 6.127 Comparison of the deflections of the pipe under static and cyclic loads in Test 1

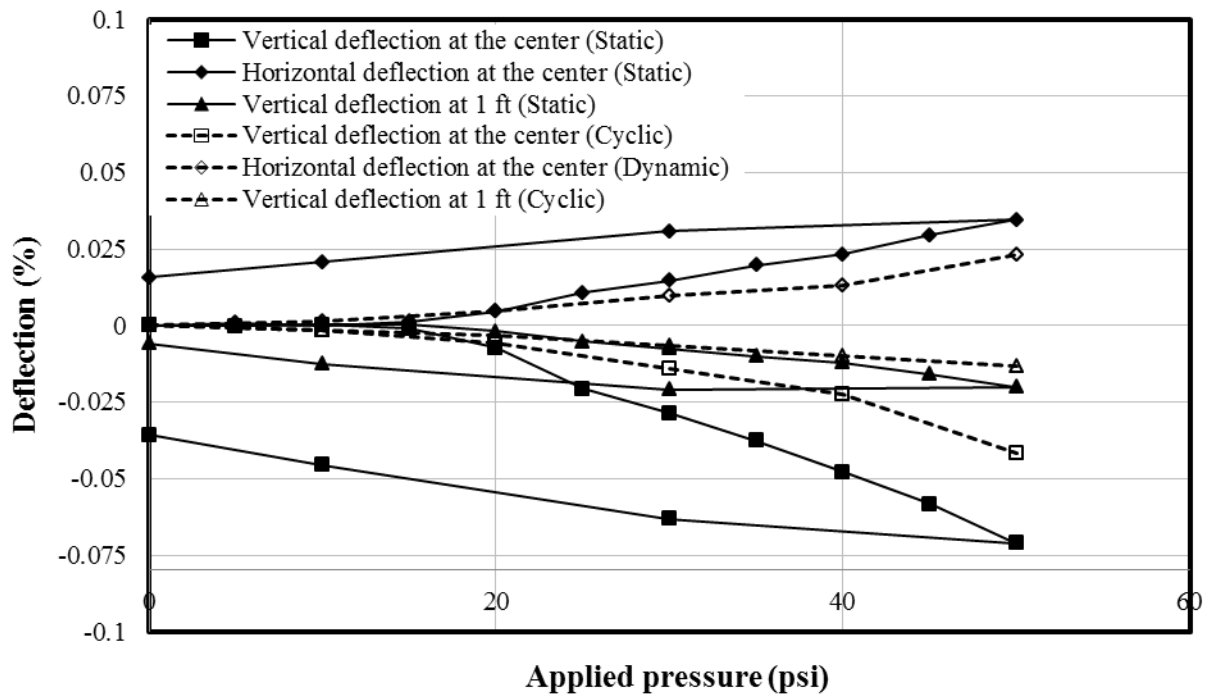


FIGURE 6.128 Comparison of the deflections of the pipe under static and cyclic loads in Test 2

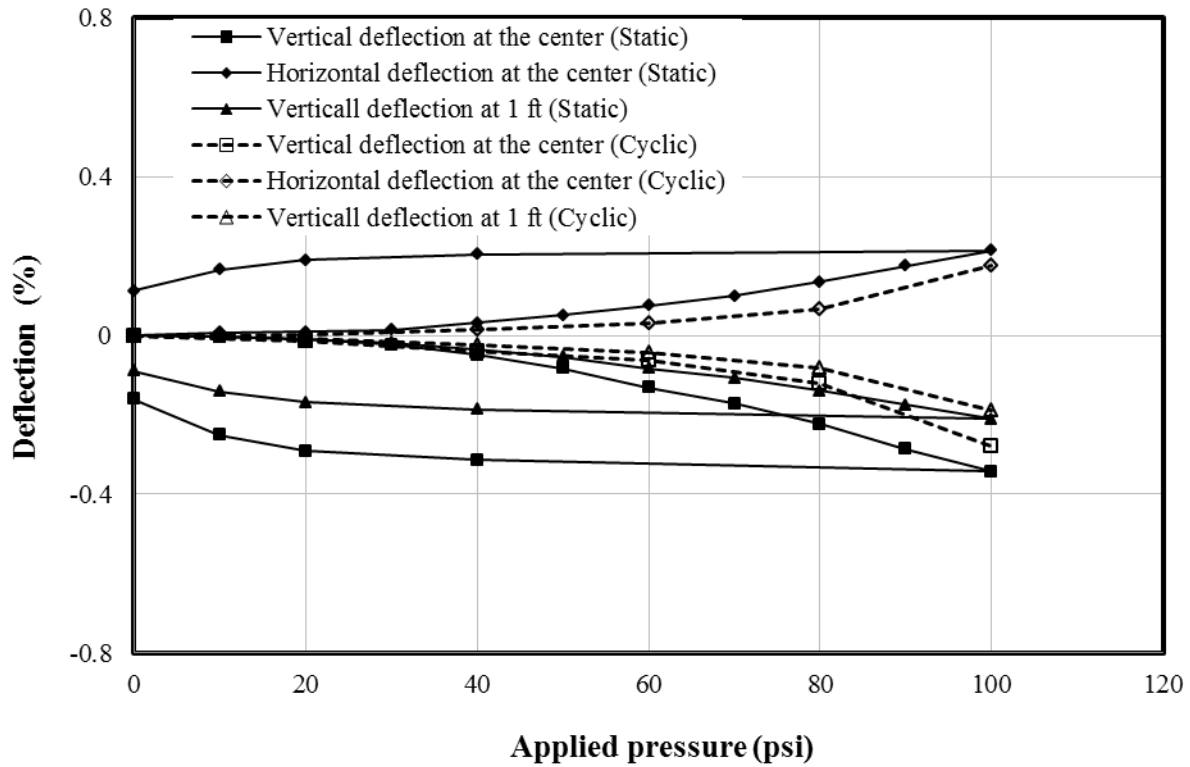


FIGURE 6.129 Comparison of the deflections of the pipe under static and cyclic loads in Test 3

Strain Results

The measured maximum strains on the steel and the plastic at various locations for each test during the installation and loading are shown in TABLE 6.9. The maximum strains on the plastic were higher than those on the steel. Most of the strains on the plastic were tensile. The strains measured on the inside and outside plastic walls were higher than those on the steel and the plastic covers at the ribs.

TABLE 6.9 Maximum measured strains on the steel and the plastic during the installation and loading

Location		Laboratory Test: Test 1								
		Installation			Static			Cyclic		
		Steel rib	Plastic cover	Plastic wall	Steel rib	Plastic cover	Plastic wall	Steel rib	Plastic cover	Plastic wall
Springline	Circum.	-0.0265	0.114	-0.137	-0.0034	0.0061	0.0129	0.0069	0.0479	-0.0269
	Radial	0.0093	0.039	-0.180	0.0031	0.0147	0.0129	-0.0011	0.0065	0.0176
Invert	Circum.	0.0075	0.152	0.054	-0.0018	0.0033	-0.0002	-0.0053	0.0296	-0.0089
	Radial			0.066			0.0051			-0.0006
Crown	Circum.			0.158	-0.0066		0.1277			0.1673
	Radial	-0.0253	-0.083	0.158	0.0019	-0.0132	0.0670	0.004	0.0265	0.0942
		Laboratory Test : Test 2								
Springline	Circum.				-0.0032	-0.0061	0.0068	0.0014	0.0019	-0.0269
	Radial				-0.0038	0.0049	-0.0203	-0.0018	0.0083	0.0082
Invert	Circum.				0.00077	0.0010	0.0045	0.0027	0.0021	-0.0074
	Radial						0.0045			0.0021
Crown	Circum.				0.00096		0.0700			0.0408
	Radial				0.00096	0.0098	0.0512	0.0014	0.0070	0.0256
		Laboratory Test : Test 3								
Springline	Circum.	0.0464	0.091	0.060	-0.013	0.0219	0.1496	0.016	0.0270	0.0309
	Radial	0.034	0.048	0.142	0.008	-0.0258	0.1019	0.0057 1	-0.0203	0.1612
Invert	Circum.	0.0227	0.045	-0.054	-0.009	0.1806	0.0258	0.0099	-0.0258	0.0412
	Radial			0.141						
Crown	Circum.			0.072	-0.0061		0.1870			0.0825
	Radial	0.0253	0.058	0.191	0.0112	0.0696	0.3483	0.013	0.0528	0.2554
		Field Test: Section A								
Springline	Circum.	-0.007			-0.00436		0.001			
	Radial		-0.25	-0.1		0.01	0.02			
Invert	Circum.			-0.1			0.0001			
	Radial		-0.07	-0.174		0.001	0.0001			

Location		Installation			Static			Cyclic		
		Steel rib	Plastic cover	Plastic wall	Steel rib	Plastic cover	Plastic wall	Steel rib	Plastic cover	Plastic wall
Crown	Circum.	0.034		-0.24	-0.011		0.03			
	Radial		0.34	0.25		0.032	0.17			
Field Test : Section B										
Springline	Circum.	-0.012		-0.1			-0.025			
	Radial		-0.2	-0.1		0.02	-0.017			
Invert	Circum.			-0.03			0.002			
	Radial		-0.1	-0.03		0.02	0.002			
Crown	Circum.	0.02		-0.33	-0.004		0.03			
	Radial		-0.28	0.25		0.038	0.2			

6.4 Safety against Structural Failure

The SRHDPE pipe was investigated at the strength limit state for: (1) wall area of the pipe, (2) global buckling, and (3) strain.

6.4.1 Wall Area of Pipe

The SRHDPE pipe was investigated at the strength limit state for the wall area of the pipe with and without considering local buckling. Since the wall cross-sections of 24 in. diameter pipe used in the laboratory and 36 in. diameter pipe used in the field are different, both 24 in. and 36 in. diameter pipes were checked against the applied thrusts. The total average measured pressures on the top of the pipe due to static/cyclic loading including the dead load (i.e., soil above the pipe and self-weight of the pipe) were calculated for all tests. The average measured pressure of 11 psi on the top of the pipe under the dead load and static load in Test 3 was the highest among all the laboratory tests. The highest pressure measured on the top of the pipe including the applied traffic and dead loads was 9.3 psi in Test Section A in the field. The

average measured pressures were then used to calculate the thrust (T_L) on the 24 in. and 36 in diameter pipes using **EQUATION 2.42**. The required wall area of the pipe was then calculated as $A_{reqd} = T_L / (\phi F_y)$, where ϕ = resistance factor (1) and F_y = the yield strength of steel (80 psi). The calculated required areas of the pipe-wall were found to be 0.0016 in.²/in. and 0.0021 in.²/in., which were less than the wall areas available, 0.031 in.²/in. for the 24 in. diameter pipe used in the laboratory tests and 0.0297 in.²/in. for the 36 in. diameter pipe used in the field test.

The wall of the pipe should also be checked considering the buckling effects in the pipe. Since the buckling tests were conducted only on the 24 in. diameter pipe, the check for the thrust considering the buckling was carried out only on the 24 in. diameter pipe. To include the effect of the local buckling, the area of the pipe wall (0.031 in.²/in.) was reduced to an effective area A_{eff} . The effective area of the pipe wall A_{eff} was determined using the stub compression test following AASHTO T341. The effective area of the pipe wall, which was calculated as $A_{eff} = P_{st}/F_y$ where P_{st} = the stub compression capacity (see **SECTION 3.1.2**) and F_y = the yield strength of steel (80 ksi), was found to be 0.025 in.²/in if the stub compression capacity obtained by the independent test laboratory TRI was used. The effective area of the pipe wall (0.025 in.²/in.) was also higher than the required wall area of 0.0016 in.²/in. These results indicate that SRHDPE pipes maintain wall stability under expected traffic loads when the pipes are installed at the shallow depth as specified in the 2007 KDOT specification or the 2007 AASHTO LRFD Bridge Design Specifications. The gross pipe-wall area was reduced by approximately 20% if the local buckling was considered. The precise preparation of the specimen ends for the stub compression test may result in the effective area A_{eff} even closer to the gross area. This result concludes that the local buckling may not be an issue for an SRHDPE pipe under a shallowly buried condition (2 feet from the surface) subjected to traffic loading.

6.4.2 Global Buckling

The wall area of the pipe was also investigated for global buckling using **EQUATIONS 2.27** and **2.28** according to the 2007 AASHTO LRFD Bridge Design Specifications. For the 24 in. diameter pipe, the critical buckling stress was found to be 270 ksi, which was much higher than the yield strength of the steel ($f_y = 80$ ksi). The critical buckling stress was found to be 76 ksi for the 36 in. diameter pipe, which was close to the yield strength of the steel ($f_y = 80$ ksi). This result indicates that global buckling is not an issue for the 24 in. diameter SRHDPE pipe. In other word, the pipe may fail with the yielding of the material before the global buckling. However, the 36 in. diameter pipe may fail either with the yielding or global buckling as the critical buckling stress is close to the yield strength of the steel.

6.4.3 Strain Limit

From **TABLE 6.9**, the highest measured strain on the steel among all the tests was 0.046%, which was less than the strain limit of 0.28% calculated at the yield point of the steel as $\epsilon = F_y/E$ (where F_y = the yield strength of the steel and E = young's modulus of elasticity of the steel). The highest measured strain on the plastic during the installation and loading among all the tests in the laboratory and field was 0.35%, which was within the permissible limit of 5% (the 2007 AASHTO LRFD Bridge Design Specifications).

6.5 Handling and Installation Requirement

The AASHTO M294-07 specifications and KDOT use the parallel plate load test to verify that corrugated HDPE pipes have minimum pipe stiffness at 5% deflection to pipe

diameter, and no buckling or loss of load before 20% deflection. The stiffness criterion at 5% deflection to pipe diameter is important for handling and installation of pipes, while the 20% deflection criterion provides necessary ultimate load capacity. From the parallel plate load test, the calculated pipe stiffness of 43 psi is more than the specified value (34 psi) per ASTM F2562/F2562M for Class 1 pipe of 24 in. in diameter at 5% vertical deflection to pipe diameter. The calculated pipe stiffness of approximately 35 psi for the 36 in. diameter SRHDPE pipe is also more than the specified value (22 psi) per ASTM F2562/F2562M for Class 1 pipe of 36 in. in diameter at 5% vertical deflection to pipe diameter. Furthermore, the load at 20 % deflection is greater than 75 % of the peak load for both 24 and 36 in. diameter pipes, although the peak load was reached before 20 % deflection. This result indicates that the 24 and 36 in. diameter SRHDPE pipes met the handling and installation requirement.

CHAPTER 7 CONCLUSIONS AND RECOMMENDATIONS

7.1 Conclusions

Steel-reinforced high-density polyethylene (SRHDPE) pipes were investigated in this study in the laboratory through compression tests of pipe specimens in air, installation of pipes in soil in a large geotechnical test box, and static and cyclic plate loading tests in the test box. The results obtained from the experimental study were also verified with the results obtained by conducting the field test. The following conclusions were drawn from these experimental studies.

7.1.1 Compression Tests in Air

1. Parallel plate loading test results showed that the tested SRHDPE pipes met both the minimum pipe stiffness and buckling limit criteria according to the ASTM F2562/F2562M. The SRHDPE pipes met the handling and installation requirement according to the ASTM F2562/F2562M.
2. Parallel plate test conducted on the exhumed pipe suggested that the installation and the loadings did not damage the structural integrity of the SRHDPE pipe.

7.1.2 Laboratory and Field Installation

3. Based on the measured earth pressures on the pipe crown both in the laboratory and field tests, the calculated vertical arching factors (VAFs) varied from 0.97 to 1.44 both in the laboratory and field tests with an average value of approximately 1.26 in the laboratory and 1.15 in the field test. Based on the criteria on the VAFs described by McGrath (1998), the SRHDPE pipe behaved as a corrugated steel pipe. The calculated VAFs were higher than the VAFs obtained using the Burns and Richard solutions based on the full-

slip pipe-soil interface but less than the VAFs based on the fully-bonded pipe-soil interface. Therefore, the SRHDPE pipe-backfill soil interface should be considered fully-bonded in design to be conservative.

4. The calculated coefficients of lateral earth pressure (K) around the pipe were found to be between the coefficient of lateral earth pressure at rest (K_o) and the coefficient of passive earth pressure (K_p) for the compacted sand backfill and the crushed stone. However, the K value for the dumped crushed stone was close to K_o .
5. The pipe exhibited peak deflections during backfilling. Both in the laboratory and field tests, the measured peak deflections were larger than those deflections of the pipe under loadings under various backfills (the Kansas River sand and the crushed stone CS-I (dumped) in the laboratory tests and the AB-3-II aggregate and the crushed stone CS-II (compacted) in the field test). The magnitude of the peak deflection found to be more dependent on the compaction efforts used in the installation of the pipe. The peak deflection during the installation of the pipe with the crushed stone backfill compacted at 89% relative density were higher than that for the crushed stone, which was placed by dumping without additional compaction. The peak deflection obtained for the crushed stone compacted at 89 % relative density using the vibratory compactor was higher than that obtained for the AB-3-II aggregate compacted at approximately 90% of the optimum maximum dry density using the tamping hammer.
6. The formula proposed by Masada and Sargand (2007) under predicted the peak deflection of the pipe in the most of the installation conditions.
7. The modified Iowa formula reasonably predicted the deflection of the pipe installed in the dumped crushed backfill but under-predicted that in the compacted backfills. The

larger measured deflection of the pipe installed in the compacted sand backfill may be due to the fact that the compaction-induced pressure on the top of the pipe was not considered.

8. The deflection maximum deflection of the SRHDPE pipe installed in the field after 30 days of construction was much less than the permissible deflection of 7.5% according to the 2007 KDOT Pipe and Culvert Specifications practice. No cracks in the pipe and no issues at joints of the pipe were found after the 30 days of installation.

7.1.3 Static Laboratory and Filed Tests

9. The Giroud and Han (2004) method accurately predicted the vertical earth pressure on the top of the pipe induced by the applied load on the surface when the stiff AB-3-I base aggregate was placed on the top of the backfills. The 2007 AASHTO LRFD Bridge Design Specifications slightly over-predicted the vertical earth pressure in the test sections with the AB-3 aggregate as a base course. This suggests that the approximate method, Giroud and Han (2004), can be used to predict the load on the of SRHDPE pipes.
10. The ratio of the average measured horizontal earth pressure from the side backfill to the pipe to the measured pressures at the pipe crown was approximately 0.32 for the compacted KR sand, from 0.16 to 0.21 for the compacted AB-3-II aggregate, from 0.08 to 0.05 for the uncompacted crushed stone CS-I, and from 0.11 to 0.08 for the compacted crushed stone CS-II.
11. The calculated coefficients of lateral earth pressure (K) for the dumped crushed stone backfill were found to be close to K_o .

12. The modified Iowa formula overpredicted the deflection of the pipe under the applied load.
13. If the horizontal deflection of a buried SRHDPE pipe is known, the vertical deflection of the SRHDPE pipe can be comfortably predicted using the relation proposed by Masada (2000).

7.1.4 Static and Cyclic Plate Loading Tests

14. The measured earth pressures around the pipe and the deflections of the pipe under static loading were higher than those under cyclic loading.
15. The SRHDPE pipe material did not yield under the static and cyclic loads when the pipes were installed at the shallow depth.
16. The SRHDPE pipes maintained wall stability against the local buckling under the static and cyclic loads when the pipes were installed at the shallow depth.
17. The 2007 AASHTO LRFD Bridge Design Specifications design theory for corrugated metal pipes suggested that the SRHDPE pipe did not have a global buckling issue.
18. The highest measured strains recorded in steel and plastic during the installation and loading in all the tests were within the permissible values.
19. The out of plane buckling observed on the ribs of the pipe in the parallel plate test in air did not occur in the buried condition.

7.2 Recommendations

This report focuses on the experimental study conducted on the SRHDPE pipes in air or buried at the shallow depth in a ditch condition with various backfills and loading conditions. In this study data were collected from the laboratory tests and verified the results with the field test.

The data were also collected during the installation of the pipe. The experimental results were verified with most of the available theoretical solutions. This study now provides enough data collected both in the laboratory and field tests on the SRHDPE pipes. The data collected in this study can be used to do the parametric study for the performance of the pipe in the future using the numerical analysis. The following research is recommended for future studies to further understand the behavior of the SRHDPE pipes:

1. Parametric study of SRHDPE pipes;
2. Theoretical development to establish the design procedure for the SRHDPE pipes.

REFERENCES

American Association of State Highway and Transportation Officials (AASHTO) (1992).
Standard Specifications for Bridge Design, Washington, D.C

American Association of State Highway and Transportation Officials (AASHTO) (1996).
Standard Specification for Corrugated Polyethylene Pipe, 300 to 1500 mm (12 to 60 in.) Diameter, Washington, D.C.

American Association of State Highway and Transportation Officials (AASHTO) (2000).
Interim AASHTO LRFD Bridge Design Specifications, Washington, D.C.

American Association of State Highway and Transportation Officials (AASHTO) M36 (2003).
Standard Specifications for Corrugated Steel Pipe, Metallic-Coated, for Sewers and Drains.
Washington, D.C, 1-23.

American Association of State Highway and Transportation Officials (AASHTO) (1998).
Standard Specifications for Bridge Construction, Washington, D.C.

American Association of State Highway and Transportation Officials (AASHTO) (2007).
Standard Specifications for Bridge Design, Washington, D.C.

American Association of State Highway and Transportation Officials (AASHTO) M294 (2009).
Standard Specifications for Highway Bridges, Washington, D.C.

American Association of State Highway and Transportation Officials (AASHTO) (2010).
Standard Specifications for Bridge Construction, Washington, D.C.

American Association of State Highway and Transportation Officials (AASHTO) T341 (2010).
Standard Method of Test for Determination of Compression Capacity for Profile Wall Plastic Pipe by Stub Compression Loading, Washington, D.C.

American Society for Testing and Materials (ASTM D2321) (2011). *Standard Practice for Underground Installation of Thermoplastic Pipe for Sewers and Other Gravity-Flow Applications.*

American Society for Testing and Materials (ASTM D2412) (2002). *Standard Test Methods for Determination of External Loading Characteristics of Plastic Type by Parallel Plate Loading.*

American Society for Testing and Materials (ASTM F2562/F2562M) (2010). *Specification for Steel Reinforced Thermoplastic Ribbed Pipe and Fittings for Non-Pressure Drainage and Sewerage.*

American Water Works Association (AWWA M11) (2004). *Steel Pipe: A Guide for Design and Installation (M11).*

Arockiasamy, M., Chaallal, O., and Limpeteeparakarn, T. (2006). "Full-scale field tests on flexible pipes under live load application." *Journal of Performance of Constructed Facilities*, ASCE, 21-27.

Bishop, R.R. and Lang, D.C. (1984). "Design and performance of buried fiberglass pipes – a new perspective." *Pipeline Materials and Design*, B.J. Schrock (ed.), ASCE, 1-12.

Brachman, R.W.I., Moore, I.D., and Munro, S.M (2008). "Compaction effects on strains in thermoplastic culverts." *Geosynthetic International*, 15(2), 72-85.

Bryan, G.H., (1891). "On the stability of a plane plate under thrusts in its own plan with applications to the buckling of the sides of a ship", *Proceedings of the London Mathematical Society*, 22, 55-67.

Burns, J.Q. and Richard, R.M. (1964). "Attenuation of stresses for buried cylinders." *Proceedings of the Symposium on Soil Structure Interaction*, the University of Arizona, Tucson, Arizona, 378-392.

Burmister, D.M (1958). "Evaluation of Pavement Systems of the WASHO Road Test by Layered System Method." *Bulletin 177*, Highway Research Board, 26-54.

Cameron, D.A. (2006). *Analysis of Buried Pipes in Granular Backfill Subjected to Construction Traffic*. Ph.D. Dissertation, the University of Sydney.

Carlstrom, B. and Molin, J. (1966) *Kunststoffe*, 56(12), 895-898.

Chambers, R.F., McGrath, T.J., and Heger, F.J. (1980). *Plastic Pipe for Subsurface Drainage of Transportation Facilities*. NCHRP Report 225, Transportation Research Board, 122-140.

Dhar, A.S. and Moore, I.D. (2006). "Evaluation of local bending in profile-wall polyethylene pipes." *Journal of Transportation Engineering*, 132(11), 898-906.

DiFrancesco, L.C. (1993). *Laboratory Testing of High Density Polyethylene Drainage Pipes*. MSc Thesis, Department of Civil Engineering, the University of Massachusetts.

Duncan, J. (1980). "Hyperbolic Stress-Strain Relationship". Proceeding of Workshop on Limit Equilibrium, Plasticity, and Generalized Stress-Strain in Geotechnical Engineering. ASCE.

Faragher, E. (1997). *Structural Performance of Thermoplastic Drainage Pipes*. M. Phil Thesis, Loughborough University, Loughborough, Leicestershire, U.K.

Faragher, E., Feleming, P.R, and Rogers, C.D.F. (2000). "Analysis of repeated load field testing of embedded plastic pipes." *Transportation Research Record 1514, Transportation Research Board*, Washington, D.C., 271-277.

Folkman, S.L. (2011). *Monitoring of DuroMaxx Pipes Installed on Manhead Road in Rich County Utah (First Three Inspections)*. Final Report Submitted to Utah Department of Transportation Research Division by Utah State University.

Giroud, J.P. and Han, J. (2004). Design Method for Geogrid-Reinforced Unpaved Roads, Part I Theoretical Development. *ASCE Journal of Geotechnical and Geoenvironmental Engineering*, 130 (8), p 776-786.

Goddard, J.B. (1992). "Plastic pipe design." *Ohio Transportation Engineering Conference*.

Goddard, J.B. (1994). *Plastic Pipe Design*. Technical Report 4.103, Advanced Drainage Systems Inc.

Gumbel, J.E. and Wilson, J. (1981). "Interactive design of buried flexible pipes - A fresh approach from basic principles." *Ground Engineering*, 14(4), 36-40.

Hardert, M.T., (2011). *Shape Measurement of Existing 120" Diameter*. Report Submitted to Contech Construction Products, Inc.

Hartley, J.D. and Duncan, J.M. (1987). "E' and its variation with depth." *Journal of Transportation Engineering*, ASCE, 113(5), 538-553.

Hashash, N.M.A. and Selig, E.T. (1990). *Analysis of the Performance of a Buried High Density Polyethylene Pipe*. Structural Performance of Flexible, Sergand, Mitchell, and Hurd (eds.), A.A. Balkema, Rotterdam, Netherlands.

Howard, A.K. (1977). "Modulus of soil reaction values for the buried flexible pipe." *Journal of the Geotechnical Engineering Division*, ASCE, 103(1), 33-43.

Howard, A.K. (1981). "The USBR equation for predicting flexible pipe deflection." *International Conference on Underground Plastic Pipe*, New Orleans, Louisiana, 37-55.

Janbu, N. (1963). "Soil Compressibility as Determined by Oedometer and Triaxial Tests." European Conference on Soil Mechanics and Foundation Engineering, Wissbaden, Germany, Vol.1, pp 19-25.

Kansas Department of Transportation (2007). *Standard Specification for Pipe and Culvert*. Kansas Department of Transportation (KDOT), Topeka, KS.

Kansas Department of Transportation (2012). *State Transportation Improvement Program Fiscal Year 2013-2016*. Kansas Department of Transportation (KDOT), Topeka, KS.

Katona, M.G. (1988). *Minimum Cover Heights for HDPE Corrugated Plastic Pipe under Vehicular Loading*. Report to Corrugated Plastic Tubing Association.

Khatri, D.K. (2012). *Experimental Evaluation of the Behavior of Steel-Reinforced High Density Polyethylene (SRHDPE) Pipes*. MSc Thesis, Department of Civil Engineering, the University of Kansas.

Kondner, R. (1963). Hyperbolic Stress-Strain Response of Cohesive Soils. *J.S.M.F.D.* ASCE, Vol. 89.

Krizek, R.J., Parmelee, R.A., Kay, J.N., and Elnaggar, H.A. (1971). *Structural Analysis and Design of Pipe Culverts*. National Cooperative Highway Research Program, Report 116, Highway Research Board, Washington, D.C.

Leonhardt, G. (1978). "Belastungsannahmen bei erdverlegten GFK-Rohren." AVK, Freudenstadt.

Marston, A. and Anderson, A.O. (1913). *The Theory of Loads on Pipes in Ditches and Tests of Cement and Clay Drain Tile and Sewer Pipe*. Iowa Engineering Experiment Station, Ames, Iowa, Bull No. 31.

Marston, A. (1930). *Theory of External Loads on Closed Conduits in Light of the Latest Experiments*. Iowa State College, Ames, Iowa, Bulletin 96.

Masada, T. (1996). *Structural Performance of Profile-Wall Plastic Pipes under Relatively shallow Soil Cover and Large Surface Loading*. PhD Dissertation, MCollege Of Engineering and Technology, Ohio University, Athens, Ohio.

Masada, T. (2000). Modified Iowa Formula for Vertical Deflection of Buried Flexible Pipe. *Journal of Transportation Engineering*, 125 (5), p 440-446

Masada, T. and Sargand, S.M. (2007). “Peaking deflections of flexible pipe during initial backfilling process.” *Journal of Transportation Engineering*, ASCE, 133(2), 105-111.

Masajedain, S. S. (2011). *Experimental Investigation of the Behavior of the Steel Reinforced High Density Polyethylene and Corrugated Metal Pipe*. MSc Thesis. The University of Texas at Arlington, TX.

McGrath, T.J. (1998). *Design Method for Flexible Pipes*. A Report to AASTHO Flexible Culvert Liaison Committee, Simpson Gumpertz and Heger Inc., Arlington, Mass.

McGrath, T.J. and Sagan, V.E. (2001). “Design of profile wall thermodynamic pipe for local buckling.” *Transportation Research Record 1170, Transportation Research Board*, 209-219.

McGrath, T.J., DelloRusso, S.J., and Boynton, J. (2002). “Performance of thermoplastic culvert pipe under highway vehicle loading.” *Pipelines 2002*, 1-14.

Meyerhoff, G.G., and Baikie, L.D. (1963). “Strength of steel culvert sheets bearing against compacted sand backfill.” *Highway Research Record*, 30, 1-19.

- Mir Mohammad Hosseini S.M., and Moghaddas Tafreshi, S.N. (2002). “Soil-structure interaction of buried pipes under cyclic loading conditions.” *International Journal of Engineering*, 15(2), 117–124.
- Moghaddas Tafreshi, S.N. and Khalaj, O. (2008). “Laboratory test of small diameter HDPE pipes buried in reinforced sand under repeated load.” *Geotextiles and Geomembranes*, 26(2), 145-163.
- Molin, J. (1981). “Flexible pipe buried in clay.” *Proceedings of International Conference on Underground Plastic Pipes*, ASCE, J. Schrock (ed.), New Orleans, 322-337.
- Moore, I.D. (2001). *Culverts and Buried Pipelines*. Geotechnical and Geoenvironment Handbook, R.K. Rowe (ed.), Kluwer Academic Publishers, 541-568.
- Moore, I.D. (2009). *DuroMaxx Pipe Assessment*. Final Report Submitted to Contech Construction Products Inc.
- Moore, I.D. and Hu, F. (1995). “Response of profiled high-density polyethylene pipe in hoop compression.” *Transportation Research Board* 1914, Transportation Research Board, 29-36.
- Moser, A.P. (1998). “Structural performance of buried profile-wall high density polyethylene pipe and influence of pipe wall geometry.” *Transportation Research Record* 1624, Transportation Research Board, 206-213.
- Moser, A.P. (2008). *Buried Pipe Design*. New York: McGraw-Hill, Third Edition.
- Neilson, F.D. (1967). “Modulus of soil reaction as determined from triaxial shear test.” *Highway Research Record* 185, Transportation Research Board, 80-90.
- Pokharel, S.K. (2010). *Experimental Study on Geocell-Reinforced Bases under Static and Dynamic Loading*. Ph.D, Dissertation, University of Kansas.

Rogers, C.D.F., Fleming, P.R., Loeppky, M.W.J., and Faragher, E. (1995). “The structural performance of profile-wall drainage pipe-stiffness requirements contrasted with the results of laboratory and field tests.” *Transportation Research Record* 1514, Transportation Research Board, Washington, D.C., 83–92.

Sargand, S., Masada, T.J., and Hurd, J.O. (1996). “Effect of rib spacing on deformation of profile wall plastic pipes buried in coarse granular backfill.” *ASTM, Geotechnical Testing*.

Schrock, B.J. (1993). “The pipe/soil stiffness ratio variable.” *Proceedings, Pipeline Infrastructure II*, M. Pickell (ed.), American Society of Civil Engineers, San Antonio, TX.

Selig, E.T. (1988). Soil Parameters for Design of Buried Pipelines. *Proceedings of the Pipeline Infrastructure Conference*, ASCE, 1988, pp 99-119.

Selig, E.T. (1990). “Soil properties for plastic pipe installation.” *Buried Plastic Technology*, STP 1093, ASTM, Philadelphia, Pa., 141-155.

Spangler, M.G. (1941). *The Structural Design of Flexible Pipe Culverts*. Iowa Engineering Station Bulletin No. 153, Ames, Iowa.

Trott, J.J. and Gaunt, J. (1976). Experimental pipelines under a major road: performance during and after Road Construction. Transportation and Road Research Laboratory Report 692, Crowthorne, Berkshire, 1-17.

Turkopp, R.C., Torp, S., and Carlstrom, B. (1985). “Buried fiberglass pipe performance and installation requirements and design calculations.” *Advances in Underground Pipeline Engineering: Proceedings of the International Conference*, 383-395.

Von Karman, T., Sechler, E.E., and Donnell, L.H., (1932). “The strength of thin plates in compression.” *Transactions ASME*, 54, 53-57.

Watkins, R.K., (1960). "Failure conditions of flexible culverts embedded in soil." *Highway Research Proceedings*, 39, 361-371.

Watkins, R.K., (1966). "Structural design of buried circular conduits." *Conduits and Behavior of Foundations*, Highway Research Record, Washington, 1-16.

Watkins, R.K. (1971). "Response of corrugated steel pipe to external soil pressures." *Highway Research Record*, 37, 86-96.

Watkins, R.J., Szpak, E., and Allman, W.B. (1973). *Structural Design of Polyethylene Pipes Subjected to External Loads*. Engineering Experiment Station, Utah State University, Logan, Utah.

Watkins, R.K. and Spangler, M.G. (1958). "Some characteristics of the modulus of passive resistance of soil: A study of similitude." *Highway Research Board Proceedings*, 37, Washington, D.C., 576-583.

Webb, M.C., McGrath, T.J., and Selig, E.T. (1996). "Field tests of buried pipe installation procedures." *Transportation Research Record* 1541, 97-106.

Whidden, W.R., (2009). *Buried Flexible Steel Pipe: Design and Structural Analysis*. American Society of Civil Engineers Manuals and Reports on Engineering Practice, No. 119.

White, H.L., and Layer, J.P. (1960). "The corrugated metal conduit as a compression ring." *Highway Research Proceedings*, 39, 389-397.

Winter, G. (1947). "Strength of thin compression flanges." *Bulletin 35 part 3*, Cornell University Engineering Experiment Station, Ithaca, NY.